THE UNIVERSITY *of* EDINBURGH

Microwave Sensing for Neurodegenerative Diseases

Imran Mohammed Saied

A thesis submitted in partial fulfilment of the requirements for the degree of

DOCTOR OF PHILOSOPHY

The University of Edinburgh

August 2020

"My Lord, Increase me in knowledge."

Quran 20:114

To my Khandaan

Declaration of Originality

I hereby declare that this thesis was composed and originated entirely by myself, that the work contained herein is my own except where explicitly stated otherwise in the text, and that this work has not been submitted for any other degree or professional qualifications.

Imran M. Saied
August 2020
Edinburgh, UK

Acknowledgements

بِسْمِ ٱللَّهِ ٱلرَّحْمَٰنِ ٱلرَّحِيمِ

All praise and glory are to Allah, the Beneficent and the Merciful, who is All-Knowing and whose knowledge encompasses everything. He grants knowledge and wisdom to those who seek it and whom He pleases. May His name be forever praised for inspirations for this work, for giving me courage and faith when there seemed to be no hope, for strength and patience when the journey was tough, and for the perseverance and grace to finish it well.

I would like to thank my supervisor, Prof. Tughrul Arslan, for his immense guidance, vision, and support during my PhD. His leadership and mentoring provided me freedom and ample opportunities to not only perform world-class research, but to also be a leader and pioneer in this area and create the foundations for future research to be undertaken in this timely field. I thank him immensely for that. I would also like to thank Prof. Siddharthan Chandran, who provided important guidance and details on the diagnosis of Alzheimer's disease that shaped the journey of my investigation, and Prof. Colin Smith, for providing access to brain tissue samples and labs that led to transformative conclusions generated in this thesis. I would also like to thank the family of Alasdair Sutherland for providing the Alasdair Sutherland Award that helped me to obtain materials to conduct some experiments in this work. Finally, I thank all my friends and colleagues of the EWireless Research Group and in SMC at the University of Edinburgh for creating a friendly and collaborative research environment.

I would like to acknowledge my parents (Sadiq Saied and Sanjida Saied) for their constant sacrifices, love, and support throughout my life. They have both been a source of guidance and inspiration for me in all matters. I am honored and grateful to have them by my side in every step of the way. This work is theirs as much as it is mine. My gratitude also goes to my sister, Dania, for being the loving sibling I need. And to Ateeq and my in-laws for their constant prayers and support.

To my wonderful family around the world: aunts (phuppus and khalas), uncles (chachas and mamu), and all my cousins, I thank you all for your love, support, and *duas* which have given me the motivation to complete this study.

My journey to PhD would not have been possible without mentioning a few more people: My *Hazrat* (Mohammed Akbar Sahib) who taught me the importance of gaining knowledge and provided the tools needed to seek it; Dr. Mahmoud Meribout who introduced me to the world of research and helped me to develop the skills needed to succeed in this area; and finally, the "Big 4" (Bhai Chacha, Phuppuma, Hamshira Aunty, and Didi Aunty) who all taught me patience, perseverance, and faith, tools that were instrumental in my upbringing to help me cope with the pressures of life.

Finally, I would like to thank my wife, Rasheena. She has been a great companion to me and has provided me constant support, love, understanding, and sacrifices during the course of my PhD. And to my princess, Fazeelah, who provided me with much needed comfort and happiness during my time in research, and for instantly removing my stress when I come home. I love you both dearly.

I dedicate this work to my grandparents (Mohammed Aslami Saied, Fathunnisa Saied, Mohamed Usman, and Muneera Begum) who have paved the way for me through their hard work and sacrifices and whom I constantly aspire to be. This work is also dedicated to the people suffering from dementia and those who take care of them. This is an area of great importance now and I hope that this work and future research can lead to more effective monitoring and treatment strategies to help ease the burden. I also dedicate this work to all my family members, past and present, who have played a role in shaping my upbringing. To Fazeelah, Yusuf, and Aafia, I hope one day this thesis leads you to gain knowledge that you can use and share for the benefit of society.

Lay Abstract

The rapidly increasing rate of the ageing population has led to a higher rate in people suffering from neurodegenerative diseases. Neurodegenerative diseases, such as Alzheimer's and Parkinson's disease, are characterised by the progressive loss of brain cells, which leads to a decline in a person's cognitive abilities, and eventually leads to death. The alarming increase in people suffering from these diseases has created a global socioeconomic burden that affects caregivers, nurses, and family members, just as much as the patient themselves. Due to the critical nature of these diseases, it is paramount that systems and devices can detect and monitor neurodegenerative diseases as early as possible, so that the right treatment can be provided to hinder its progression. Existing technologies have provided key results in the detection and monitoring of neurodegenerative diseases. However, they are limited by their bulky size, high costs, and inconvenient or invasive approach.

Meanwhile, microwave sensing technology has generated promising results in several medical applications, such as cancer and stroke detection. The ability to fabricate components easily and integrate them into a wearable prototype makes microwave sensing a promising non-invasive, cost-effective, and portable or wearable solution for medical diagnostics. This work proposes the use of microwave sensing as an inexpensive, non-invasive, reliable, accurate, efficient, and wearable tool for monitoring the progression of neurodegenerative diseases. For evaluation, models were created to emulate symptoms of Alzheimer's disease to demonstrate the technology. It is observed that microwave sensing was able to detect brain atrophy and lateral ventricle enlargement with a minimum change of 5%. In addition, microwave sensing could non-invasively detect and image regions of the brain affected by Alzheimer's disease pathology, providing a transformational and major improvement compared to PET scans that rely on biomarkers. Moreover, microwave sensing could detect Alzheimer's disease at one of its earliest stages: mild cognitive impairment. This work provides a promising and transformative approach for wearable and non-invasive neurodegenerative disease monitoring.

Abstract

Neurodegenerative diseases, such as Alzheimer's disease, is the progressive loss of neurons in the brain that leads to a gradual loss of a person's cognitive functions and eventually leads to death. Key changes that occur in the brain, because of these diseases are faster rates of brain atrophy, lateral ventricle enlargement, and the accumulation of beta amyloid plaques and tau tangles in the brain. Currently, diagnostic tools, such as MRI, CT, and PET scans are used to determine the presence of these diseases by studying the scans over time. Although these systems can provide an accurate diagnosis of the current stage of neurodegeneration in an individual, they have several limitations. This includes high costs, long scanning times, bulky size, and nonportable. In the case of PET scans, these systems can be invasive as it requires patients to be injected with a radioactive biomarker to detect the presence and spread of beta amyloid plaques and tau tangles in the brain. As a result, there is a need for portable and wearable devices that will allow patients to comfortably wear and monitor the progression of neurodegeneration in their brain. In addition, having a portable and wearable technology for neurodegeneration monitoring can be efficient in obtaining measurements at the convenience of the patient while they are at home or in a clinic.

Radar-based microwave imaging technology can offer a low cost, non-invasive and non-ionisation method to complement these existing imaging techniques. Moreover, microwave sensing and imaging technology has been verified for detecting several brain diseases such as stroke and brain tumours. Several studies in recent years have focused on the development of portable and wearable devices and antennas to facilitate frequent or real-time monitoring of a patient while, at the same time, being more comfortable for patients to wear. These benefits and ongoing advancement in the development of wearable microwave head imaging devices served as an incentive for investigating and validating this technology for detecting and monitoring the progression of neurodegenerative diseases, as this is an area that is in great need of timely diagnosis. Furthermore, the wearable device can be integrated into different microwave imaging setups such as real-time wearable head imaging systems, portable

systems, and conventional stationary imaging tools for use in hospitals and clinics. This thesis presents the investigation and validation of microwave sensing and imaging for detecting changes in the brain associated to Alzheimer's disease, and provides proof-of-concept work in the design and development of wearable prototypes using flexible antenna arrays for a wearable microwave imaging neurodegeneration monitoring device (MIND).

The design and characterisation of sensing antennas using flexible materials that will be used for validating the conditions of AD and integrated into wearable MIND devices, are presented in the first stage of this study. There are two main variations of monopole antennas that have been investigated in this research, namely stepped and rectangular configurations. The antennas have been fabricated using a conductive textile material and different flexible substrate materials such as textile and silicone rubber. Wideband performances of the antennas have been achieved by optimising the length of the antenna, thickness of the substrates, and width of the feeding lines. In addition, the efficiencies of the fabricated antennas were tested using a realistic human head phantom by evaluating their impedance matching performances when operating near the head phantom.

The second and third stages of this study evaluates microwave sensing for detecting two physiological changes related to Alzheimer's disease: brain atrophy and lateral ventricle enlargement, respectively. Simulations were carried out to investigate the effects of these symptoms on the antenna's reflection and transmission coefficient values. Experiments were conducted using real lamb brains and an artificial phantom that represents the buildup of cerebrospinal fluid in the lateral ventricles when they enlarge. Two felt-based antennas were placed at different points around the head and subsequent reflection and transmission coefficient data were captured, processed, and analysed. It was found that distinct changes could be seen in both reflection and transmission coefficient data with increasing changes in brain atrophy and lateral ventricle enlargement, respectively.

The validation of microwave sensing in detecting brain tissues affected with beta-amyloid plaques and tau tangles is investigated in the fourth stage of this study and serves as a key validation point for using microwave sensing for detecting Alzheimer's

disease. This stage contains several novel and transformative studies that have not been conducted before. The first part of this research focuses on measuring and recording dielectric properties of human brain tissues with severe Alzheimer's disease pathology and comparing them to dielectric properties of healthy human brain tissues obtained from literature. Measurements were obtained on both the grey matter and white matter regions. The second part discusses about the simulation models that were developed to validate the antennas' performance in detecting the accumulation of affected brain tissues during different stages of AD inside a realistic human voxel model. Finally, the last part discusses about the experiments that were conducted to validate the antennas' ability to detect varying levels of affected brain tissues by using a multi-layered artificially fabricated phantoms to represent a human brain.

The fifth stage of this study investigates the use of a microwave in space-time beamformer imaging algorithm to highlight the presence and location of brain tissues that are affected by beta amyloid plaques and tau tangles. Reflection coefficient data obtained from the experiments was used and the imaging algorithm was modified to map energy values in the head based on the antennas' location around the head. Several modifications to the algorithm were made and many iterations of the algorithm were executed with the data to improve the quality of the reconstructed images. Results showed that the imaging algorithm could successfully highlight areas of the brain that were affected by Alzheimer's disease pathology. In addition, the results provided in this section provides an indication of how microwave imaging could be used as a viable tool for non-invasive and safe monitoring of Alzheimer's disease.

The final stage of this study presents the development of wearable antenna arrays using the proposed flexible antennas. The first prototype was built using an array of 6 flexible felt-based antennas and a conformal absorbing material backed with a conductive sheet to suppress the back lobe radiation of the monopole antennas. Additionally, the absorber also acts as a mounting base to hold the antennas where the wearable device can be comfortably worn like a hat during the measurement and monitoring processes. The effect of mutual coupling between adjacent antennas in the array was investigated and optimised. However, the absorbing material made the device slightly rigid and bulky. Therefore, a second prototype was developed by integrating the silicone rubber-based antennas into a lightweight deerstalker hat that can be worn

on different sizes of human heads. Furthermore, the inner lining of the hat was spacious enough to house the antennas. In addition, a reconfigurable and compact switching circuit was fabricated using low cost off-the-shelf-components and integrated with the antenna array to form a novel wearable MIND device that eliminates the use of external bulky switching network and provides a convenient way of switching between active antennas. The reconfigurable switching circuit prototype was fabricated using a flexible protoboard and several 1P1T switches that connects the antennas with the VNA port through a SMA breakout board. Insertion and return losses were investigated to determine the performance of the antennas with the switching circuit.

The results reported in this thesis makes a valuable and transformative contribution to ongoing Alzheimer's disease research in diagnosing and monitoring early stages of the disease. In addition to Alzheimer's disease, this work could also be applied to other similar neurodegenerative diseases, such as Lewy Body dementia and frontotemporal dementia. Due to the ability of developing wearable and portable devices with this technology, it has the potential of providing a conformable, convenient, and more timely solution and diagnosis to patients, while at the same time easing the burden for nurses and care givers in providing the right treatment and understanding the progression or stage of the disease of their patients. This study impacts not just research for Alzheimer's disease, but also can impact areas such as microwave medical imaging, social care, and neurodegenerative disease research. In addition, it is expected that low-cost, compact, and wearable radar-based microwave head imaging devices and flexible antennas and circuits can be fully realised in the future for wide range of applications including static scanning setup in hospitals, portable equipment in ambulances and as a standalone wearable head monitoring system for remote and real-time monitoring purposes.

Table of Contents

List of Figures

List of Tables

List of Symbols

π	Pi
r	Effective radius of equivalent cylindrical monopole antenna
L	Planar monopole patch length
W	Planar monopole patch width
h	Thickness of the substrate
c	Speed of light
λ	Wavelength
f_L	Lowest band-edge frequency
k	Dielectric layer
ε_{eff}	Effective dielectric constant
ε_R	Dielectric constant of the substrate
Z_0	Characteristic impedance of the microstrip feeding line
W_f	Width of the microstrip feeding line
Z_{in}	Input impedance
Z_A	Impedance of antenna
Z_1	Characteristic input impedance of quarter wave transmission line
F	Fidelity factor
$f(t)$	Excitation pulse
$g(t)$	Received pulse at the antenna
r_{near}	Near-field region
λ_m	Operating wavelength in the medium of transmission
D	Largest diameter of antenna
σ	Electrical conductivity
ρ	Mass density of tissue
E	Received electric field from radiated energy
σ_{37°	Adjusted conductivity
$\varepsilon_{r,37^\circ}$	Adjusted relative permittivity
TC_σ	Derived average temperature coefficient of conductivity

TC_ε	Derived average temperature coefficient of relative permittivity
T_t	Temperature of tissue when dielectric measurement was taken
$\varepsilon(\omega)$	Complex relative permittivity
$\varepsilon'(\omega)$	Relative permittivity
$\varepsilon''(\omega)$	Loss factor
ω	Angular frequency
ε_0	Permittivity of free space
$\varepsilon_C(\omega)$	Four-pole Cole-Cole model
τ_i	Relaxation time
α_i	Dispersion region coefficient
σ_s	Static conductivity
$\Delta\varepsilon_i$	Magnitude of dispersion
ε_{si}	Static permittivity
ε_∞	Infinite permittivity
L_n	Location of antennas
d	Distance between antenna and imaging area
x_0, y_0	Coordinates of image pixel
a	Diameter of imaging area
N	Number of input samples for each antenna
$I[n]$	Intensity vector value
A_n	Signal at Antenna *n*
N_A	Total number of antennas
S_{11}	Reflection coefficient
S_{21}	Transmission coefficient

Abbreviations and Acronyms

Aβ	Amyloid Beta
AD	Alzheimer's disease
BA	Brain Atrophy
BOLD	Blood Oxygen Level-Dependent
CT	Computed Tomography
DAS	Delay and Sum
DAS-CF	Delay and Sum Coherence Factor
DSC	Dice Similarity Coefficient
EM	Electromagnetic
fc-MRI	Functional Connectivity Magnetic Resonance Imaging
FDG	Fluorodeoxyglucose
fMRI	Functional Magnetic Resonance Imaging
FTLD	Frontotemporal Lobar Degeneration
IDFT	Inverse Discrete Fourier Transform
IFFT	Inverse Fast Fourier Transform
LBD	Lewy Body Dementia
LVE	Lateral Ventricle Enlargement
MCI	Mild Cognitive Impairment
MIND	Microwave Imaging for monitoring Neurodegeneration Device
MIST	Microwave Imaging via Space-Time
MRI	Magnetic Resonance Imaging
MWI	Microwave Imaging
MWS	Microwave Sensing
MWT	Microwave Tomography
PD	Parkinson's disease
PET	Positron Emission Tomography
PiB	Pittsburgh Compound-B Tracer
PMA	Planar Monopole Antenna
RF	Radio Frequency

RPMA	Rectangular Planar Monopole Antenna
SAM	Specific Anthropomorphic Mannequin
SAR	Specific Absorption Rate
SEM	Scanning Electron Microscope
SPMA	Stepped Planar Monopole Antenna
UWB	Ultra-wideband

Chapter 1

Introduction

The background and motivation of this research for using microwave and radio frequency (RF) sensing to monitor neurodegenerative diseases, such as Alzheimer's disease (AD), is presented in this chapter.

1.1 Research Motivation

Neurodegenerative diseases, such as AD and Parkinson's disease (PD), are an incurable and progressive disease that have become a major public burden in recent years. There are an estimated 850,000 people in the U. K. affected by AD, and it is the sixth leading cause of death in the U.S.A [1], [2]. Current diagnostic methods for neurodegenerative diseases involve patients undertaking several cognitive assessment tests and brain scans using magnetic resonance imaging (MRI), computed tomography (CT), or positron emission tomography (PET) scans [3]. All these modalities have their own advantages and disadvantages depending on the types of symptoms or changes (both physiological and pathological) that can occur in the brain. In general, the main goals of these systems are to provide accurate, fast, safe, and cost-effective imaging to patients to detect the disease as early as possible and monitor its progression so that the right treatment can be administered to them.

Microwave sensing (MWS) for medical applications is a novel method that has been the focus of extensive research over the past two decades, undergoing extensive research through computer simulations and experimental work. This method was first introduced back in 1973 to detect lung diseases [4],[5], Since then, microwave technology for medical applications has been extensively studied and applied to different types of diseases including breast and lung cancers, traumatic brain injuries, bone fractures, and stroke [6], [7], [8]–[15].

Microwave medical imaging can be classified into two major groups: microwave tomography and radar-based technique (or microwave imaging (MWI)). Microwave

tomography (MT) aims to reconstruct the actual dielectric profile of a human body while MWI systems operate by transmitting short pulses to detect the main electromagnetic (EM) signal scatterers inside the body. In addition, MWI differs from MWS in that while MWS only focuses on capturing changes in the signal data, MWI takes the process further by implementing an imaging algorithm to reconstruct images using the signal data. Nonetheless, all the techniques rely on the scientific study that shows the malignant tissue (i.e., cancerous tissue or haemorrhagic stroke (the blood clot formed inside the brain due to ruptured vein)) based on it having a different dielectric constant value than the surrounding healthy tissues [16], [17]. The scattered waves are then collected and analysed to produce a valuable image which would determine the location of the anomaly inside the imaged body part.

Radar-based microwave imaging technique was initially applied for stroke detection in [18], [19]. The main advantage of using radar-based system compared to tomography technique is that it requires less computational power which can reduce the overall time for detection; hence, paving the way for a fast or even real-time monitoring system. In comparison to a MT system which reconstructs the dielectric profile of the imaged body, the main objective of radar-based technique is to create an image of the main scatterers inside the human body which is normally attributed to the existence of malignant tissues. In [19], 16 Vivaldi antennas were used to scan a realistic head phantom. The operating frequency range of the antenna is from 1 GHz to 4 GHz. The selection of the frequency band was made to ensure sufficient penetration depth is achieved to scan the lossy multi-layer human head as well as to provide high resolution image. Subsequently, portable microwave systems using compact directional antennas for traumatic brain injuries were proposed in [20]. A compact transceiver was used for the signal generation and acquisition. A successful detection of a bleeding inside a realistic head phantom was reported.

Rapid development in the field of compact, wearable, and portable electronics has driven innovation in the health sectors where a lot of focus have been given to implement a remote health monitoring system [21]. The monitoring devices must be designed to be conformable to the user, easy to use and low cost. One of the main advantages of wearable devices for medical applications is that they can be comfortably

worn and used by patients at home instead of being taken to clinics to perform scans. To alert medics in case of an emergency, an alerting system that directly connects the patients to rapid response teams can be established over wireless communication channels [21]. An example of remote monitoring systems in the literature is a pulmonary edema monitoring sensor that was presented in [22]. The system was proposed to provide real-time monitoring of internal organs for patients that require supervised recovery from a surgical procedure.

In this research, microwave sensing (MWS) and MWI techniques were investigated to determine its effectiveness as a viable option for non-invasive and early detection of AD, particularly in identifying its three main conditions: 1) brain atrophy, 2) lateral ventricle enlargement, and 3) accumulation of AD pathology in brain tissues. As part of the research work conducted for this thesis, wearable and flexible antenna arrays were designed, simulated, and fabricated from textile and silicone rubber substrates. These were then validated on phantoms mimicking several symptoms of AD. In addition, as a proof-of-concept, these antennas were integrated into two wearable hat-like prototypes along with a switching circuit, to show how they could be used as a standalone wearable device for monitoring AD conditions. Studies have suggested that early detection of AD is paramount to providing the necessary treatments that can help patients to slow down the progression of the disease and help alleviate the burden faced by caregivers [23]. Thus, there is a pressing need to provide constant monitoring and frequent checking for patients-at-risk. In addition, the major disadvantage with current diagnostic systems (e.g., MRI, CT, and PET scans) are that patients must take several iterations of these tests and scans over a span of many months and/or years before a diagnosis is confirmed. At which point, the disease has advanced to a stage where it is difficult for caretakers to manage patients and provide the right treatment to them. Another disadvantage is that the systems used to perform brains scans are expensive, non-portable, sometimes invasive, and can be uncomfortable due to their claustrophobic nature. In addition, these technologies do not provide an indication of neurodegenerative disease at earlier stages and are not suitable for constant monitoring of patients due to their large size and high cost. Since flexible antennas are used as sensors in the proposed microwave imaging system, the concept of wearable device for head imaging specifically for AD detection is possible for real-

time monitoring applications. Furthermore, the proposed technology, along with the diagnostic methodology used for detecting AD, can be utilised for detecting and monitoring other types of neurodegenerative diseases or dementias, such as PD and Lewy Body dementia (LBD).

1.2 Research Investigations

The main challenge of the research study that is being investigated is the overall validation of microwave sensing and imaging techniques as a viable option for non-invasive monitoring of Alzheimer's disease, and other neurodegenerative diseases. Other challenges that arose from this research include:

1. the design of suitable wideband antennas using several flexible antenna substrates,
2. the development of reconfigurable RF switching circuits to realise on an integrated wearable microwave head sensing device when combined with flexible antenna arrays,
3. the dielectric measurements of brain tissues with AD pathology and comparing with those from a healthy human brain,
4. the performance evaluation of the wearable device using realistic head phantoms that mimic the physiological and pathological changes in the brain associated with AD, and
5. the development of a microwave imaging via space-time algorithm that creates a useful image of the brain that indicates the presence and location of plaques and tangles.

1.2.1 Design Challenges

A. Antenna Design

For radar-based microwave biomedical imaging, a wideband antenna is required to investigate how changes in the brain related to AD affect the signal parameters at different frequencies. Some changes affect one side of the brain while the other side is

unaffected. In addition, these antennas will adapt to a microwave imaging algorithm such as confocal delay-and-sum technique to reconstruct an image of the main scatterers inside the human body. The scattered signals are due to differences in dielectric constants of unhealthy tissues (e.g., tumours or strokes) from their healthy surrounding tissues. To apply microwave technology for head imaging and AD detection, a proper antenna design is crucial to ensure that the sensing antenna can detect three key changes that occur in the brain: 1) brain atrophy (BA) [24], 2) lateral ventricle enlargement (LVE) [25], and 3) accumulation and spread of amyloid beta (Aβ) plaques and tau tangles in different regions of the brain [26]. The antenna design process is made even more challenging considering that the human head consists of several layers of lossy biological tissues in addition to a low dielectric contrast between the blood and the brain.

This research investigates two wideband antenna designs with the aim of operating at the optimal frequency band for microwave head imaging applications, as well as, detecting the AD brain changes effectively. In addition, a novel flexible antenna array configuration for radar-based head imaging is investigated, developed and optimised for wearable applications. The use of flexible antennas instead of typical rigid antennas utilised in the existing wideband microwave head imaging systems provides many advantages, such as being conformal to the head, light weight, low cost, and providing better comfort to the wearer. Although the area of wearable antennas is well researched, their applications for health monitoring particularly for head imaging are still in its infancy stage and more research and testing must be done before they can be put for practical use.

B. Dielectric Measurements of Brain Tissues with Alzheimer's disease Pathology

Before validating the antennas to detect the accumulation of Aβ plaques and tau tangles in the brain, it is important to understand the dielectric properties of brain tissues affected with plaques and tangles because of AD. The dielectric properties indicate how electromagnetic fields are transmitted, absorbed, and reflected in different biological tissues [27]. These properties, the relative permittivity and conductivity, are inherent characteristics of all tissues. Understanding these properties is therefore important for dosimetry studies, optimizing wireless telecommunication devices, and designing EM

or RF medical diagnostic devices [28]-[29]. Comparing dielectric properties, such as permittivity and conductivity, for both AD and healthy brain tissues is crucial in determining whether MWS and MWI techniques are effective in providing non-invasive and early detection of the level of AD pathology in the brain. In this novel and groundbreaking study, brain tissues of patients with severe AD were obtained and dielectric properties were measured for both the grey matter and white matter regions. These were compared with measured dielectric properties for healthy brain tissues that were originally reported in [30]. Verifying the differences in dielectric properties provides the essential validation and incentive of proceeding further into the validation of antennas and MWI techniques for non-invasive detection of AD, by creating realistic head phantoms that mimic properties brain tissues affected plaques and tangles.

C. Performance Evaluation of Developed Antennas on Realistic Head Phantoms Emulating Progression of Alzheimer's disease

After the antennas were fabricated, its performance was verified based on its ability to detect the progression of AD from increasing changes in BA, LVE, and increasing levels of AD pathology (i.e., plaques and tangles). To validate performance for BA conditions, artificial head phantoms were fabricated using actual lamb brains. The use of actual brain samples in the experiments reflects the heterogeneity of actual human brain where this can give more valuable information regarding the sensing capability of the proposed wearable device. Different sizes of the head phantom are created to emulate increasing levels of BA that occurs as AD progresses. For LVE, several phantom objects are fabricated using coconut oil and salt to represent the increasing levels of cerebrospinal fluid (CSF) that builds up in lateral ventricles as they enlarge.

Finally, to achieve the change in AD-infected brain tissues, a realistic head phantom that resembles a real human head with similar dielectric properties must be developed. Therefore, a head phantom is initially fabricated using low cost and widely available materials such as tap water, agar, sugar, and salt based on methods in the literature [11], [31]. The electrical properties of the fabricated phantom for the healthy brain tissues are measured to confirm with the data obtained from real human head reported in [30], while fabricated phantoms mimicking the AD-affected brain tissues are measured to confirm with the data obtained during the dielectric measurements. Different sizes of

the head phantom are created to emulate the symptom of brain atrophy that occurs as AD progresses. In addition, several objects are fabricated to represent CSF that builds up in the lateral ventricles to emulate the second symptom of lateral ventricle enlargement. Finally, using the measurements obtained for the brain tissues with plaques and tangles, several phantoms were created that mimicked the increase of plaques and tangles in the brain because of AD. Considering that the electromagnetic wave interaction within the human head is different from that of free space, no far-field measurements of the antennas are conducted.

D. Development of Imaging Algorithm Based on MIST

Another challenge that needs to be addressed is to transform the measured data from the flexible antennas into an image that can show the size and location of plaques and tangles in the brain, thus providing a novel and non-invasive approach of imaging these anomalies effectively. This research investigates the adoption of the microwave imaging via space-time (MIST) beamforming algorithm, first reported in [32], [33], by using the collected reflected signals from the antennas to create a 2-D image of the cross section of the head phantom in both simulation and experimental works. Since the signals acquisition is carried out in frequency domain in the experiments, an inverse discrete Fourier transform (IDFT) is used to convert the data to the time domain signals. An interpolation technique is then used to estimate the depth of plaques and tangles according to the measured backscattered signals in the MIST algorithm. Finally, a filter is used to remove any unwanted pixels, and highlight only the areas with the largest energy footprint and therefore, having the reconstructed images indicate the location of AD-affected brain tissues with sensible accuracy.

E. Reconfigurable Switching Circuit

To develop a wearable device for head imaging applications, a compact and reconfigurable RF switching system that can be integrated with the proposed flexible antennas was designed and fabricated. One of the main challenges to develop a wearable head imaging system is to integrate all the required components such as the antennas and the switching circuit in a compact configuration. As a comparison, the existing microwave head diagnostics in the literature either utilise bulky external

switching systems for array configurations or use rotating platforms with only single antenna in the systems [34], [19]-[21], while one existing switching circuit is compact, but not flexible [35]. Although the use of external switching systems is acceptable for their intended application as a portable imaging system, it is not suitable for wearable applications. Moreover, the proposed wearable interface exhibits a compact structure which would make the existing microwave head imaging systems become more portable. Therefore, a simple, low-cost reconfigurable RF switching circuit is developed where it is integrated with flexible antennas to form a unified wearable device with all components conformal to the head.

1.2.2 Research Objectives

The main objective of this research is to validate whether MWS and MWI can be a viable solution that efficiently detects and monitors the progression of neurodegenerative diseases. In addition, the research objectives that were identified for this thesis are the following:

1. To investigate the use of MWI and MWS for early detection of Alzheimer's disease.
2. To investigate flexible antennas for wearable microwave head imaging applications.
3. To investigate the dielectric properties of brain tissue samples with AD and compare them with healthy brain tissues.
4. To produce realistic head phantoms that mimic the progression of AD based on three key changes: 1) BA, 2) LVE, and 3) accumulation of plaques and tangles.
5. To validate the wearable antennas on fabricated head phantoms.
6. To develop and implement a modified MIST algorithm for the head to detect and locate plaques and tangles non-invasively.
7. To implement and evaluate an array of flexible antennas for mono-static radar-based imaging systems.

8. To develop a compact and reconfigurable RF switching circuit to be integrated with the proposed flexible antenna array.

1.3 CST Microwave Suite Simulation Setups

The "simulations" referred to in this thesis are computer models that have been designed to test the performance of the wearable antennas in free space and with human voxel models that replicate the conditions of AD in a human brain. In order to create these simulation models, CST Microwave Studio Suite was used. CST Microwave Studio Suite is a specialist tool for the 3D EM simulation of high frequency components. The software enables fast and accurate analysis of high frequency devices such as antennae, filters, couplers, planar and multi-layer structures, and signal integrity and electromagnetic coupling effects. CST software makes available Time Domain and Frequency Domain solvers. It also offers further solver modules for specific applications. By having a CAD-based interface, CST allows users to design their antennas and environment freely and specify different materials that make up the antenna structure, while incorporating simple tools that will help calculate different parameters and ensuring that the antenna design meets the intended requirements, such as impedance matching.

When creating a simulation model in CST, the following steps are performed:

1. **Choose Project Template** – In this step, we generally create a new project template in CST for the "Antennas" application area, and then choosing the type of antenna as our workflow. For this thesis, the "Planar" workflow was chosen as both antennas developed are planar monopole antennas. Finally, we choose either a frequency-domain or time-domain solver type, depending on the type of analysis needed.
2. **Specify Units** – In this step, units are determined for frequency (GHz), time (ns), and dimension (mm) that are to be used in the simulation models.
3. **Define Parameters, Geometry, and Materials of Antenna** – In this step, the main design procedure of the antenna is carried. Here, initial shapes are chosen and modified based on the requirements of the antenna. Dimensions

of antennas are stored as parameters in CST so that they can be easily used. Finally, materials with dielectric properties are chosen for the different antenna parts so that they can be represented in the CST models. The user can choose materials from the CST library, or create their own materials with their own dielectric properties. Materials can also be created and defined for objects that represent the human brain and diseases, which was carried out in Chapter 5 (see Chapter 5, Section 5.2).

4. **Create the Port** – This important step is what creates the port that simulates the antenna model in CST to work as if it was connected to a real VNA. In particular, CST performs the essential calculations needed to create a waveguide port that is matched to a 50 Ω impedance, thus allowing basically any antenna geometry to be created and tested in the simulation. Of course, one should still ensure that basic antenna design formulas (Eqns. 3.1 – 3.7) are used beforehand to understand whether the antenna is correct or not.

5. **Create mesh** – In this step, the mesh size is set to allow the CST to run the simulation model and obtain accurate results that show the performance of the antenna. In general, the higher the mesh size, the more accurate the results. However, larger mesh sizes increase the overall time of the simulation model. In this thesis, all free space simulations had a mesh size of 3-5 million mesh cells, whereas for the simulations with head models (as discussed in Chapters 4 and 5), the size of the mesh cells was set between 12 to 15 million mesh cells.

6. **Run simulation and optimise design** – In this final step, the simulation model is run. Once the model completes, several results, such as the S-parameters, farfield radiation patterns, surface current distribution, and other similar results are analysed. These results are used to optimise the design of the antenna further to ensure that it meets the intended design specifications.

As part of the initial research work in investigating and validating of MWS for neurodegenerative diseases in CST, the following simulations were created and performed:

1. Design, optimisation, and validation of wearable stepped monopole and rectangular monopole antennas in free space (see Chapter 3, Sections 3.2.1 to 3.2.3) and near human head voxel model (see Chapter 3, Sections 3.2.4 and 3.3).
2. Design of realistic head voxel simulation models that emulate BA and LVE conditions and validation of antennas on those models (see Chapter 4, Sections 4.1 and 4.3).
3. Design of realistic head voxel simulation models that emulate pathological progression of AD-affected brain tissues in the brain based on Braak's staging [26] and validation of antennas on those models (see Chapter 5, Section 5.2).
4. Validation of both types of antennas in arrays in free space and near human head model prior to development of wearable prototypes (see Chapter 6, Sections 6.1 to 6.2).

1.4 Original Contributions of Thesis

The research undertaken has contributed to the following key contributions:

1. Validation of MWS as a non-invasive tool to detect, monitor, and image the progression of AD.
2. Dielectric measurements of brain tissue samples with AD pathology and its comparison to healthy brain tissues.
3. Determination of the earliest level of AD that can be detected by the proposed flexible antennas. Determine the following: 1) smallest levels of BA, 2) smallest increase in LVE, and 3) smallest levels of plaques and tangles.
4. Performance verification of flexible antennas on realistic artificial human heads mimicking the different conditions of AD.

5. A modified MIST imaging algorithm for reconstructing images showing the size and location of Aβ plaques and tangles in the brain non-invasively.
6. Flexible wideband antennas for wearable head imaging applications that utilised textile and silicone rubber substrates.
7. Wearable prototype employing the proposed flexible antennas in an array configuration along with integrated reconfigurable RF switching circuit.

1.5 Overview of the Thesis

The thesis is organised into nine chapters as follows:

Chapter 1: Introduction

This chapter presents the background and motivation to carry out the research. A brief introduction of neurodegenerative diseases, current diagnostic methods, and limitations of those systems. In addition, a brief introduction of the microwave technology for biomedical sensing and imaging is provided by comparing several approaches notably microwave sensing using microwave tomography and radar-based microwave systems.

Chapter 2: Overview

This chapter presents the literature review on diagnostic systems and methods for detecting neurodegenerative diseases, microwave sensing and imaging. In this chapter, current diagnostic systems, and methods for detecting AD, along with a comprehensive review on MWI for head sensing and imaging applications are thoroughly described. A wearable microwave imaging for monitoring neurodegeneration device (MIND) concept is presented that utilises the proposed wearable antennas integrated with the reconfigurable RF switching system developed in this thesis.

Chapter 3: Flexible Antenna Design and Fabrication

This chapter discusses the design and development of flexible antennas for the wearable MIND applications. Specifically, the chapter discusses about the use of two different antenna substrates: felt and silicone rubber. Computational simulation models and resulting performance metrics are presented and discussed about in the chapter. In

addition, the chapter also shows the actual experiment setup. Fabrication of the antennas, and results.

Chapter 4: Validation of Microwave Sensing for Alzheimer's Disease – Physiological Changes

This chapter presents the validation of MWS on two common physiological changes in the brain associated with AD: BA and LVE. First, the chapter discusses about the computational simulation models and experiments conducted to validate MWS for BA. In particular, the chapter also talks about the phantoms that were created for the experiments, as well as, discusses about the key findings from the resulting antenna signals that correlate with different levels of BA. The second part of the chapter deals with the validation of MWS with LVE. In particular, the chapter details the computational simulation models that were created and used to emulate this symptom, as well as, the practical experiments that were performed, including the fabrication of the phantoms that mimic LVE. The chapter also provides analysis on the resulting antenna signals and how it correlates with the different levels of LVE.

Chapter 5: Validation of Microwave Sensing for Alzheimer's Disease – Pathological Changes

This chapter comprehensively discusses about the work involved in validating MWS and MWI for detecting areas of the brain affected by the accumulation of beta-amyloid plaques and tau tangles. First, the chapter discusses about the dielectric measurements of brain tissue samples from AD patients and compared to those of a healthy person. The chapter then presents several computational simulation models that were developed to accurately recreate different stages of AD with varying levels of brain tissues affected with plaques and tangles in the brain. Next, experiments were conducted using the proposed textile-based antennas on realistic head phantoms that were fabricated to mimic the increasing levels of brain tissues affected by plaques and tangles.

The final part of the chapter describes the development of the MIST beamforming algorithm that uses the reflection coefficient data from the experiments to reconstruct

areas of the brain affected with plaques and tangles. The MIST algorithm is modified in this research to be used for head imaging. Reconstructed images from the MIST algorithm are presented and compared with the actual phantoms.

Chapter 6: Wearable Neurodegeneration Monitoring Devices

This chapter discusses the development of two wearable MIND systems: one for the textile-based antennas and another for the silicone rubber-based antennas. Measurements were made to analyse the reflection coefficients and the mutual coupling performance of the antenna array for both prototypes. In addition, electromagnetic simulations were carried out for both prototypes to investigate the spatial electrical field distribution inside the human head. The next part of this chapter discusses the development and validation of the reconfigurable RF switching circuit that was integrated on the MIND devices to allow manual switching between active antennas. Performance evaluation of the RF switching circuit discussed about in this chapter. Finally, the chapter ends with a discussion on the specific absorption rate (SAR) for the MIND devices to verify that they comply with the regulations set by the governing body.

Chapter 7: Conclusion and Future Work

This chapter concludes the research studies conducted and described in this thesis. Contributions of this thesis are re-highlighted and further research based on the developed wearable MIND system, imaging method, and phantom fabrications are suggested for future work.

1.6 Publications Arising from the Research

During this research, the following journals and conference papers have been published and submitted:

Journal papers:

1. I. Saied, S. Chandran and T. Arslan, "Integrated Flexible Hybrid Silicone-Textile Dual-Resonant Sensors and Switching Circuit for Wearable Neurodegeneration Monitoring Systems," in IEEE Transactions on Biomedical

Circuits and Systems, vol. 13, no. 6, pp. 1304-1312, Dec. 2019, doi: 10.1109/TBCAS.2019.2951500.

2. I. Saied and T. Arslan, "Non-invasive Wearable RF Device Towards Monitoring Brain Atrophy and Lateral Ventricle Enlargement," in *IEEE Journal of Electromagnetics, RF and Microwaves in Medicine and Biology*, vol. 4, no. 1, pp. 61-68, March 2020, doi: 10.1109/JERM.2019.2926163.

3. I. Saied, T. Arslan, S. Chandran, C. Smith, T. Spires-Jones, and S. Pal, "Non-Invasive RF Technique for Detecting Different Stages of Alzheimer's Disease and Imaging Beta-Amyloid Plaques and Tau Tangles in the Brain," in *IEEE Transactions on Medical Imaging*, 2020, doi: 10.1109/TMI.2020.3011359.

Conference papers:

1. I. Saied and T. Arslan, "Wideband Textile Antenna for Monitoring Neurodegenerative Diseases," *2018 IEEE 29th Annual International Symposium on Personal, Indoor and Mobile Radio Communications (PIMRC)*, Bologna, 2018, pp. 356-360, doi: 10.1109/PIMRC.2018.8580966.

2. I. Saied and T. Arslan, "Microwave Imaging Algorithm for Detecting Brain Disorders," *2019 29th International Conference Radioelektronika (RADIOELEKTRONIKA)*, Pardubice, Czech Republic, 2019, pp. 1-5, doi: 10.1109/RADIOELEK.2019.8733477.

3. I. Saied, M. S. R. Bashri, T. Arslan, C. Smith and S. Chandran, "Dielectric Measurements of Brain Tissues with Alzheimer's Disease Pathology in the Microwave Region," *2019 IEEE International Symposium on Medical Measurements and Applications (MeMeA)*, Istanbul, Turkey, 2019, pp. 1-6, doi: 10.1109/MeMeA.2019.8802179.

Chapter 2

Overview

In this chapter, a comprehensive review on current diagnostic systems used for neurodegenerative diseases (ND) and the use of microwave technology for head imaging applications is presented. Currently, medical imaging systems used in clinics or hospitals for diagnosing ND, such as AD, are MRI, CT, and PET. These systems have provided medical practitioners with images of the brain structure and chemical compositions of the brain to assist them in diagnosing the type and stage of potential ND a patient could have. The data provided by these methods vary in terms of resolution, operating procedure, and implementation cost. However, these systems have several disadvantages that can limit its effectiveness and be unsuitable for patients to use repeatedly.

Microwave techniques, such as MWI and MWS, offer many advantages compared to the above methods such as being low cost, non-ionising, and easy to use. MWS technology has been applied to detect several medical conditions such as: tumours, stroke, internal bleeding, bone generation, congestive heart failure, tissue healing, respiratory rate, and vital sign monitoring [5]-[6], [9], [13] [19], [36]-[38]. The fundamental working principle of microwave technology is based on the difference of the electrical properties particularly the permittivity and the conductivity between the healthy and unhealthy tissues in the human body, as illustrated in Fig. 2.1. When illuminated with electromagnetic (EM) wave, these tissues will scatter the signal differently where the collected reflected signal can be used to diagnose any potential diseases inside the human body.

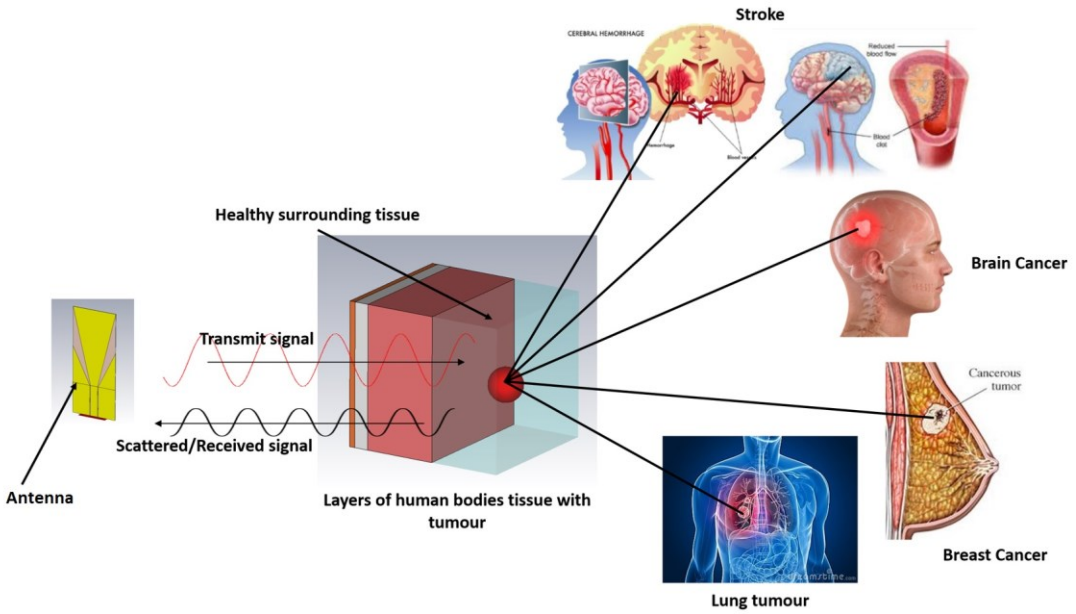

Figure 2.1: Diagram showing fundamental principle of MWS in detecting different medical conditions.

2.1 Overview of Neurodegenerative Diseases

ND are diseases in the brain that result from a progressive loss of structure or function of neurons, that leads to the death of neurons. Many ND are caused by genetic mutations, which are in mostly unrelated genes [39]. In addition, many ND can also be caused by protein misfolding, where proteins in the body fail to fold, therefore resulting in the proteins becoming structurally abnormal and thereby disrupting the function of cells, tissues, and organs [40]. Some examples of ND are: AD, PD, Huntington's disease, and amyotrophic lateral sclerosis (or Lou Gehrig's disease). Of the following, AD is considered to be the most common form of ND. In the U.S., AD is the most expensive disease in terms of care, and the sixth leading cause of death in the U.S. [1]. AD is also the leading cause of death in women and the second leading cause of death in men in the U.K. [2] In this thesis, the research focuses on using AD to validate with MWS and MWI techniques.

2.1.1 Background on Alzheimer's disease

AD is found to begin in patients aged 60 years and above. The most common early symptom is short-term memory loss. As the disease progresses, symptoms can include problems with language, disorientation, loss in concentration, mood swings, behavioral issues, and eventually leading to loss of bodily functions and death [41]. The life expectancy of those diagnosed with AD is between 3 to 9 years [41]. One of the distinguishing features of AD is the progressive shrinkage, or atrophy, of the brain and hippocampus [24]-[25], [42]-[44]. In advanced AD, the surface layer covering the cerebrum withers and shrinks, affecting the ability to plan, recall, and concentrate. In addition, the hippocampus also shrivels, resulting in the patient not being able to create new memories. It has been found that the brain volume can reduce by more than 22% of the normal brain in AD patients and that the brain's weight after AD frequently falls under 1 kg as compared to the normal adult brain weight of 1.2 to 1.4 kgs [45]. While brain atrophy appears in the normal aging process for humans, those with AD are found to have a much larger degree of brain atrophy. In addition to BA, it has also been found that the size of the ventricles in the brain, namely the lateral ventricles that contain CSF, enlarge substantially in those who have AD [25], [46]-[48]. AD subjects had significantly larger left and right lateral ventricular volumes when compared to healthy subjects. These differences were largely driven by differences in the frontal horns bilaterally, but differences in the left body/occipital horn were also significant. Figure 2.2 shows a screenshot comparison of a normal brain and a brain with severe AD, specifically having more prominent BA and LVE.

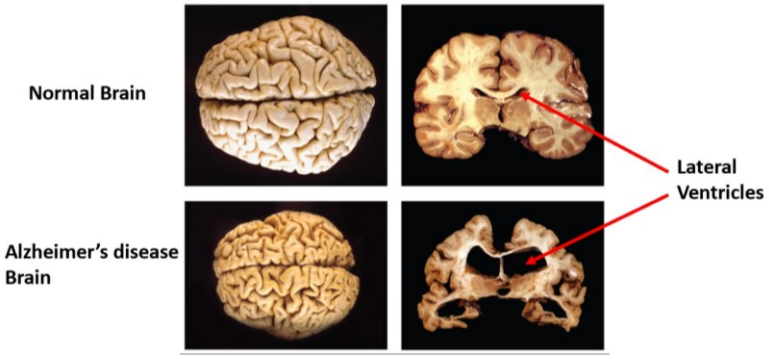

Figure 2.2: A normal healthy brain (top row) vs a brain with severe AD (bottom row). Both BA and LVE are prominent in the brain scans for AD.

Finally, a change related to AD that is widely recognised as a key indicator of AD is the presence of Aβ plaques and tau tangles in the brain [49],[50]. Aβ protein shows up in irregular clumps in the brain. These clumps stick together to form plaques that interrupt the signals between synapses [49]. In addition, the tau protein, which is used to stabilize microtubules in the brain, are found to be tangled. As a result, the brain is not able to transport cell nutrients along parallel structures, which eventually leads to death [50]. The cause for AD is still mostly unknown today. Due to the debilitating symptoms and burden of care it provides on family members and caregivers of patients with AD, it is important to determine ways to detect, diagnose, and monitor the progression of the disease as early as possible so that timely treatments can be provided.

2.1.2 Current Diagnostic Imaging Methods for Alzheimer's disease

Imaging has been investigated for several roles in the study of AD for several decades. However, in the last couple of decades, there has been a shift in the role that imaging plays for AD from a minor exclusionary role to a central diagnostic role. Imaging provides insights into the effects of AD in the brain. Historically, imaging, first CT and then MRI, was used only to exclude potentially surgically treatable causes of cognitive decline. Now its position in diagnosis also includes providing positive support for a clinical diagnosis of AD in individuals by identifying characteristic patterns of structural and functional cerebral alterations (e.g., BA and LVE). Currently, by using PET scans, doctors can visualize the specific molecular pathology of the disease. Furthermore, imaging has also found increasing uses for drug discovery, safety marker, and outcome measurement [3]. This section aims to highlight current AD imaging modalities, including structural and functional MRI and PET scans of cerebral metabolism, Aβ-tracers, and tau-protein tracers, that have shown success in characterizing changes in the brains of patients with AD. However, none of the imaging modalities can serve all purposes as each have unique strengths and weaknesses, which will be discussed in this section.

A. Structural MRI

MRI utilizes the fact that protons have angular momentum which is polarized in a magnetic field. This means that a pulse of radiofrequency can alter the energy state of

protons and, when the pulse is turned off, the protons will, on returning to their energy stage, emit a radiofrequency signal. By a combination of different gradients and pulses, "sequences" can be designed to be sensitive to different tissue characteristics. In broad terms structural MRI in AD can be divided into assessing atrophy (or volumes) and changes in tissue characteristics which cause signal alterations on certain sequences.

Structural MRI is mainly used to characterize BA. AD is characterized by a sudden presence and unstoppable progression of atrophy that is first manifest in the medial temporal lobe [51]. The entorhinal cortex is typically the earliest site of atrophy, closely followed by the hippocampus, amygdala, and para hippocampus [52]-[54]. These losses then spread to other areas of the brain usually in a symmetrical fashion. Figure 2.3 shows a series of structural MRI images for a patient with AD.

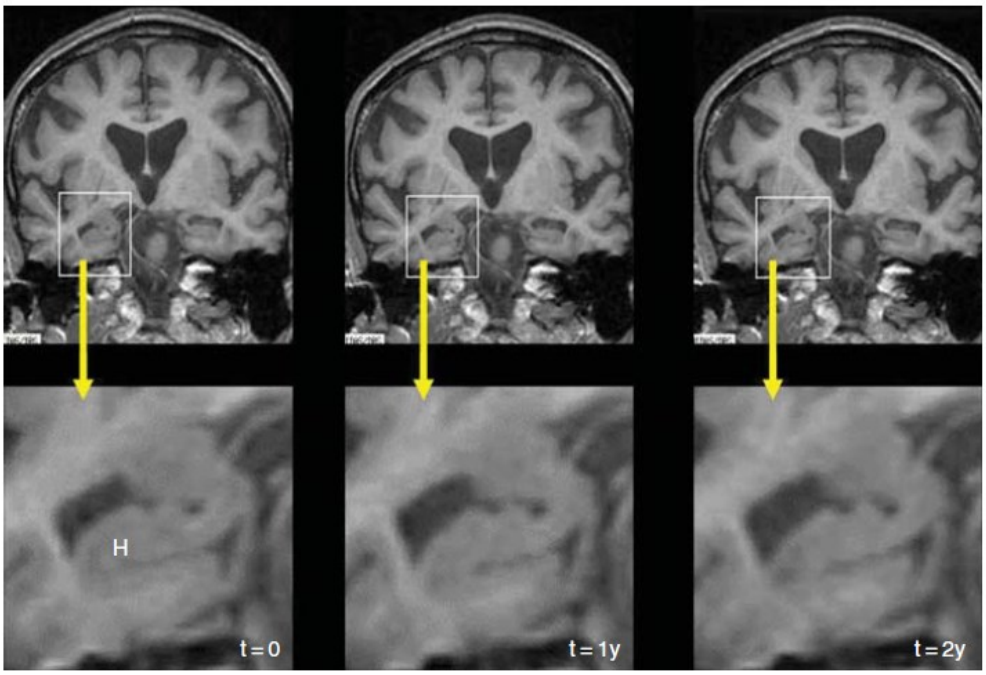

Figure 2.3: Series of structural MRI scans, each taken approximately 1 year apart, showing progressive hippocampal atrophy as individual progressed to AD [3].

This sequence of progression of BA on MRI most closely fits histopathological studies that have derived stages for the spread of neurofibrillary tangles [55]. It is increasingly clear that by the time a typical AD patient comes to diagnosis, atrophy is well established. Even in mildly affected individuals, entorhinal volumes are already reduced by approximately 20 to 30% and hippocampal volumes by approximately 15

to 25% [51]-[53]. By the time a clinical diagnosis is made, atrophy is also quite widespread with whole brain volumes down by roughly 6% and rates of BA having gradually accelerated to 0.3% per year in the 2 to 4 years up to a diagnosis [56]-[58].

The biggest strength of structural MRI is its availability. Its value in dementia diagnosis comes from the fact that European and U.S. guidelines recommend that all subjects with cognitive decline undergo structural imaging (MRI or CT) and that it is part of a proposed diagnostic criteria for AD and other dementias [59]-[62]. In most centers, MRI is regarded as an essential for investigating dementia. Although not as rapid as CT, a typical high-resolution volumetric sequence can be acquired in 5 to 10 min and more basic sequences in considerably less time. MRI is safe and as it does not involve ionizing radiation individuals can be imaged serially without concerns about carcinogenicity [3]. MRI offers a range of different sequences that can probe different tissue characteristics, giving it the advantage of providing multiple clinical and research measures in the same scan.

A limitation of structural MRI is that it lacks molecular specificity. It cannot directly detect the hallmarks of AD (beta-amyloid plaques or neurofibrillary tangles). In addition, BA patterns seen in structural MRIs overlap with other diseases and unusual forms of AD have atypical patterns of atrophy too. But most importantly, more severely affected individuals and those with claustrophobia, MRI may not be tolerated due to the structure and bulky nature of the system whereas a rapid CT scan may be more feasible [3]. In terms of measuring progression, volume changes on MRI may be produced by factors other than the progression of neuronal loss and as such assessment of disease modification may be obscured, at least in the short term, by such spurious effects. Overall, the availability, ease of use, and multiple applications of structural MRI in AD mean it will play a central role in research and practice for some years to come.

B. Functional MRI

Functional MRI (fMRI) is being increasingly used to probe the brain's functionality in memory and other cognitive domains in aging and early AD patients [63]. fMRI is a non-invasive imaging technique which provides an indirect measure of neuronal activity, inferred from measuring changes in blood oxygen level–dependent (BOLD)

MR signal [63]-[64]. BOLD fMRI is considered to reflect the integrated synaptic activity of neurons via MRI signal changes due to changes in blood flow, blood volume, and the blood oxyhemoglobin/deoxyhemoglobin ratio [65]. fMRI can be acquired during cognitive tasks, typically comparing one condition to a control condition (e.g., viewing familiar information or visual fixation on a crosshair), or during the resting state to investigate the functional connectivity (fc-MRI) within specific brain networks. Both task-related and resting fMRI techniques have the potential to detect early brain dysfunction related to AD and monitor therapeutic response over relatively short time periods. Figure 2.4 shows a fMRI scan highlighting regions of the brain with increased activity.

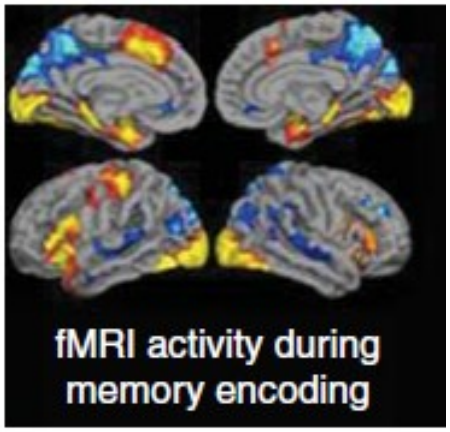

Figure 2.4: fMRI scan showing regions in the brain with increased activity (yellow/red) or decrease activity (blue) during successful encoding [3].

Much of the early fMRI work in MCI and AD used episodic memory tasks and was focused on the pattern of fMRI activation in the hippocampus and related structures in the medial temporal lobe. In patients with clinically diagnosed AD, the results have been quite consistent, showing decreased hippocampal activity during the encoding of new information [66]-[70]. Several studies have also reported increased prefrontal cortical activity in AD patients, suggesting that other networks may increase activity as an attempted compensatory mechanism during hippocampal failure [71]-[72]. Interestingly, the default network regions showing abnormal task-related fMRI activity in MCI and AD also overlap the brain regions with the highest amyloid burden in AD patients [73]-[75].

The main disadvantage of fMRI in aging, MCI, and AD populations thus far has been its limited study focus on relatively small number of research groups. There are multiple challenges in performing longitudinal fMRI studies in patients with neurodegenerative dementias. It is most likely that fMRI will remain quite problematic in examining patients with more severe cognitive impairment, as these techniques are very sensitive to head motion [3]. If the patients are not able to adequately perform the cognitive task, one of the major advantages of task fMRI activation studies is lost. Resting state fMRI may be more feasible in more severely impaired patients; however, it is critical to complete further validation experiments. BOLD fMRI response is known to be variable across subjects, and very few studies examining the reproducibility of fMRI activation in older and cognitively impaired subjects have been published to date [76]-[77]. Longitudinal functional imaging studies are needed to track the evolution of alterations in the fMRI activation pattern over the course of the cognitive continuum from preclinical to prodromal to clinical AD, which can take years or decades.

C. Fluorodeoxyglucose (FDG) PET

FDG PET is primarily used to indicate synaptic activity in the brain. Since the brain uses glucose as its source of energy, the glucose analog FDG is a suitable indicator of brain metabolism and is conveniently detected with PET. A substantial body of work over many years has identified a FDG-PET endophenotype of AD (Fig. 3)—that is, a characteristic or signature ensemble of limbic and association regions that are typically hypometabolic in clinically established AD patients [78]-[81]. Metabolic deficits in AD gradually worsen throughout the course of the disease. Bilateral asymmetry is common at early stages, more advanced disease usually involves prefrontal association areas, and in due course even primary cortices may be affected. Interestingly, the regions initially hypometabolic in AD are anatomically and functionally interconnected and form part of the large-scale distributed brain network known as the default mode network [82]. We now know in addition that these regions are highly vulnerable to Aβ deposition [83]-[84]. Figure 2.5 shows an image taken from FDG-PET for a patient with AD compared to a normal control subject.

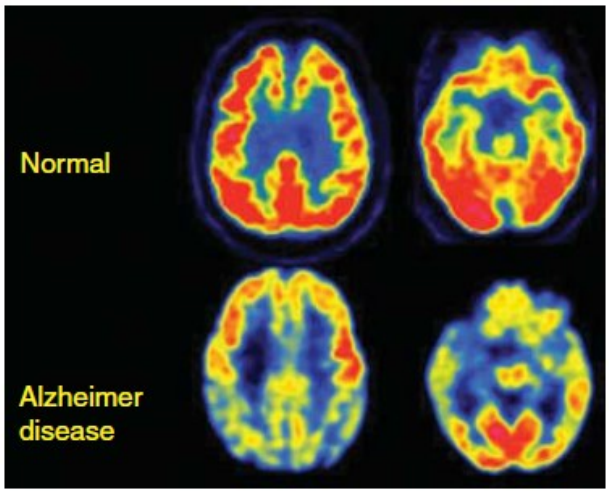

Figure 2.5: FDG PET images of a normal control subject and a patient with mild AD. Note severe hypometabolism (highlighted in yellow and blue colour) which is consistent with areas affected by AD [3].

Over the course of three decades, FDG PET has emerged as a robust marker of brain dysfunction in AD [3]. Its principal value is twofold: first, clinical utility has been documented when confounding conditions (e.g., LBD or frontotemporal lobar degeneration [FTLD]), are in question. Thus, when frontotemporal rather than temporoparietal hypometabolism is prominent, a clinically uncertain AD diagnosis may be changed to FTLD [85]. Second, FDG has emerged as a robust biomarker of neurodegeneration with which hypometabolism can be observed to precede the appearance of cognitive symptoms and to predict the rate of progressive cognitive decline in individuals who are later found to have progressed to AD [86]-[87]. Most importantly for AD treatment research, a recent study FDG data found that AD and MCI groups each showed progression of AD-like hypometabolism over 1 year that paralleled changes in a standard clinical endpoint [88].

In this context, a single, specific AD-related alteration in FDG metabolism has not been identified and therefore the FDG-PET abnormalities are assumed to be the net result of some combination of processes putatively involved in the pathogenesis of AD including, but not limited to, expression of specific genes, mitochondrial dysfunction, oxidative stress, deranged plasticity, excitotoxicity, glial activation and inflammation, synapse loss, and cell death [3]. FDG PET is relatively expensive and, like all PET techniques, has more limited availability, although its use in oncology has dramatically

increased availability in the USA over the past decade. It requires intravenous access and involves exposure to radioactivity, although at levels well below significant known risk. Brain FDG retention is a nonspecific indicator of metabolism that can be deranged for a variety of reasons (e.g., ischemia or inflammation) and may in certain individuals be irrelevant or only indirectly related to any AD-related process.

D. Amyloid PET

Amyloid imaging can detect cerebral β-amyloidosis and appears specific for this type of amyloid pathology [89]. In the setting of clinical dementia, particularly in clinically atypical presentations, this has important diagnostic utility. Several studies that have performed amyloid PET on clinically diagnosed AD patients found that 96% of AD patients were amyloid positive (Fig. 4) [90]-[93]. Amyloid PET utilises amyloid tracers, such as the widely evaluated Pittsburgh Compound-B (PiB) [94] and fluorine-18-labelled (F-18) tracers [95]. The obvious strength of amyloid imaging is that it has allowed the determination of brain Aβ content to be moved from the pathology laboratory into the clinic. In addition, a unique strength of amyloid PET across the entire clinical spectrum is the regionally specific nature of the quantitative data [3]. However, although amyloid PET can quantify Aβ load throughout the brain, it is not clear what pool of brain Aβ is represented by changes in AD. Figure 2.6 shows Amyloid PET scan images taken using the PiB tracer for normal, MCI, and AD subjects.

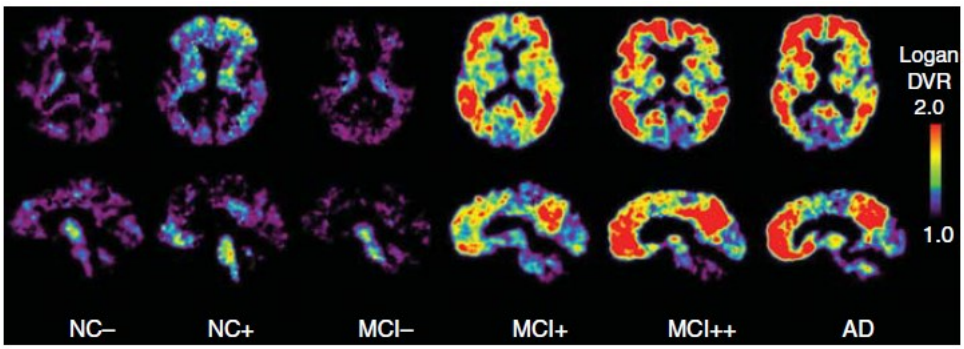

Figure 2.6: Amyloid PET images using PiB tracer for normal control, MCI, and AD subjects that displays a range of Aβ deposition [3].

Major deterrents to the widespread use of amyloid PET remain cost and availability. Availability has been improved by the development of F-18-labeled agents that can be distributed to PET scanners not associated with a cyclotron. Cost remains an issue, especially where CSF measurement of Aβ can provide very similar information when the question is simply the presence or absence of brain Aβ deposition. Being an early event in the pathogenesis of AD, amyloid PET is not a good surrogate marker of progression during the clinical stage of the disease [96]. This role is filled much better by structural MRI and FDG PET [97]. Similarly, amyloid imaging gives much more of a binary diagnostic readout than techniques such as MRI and FDG PET. That is, amyloid imaging has a certain specificity for the pathology of AD, but when that pathology is absent, a negative amyloid PET scan will be identical regardless of the non-AD etiology of the dementia. In contrast, MRI and FDG PET may give an indication of a frontotemporal or vascular pathology when an amyloid PET scan would be ambiguously negative in both cases. In addition, threshold of sensitivity of amyloid PET has yet to be precisely determined [98].

E. Tau PET

Tau deposition has been found to be highly associated with neuronal loss, neurodegeneration, and cognitive decline [55], [99]-[100] which, together with the recent failure of anti-amyloid drug trials, has fueled the interest in tau as a therapeutic target [101]. Selective tau PET tracers have been developed in recent years, enabling in-vivo visualization of tau deposition. Several tau tracers are in different stages of clinical development [102]-[105]; however, none of them have been FDA-approved for clinical use in the evaluation of AD yet. Tau PET imaging has the potential to accurately diagnose levels of tau proteins (called “tauopathy”), precise assessment of disease severity, disease progression, efficacy of potential disease-modifying anti-tau treatments, and inform patient enrollment for trials [105]. As a result, this enables PET imaging to track both tau and Aβ deposition over time, offering a unique opportunity to understand how the relationship between these misfolded proteins impacts the development of cognitive decline.

An ideal tau tracer must fulfill the general requirements for any brain PET tracer, including ample blood-brain barrier penetration, low toxicity, low non-specific binding,

rapid uptake and clearance from the brain, and no radiolabeled metabolites in the brain [106]. Pharmaceutical companies are developing tracers to support the advancement of novel therapies that target tau proteins. 18F-AV-1451 is the most widely used tau tracer to date. It has shown patterns of cortical retention that is like known distributions of tau in AD. In addition, it also indicates a strong correlation with the severity of the disease (see Fig. 1). Despite the success of initial studies 18F-AV-1451 presents some drawbacks. First, reliable quantification is challenging, as the specific signal continues to increase through the duration of the PET scan in high-binding AD patients and, second, it binds to substances in the brain other than tau such as melanin and hemorrhage metabolites, thus providing a wrong indication of where tau is located [107]. Figure 2.7 shows images from tau PET scan using the 18F-AV-1451 tracer for normal, MCI, and AD subjects.

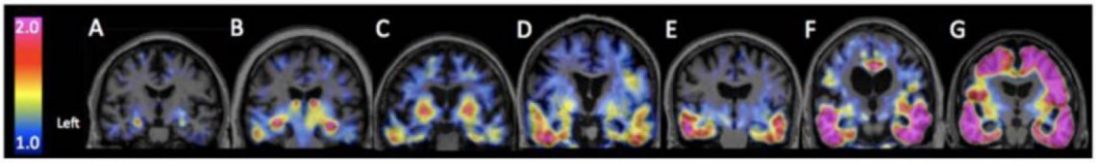

Figure 2.7: Tau PET images using 18-F-AV-1451 tracer for normal control (A-C), MCI (D-E), and AD (F-G) subjects that displays a range of tau protein deposition [99].

Tau imaging also has other challenges associated with it. As summarized in [105], tau proteins present different isoform composition, different ultrastructure (paired helical or straight filaments), and different patterns of deposition in various tauopathies. As a result, a single tau PET tracer may not bind to all these heterogeneous tau deposits or may bind them with different affinities. In addition, tau is largely an intracellular protein, so the tau tracer must cross the cell membrane, as well as the blood–brain barrier. Also, because current tau PET tracers share β-sheet binding properties, they need to achieve selectivity for tau aggregates over amyloid-β and other misfolded proteins with similar structural motifs [106]. This is particularly critical in AD, as tau deposits are co-localized with Aβ plaques but at much lower concentrations [108].

F. Advances in Biomarkers for Alzheimer's Disease

Sections 2.1.2.A to 2.1.2.E all discussed about the different imaging modalities currently used for AD diagnosis and progression monitoring. However, it is also

important to touch upon the biomarkers that are used in these scans. Various imaging and CSF biomarkers are widely used in AD and brain aging research. A recent position paper outlined a classification scheme, called AT(N), for biomarkers used in AD research [109]. This scheme recognizes three general groups of biomarkers based on the nature of the pathologic process that each measure: 1) biomarkers of Aβ plaques (labeled "A") are cortical amyloid PET ligand binding or low CSF Aβ42, 2) biomarkers of fibrillar tau (labeled "T") are elevated CSF phosphorylated tau (P-tau) and cortical tau PET ligand binding, and 3) biomarkers of neurodegeneration or neuronal injury [labeled "(N)"] are CSF T-tau, FDG PET hypometabolism, and atrophy on MRI.

The paper also went on to determine what biomarker signature defines AD. It was agreed that only biomarkers that are specific for hallmark AD proteinopathies (i.e., Aβ and pathologic tau) should be considered as potential biomarker definitions of the disease. An important point highlighted in [109] is the first biomarkers to become abnormal in carriers of deterministic AD mutations are those of Aβ. Studies suggest that although β-amyloidosis alone is insufficient to cause cognitive deterioration directly, it may be sufficient to cause downstream pathologic changes (i.e., tauopathy and neurodegeneration) that ultimately lead to cognitive deterioration [110]. This was also found to be case for people with mild cognitive impairment (MCI) that progressed to AD, therefore leading to the consensus of MCI being an initial, early stage of AD [88]. Consequently, a widely held view is that amyloid biomarkers represent the earliest evidence of AD neuropathologic change currently detectable in living persons [111]. This suggests that abnormal β-amyloidosis biomarkers alone could serve as the defining signature of AD. However, both Aβ and paired helical filament (PHF) tau deposits are required to fulfill neuropathologic criteria for AD [112], which suggests that evidence of abnormalities in both Aβ and pathologic tau biomarkers should be present to apply the label "Alzheimer's disease" in a living person.

Although these biomarkers are promising, as mentioned in the previous sections, they each have their own limitation. Aβ biomarkers, such as PiB and F-18, while are established in the field as the main tool for AD detection, may not provide an accurate diagnosis due to Aβ uptake that may occur in other areas. In addition to this, tau-based biomarkers, such as 18F-AV-1451, while promising in their impact for diagnosing AD,

are still not established in the field and requires more clinical trials in order for it to reach the level of Aβ-based biomarkers. Finally, neurodegeneration biomarkers are also established in the field and are used in conjunction with Aβ and tau biomarkers to provide a holistic view of the level of AD in the brain. However, by itself, neurodegeneration biomarkers are not sufficient and may show changes in the brain that are similar to AD, but does not make it a complete diagnosis of AD. A final point, and major limitation of all these AT(N) biomarkers, is that a scan of each of them are needed to provide a complete view of the level of neurodegeneration, as well as a complete understanding and interpretation whether the patient truly has AD or not. This means that the patients would have to take all scans from each biomarker group and compare them to have a better diagnosis of AD or not. This is the most important area in the advancement of biomarkers where MWI and MWS could make an impact in utilizing one single system to capture all the necessary changes in the brain that could provide a complete diagnosis of AD.

Another biomarker that has been investigated in the last two decades is the use of EEG data. There is a vast literature on EEG abnormalities in pathological brain aging [113]-[116]. AD patients contain excessive delta waves and a significant decrement of posterior alpha rhythms [117]. Furthermore, a prominent decrease of EEG spectral coherence in the alpha band in AD has been reported [118]. The analysis of EEG coherence (the phase different of the oscillations of a given frequency at two different electrodes) has been shown to contribute to the differentiation of AD and to the prediction of MCI conversion to AD [118]. However, these findings were usually significant only at a group level [119]; moreover, relatively small samples were investigated with a briefer than required follow up.

G. Hyperspectral Imaging of the Retina

A newly researched non-invasive techniques was discussed about in [120] which investigated the use of hyperspectral imaging of the retina to detect traces of the Aβ proteins. As Aβ has a wavelength-dependent effect on light scatter, the authors in [120] investigated the potential for in vivo retinal hyperspectral imaging to serve as a biomarker of brain Aβ. Significant differences in the retinal reflectance spectra were found between individuals with high Aβ burden on brain PET imaging and mild

cognitive impairment, and age-matched PET-negative controls. Retinal imaging scores were also found to correlate with brain Aβ loads. The findings were validated in an independent cohort, using a second hyperspectral camera. While this is promising, it was noted in [120] that a patient had to be omitted due to excessive blinking. This leads to questions on how reliable the system would be for patients with severe AD who may not cooperate with such scans. In addition, the sensitivity of hyperspectral imaging to frequent movement of the patients and repeated blinking will affect the overall effectiveness of this technology to detect levels of Aβ properly.

2.2 Microwave Head Imaging Systems

The human head consists of several tissue layers with high losses which makes the imaging process challenging when using radar-based microwave techniques. Nonetheless, based on the initial studies reported in [7], [121], MWI for head imaging is feasible and has potential. The main finding is that to provide better signal penetration inside the head, low frequency electromagnetic waves are required. In addition, the skull's low water content compared to other tissues inside the brain, such as grey matter, white matter, and CSF, results in higher penetration depth that allows microwave signals to propagate through it without much attenuation [122]. Therefore, it is expected that the skull would not pose any significant challenges for microwave signals to probe the brain. There are two main techniques used in microwave technology to image the human head. These are microwave tomography (MWT) and radar-based wideband systems. Both methods have their own advantages and limitations. The main differences between them are based on the frequency characteristic utilised on both systems and the final reconstructed image. MWT tries to estimate the dielectric properties of the human body while radar-based approach attempts to find the location of the main scatterers inside it. Since MWI and MWS has not been used for AD detection prior to this work, this section will focus primarily on current literature of MWI and MWS for head imaging that have been developed so far.

2.2.1 Background on Radiofrequency and Antenna Characterisation

Before mentioning what RF is, a brief background of electromagnetic waves and electromagnetic radiation is provided. Electromagnetic radiation involves both electric fields, which are generated through changing voltages, and magnetic fields which are generated through changing currents. As defined by the now well-known theories and formulas of James Clerk Maxwell [123] on electromagnetism, the key to this propagation phenomenon is the self-sustaining relationship between the electric and magnetic components of electromagnetic radiation. A changing electric field generates a magnetic field, and a changing magnetic field generates an electric field. This mutual oscillating relationship between electric and magnetic waves is what creates electromagnetic waves. The change in the fields also creates the energy that allows the wave to travel or *propagate* as electromagnetic radiation. RF waves are essentially a subset of this large electromagnetic wave spectrum that typically includes electromagnetic waves in the frequency range from 20 kHz to around 300 GHz. Microwaves are a subset of RF waves which are typically in the range of 300 MHz to 300 GHz. Within this range, there are several microwave frequency bands that each have their own characteristics and suitability based on the application they are applied to [124]. For this thesis, which uses microwaves for medical sensing and imaging, we are only focusing on the L band and S band microwave regions. These are characterised by frequency ranges of 1 to 2 GHz (L band) and 2 to 4 GHz (S band) respectively. In addition, these regions have a wavelength range of up to 30 cm, which will be acceptable for head imaging applications.

An important part of any RF system is the design and characterisation of antennas. Antennas need to be designed such that they can transmit and receiving RF waves at certain frequency ranges with minimum attenuation as possible. In general, antennas are electrical devices that converts electric power into RF wave and vice-versa. These are the messengers that enable the transfer of data and signals between one device to another *wirelessly*, and are essentially, along with RF, the backbone of today's wireless communication systems. A signal from a transmission line or the guiding device (hence the term guided wave) like a co-axial cable, is given to an antenna, which then converts

the signal into electromagnetic energy to be transmitted through space (hence the term free space). Antennas can be used for both transmission and reception of electromagnetic radiation (i.e., a transmitting antenna will collect electrical signals from a transmission line and converts them into radio waves, whereas a receiving antenna does accepts radio waves from the space and converts them to electrical signals and gives them to a transmission line).

It is also important to understand the characteristics of an antenna used in the system as these define the operational characteristics of the overall RF communication systems. Some of the fundamental characteristics of antennas are listed below and used in Chapter 3 when designing the antenna that was used for this thesis:

A. Radiation Pattern

A practical antenna cannot radiate energy in all directions with equal strength. Radiation from an antenna is usually found to be maximum in one direction whereas it is minimum or almost zero in other directions. Field strength is the quantity that is used to represent the radiation pattern of an antenna. It is usually measured at a point located at a particular distance from the antenna. Field strength can be measured by calculating voltage at two different points on an electric line and dividing the result with the distance between the two points. Hence, the units of field strength are volts per meter. Graphically speaking, the field of strength is plotted as a three-dimensional graph as it is the measure of the electromagnetic field strength at equidistant points from the antenna. If the graph of radiation of antenna is just a function of direction, then it is simply called as radiation pattern. But if it is expressed in terms of the electric field strength in V/m, then it is called field strength (or radiation) pattern. In addition, the radiation of the antenna is also a function of the power per unit solid angle and is called power radiation pattern.

B. Radiation Intensity

The radiation intensity of an antenna is the power per unit solid angle. It is represented by U and is independent to the distance from the antenna. Units of radiation intensity are Watts per steradian (W/Sr).

C. Directivity and Gain

Ideally, an antenna which radiates energy in all directions equally i.e., an omnidirectional antenna is called as isotropic antenna. This is just a hypothetical situation and an isotropic antenna does not exist in practice. But if we consider an isotropic antenna, then its power density will be same at all points on the sphere of radiation. Hence, the average power of an antenna (units of W/m^2) as a function of radiated power is:

$$P_{avg} = \frac{P_{rad}}{4\pi r^2} \tag{2.1}$$

Where *r* is the radius of the sphere of radiation. The ratio of power density to the average power radiated is known as directive gain. Directivity of an antenna is a measure of concentration of radiation in the direction of maximum radiation or the ratio of maximum power density to average power radiated.

D. Radiation Efficiency and Power Gain

All practical antennas will have ohmic losses as they are made up of conducting materials with finite conductivity. Radiation efficiency is ratio of radiated power to the input power. Power gain of an antenna is the ratio of the power radiated in a direction to the total input power.

E. Input Impedance

It is important to take care to match the input impedance of the antenna to that of the input transmission line. If the input impedance does not match, then the system degrades over time due to the reflected power.

F. Effective Length

The length of an imaginary linear antenna with uniformly distributed current is defined as the effective length of an antenna such that both these antennas have same far field in π/2 plane.

G. Bandwidth

The bandwidth of antenna is defined as the range of frequencies over which the characteristics of the antenna are maintained to the specified value. This is because, the

requirements for the characteristics of an antenna like the gain, impedance, standing wave ratio etc. may change during operation.

H. Effective Aperture

Generally, the term effective aperture or effective area is associated with the receiving antenna. Effective aperture (or "area") of an antenna is the measure of the ability of an antenna to extract energy from the electromagnetic wave. Effective aperture of an antenna is the ratio of the power received at the load to the average power density produced by the antenna.

I. Antenna Polarisation

Antenna polarization refers to the physical orientation of the electromagnetic wave radiated in a given direction. Polarization of an EM wave is a time varying direction and relative magnitude of the electric field vector. If the direction is not specified, then the polarization in the direction of maximum gain is considered.

2.2.2 Microwave Head Tomography System

In MWT, narrowband or multi-band antennas are mainly used to reconstruct the dielectric properties of the human head [125]. Antennas are placed around the head and a matching medium is used to reduce the air-to-skin reflections; hence, increasing the transmitted signal inside the head. A feasibility study on using MWT to image the human head was presented in [7] using computational methods for stroke detection. Realistic electrical properties of the head tissues were input into the simulator where different sizes of stroke were used. Two different arrays of transmitters and receivers were used in the setup: 1) 32 × 32, and 2) 64 × 64. The transmitters and receivers were placed around the working chamber of radius 11 cm. Both single and multi-frequency schemes were carried out across the frequency range of 0.5 GHz up to 2 GHz. Although the use of higher frequency at 2 GHz is desirable for good spatial resolution, the stroke injury area was not reconstructed successfully compared to using lower frequencies at 0.5 GHz and 1 GHz for the single frequency approach. This is due to the higher attenuation of the EM signal as the frequency increases. However, multi-frequency technique permits the use of higher frequency for improved detection capability [7].

Based on the numerical study presented above, the group developed a novel EMT imaging scanner for human brain imaging [125]-[126]. The scanner as shown in Figure 2.8 was used in initial clinical studies for stroke detection.

Figure 2.8: EMTensor Brain Imaging System (1st Generation) [125].

The 3D EMT system consists of 160 ceramic loaded waveguide antennas operating at a frequency range of 0.9 to 1.1 GHz. To reconstruct the image of the head, an iterative solver based on gradient inversion method was implemented. The imaging result of the system was found to be generally accurate in reconstructing an image of ischemic stroke in a patient. The reconstructed image was also found to be like an image of the same patient from an MRI scan [126]. The capability of the system for head imaging was validated since the area of the stroke shown using the EMT system agrees well with the MRI image. However, one major disadvantage with MWT systems is that reconstructing the dielectric map of the head requires more computational resources than those of other MWI systems, such as wideband radar-based microwave systems.

2.2.3 Microwave Head Sensing System

A MWS system was proposed in [28], [127]. The main objective of the system was to help doctors differentiate types of stroke a patient might have so that a correct treatment could be given. The frequency used in the system is 0.3 to 3 GHz. Two different

prototypes with ten and twelve antennas arranged around the head are shown in Figure 2.9.

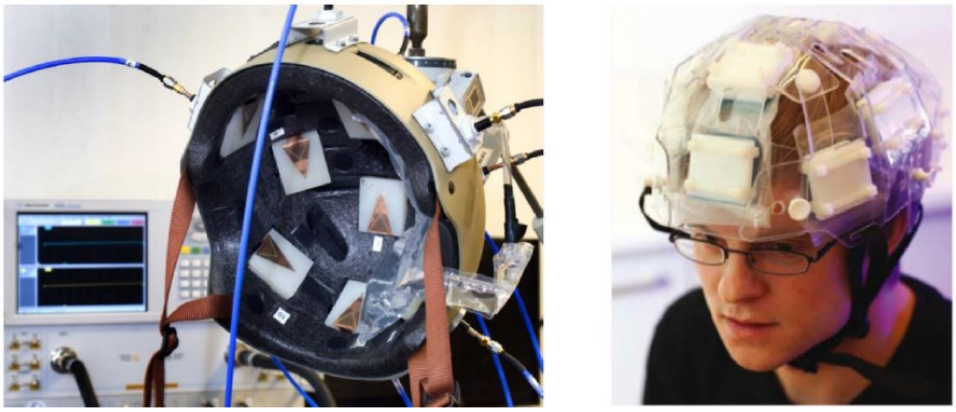

(a) (b)

Figure 2.9: (a) First MWS prototype with 10 patch antennas, and (b) second MWS prototype with 12 patch antennas [28].

Measurements were made to acquire the scattered data of the different transmission channels for patients with known conditions. A supervised machine leaning algorithm based on a subspace classifier method used the collected data to train the system. It was reported that the system was able to differentiate stroke patients from healthy volunteers, as well as classify the type of stroke that was present. A newer prototype was reported in [12] for detection of other head diseases such as subdural hematoma as shown in Figure 2.10.

Figure 2.10: Strokefinder MD100 device by Medfield Diagnostics AB [12],[128].

It was reported that based on the clinical trial conducted, the sensitivity of the system was 100% while its specificity was 75%. The sensitivity of a clinical trial shows the ability of the test to correctly identify patients with the disease. On the other hand, the specificity refers to the ability of the test to correctly identify patients without the disease [129]. The prototype is portable, and a full measurement takes about 45 seconds to complete. However, a major limitation of the proposed MWS devices is the inability of producing images that determine the position and the size of the brain disease, which would be very valuable to medical practitioners to plan surgeries and treatment strategies for patients based on their current conditions.

2.2.4 Wideband Radar-based System

Wideband radar-based system for head imaging offers several advantages over MWT and MWS systems. In radar-based head imaging system, the main objective is to identify and locate main scatterers inside the head which indicates the presence of anomalies in the brain that is different form healthy tissues. Compared to MWS systems, an estimated location and volume of affected tissues can be determined, that will allow doctors to know where the disease is located. In terms of the mathematical complexity and computational resources issue in solving inverse scattering electromagnetic problem that is faced in MWTs, the use of wideband radar-based systems provides the ability to simplify data processing, reduce the computation resources, and time to reconstruct the image inside the head. In addition, wideband radar-based systems have the capability of being developed as portable and wearable devices for head imaging that can provide fast detection and/or real-time monitoring of diseases, making it a more effective option compared to MWT.

Wideband radar system for head imaging is mainly utilised in three different approaches which are mono-static, bi-static, and multi-static configurations. All these configurations have their own advantages and limitations. Feasibility study using radar-based technique for head imaging was reported in [130] using numerical simulations. Vivaldi antenna was adopted in the simulations due to its directional radiation beam and high gain. A 3-D spherical head model consisting of several biological tissue layers such as: skin, skull (bone), grey matter, and white matter, was used in the simulation

where a 3 cm diameter hemorrhagic stroke with similar dielectric properties to blood was embedded. By using a bi-static approach, one antenna was used to transmit EM signals while the other antenna received the back-scattered signal. The operating frequency of the antenna was between 1.5 to 5 GHz, and the spacing distance between adjacent antennas was kept at 20 mm. The process of transmitting and receiving the signal was then repeated for different pre-defined positions to sweep the whole aperture of the head model. An improved version of delay-and-sum (DAS) algorithm called DAS Coherence Factor (DAS-CF) was applied to create an image of the head model. This study shows promising result in using radar-based technique for stroke detection. Another numerical simulation was carried out in [131] using a similar method but with antennas that operate at a higher frequency range (between 5 to 10 GHz) for brain cancer detection. It has been shown that higher frequency range will not be able to penetrate deep inside the human head. Only tumours which were close to the surface of the head model showed differences in the scattered signals. This signifies the importance of using low frequency levels (i.e., below 4.5 GHz) for ideal penetration [132].

In [133], a numerical simulation was carried out to detect haemorrhagic stroke by comparing the difference of the reflection coefficient (S_{11}) signals between healthy and unhealthy heads. It was reported that across the frequency range from 2 to 3.5 GHz, the reflection coefficient of the probing antenna had a higher level of loss when the antenna is facing a section of the head phantom with hemorrhagic stroke compared to a healthy head model. Based on this finding, a complete microwave head imaging based on radar-based technique was proposed in [134] which used 16 Vivaldi antennas as shown in Figure 2.11.

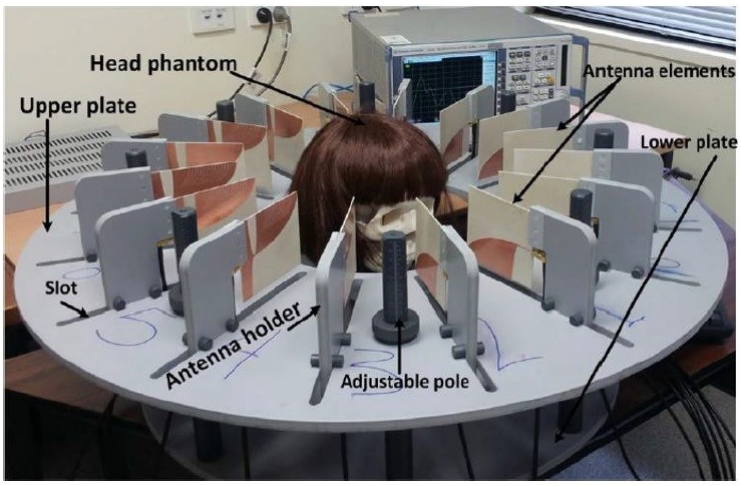

Figure 2.11: Radar-based microwave head imaging system using Vivaldi antennas [134].

The operating frequency range of the antennas is from 1 to 4 GHz and operated in a mono-static configuration where the same antennas act as transmitter and receiver. To adapt the confocal imaging algorithm, an inverse Fast Fourier transform (IFFT) was applied to the measured S_{11} data to convert it to time-domain signals. A realistic artificial human head phantom was fabricated for testing purposes and matching medium was used in the system to reduce the complexity of the system. The distance between the antennas and the head model was kept at 5 mm during the measurements. The images reconstructed were able to successful show two hemorrhagic stroke objects that were placed in the phantoms.

An improvement on the antenna design proposed in [134] was carried out by the same research group by utilising a 3-D folded dipole antenna structure for portable microwave imaging system for traumatic brain injuries detection [10]. To make the imaging system portable, a custom-made compact transceiver system was used in the measurement setup for signal transmission and data acquisition. Several variations of the antennas have been reported in [10], [18], [135]. A realistic human head phantom was fabricated using 3-D printing technology to validate the detection capability of the systems. The same group also developed an improved prototype for future clinical trial as illustrated in Figure 2.12 that contained 16 of the 3-D folded compact antennas [20]. The portable microwave system for head imaging was aimed for on-site rapid diagnostic of traumatic brain injuries which could occur in vehicular accidents, sports,

or other causalities. A further improvement of this system was recently published in [136].

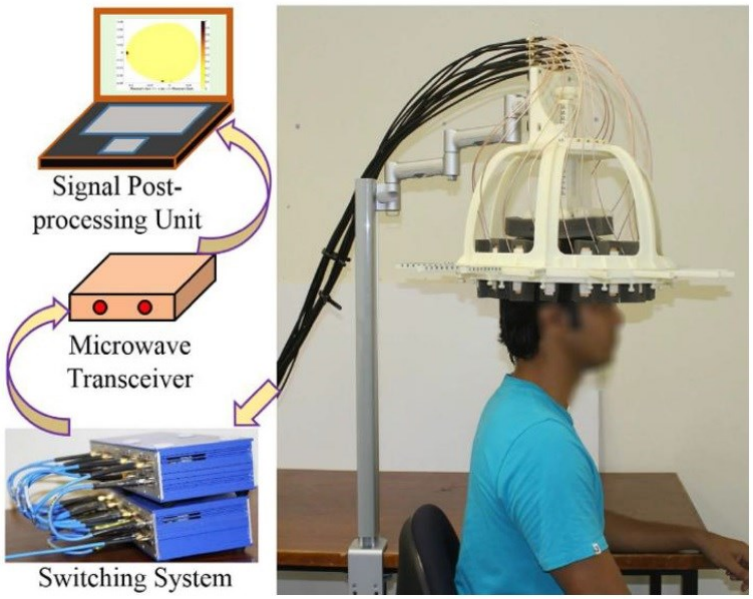

Figure 2.12: Microwave head imaging system that utilises 3-D folded compact antennas for on-site rapid diagnosis of intracranial hematoma [20].

Wearable MWI devices for head imaging have been recently proposed in several studies [132]-[133], [137]-[138]. Two prototypes were discussed in [118] that each utilised flexible and low-profile antennas. One prototype, shown in Figure 2.13, used 12 antennas that were fabricated on a thin and flexible polyethylene terephthalate film (PET-film) substrate. The wearable had an absorber material to absorb any backward signals generated from the antennas. Another prototype, shown in Figure 2.14, was a novel headstrap-based wearable MWI device that contained 12 directional monopole antennas fabricated using textile substrates. Another interesting part about the device and related studies was the design and use of a compact switching circuit that could be placed on the device [139]; thus, making the system wearable, portable, and allows for fast data acquisition with the automated switching circuit that was used.

Figure 2.13: First prototype of wearable microwave head imaging device with thin flexible antennas on PET-film substrate [132].

Figure 2.14: Wearable head strap-based microwave imaging device with textile-based antennas [132].

2.3 Overview of MWI/MWS for Neurodegenerative Disease

As discussed earlier, almost all the work for MWI for head imaging is solely applied for stroke and brain cancer detection. To the best of the author's knowledge, there are currently no reported development or investigations of MWI and/or MWS techniques for AD detection and progression monitoring. The only known work that has investigated the use of RF for detecting AD is reported in [140]. The study discusses about the investigation of measuring changes in dielectric properties of CSF to determine the presence of Aβ proteins. This is done by using an implantable antenna. Although, the study is promising, it has several limitations. First, it focuses on measurements obtained from canine tissues, which are different from those of humans. Second, it aims to detect the presence of proteins that are in the CSF layer that surrounds

the brain. This is not an indication of early stage of AD and therefore would have limited practical use for early-stage detection or monitoring of AD. Finally, the most important limitation is the use of an implantable antenna. This would not be ideal for patients with AD and therefore makes it less attractive compared to other systems. Another study by a research group in UCL also investigates the use of microwave sensing for detecting dementia; however, rather than detecting changes in the brain, their research focuses more on recording other vital parameters, such as heart rate and movement, to determine the state of neurodegeneration in the brain [114]-[115]. While the group utilises a non-invasive and unobtrusive approach to detecting these parameters, they are not adequate in determining the stage or progression of neurodegeneration in the brain.

Given this, there is a pressing need for a non-invasive and efficient technique that will allow for early detection and progression monitoring of AD in patients. A wearable device for wideband microwave head imaging can be used for frequent measurements or even as a real-time monitoring device. It also has the benefit of being portable, which eliminates the need of having patients with AD coming all the time to clinics or hospitals to take scans. The wearable nature of the device also ensures that it is comfortable for patients to wear. To do this, antennas should be designed to be flexible and conformable to the patient, as these are the main priorities. In addition, antennas need to be validated to ensure that it can detect varying levels of BA, LVE, and brain tissues affected by AD pathology, all of which are extremely important for understanding the progress of the disease and how caregivers and doctors should provide the right treatment accordingly. Finally, the imaging algorithm needs to be tailored for this study by detecting the regions affected by AD and highlighting them in the reconstructed images, thus providing a transformative and novel approach for non-invasive imaging of AD that eliminates the use of invasive tracers (e.g., FDG, PiB, etc.).

2.4 Summary

This chapter provides a comprehensive overview of current diagnostic systems for detecting and monitoring neurodegenerative diseases, specifically AD and discusses

the advantages and disadvantages of each. Major limitations of current AD diagnostic systems are that they are bulky, expensive, can be difficult for AD patients to perform, and in the case of PET scans, requires invasive methods. Next, a review of microwave head imaging systems was discussed highlighting the current trend of wideband radar-based imaging and its advantages. This is driven by findings that low frequency EM signals have potential of detecting anomalies inside the brain, with several promising results obtained by experiments. Finally, an overview of current investigation of microwaves for AD detection was presented. It is found that currently, no MWI or MWS technique have been investigated for detecting the physiological and pathological changes in the brain associated with AD. The only study to have utilised this technique had several issues which limits the practicality and effectiveness of the results. This has led to the novel investigations that is being discussed in this thesis. Specifically highlighting novel studies related to:

1) dielectric measurements of brain tissues with AD pathology,
2) use of MWI and MWS techniques to non-invasively determine BA, LVE, and accumulation of plaques and tangles, and
3) development of imaging algorithm to take recorded signals from antennas and reconstruct regions of the brain affected with AD pathology.

This has also led to the development of two proposed wearable MIND systems that hopefully can be used for efficient diagnosis and progression monitoring of AD, and could be used in not just clinics and hospitals, but also at care homes and places where the patient resides.

Chapter 3

Flexible Antenna Design and Fabrication

In order for the MIND device to detect and monitor changes in the brain effectively, it is paramount that the antennas are designed such that they can efficiently probe into the regions of the brain where BA, LVE, and accumulation of AD-affected tissues take place. For a mono-static head imaging system, each antenna will act as both a transmitter and receiver. Several design parameters of an antenna need to be considered to ensure that it is suitable for the wearable MIND device. These include sufficient penetration of EM signal inside the human head, compactness of the antenna, flexibility, and good impedance matching performance considering that the antenna needs to operate at close proximity or in contact with the head. This chapter will describe the requirements of designing antennas for wearable head imaging systems and subsequently presents the development of two types of antennas that were fabricated using textile substrate and silicone rubber substrate, respectively.

3.1 Requirement of a Wearable Antenna for Head Imaging Systems

In order for antennas to be suitable for wearable biomedical imaging applications, they need to be flexible, lightweight, and conformable to the person wearing it, especially for patients with AD. As a result, typical rigid antennas made from FR-4 or printable circuit boards (PCB) technology are no longer suitable for these wearable applications. Furthermore, because a low-profile antenna is vital to ensure that the antenna can be integrated into wearable hats or structures and be comfortably worn by patients, high-profile antennas, such as Vivaldi antennas, although capable of providing high gain and directional radiation beam patterns, are not suitable for wearable applications.

Several antenna designs used for radar-based microwave head imaging were investigated. One of the most adopted antennas is travelling wave antennas such as Vivaldi antenna. The selection of Vivaldi antenna is mainly driven by its directional radiation pattern and high gain. Vivaldi antennas were proposed in [19], [130]-[131] for head imaging in both numerical and experimental studies. Due to its inherently large structure, several methods have been proposed to miniaturise its dimension, such as cutting slots on the radiating elements of the antenna or using high permittivity substrate. Nevertheless, due to its high-profile structure along the direction of propagation, Vivaldi antennas are unsuitable for wearable applications.

Several compact antenna designs were in [10], [13], [20], [134] by utilising 3-D folded dipole antenna where the profile of the antennas was reduced significantly. Moreover, due to the metallic ground plane of the antennas, the directivity of the antenna is increased compared to typical dipole configuration. One of the design variations of the antennas is shown in Figure 3.1. The total dimension of the proposed antenna is 20mm × 80mm × 10mm. The compact structure of the antenna has paved the way for portable microwave imaging applications; however, its rigidity still makes it unsuitable for wearable MWI or MWS devices.

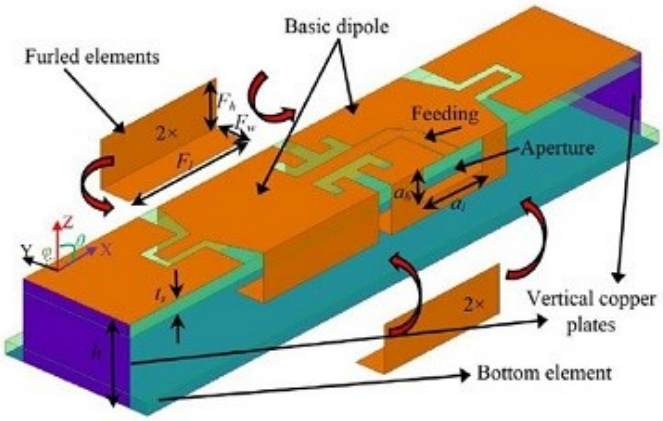

Figure 3.1: 3-D compact folded dipole antenna for microwave head imaging [134].

In this thesis, the focus for designing the antenna for the wearable MIND device is based on utilizing flexible materials for both the radiating and substrate parts, respectively. There are several studies that explored the design and fabrication of flexible and wearable antennas for several applications such as wireless body area

network (WBAN), medical, and indoor/outdoor positioning [141]–[145]. In recent years, the introduction of methods such as inkjet printing, conductive textiles, and polymer fabrication to the antenna community has given rise to the development of novel and highly flexible antennas [146]-[148].

The use of inkjet printing method makes it possible to print an antenna on any thin and flexible substrate. The most used substrate for flexible antennas is a polymer-based material such as Kapton polyimide and PET-film [149]-[150]. Figure 3.2 shows an inkjet-printed antenna on a PET-film that was proposed in [151]. However, a disadvantage with this method is that most of the antenna designs rely on a CPW-fed structure due to the thinness of the film substrate. As a result of this, most inkjet-printed antennas will be omnidirectional and the antenna and may not have the required penetration depth that would be suitable for monitoring conditions related to AD.

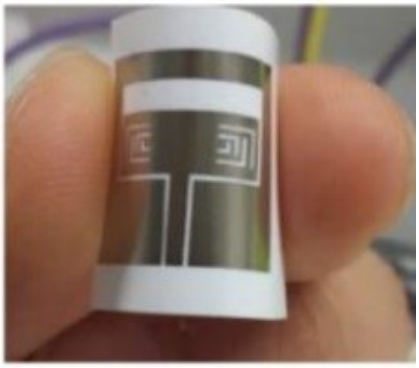

Figure 3.2: Patch antenna fabricated on PET film using inkjet-printing [151].

Conductive textiles have been widely employed for the construction of wearable antennas to facilitate seamless integration with garments [147], [152]-[154]. Wearable textile antennas are mainly planar, specifically microstrip patch antennas. It is found that the dielectric constant, moisture, temperature, loss tangents, thickness of the substrate, conductivity, and deformation, all influence the performance and the characteristics of the textile wearable antenna. In general, textile materials have a very low dielectric constant, between 1 and 2. The low dielectric constant reduces the surface wave losses that are tied to guided wave propagation within the substrates. The thickness of the substrate material is also an important parameter in the design of antennas. For a fixed relative permittivity, the substrate thickness may be chosen to

maximize the bandwidth of the planar antenna. The choice of the substrate's thickness is a compromise between efficiency and bandwidth of the antenna. Moreover, the thickness of the substrate also influences the geometric sizing of the antenna. Figure 3.3 shows a fabricated textile-based sensor.

Figure 3.3: Wideband textile antenna for microwave medical imaging [17].

Although the use of textile materials enhances the wearability and compactness of the fabricated antenna, there are some limitations associated with the design. First, moisture dramatically affects the performance of an antenna because water has a higher dielectric constant than fabric. The fibers are constantly exchanging water molecules with the air and changes dynamic equilibrium with the temperature and humidity of the air surroundings. Regain, which is defined by the ratio of the mass of absorbed water in a specimen to the mass of the dry specimen, represents the sensitivity of the fabric to moisture [155]. Since fabric antennas are used near or on the skin, aspects of wetness due to human sweat on the antenna becomes more important [156]. Another limitation is that the human body is subject to many small movements, even while standing and sitting that will affect the performance of the antennas. Thus, significant variations in the channel could occur due to these subtle changes. In such conditions, characterization of RF propagation needs to account for both the variable positioning of the antennas on the body, as well as variations in the channel due to body movements [157]. Finally, the embroidery technique includes the degeneration of the conductivity of the embroidered layer over washing which, in turn, affects the antenna properties [158]. In addition, they are prone to fraying during the embroidery process, unless the

right needle, proper speed, and tension are applied, which needs a very precise fabrication process, as shown in Figure. 3.4.

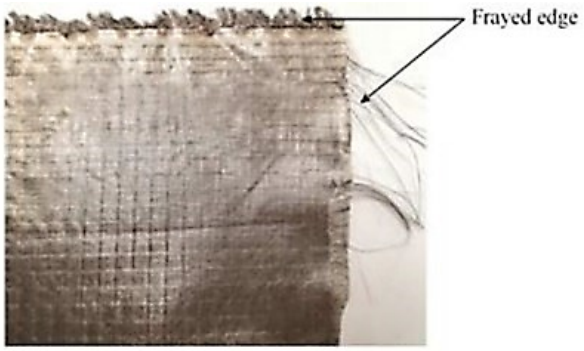

Figure 3.4: Example of fraying that is visible on the edge of fabrics [159].

As an alternative to embroidery, commercial woven conductive fabrics are available in the form of fabric sheets that can be used to realize the antenna metallic patterns stitched into the clothing. However, they also have the same issues of conductive layer deterioration and fraying that can be avoided by shaping fabrics using precise laser cutting machines [159].

Finally, another technique that has been investigated extensively in recent years for flexible antenna designs is the use of silicone-based materials, such as silicone rubber and polydimethylsiloxane (PDMS) [148], [159]. Polymers in general are low-permittivity materials with low loss, which make them a suitable option for higher-frequency applications. In addition, they are stable to a wide range of environments due to their low water absorption together with high flexibility and stretchability. For this reason, flexible polymers such as PDMS and silicone rubber (Ecoflex) are used as the antenna substrate [160]-[161]. A major challenge identified in utilizing polymers for antenna development is the poor adhesion of metal to the polymer, which might cause separation of the antenna conductive parts from the non-conductive parts such as the substrate. For this reason, polymers were employed to construct wire-type antennas, which require minimal surface contact between the conductive part and the polymer. Some promising solutions to circumvent this challenge embed the conducting parts of the antenna within a thin layer of polymer. This embedding approach has been demonstrated with various types of conductive materials. Among them are carbon

nanotube sheets, copper mesh, silver nanowires, embroidered threads, and, most recently, conductive fabrics which turned out to be a simple yet effective solution [160]-[167]. One such antenna is shown in Figure 3.5.

Figure 3.5: Images of the fabricated PDMS-embedded conductive fabric antenna [168].

An embedded antenna protects the conductive layer from harsh environments, temperatures, and moisture, which may happen from repeated sweating, that can affect the weak attachment between the metal and the polymer [161],[163]. Among polymers, PDMS presents advantages of high flexibility and stretchability and has a reasonably acceptable loss factor at microwave frequencies. The preparation of PDMS can also be done at room temperature through a simple low-cost process [166]. With its characteristics of water resistance, chemical inertness, high heat resistance (up to 400°C), and stability under ultraviolet exposure, PDMS is very resilient to extreme environments [159].

The PDMS-embedded conductive-fabric technique presents excellent opportunities for realization of various types of conformal antennas. The antennas were realized using conductive fabric which was embedded within the polymer. A rather strong adhesion of conductors to dielectric was achieved. Excellent results in terms of integration can be achieved when conductive fabric is utilized for constructing the metallic parts. The reason is the porous nature of the conductive fabric that allows for the creation of the polymer-polymer bonding. This bonding helps in sealing the PDMS fabric attachment, thus leading to a robust mechanical integration between the two materials. Such a phenomenon was understood though sample observation under a scanning electron microscope (SEM) as shown in Figure 3.6.

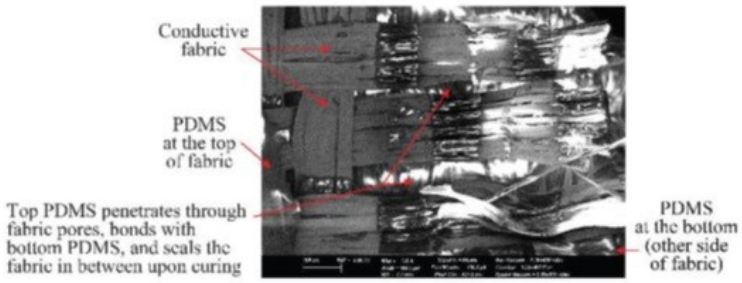

Figure 3.6: Scanning electron microscope image of the fabric that is bonded with PDMS [159].

A limitation of this embedding technique is that the conductivity of the conductive parts is relatively low compared to the metals which influence the antenna performance [159]. In addition, the loss tangents of the polymers, especially in the higher frequency ranges, is high, which influences the antenna efficiency and as a result affects the antenna's gain. To compensate for this, it was suggested in [168] to use different conductive fabrics for different conductive parts of the antenna, to double-coat the fabric, to develop a coating material with higher conductivity, or to decrease the loss of the polymer through other-material inclusions.

Based on the literature, there are promising techniques and methods for fabricating flexible antennas for a practical wearable head imaging device. Therefore, as part of the core investigation of this thesis on MWI and MWS for AD monitoring, flexible antennas developed using textile and silicone rubber substrates for wearable head imaging applications were designed, fabricated, and experimentally validated, to verify its performance for monitoring BA, LVE, and accumulation of plaques and tangles in the brain.

3.2 Design of Wideband Planar Monopole Antennas using Flexible Substrates

Based on the requirements outlined in the previous section, it was decided to design and use a planar monopole antenna (PMA) because of several advantages that it has over other antenna types, including being wideband, low-profile, compact, and able to transmit and receive wideband signals without significant distortions. Many variations

of PMAs were investigated that utilised various shapes and slots for the radiating elements of the antennas including squares, rectangles, circles, ellipses, and trapezoids [169] – [174].

In this section, two variations of PMAs were investigated and optimised for wearable sensing antenna for microwave head imaging device. In addition, the impedance bandwidths of the antennas were optimised to cover the operating frequency range from 1.5 GHz up to 3 GHz which allow enough penetration depth of the EM signals inside the human head to efficiently capture all physiological and pathological changes associated with AD located in different regions of the brain. Specifically, radiation at the lower end of the operating frequency would enable the antenna to transmit and receive waves from deeper areas of the brain, while the radiation emitted at the higher frequency range would enable the antenna to transmit and receive waves from the surface of the brain closest to the antenna. The optimisation of the bandwidth of the PMAs depends on two main aspects of the antenna structure which are the shape and dimension of the radiating part and the feeding line [18]. Full-wave simulations were carried out using CST Microwave Studio which adopts finite-difference time-domain method. Finally, the simulations results were compared to the measured results for validation.

3.2.1 Antenna Design Procedure

Planar monopole antennas have various radiating patch shapes which include square, rectangle, circular, elliptical, and trapezoidal shape as illustrated in Figure 3.7 [174].

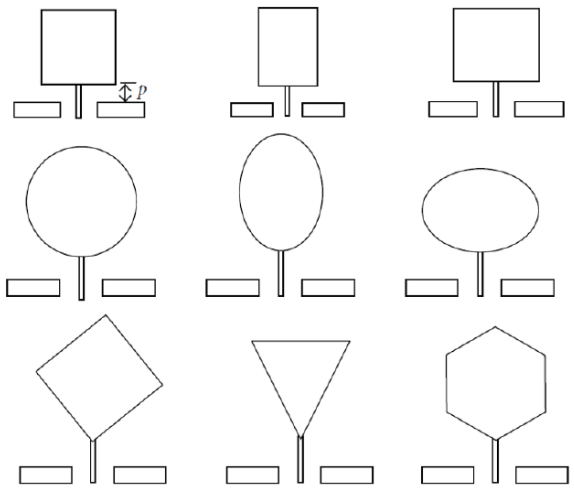

Figure 3.7: Various shapes of planar monopole antennas [174].

These radiating patches are mainly fed using two types of transmission lines which are microstrip line or co-planar waveguide. The lowest operating frequency of the monopole antennas mainly depends on the maximum length of the radiating patch and the permittivity of the substrate used whereas the bandwidth of the antennas depends on the impedance matching of the 50Ω feeding line to the various modes excited by the antennas.

To estimate the lowest band-edge frequency of the monopole antennas, the standard equation derived for cylindrical monopole antennas can be used with appropriate modification [175],[177]. This could be used to analytically design the antenna for the lower-edge frequency by equating its area (or in this case rectangular monopole with length *L* and width *W*) to an equivalent monopole antenna of the same height, *L* and equivalent radius, *r* as given in Equation 3.1 below [175]. The formula given in Equation (3.2) is used to find the lowest band-edge frequency and was adopted for PMAs by taking the length of the patch of the planar monopole, *L* in cm as that of an equivalent cylindrical monopole antenna and *r*, which is the effective radius of the equivalent cylindrical monopole antenna, in cm, and h is the height between the radiator and ground plane in cm (or the thickness of the substrate).

$$2\pi rL = WL \tag{3.1}$$

$$f_L = \frac{c}{\lambda} = \frac{7.2}{(L+r+h)} \tag{3.2}$$

Further modification on Equation (3.2) is done to consider the dielectric layer that is on one side of the printed monopole antenna [176]. This causes an increase in the effective dimensions of the monopole, therefore leading to a reduction in the lower band-edge frequency. As a result, a more appropriate equation for estimating the lower operating band-edge frequency of PMAs is given by [175]:

$$f_L = \frac{c}{\lambda} = \frac{7.2}{\{(L+r+h)\times k\}} \tag{3.3}$$

The lowest operating band-edge frequency of the monopole antenna can be reduced by increasing the length of the antenna. As for the bandwidth, appropriate feeding line must be designed to match with the excited modes of the antenna. This is normally

achieved by implementing various feeding line structures with the help of EM simulators by carrying out parametric optimisations on the structures.

The structure of a typical PMA is shown in Figure 3.8 and consists of a microstrip line, radiating patch, ground plane, and substrate.

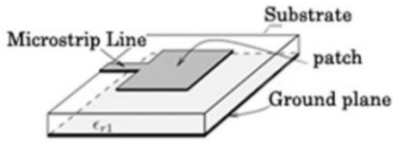

Figure 3.8: Structure of a planar monopole antenna that is like a patch antenna [176].

The Antenna is fed with a microstrip line where the line is then transitioned into the rectangular radiating patch structure. In this configuration, field lines are found to propagate inside the substrate and some of them extend to the outer space. This causes a fringing effect which causes the PMA's dimensions to look greater than its actual measurement. As a result, an effective dielectric constant is introduced to account for fringing and the wave propagation in the microstrip line. This is done through the following formula (Equation 3.4):

$$\varepsilon_{eff} = \frac{\varepsilon_R+1}{2} + \frac{\varepsilon_R-1}{2}\left[\frac{1}{\sqrt{1+12(\frac{h}{W})}}\right] \tag{3.4}$$

where ε_{eff} is the effective dielectric constant and ε_R is the dielectric constant of the substrate. The length (L) and width (W) of the radiating patch can then be calculated based on the following formulas below (Equations 3.5 and 3.6, respectively):

$$W = \frac{\lambda}{2}\sqrt{\frac{2}{\varepsilon_R+1}} \tag{3.5}$$

$$L = \frac{\lambda}{2\sqrt{\varepsilon_{eff}}} - 0.824h\left(\frac{(\varepsilon_{eff}+0.3)(\frac{W}{h}+0.264)}{(\varepsilon_{eff}-0.258)(\frac{W}{h}+0.8)}\right) \tag{3.6}$$

where λ is the wavelength can be determined from Equation 3.3. As a final step in the design of the antenna, it is important that the impedance of the microstrip feeding line of the PMA antenna is properly matched and characterized to a 50 Ω impedance to ensure that RF signals are generated from the source to the antenna with as minimum

loss as possible. This can be done by optimizing the width of the microstrip line using Equation 3.7.

$$Z_0 = \frac{120\pi}{\sqrt{\varepsilon_R}\left(\frac{W_f}{h}+1.393+0.667\times ln\left(\frac{W_f}{h}+1.44\right)\right)} \quad (3.7)$$

where Z_0 is the characteristic impedance of the microstrip feeding line and W_f is the width of the microstrip feeding line.

Since the purpose of this thesis is primarily on the investigation of MWI and MWS for detecting AD, it was decided to only focus on one antenna type as the basis of this work with few design considerations. This allowed me to focus on validating MWS and MWI techniques for detecting BA, LVE, and accumulation of plaques and tangles in the brain and therefore validating MWS technology as a proof of concept for non-invasive detection and monitoring of AD. By considering the shape of the human head, and in view of making an array of antennas that would fit around the head, two shapes were considered: a stepped monopole antenna structure (SPMA) and a rectangular-shape planar monopole antenna (RPMA). In addition, this thesis discusses about the development of the two antennas different flexible substrates: 1) felt for the SPMA and 2) silicone rubber for the RPMA. The radiating patches and ground planes were designed based on properties for a conductive textile material. Design and optimization of the proposed antenna structure were carried out using computational models in CST Microwave Studio. By using a specific anthropomorphic mannequin (SAM) head phantom model in the CST Microwave Studio software as a reference, the SPMA and RPMA were designed such that its length is longer than its width. By choosing this antenna as the starting point of the antenna design, an array of up to 6 antenna elements were developed and arranged in an elliptical configuration around the head for the two MIND devices that will be presented later in Chapter 8. The length and width of the radiating shapes, width of the feeding line, and thickness of the substrates were some of the properties investigated for the proposed antennas to find the optimal design to fulfil the requirements of the MIND device, as mentioned in Chapter 3, Section 3.1 and using Equations 3.1 to 3.7. Since the antenna will be bent to follow the contour of the head, its effect on the impedance matching of the antennas will also be investigated.

3.2.2 Stepped Monopole Antenna on Felt Substrate

The first antenna that is investigated is an SPMA antenna that uses a felt substrate. An initial design of the SPMA antenna is shown in Figure 3.9 that was based on the work done in [178]. with initial dimensions of the length and width of the radiating patch being 85 mm and 35 mm, respectively.

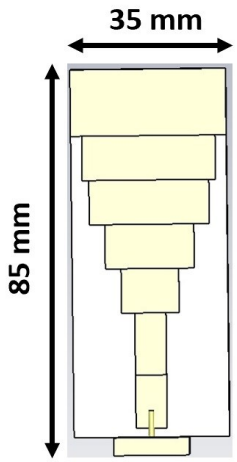

Figure 3.9: Initial design of the SPMA on felt substrate.

A 0.1-mm-thick flexible conductive textile, Shieldex Zell is utilized as the radiating patch of the antenna, while the substrate is made of RS-PRO Viscose Wool Felt material with a measured relative permittivity, ε_r and loss tangent, $tan\,\delta$ of 1.55 and 0.068 respectively and a thickness of 6 mm. By using the Equation 3.1, the lowest band-edge frequency is obtained to validate whether sufficient penetration depth is achieved for the MIND device. This value was found to be 1.3 GHz. The length of the microstrip feeding line was then chosen to match 50 Ω based on Equation 3.6. The antenna was then simulated in the EM solver to validate its performance against theoretical calculations and optimise its parameters. This was done to satisfy the main objective of finding the optimal lower edge operating frequency that ensures sufficient penetration depth is achieved for the MIND device in order to detect changes in certain regions of the brain due to AD. The lowest band-edge frequency that was obtained in the simulation was 1.65 GHz as shown in Figure 3.10.

It can be seen in Figure 3.10, that the required bandwidth of the antenna is not suitable for the application. As a result, further design optimisations had to be done on the geometry of the radiating patch and the feeding line.

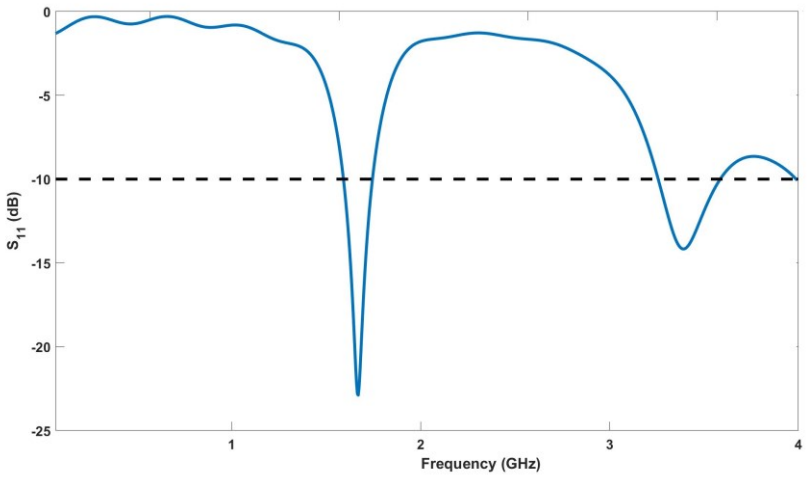

Figure 3.10: Simulated reflection coefficient for the SPMA antenna shown in Figure 3.9.

Several approaches in antenna design have been reported in [179]-[182] that focuses on improving different parameters of the antenna. One such design is the implementation of a stepped gradient that could improve the bandwidth of the antenna [180]. This was used as the basis of the SPMA antenna design in this thesis. Since the design of the antenna utilises textile materials, the performance of a textile antenna is very sensitive unstable due to tolerance issues such as stretch effect, fraying, humidity effect and bending that needs to be considered due to the flexible textile structure that may cause performance degradation.

Therefore, it is important to ensure that the antenna can perform by identifying a suitable feed line technique [182]. The key for an antenna to work efficiently is to ensure maximum power transfer between the source and the antenna, such as the signal is fed at a point where the input impedance is 50 ohms. In addition, changes to the feeding line can improve both the bandwidths of monopole antennas and impedance matching. However, an important factor to consider is the convenience of implementing the proposed changes on the actual conductive textile material that will be used for fabricating the antenna. For instance, in [182], the authors found that implementing the coaxial feed technique was more suitable for the textile patch antenna because the

correct input impedance can be achieved easily in fabrication as compared to the transmission feed line technique. Although this is good, the coaxial feed line technique relies on the connection of the connector to the radiating patch from the back of the antenna structure. This can cause tearing on the radiating patch which would hinder the antenna's performance. In addition, by incorporating the coaxial connector at the back, this would make the overall structure of the antenna to be bulky in size, which would not be suitable for the proposed SPMA.

Another promising technique for modifying the feed line for impedance matching, is to use an inset feed as shown in Figure 3.11 [183]. However, such a design in a conductive textile would be difficult to do precisely. In addition, this sort of modification may cause unwanted effects on the radiating structure because of fraying, which would be present from manual cutting of the inset feed lines on the antenna structure. As a result, it was decided to optimise the feeding line by implementing a quarter-wavelength transmission line (QWTL) [184] as shown in Figure 3.12.

Figure 3.11: Antenna with inset feed line.

Figure 3.12: Antenna with quarter wavelength transmission line.

By using QWTL, the goal is to match the input impedance (Z_{in}) to the characteristic impedance of the microstrip transmission line (Z_0). If the impedance of the antenna is Z_A, then the input impedance viewed from the start of the QWTL becomes [184]:

$$Z_{in} = Z_0 = \frac{Z_1^2}{Z_A} \tag{3.8}$$

where Z_1 is the characteristic impedance of the QWTL as shown in Figure 3.12. It can be seen in Equation 3.8 that Z_{in} can be altered by the selection of Z_1 such that $Z_{in} = Z_0$ and the impedance is matched. As a result, Z_1 can be altered by changing the width of the QWTL strip. The wider the strip is, the lower the characteristic impedance is for that section of the line.

For the proposed SPMA, the focus was placed on altering the width of QWTL strip such that the antenna could obtain optimal bandwidth. From the initial SPMA design, the QWTL strip was altered to 3 different widths as highlighted in Figure 3.13. Parametric optimisations were carried out on the feeding line widths, W_{feed}, and keeping the width of the QWTL at 7 mm. The resulting reflection coefficients are shown in Figure 3.14. The widest bandwidth obtained was 3.55 GHz when W_{feed} is 17 mm, which provided an improved reflection coefficient for the antenna that covers a frequency range of 1.1 GHz to 4.65 GHz.

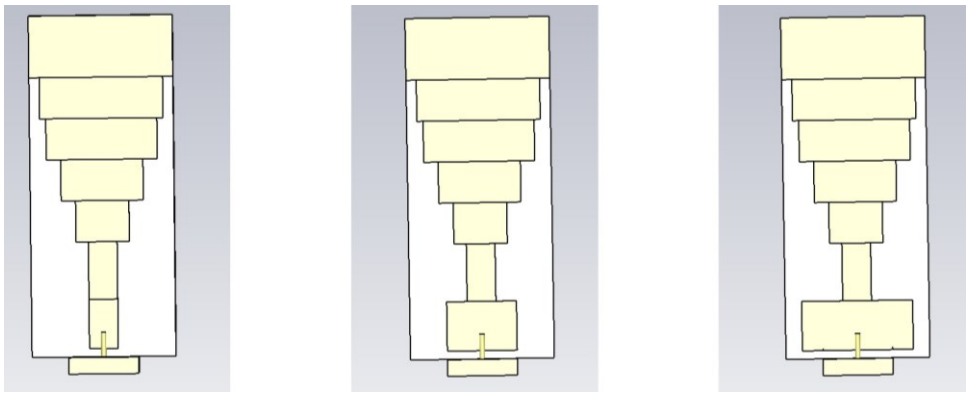

(a) (b) (c)

Figure 3.13: Optimisation of the impedance bandwidth of the proposed antenna by varying the width of the feed line (W_{feed}): (a) $W_{feed} = 7\ mm$, (b) $W_{feed} = 17\ mm$, and (c) $W_{feed} = 27\ mm$.

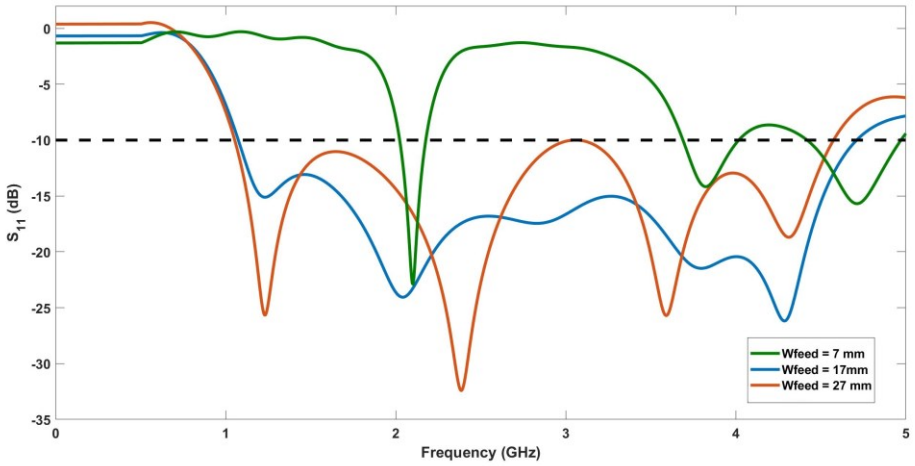

Figure 3.14: Simulated reflection coefficients for different values of feed line width, W_{feed}.

Based on the simulations in CST, the optimal design of the parameters was obtained and listed in Table 3.1, while Figure 3.15 shows the final front and back design of the felt-based SPMA.

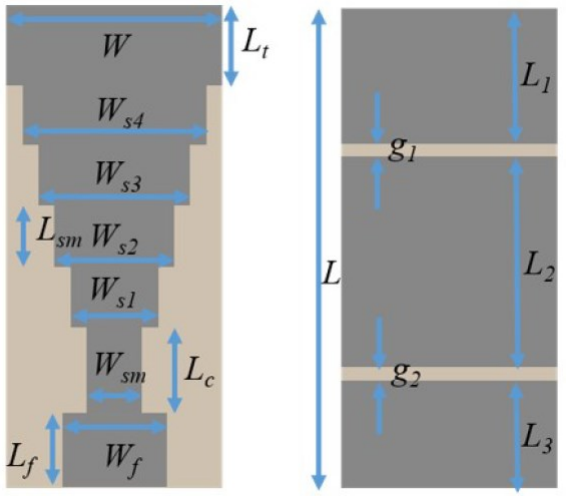

Figure 3.15: Geometry of the final optimised SPMA on felt substrate (a) Top view and (b) Bottom view.

Table 3.1: Geometric parameters of stepped monopole antenna on felt substrate

Antenna Parameters	**Symbol**	**Value (mm)**
Width	W	35
Length	L	85
Feeding Line Width	W_f	17
Feeding Line Length	L_f	12
QWTL Width	W_Q	7
QWTL Length	L_Q	14
Step 1 Radiating Patch Width	W_{s1}	13
Step 1 Radiating Patch Length	L_{s1}	10
Step 2 Radiating Patch Width	W_{s2}	20
Step 2 Radiating Patch Length	L_{s2}	10
Step 3 Radiating Patch Width	W_{s3}	27
Step 3 Radiating Patch Length	L_{s3}	10
Step 4 Radiating Patch Width	W_{s4}	30
Step 4 Radiating Patch Length	L_{s4}	10
Top Radiating Patch Width	W_t	35
Top Radiating Patch Length	L_t	15
Top Ground Plane Length	L_1	25
Middle Ground Plane Length	L_2	30
Bottom Ground Plane Length	L_3	25
Gap 1	g_1	3
Gap 2	g_2	2
Substrate Thickness	h	6

To investigate the polarization of the antenna, the surface current at several operating frequencies over the antenna bandwidth were simulated as shown in Figure 3.16. The induced surface current distributions are aligned in the same *Y*-direction for all frequencies, which provides a high co-polarisation of the antenna across its bandwidth. This signifies that the antenna can capture scattered waves during measurements.

(a) (b) (c)

Figure 3.16: Surface current distribution on the antenna at (a) 1.5 GHz, (b) 2.5 GHz, and (c) 3 GHz.

A. Simulated Radiation Pattern of Stepped Monopole Antenna on Felt Substrate

Figure 3.17 shows the simulated 2-D radiation patterns of the felt-based SPMA antenna at 1.5 GHz. It can be observed that the radiation patterns are nearly directional in both the H-plane and E-plane. 3-D radiation patterns of the antenna are illustrated in Figure 3.18. As the frequency increases from 1.5 GHz to 3 GHz, the direction of the main lobe slightly diverts from the boresight direction by 30°. The maximum simulated gain of the antenna varies from 1.8 dBi to 4.11 dBi from 1.5 GHz to 3 GHz.

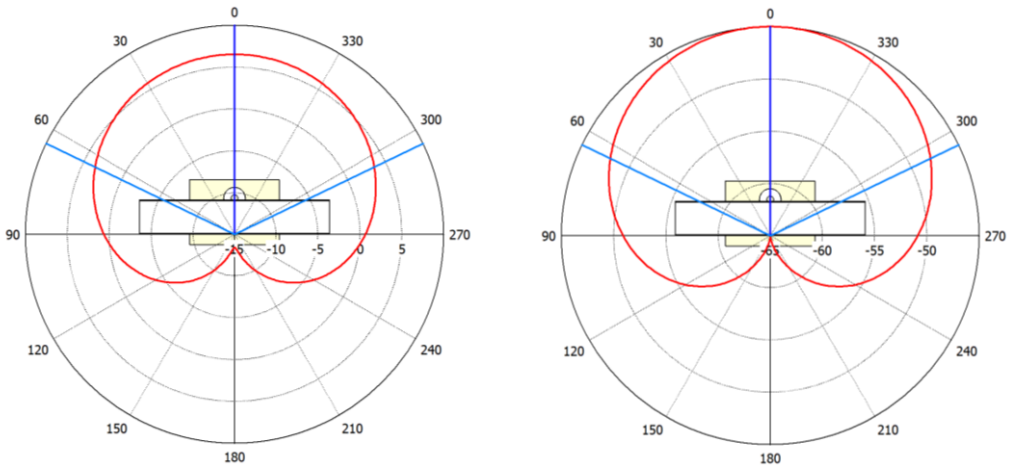

Figure 3.17: Simulated E-(XZ) and H-(XY) plane 2-D far-field radiation patterns at 1.5 GHz.

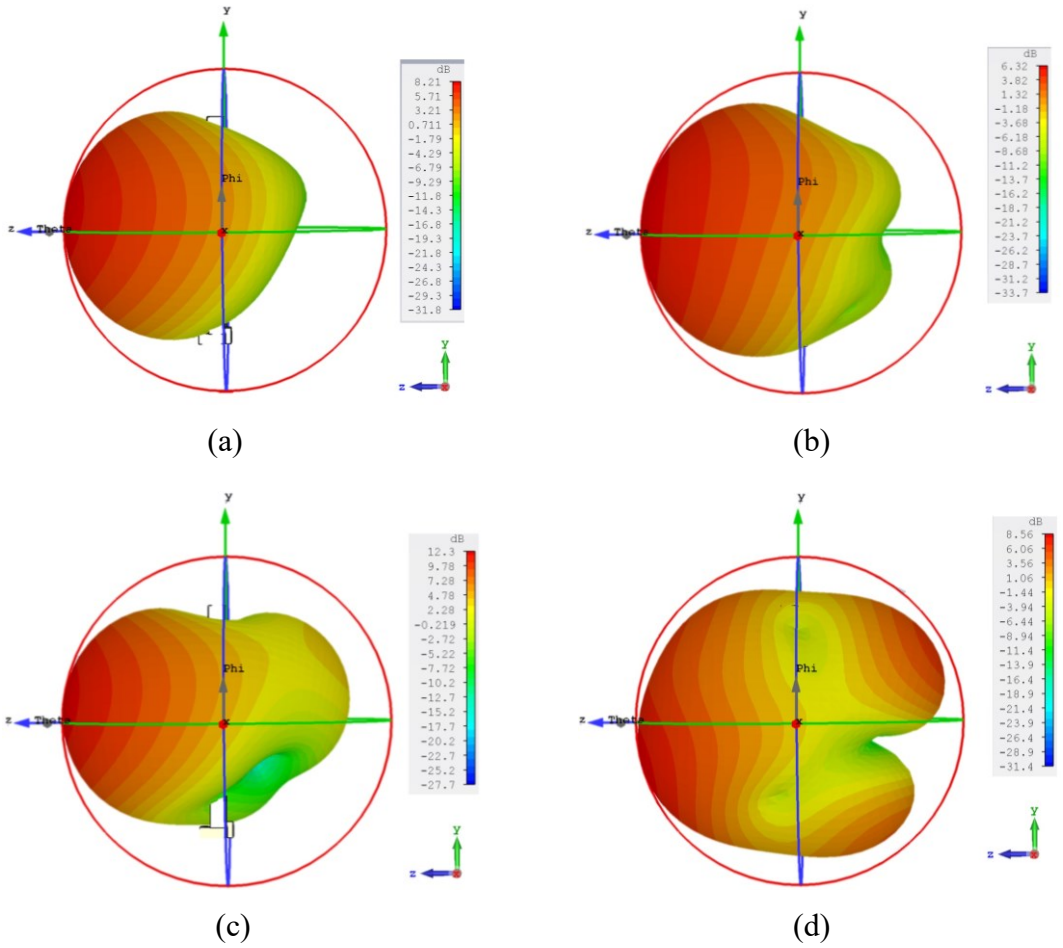

Figure 3.18: Simulated 3-D radiation patterns of the antenna at (a) 1.5 GHz, (b) 2 GHz, (c) 2.5 GHz, and (d) 3 GHz.

B. Time-domain Characterisation of Stepped Monopole Antenna on Felt Substrate

Since the probing antenna operates mainly in the near-field, its performance should also be investigated in time-domain. To characterise the time-domain performance of the antenna, the Gaussian pulse in the CST Microwave Studio was utilised. The frequency bandwidth of the pulse was set from 1.5 GHz to 4 GHz based on the operating bandwidth of the proposed antenna. In order to examine the performance of the antenna in the time domain, the fidelity factor and time domain amplitude responses around the antenna were calculated using the EM simulator. The fidelity factor shows the level of distortions of the radiated pulses in various directions. The value of fidelity factor varies between 0 and 1, with 1 representing the minimum and 0 representing maximum distortion of the pulses. For excitation pulse, $f(t)$ taken as the template waveform and

the received pulse at any direction from the antenna, $g(t)$, the fidelity factor can be calculated by [16]:

$$F = max \int_{-\infty}^{\infty} f(t) \times g(t+\tau)dt \quad (3.9)$$

In the electromagnetic solver, co-polarized electric field (E_y) probes were positioned at a distance of 40mm from the centre of the antenna and at angular differences of 90° apart from each other. The computed time-domain responses received by the probes surrounding the antenna are shown in Figure 3.19.

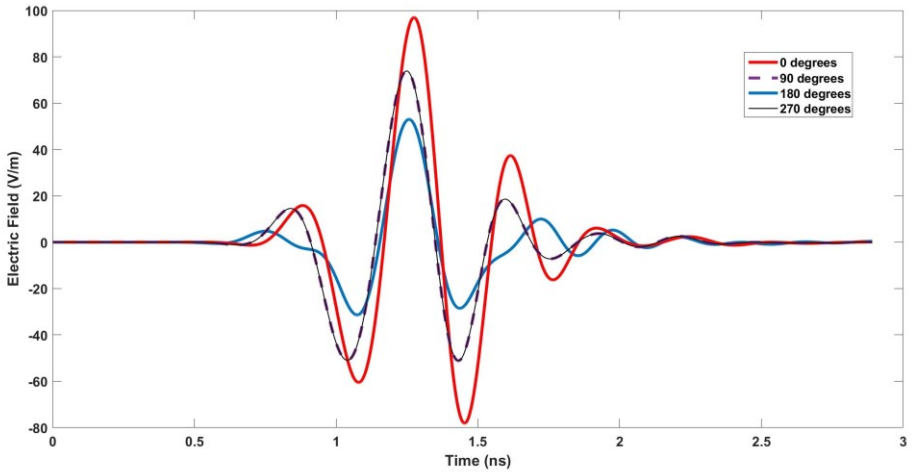

Figure 3.19: Simulated received near-field time-domain pulses radiated by the antenna at different angles in the H-plane.

Table 3.2: Fidelity factor of stepped monopole antenna on felt substrate

Angle (Degrees)	**Fidelity Factor**
0°	0.998
90°	0.9146
180°	0.8955
270°	0.9146

High fidelity factors of more than 0.89 were observed at H-plane as listed in Table 3.2 at all angles. This indicates a stable transmitted pulse performance which is crucial for the proposed head imaging system where the proposed antenna can transmit and receive a pulse with minimal distortion.

3.2.3 Rectangular Monopole Antenna with Silicone Rubber Substrate

The second antenna design that was studied was the use of silicone-rubber as the substrate. By using silicone rubber, the antenna design could be made more flexible and allow the Shieldex Zell conductive textile radiating patch to be embedded in the silicone rubber material that would protect it from water and dust. The silicone rubber used for this design was a Shore A8 silicone rubber that can flex and stretch without breaking its overall structure. The silicone rubber is a Tap Plastics Platinum Silicone Rubber and has a measured relative permittivity, ε_r and loss tangent, $tan\,\delta$ of 2.99 and 0.032, respectively. In addition, it has a tensile strength of 218 psi and a tear resistance of up to 20 ppi. Due to the change in permittivity value from the felt substrate in Section 3.2.2, another set of antenna design and optimization had to be done to set the different parameters, mainly the width of the QWTL line and thickness of the substrate. to achieve similar performance as those obtained for the felt-based SPMA discussed in Section 3.2.2.

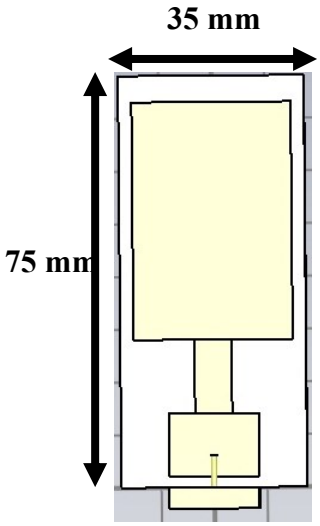

Figure 3.20: Initial design of the RPMA on silicone rubber substrate.

First, an initial design of antenna was created in CST using a rectangular monopole antenna structure, as shown in Figure 3.20, with the same QWTL width as was used for the felt-based SPMA from 3.2.2. However, in this design, it was decided to reduce the overall length of the antenna structure to 75 mm to investigate its performance while

being slightly more compact than the previous SPMA design. In addition, the substrate was replaced with that of the silicone rubber. It was found that the silicone rubber based RPMA had a similar performance to that of the felt-based antenna, which was promising as the QWTL did not require any modification. However, because silicone rubber would encapsulate both the radiating and ground planes, there will be a layer of silicone rubber that surrounds the overall antenna. This was done in CST by creating a superficial layer with thickness of 0.5 mm that is placed on both the top of the radiating patch and the ground plane. This needed to be considered and optimized along with the gap between the radiating patch and ground plane so that the antenna could maintain its performance, as well as be compact and thin enough to be integrated into a wearable MIND device. Substrate thicknesses (i.e., distance between the ground plane and radiating patch) of 6, 5, 4, and 3 mm were investigated. The resulting reflection coefficients are shown in Figure 3.21.

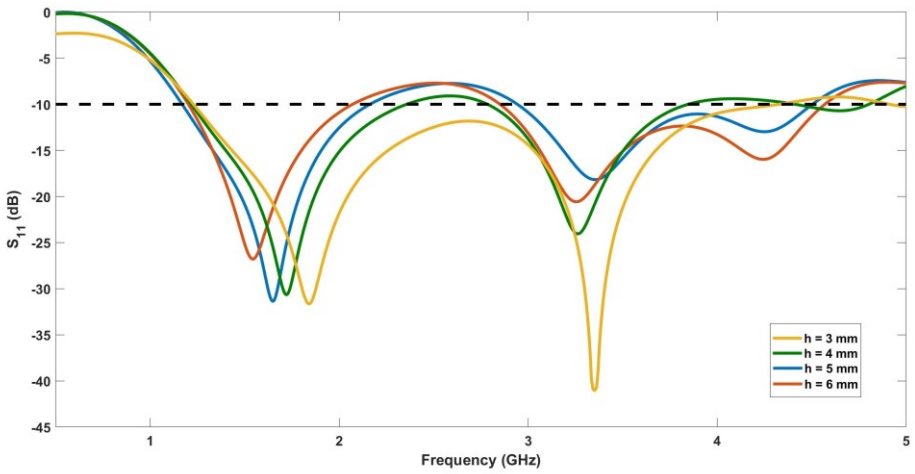

Figure 3.21: Reflection coefficients for varying thickness levels of the substrates.

The final optimised RPMA antenna embedded in silicone rubber is shown in Figure 3.22 along with the final optimised parameters that are listed in Table 3.3 and represented in Figure 3.23. The operating frequency range of the antenna is from 1.08 GHz to 4.13 GHz with a bandwidth of 3.05 GHz.

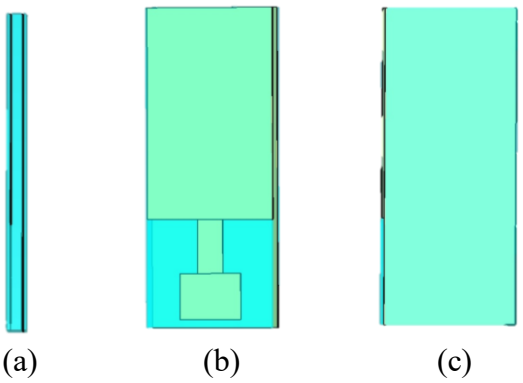

Figure 3.22: (a) Side, (b) Top, and (c) Bottom view of the RPMA antenna embedded in silicone rubber.

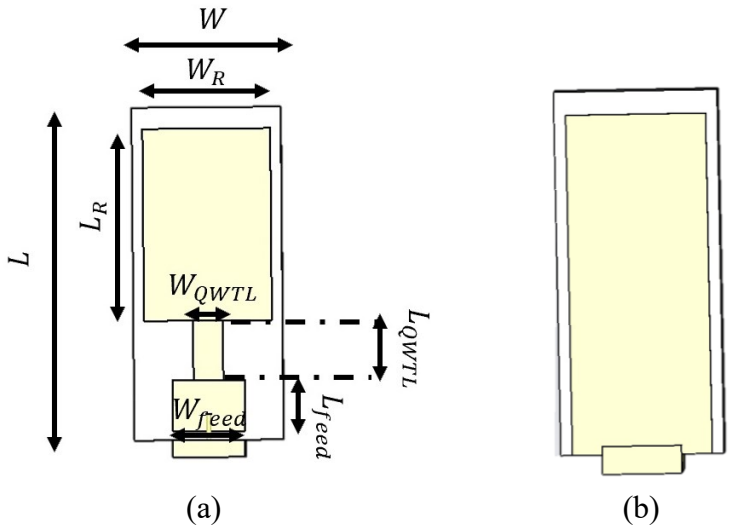

Figure 3.23: Geometry of the final optimised RPMA embedded in silicone rubber substrate (a) Top view and (b) Bottom view.

Table 3.3: Geometric parameters of rectangular monopole antenna on silicone rubber substrate

Antenna Parameters	**Symbol**	**Value (mm)**
Width	W	35
Length	L	75
Radiating Patch Width	W_R	30
Radiating Patch Length	L_R	50
Feeding Line Width	W_{feed}	17
Feeding Line Length	L_{feed}	12
QWTL Width	W_{QWTL}	7
QWTL Length	L_{QWTL}	13
Substrate Thickness	h	3

A. Simulated Radiation Pattern of Rectangular Monopole Antenna Embedded in Silicone Rubber Substrate

Figure 3.24 demonstrates the simulated 2-D radiation patterns of the silicone rubber-based RPMA antenna at 1.5 GHz. It can be observed that the radiation patterns are directional in both the H-plane and E-plane, thus the antenna exhibits directional pattern. 3-D radiations patterns of the antenna at three frequencies within the operating frequency are depicted in Figure 3.25.

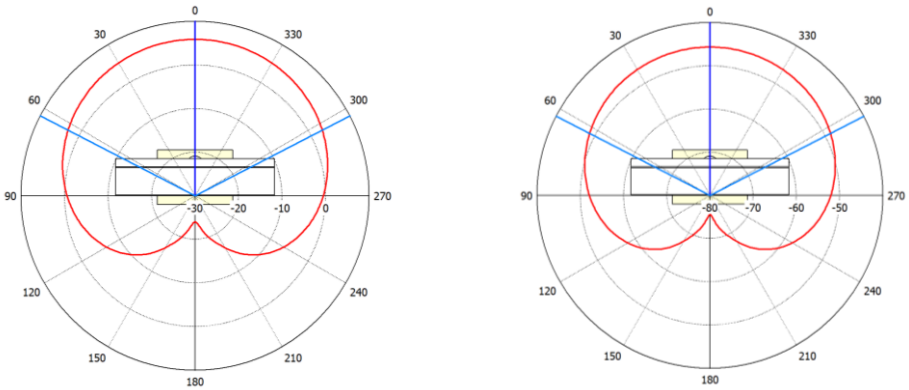

Figure 3.24: Simulated E-(XZ) and H-(XY) plane 2-D far-field radiation patters at 1.5 GHz for RPMA with silicone rubber substrate.

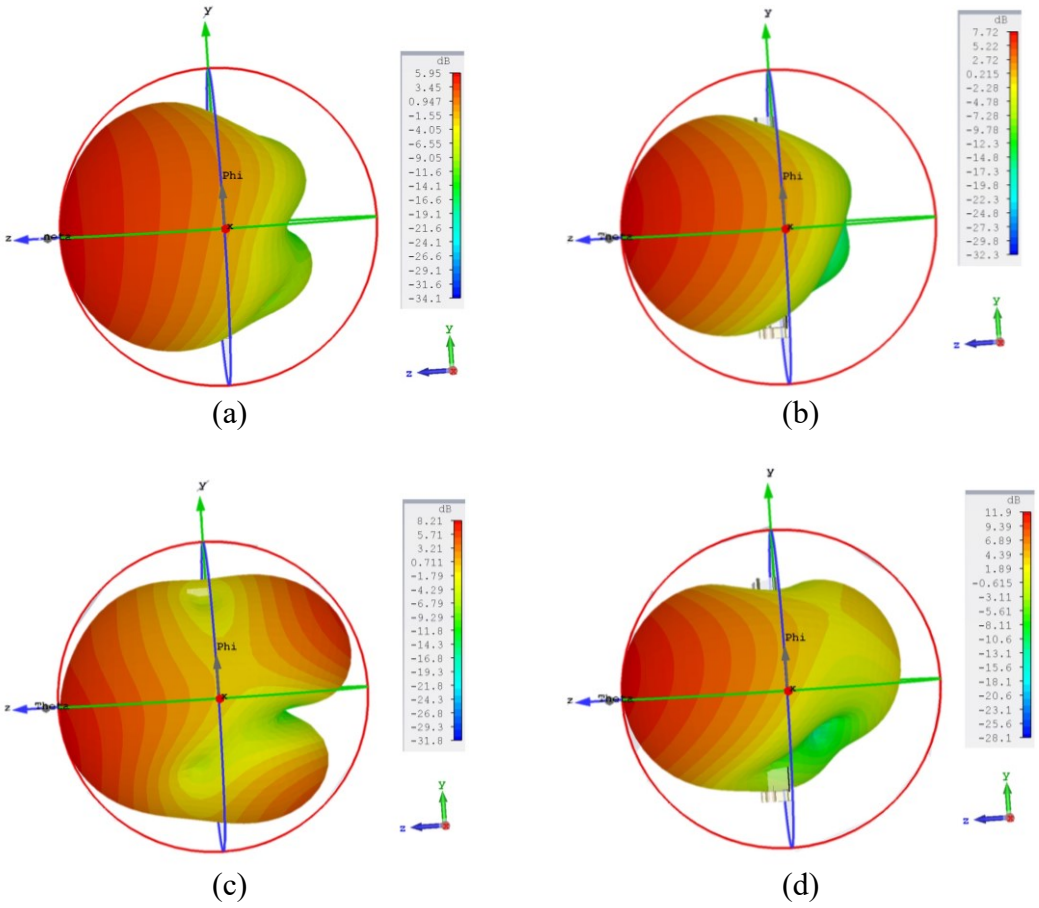

Figure 3.25: Simulated 3-D radiation patterns of the RPMA antenna with silicone rubber at (a) 1.5 GHz, (b) 2 GHz, (c) 2.5 GHz, and (d) 3 GHz.

B. Time-domain Characterisation of Rectangular Monopole Antenna Embedded in Silicone Rubber Substrate

The computed time-domain responses received by the probes surrounding the silicone rubber-based RPMA antenna are shown in Figure 3.26. For this antenna design, high fidelity factors of more than 0.94 are again observed at H-plane as tabulated in Table 3.4. This shows that the antenna will be able to radiate a pulse with minimal distortion which is important for the head imaging applications.

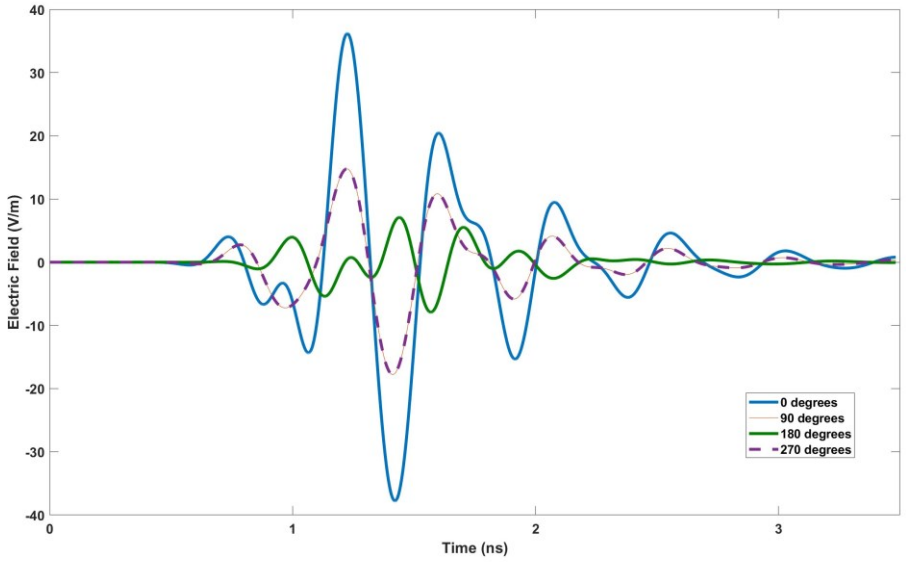

Figure 3.26: Simulated received near-field time-domain pulses radiated by the antenna at different angles in the H-plane.

Table 3.4: Fidelity factor of rectangular monopole antenna on silicone rubber substrate

Angle (Degrees)	Fidelity Factor
0°	0.9954
90°	0.9541
180°	0.8237
270°	0.9541

3.2.4 Performance Evaluation of Proposed Antennas Near Human Head

Antennas that are used for medical MWI and MWS applications have a chance of deteriorating in terms of their performance when they are placed on or near the human body. For the MIND device, the antenna needs to be placed in direct contact with the head so that most of the transmitted energy is propagated into the brain tissues. As a result, simulations were performed on CST Microwave Suite to validate the antenna design based on the effects of lossy head tissues on the characteristic and performance of the proposed SPMA and RPMA antennas. This would require necessary

optimization in the antenna design to improve and optimise its performance. In addition, the effects of bending on the antenna's reflection coefficient are investigated since the antennas will be slightly bent to follow the contours of an artificial head phantom.

A. Stepped Monopole Antenna on Felt Substrate

Figure 3.27 shows the configuration of the felt-based SPMA antenna when bent to conform to the shape of a specific anthropomorphic mannequin (SAM) head phantom in the CST Microwave Studio.

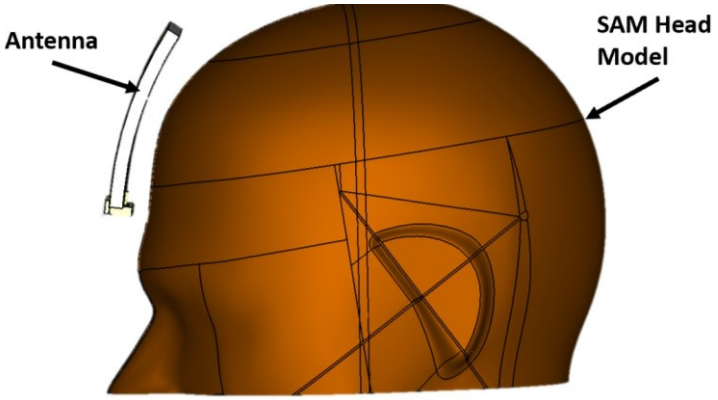

Figure 3.27: Antenna placement on the SAM head model in CST simulation models.

A 6 mm separation between the antenna and the head phantom was specified in the simulation. In the actual experiments, this separation is provided using felt material which acts as a spacer between the antenna and the head, and also protects the antenna structure from sweat, dust, and water content that would affect its performance. The S_{11} result of the antenna is shown in Figure 3.28. It is seen that the S_{11} responses differ between the two cases where the impedance matching of the antenna deteriorates across the frequency range of 1.8 GHz to 3.3 GHz when the antenna is placed on the head phantom. However, the impedance matching is still below -10 dB which indicates that the antenna's performance is still acceptable. The lower operating frequency edge of the antenna does not change whereas the upper frequency range slightly increases from 4.65 GHz to 4.71 GHz. This results in increase of the impedance bandwidth of the antenna from 2.2 GHz to 2.7 GHz when operates in presence of the head phantom. The simulation results confirm that the antenna's impedance matching is still below -10 dB

when operating in close proximity of the head phantom. As a result, no further optimisations on the antenna design was required.

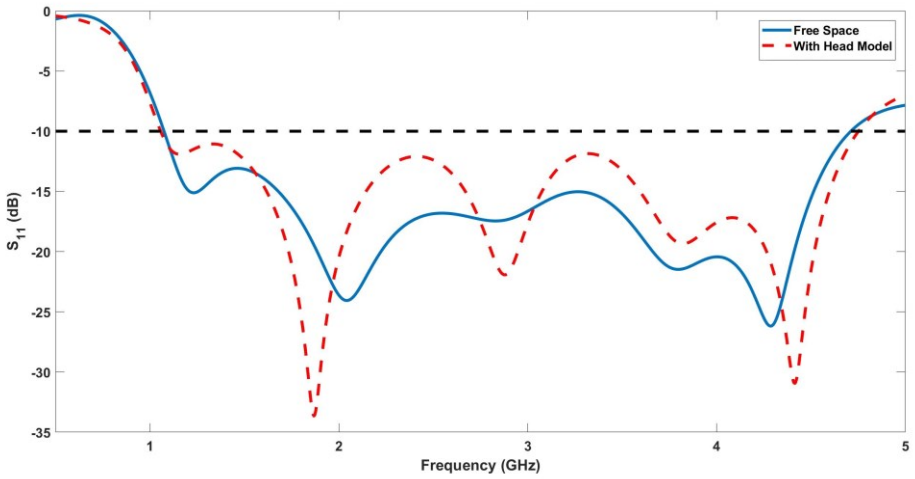

Figure 3.28: Simulated reflection coefficient of the felt-based stepped monopole antenna in free space and on the head model.

For microwave imaging systems, the regions of where the antenna operates depend on the antenna size, its operating frequency range, and the permittivity of the imaged body parts. For the proposed antennas that were designed to operate mostly within the frequency range of 1.5 GHz to 3 GHz, the near-field region, r_{near} extends from 31cm (1.5 GHz) to 62cm (3 GHz) calculated using equation (3.10) [132].

$$r_{near} < \frac{2D^2}{\lambda_m} \tag{3.10}$$

where the average permittivity of the head phantom is assumed to be 40. λ_m is the operating wavelength in the medium and *D* is the largest dimension of the antenna. For both antenna designs, the largest dimension of the antennas is 70 mm. Since the size of average human head is less than the calculated near-field range, this confirms that the antennas mainly operate within the near-field region in the microwave head imaging.

To further validate that the performance of the antenna is intact when operating near the human head, time-domain characterisation was carried out by radiating a pulse into the head. A field probe was placed inside the head at 0° from the boresight direction of the antenna at 50 mm from the centre of the antenna as illustrated in Figure 3.29 to

calculate the field strength and shape of the pulse when the signal propagates from the antenna towards the head.

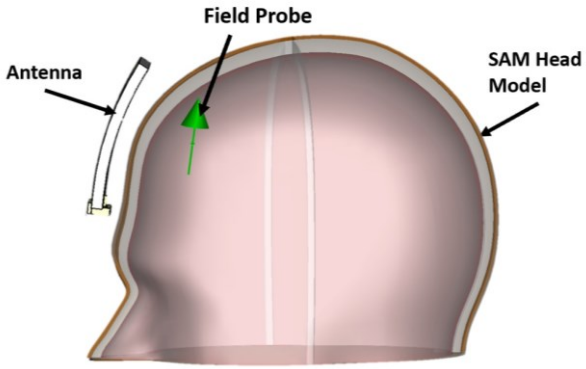

Figure 3.29: Placement of the field probe inside the head phantom.

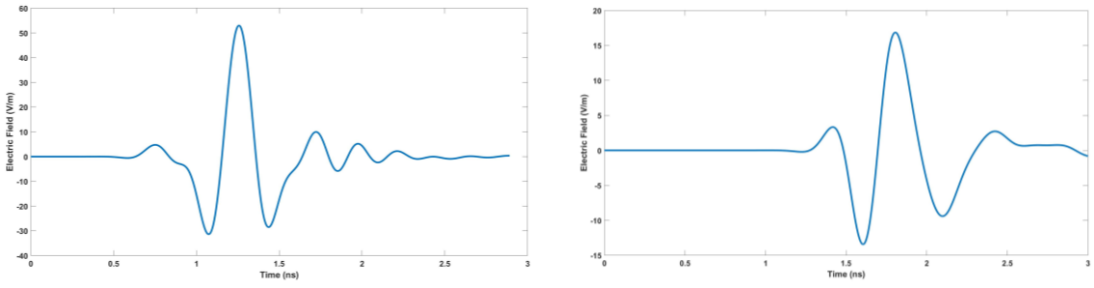

(a) (b)

Figure 3.30: Simulated received near-field time-domain pulses radiated by the felt-based stepped monopole antenna at 0° (a) in free space and (b) with head model in the H-plane.

Figure 3.30 shows the comparison of the received transmitted pulses with and without the head phantom. The amplitude of the pulse is reduced when the head phantom is present by a factor of 3 confirming that the head phantom consists of several layers of lossy biological tissues that greatly weaken the strength of the transmitted EM wave. In addition, a noticeable delay of the pulse received at the 0º probe for the case with head phantom is due to the reduction of the EM wave velocity when travelling through a high permittivity medium. In terms of the pulse integrity, the fidelity factor of the received pulse inside the head phantom was calculated using Equation (3.8). A fidelity factor of 0.92 is achieved confirming that the pulse radiates with minimal distortion in presence of the head phantom. Another important observation that can be made is that the width of the transmitted Gaussian pulses inside the head phantom is

slightly longer than that of free space that demonstrates pulse spreading occurs when the signal propagates inside the lossy and dispersive head phantom.

B. Rectangular Monopole Antenna Embedded in Silicone Rubber Substrate

For the second antenna design (i.e., silicone rubber-based RPMA), the same bending configuration was applied to the antenna as illustrated in Figure 3.29 and placed on the head model. The S_{11} result of the antenna is shown in Figure 3.31.

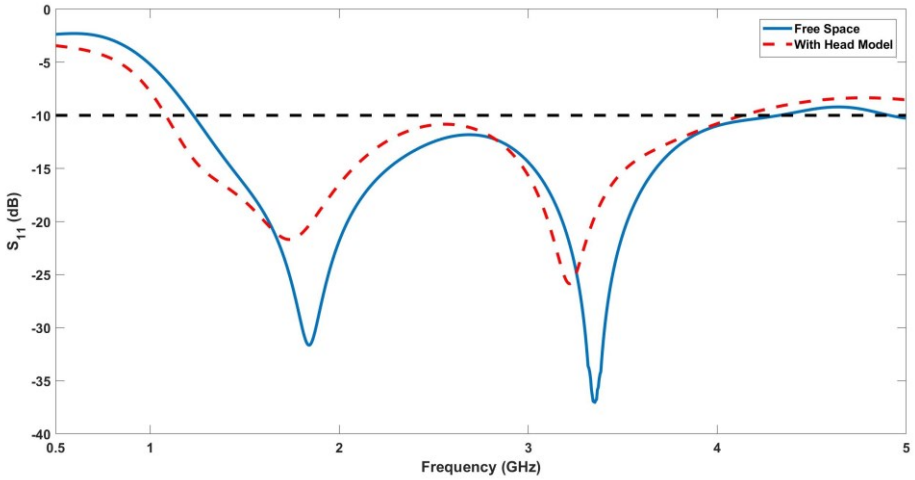

Figure 3.31: Simulated reflection coefficient of the silicone rubber rectangular monopole antenna in free space and on the head model.

It is seen that the S_{11} responses differ between the two cases where the impedance matching of the antenna deteriorates across the frequency range of 1.8 GHz to 3.3 GHz when the antenna is placed on the head phantom. However, the impedance matching is still below -10 dB which indicates that the antenna's performance is still acceptable. The lower operating frequency edge of the antenna does not change whereas the upper frequency range increases from 3.5 GHz to 4 GHz. This results in increase of the impedance bandwidth of the antenna from 2.2 GHz to 2.7 GHz when operates in presence of the head phantom. The simulation results confirm that the antenna's impedance matching is still below -10 dB when operating in close proximity of the head phantom. As a result, no further optimisations on the antenna design was required.

To further validate that the performance of the antenna is intact when operating in close proximity to the human head, time-domain characterisation was carried out by

radiating a pulse into the head that was done using the same method for the felt-based SPMA and shown in Figure 3.29. Figure 3.32 shows the comparison of the received transmitted pulses with and without the head phantom.

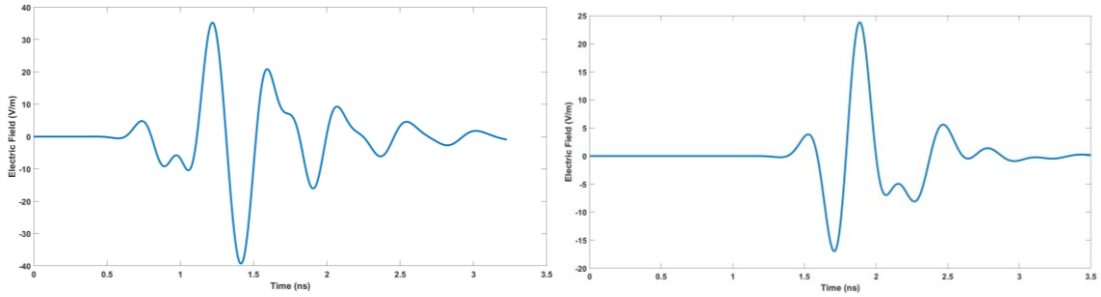

(a) (b)

Figure 3.32: Simulated received near-field time-domain pulses radiated by the silicone rubber-based rectangular monopole antenna at 0° (a) in free space and (b) with head model in the H-plane.

The amplitude of the pulse is reduced when the head phantom is present by a factor of 2 confirming that the head phantom consists of several layers of lossy biological tissues that greatly weaken the strength of the transmitted EM wave. In addition, a noticeable delay of the pulse received at the 0^0 probe for the case with head phantom is due to the reduction of the EM wave velocity when travelling through a high permittivity medium. In terms of the pulse integrity, the fidelity factor of the received pulse inside the head phantom was calculated using Equation (3.7). A fidelity factor of 0.92 is achieved confirming that the pulse radiates with minimal distortion in presence of the head phantom. Another important observation that can be made is that the width of the transmitted Gaussian pulses inside the head phantom is slightly longer than that of free space that demonstrates pulse spreading occurs when the signal propagates inside the lossy and dispersive head phantom.

3.2.5 Fabrication and Measurement Results

In order to validate the performance and characteristics of the proposed antenna designs in the practical setting, antennas were fabricated. The first prototype was a SPMA that was fabricated using the Shieldex Zell conductive fabric for the radiating patch and slotted ground plane and felt textile as the substrate. The second prototype was a RPMA that was fabricated using Shieldex Zell conductive fabric for the radiating patch and

ground plane and embedding the two inside a silicone rubber substrate. Both antenna prototypes were validated using a VNA and their reflection coefficient was measured and compared to simulation results for validation.

A. Stepped Monopole Antenna on Felt Substrate

Figure 3.33 shows the fabricated felt-based SPMA antenna that was fabricated using, textile materials, namely a conductive textile sheet, Shieldex® Zell, and felt, which acted as the substrate.

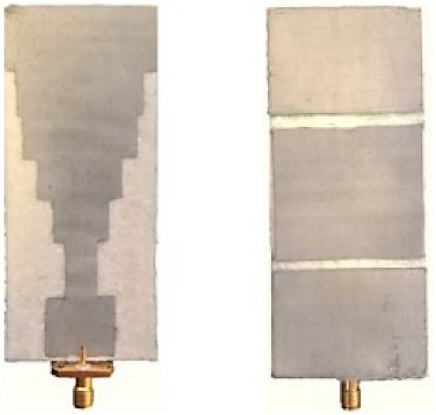

Figure 3.33: Top and bottom view of the fabricated felt-based stepped monopole antenna.

The reported measured conductivity of the fabric is 1.29×10^4 S/m at 2 GHz [132]. The measured permittivity, ε_r and the loss tangent, tan δ of the felt are 1.55 and 0.068 obtained using a dielectric probe. The fabrication of the fully textile antenna was carried out using manual cutting tools. To fasten the conductive sheet onto the felt substrate, an ironing process was carried out to activate the heat-activated adhesive on the reverse side of the conductive fabric. The fully textile-based antenna can be integrated seamlessly into a patient's head garments for wearable applications.

The fully textile-based SPMA antenna is designed with the aim to provide better integration of the antenna with clothing suitable for wearable head monitoring systems. The utilisation of textile materials is to improve the comfort of the wearer in comparison to other materials. Moreover, the proposed antenna can be embedded in clothing items for realisation of wearable head monitoring systems. Figure 3.34 depicts the measured reflection coefficient of the antenna in comparison with the simulated results for both

in free space and on the artificial head phantom. The measured S_{11} signals for both cases demonstrate noticeable increase in the impedance bandwidth of the antenna compared to the simulation results.

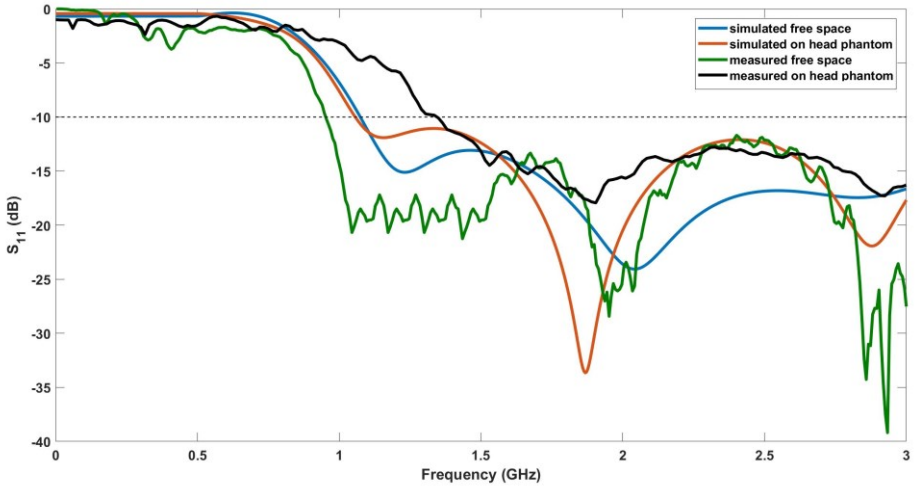

Figure 3.34: Simulated and measured reflection coefficient of the felt-based stepped monopole antenna.

It is seen that the impedance bandwidth of the textile antenna in presence of the head phantom is from 1.26 GHz to 2.76 GHz increases by 480 MHz compared to the simulation result. Again, for the final prototype, the performance of the antenna does not deteriorate when measured on the artificial head phantom suggesting that the antenna has been optimised for use as sensing antenna in the wearable head imaging system. Moreover, the increase in measured bandwidth of the antenna is beneficial to the overall performance of the imaging system.

B. Rectangular Monopole Antenna Embedded in Silicone Rubber

The prototype of the fabricated RPMA antenna embedded in silicone rubber substrate is shown in Figure 3.35. By using silicone rubber, the antenna design could be made more flexible and allow the Shieldex Zell conductive textile radiating patch to be embedded in the silicone rubber material that would protect it from water and dust. The silicone rubber used for this design was a Shore A8 silicone rubber that could flex and stretch without breaking its overall structure. The silicone rubber is a Tap Plastics Platinum Silicone Rubber and has a measured relative permittivity, ε_r and loss tangent,

$tan\,\delta$ of 2.99 and 0.032, respectively. The fabrication method of the sensor is shown in Fig. 3.36. First, a 1 mm silicone rubber mold was created. After the mold cured, the ground plane of the antenna was placed on top. 3 mm of silicone rubber was then poured on the sensor, which encapsulated the ground plane when cured..

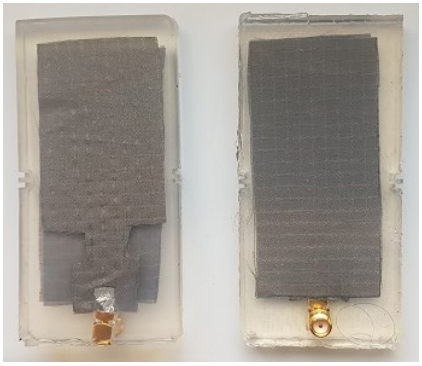

Figure 3.35: Top and bottom view of the fabricated silicone rubber-based rectangular monopole antenna.

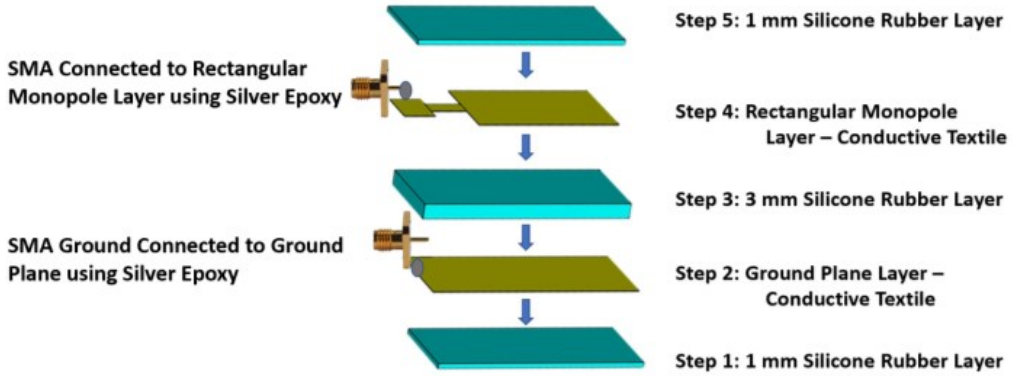

Figure 3.36: Diagram showing the method in which the different layers of the rectangular monopole antenna embedded in silicone rubber was fabricated.

Once cured, the rectangular monopole patch of the antenna was then placed on top of the structure and another 1 mm of silicone rubber was poured on the structure to encapsulate it. After the overall structure was cured, a slot was made at the feeding line and ground plane side. A SMA connector was then attached to the antenna using silver epoxy. The antenna is fed with a microstrip line where the line is then transitioned into a rectangular monopole structure. In order to improve the directionality of the antenna, the ground plane is placed at a distance of 3 mm away from the patch so that it reflects the backward propagated RF signals in the forward direction.

As in the case for the felt-based SPMA, the reflection coefficient for this antenna was measured and validated with the simulation Figure 3.37 depicts the measured reflection coefficient of the antenna in comparison with the simulated results for both in free space and on the artificial head phantom.

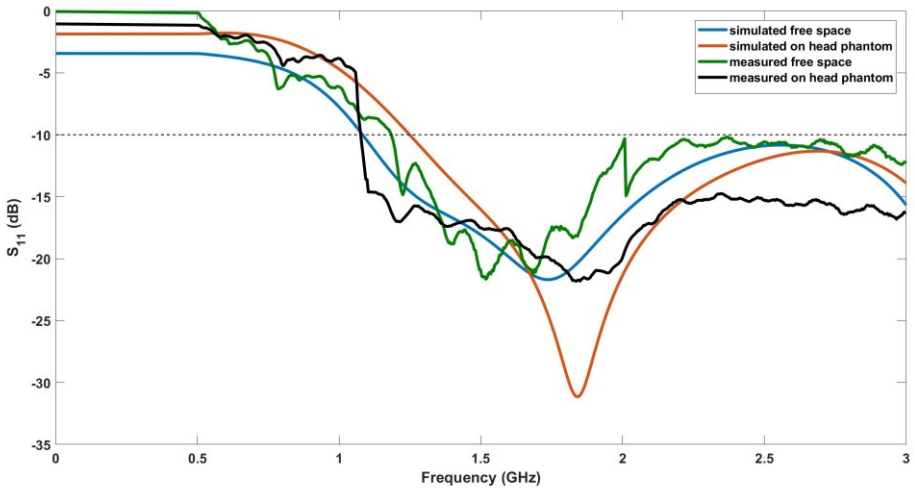

Figure 3.37: Simulated and measured reflection coefficient of the silicone rubber-based rectangular monopole antenna.

The measured S_{11} signals for both cases demonstrate noticeable increase in the impedance bandwidth of the antenna compared to the simulation results. It is seen that the impedance bandwidth of the textile antenna in presence of the head phantom is from 1.26 GHz to 2.76 GHz increases by 480 MHz compared to the simulation result. Again, for the final prototype, the performance of the antenna does not deteriorate when measured on the artificial head phantom suggesting that the antenna has been optimised for use as sensing antenna in the wearable head imaging system. Moreover, the increase in measured bandwidth of the antenna is beneficial to the overall performance of the imaging system. It is also important to note that there were no significant changes in the performance of the antenna due to the encapsulation of the antenna structure in silicone rubber. This is due to the thin outer layers (i.e., 1 mm of silicone rubber) on either side of the antenna, which ensures that the lossy material is minimised and that the radiated RF waves from the antenna can move out of the encapsulated structure without significant disturbances.

3.3 Specific Absorption Rate and Maximum Allowed Transmitted Power

In order to validate the safety requirement of the proposed MIND devices, it is important to measure the specific absorption rate (SAR) [185] – [187] of the emitting antennas on the human head. SAR is a measure of how EM waves is absorbed by human tissues. SAR is a function of electrical conductivity, σ (Siemens/meter), the received E-field from the radiated energy, E (Volts/meter), and the mass density of the tissue, ρ (kg/m^3). SAR can be calculated by averaging over a specific volume (typically measured over 1g or 10g of tissue) using Equation (3.11) below.

$$SAR = \frac{\sigma}{\rho}|E|^2 \tag{3.11}$$

In this thesis, SAR values were calculated at several frequencies within the operating frequency band of the antenna by varying the transmitted power from 1 mW to 100 mW and investigating the effects of the EM wave exposure to the human head. The maximum limit of SAR imposed by the UK government is 2 W/kg for 10 g of tissue mass. It is therefore important that the proposed MIND devices comply with the specified SAR limit to ensure safe diagnosis [188]. Figure 3.38 shows the peak SAR values from 1 GHz to 3 GHz. The calculated SAR values for both antennas were found to be well below the regulated maximum limit for 1 mW, 10 mW, and 100 mW of transmitted power respectively, indicating the feasibility of using the proposed antennas for wearable microwave head imaging systems.

In addition, the EM waves absorbed by the biological tissues increases linearly with the transmitted power. Therefore, it should be noted that transmitted power of more than 100 mW should be avoided to ensure safe operation of the imaging system. To investigate the spatial SAR distribution across the operating frequency of the antenna, another simulation was carried out by transmitting 10 dBm of power towards the artificial head phantom in the simulation.

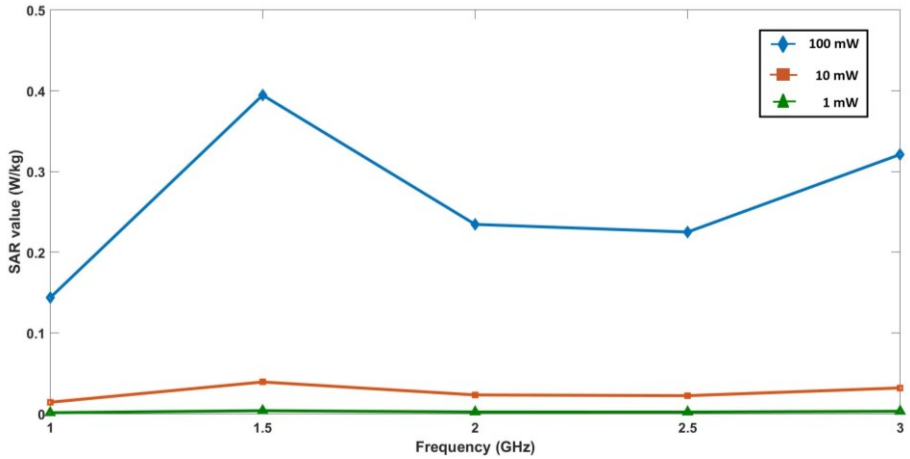

(a)

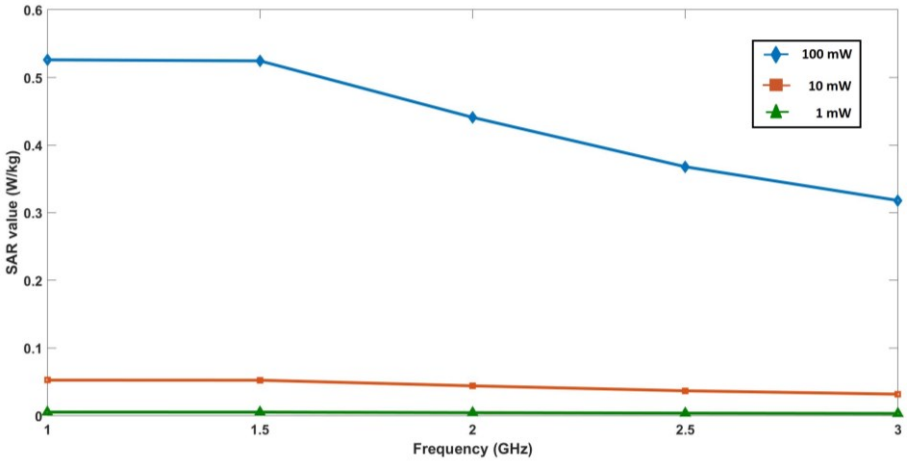

(b)

Figure 3.38: Simulated maximum SAR values over the operating frequency of the antenna for (a) textile-based SPMA and (b) silicone rubber-based RPMA.

Figure 3.39 shows the spatial SAR distribution at four frequencies namely 1.5 GHz, 2 GHz, 2.5 GHz, and 3 GHz. It is seen that at 1.5 GHz, the electromagnetic power absorption occurs at a deeper region of the head compared to other frequencies. Meanwhile, at 3 GHz, the power loss is mainly localised at the outer layers of the head phantom. It can be concluded that low frequency microwave signal can penetrate deeper into the human head compared to higher frequency signal where most of the power is absorbed at the most outer layers of the head.

The effects of the exposure of radio waves on the human body has been an ongoing research topic. Several reports have been published that indicate microwave radiation

might have biological effects on humans based on the tests carried out on rats [189] – [191]. However, the test in [191] was carried out with a SAR value of 0.6 W/kg for 2 hours over 3 months on rats which is much more than the required power and time for the proposed system for AD detection and monitoring applications.

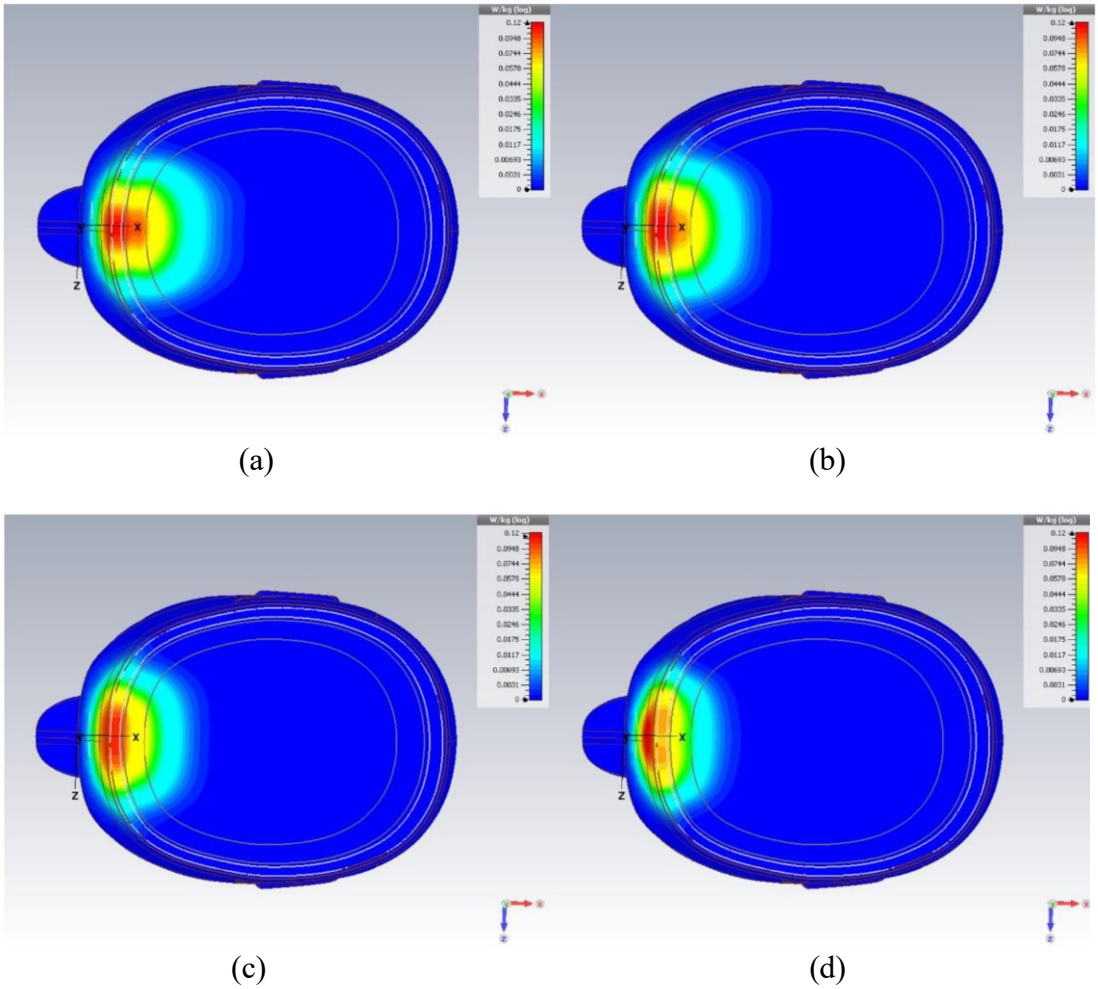

(a) (b)

(c) (d)

Figure 3.39: Simulated SAR distribution inside an artificial human head at (a) 1.5 GHz, (b) 2 GHz, (c) 2.5 GHz, and (d) 3 GHz.

Moreover, it was found in [192] that there was no evidence to support that microwave radiation could increase the risks of cancer in humans. In addition, the advantages of using the proposed MIND systems to detect, monitor, and non-invasively image AD conditions in patients far outweighs any potential side effects, since AD patients requires constant monitoring to provide timely treatment and intervention as needed.

3.4 Summary

This chapter discussed the development of flexible antennas that will be integrated into wearable MIND devices and used for wearable microwave head imaging applications. The antennas have been developed based on several requirements, such as: flexibility, lightweight, wideband, and compactness. The proposed antennas are mainly based on planar monopole configuration to provide low-profile characteristic where the antennas can be fitted into an array to be mounted on the human head. These antennas can be categorised into two main designs based on their substrates. The first antenna design is a stepped monopole antenna on felt substrate. A second antenna design is a rectangular-shaped monopole antenna embedded in a silicone rubber substrate. Both prototypes show similar performance in terms of impedance bandwidth and radiation patterns. For the second design, the length of the overall structure and thickness of the substrate was reduced to improve the antenna's performance and had the additional benefit of making the antenna more compact. The S_{11} responses of the antennas were measured and compared with the simulation results. A good agreement has been obtained in terms of impedance bandwidth for all the antenna prototypes. As the thesis shifts its focus and emphasis in the next chapters to the investigation of using MWS to detect different AD symptoms, it was decided to use the felt-based SPMA antenna design in the experiments due to its ease of fabrication and ability to take quick measurements. However, Chapter 8 then discusses the investigation of antenna arrays for both the antenna designs, as well as the subsequent development of two wearable prototypes.

Finally, to measure the safety aspects of the proposed antennas, SAR values at different transmitted power levels and frequencies were calculated in CST Microwave Studio. It was found that to ensure the proposed wearable imaging system operates within the safety regulations imposed by the relevant governing body, the power transmitted by the sensing antenna should be limited to 0.1 W. It is also found that low-frequency microwave signals provide better penetration depth inside the human head compared to higher frequency signals. As a result, it is very crucial to use low-frequency microwave signals in the range of 1 GHz to 3 GHz for head imaging systems.

Chapter 4

Validation of Microwave Sensing for Alzheimer's Disease - Physiological Changes

In this chapter, microwave sensing is validated for detecting two physiological changes that occur in the brain due to AD: BA and LVE. BA is a common physiological change associated with AD, through simulations that are performed on CST and experiments using artificial head phantoms that are made of lamb brains emulating the progression of BA. First, several simulation models were created in CST Microwave Suite using a multi-layer SAM head model. BA was emulated in these models by scaling the size of the grey matter and white matter regions in the head, and replacing the gap with a CSF layer. The felt-based SPMA was placed at 6 locations on the head to capture reflection and transmission coefficient data. For each level of BA decrease, reflection and transmission coefficient data were measured for each antenna and averaged. In the next stage, a realistically shaped artificial head phantom is fabricated using frozen lamb brains. Controlled amount of the outer layer of the lamb brain were removed and the empty space was replaced with an artificial phantom that had characteristics of CSF, thus emulating the characteristic of BA in an experiment setting.

After validating BA, microwave sensing was then validated on the enlargement of lateral ventricles in the brain. Table 4.1 shows the size of ventricle enlargement (represented as *mean* ± *standard deviation*) between AD patients, normal elderly people, and those with mild cognitive impairment (MCI) [48].

Table 4.1: Comparison of lateral ventricle volume changes between normal elderly, MCI, and AD patients [48]

Patient Type	**Baseline ventricular volume (cm^3)**	**Ventricular Enlargement after 6 months (cm^3)**	**% Ventricular Enlargement after 6 months**
Normal Elderly	38.3 ± 19.1	0.6 ± 1.4	1.5 ± 4.3
MCI	45.8 ± 21.4	1.6 ± 2.4	3.4 ± 6.1
AD	49.9 ± 25.3	2.6 ± 2.0	5.7 ± 4.9

As with the BA cases, MWS validation detecting LVE is performed through CST simulations and experiments. First, several simulation models were created in CST Microwave Suite using a multi-layer SAM head model. LVE was emulated in these models by adding an object that is defined with dielectric properties of CSF and placed inside the SAM head model in an area that approximately represents the ventricles' location in the brain. This object is then scaled in size to emulate increasing LVE levels. The felt-based SPMA was placed at 6 locations on the head to capture reflection and transmission coefficient data, as was done in the BA case. For each level of LVE increase, reflection and transmission coefficient data were measured for each antenna and averaged. In the next stage, a realistically shaped artificial head phantom is fabricated using frozen lamb brains. An artificial oil-based phantom was fabricated and placed in the centre of the lamb brain to emulate the location of the ventricles. Objects of different volumes were created and placed in the lamb brain phantom to emulate the increase of CSF in the lateral ventricles because of LVE. In addition, to improve the lifespan of the phantom, preservative material such as sodium benzoate is used to kill the bacteria, fungi and spores that may grow on the artificial tissue for repeatable testing purpose.

4.1 Simulation Models of Brain Atrophy Cases

The simulations for testing the antenna measurements for BA were performed in near field using CST Microwave Suite. In order to simulate BA, a realistic SAM human head

model was used that contained several tissues, such as: skin, skull, blood, white matter, and grey matter. 6 felt-based SPMA antennas, that were discussed in Chapter 3, were placed at specific points on the human head model next to the skin, as shown in Figure 4.1, and near-field measurements were obtained in the simulations. Progression of BA was simulated by uniformly reducing the size of grey matter and white matter regions in the SAM model. The resulting gap was replaced with CSF. The size of the other objects (i.e., skull, skin, and blood) were kept constant. Simulation models were run for each case and subsequent reflection (S_{11}) and transmission (S_{21}) coefficient data from each antenna was captured and analysed. Figure 4.2 shows the screenshot of the simulation models used in CST to represent different levels of BA.

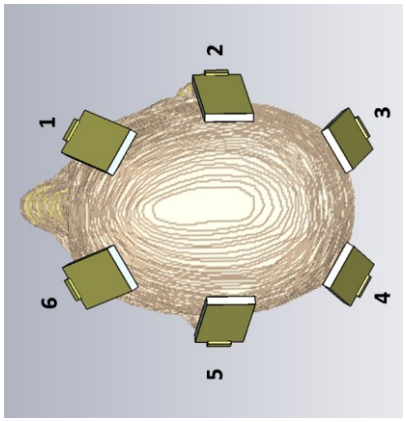

Figure 4.1: Image of the SAM head model in CST along with the locations of the antennas.

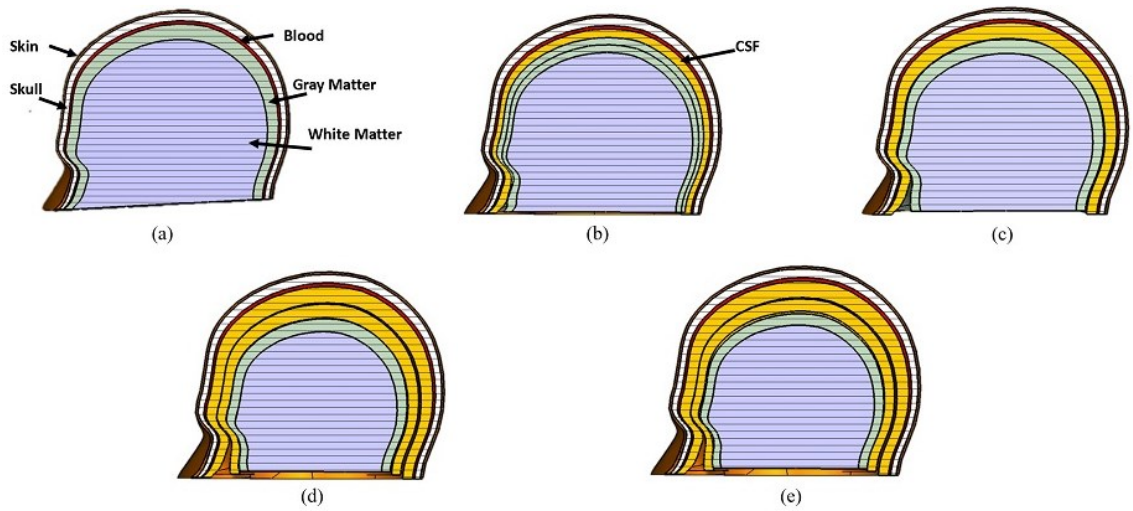

Figure 4.2: Simulation models that were used to represent the following cases: (a) Normal brain, (b) 5% brain atrophy, (c) 10% brain atrophy, (d) 20% brain atrophy, and (e) 25% brain atrophy.

4.1.1 Reflection Coefficient Measurements

Figure 4.3 shows changes in S_{11} plots for different brain atrophy cases compared to the S_{11} plot of a normal full-size brain with a *mean* ± *standard deviation* of -7.4400 ± 5.8268. The plot shows that as the brain volume decreases, there is an overall downward shift in the S_{11} plot, which indicates more loss in the signal as they do not get reflected. 5% brain atrophy shows an insignificant change in the S_{11} plots due to the small amount of change in the brain size. However, for the case of 20% and 25% brain atrophy, at 1.5 GHz, the signal loss is almost double the S_{11} value associated with the full brain case, thus validating the antennas' capability of detecting brain atrophy in reflection mode.

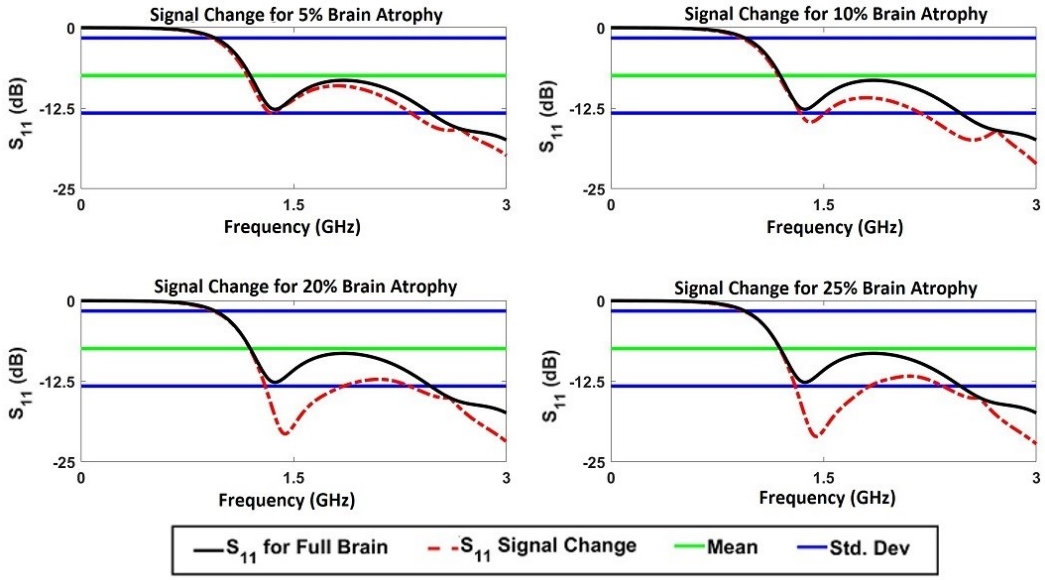

Figure 4.3: Simulation plots showing changes in reflection coefficient between a normal brain and a brain with 5%, 10%, 20%, and 25% brain atrophy.

4.1.2 Transmission Coefficient Measurements

Figure 4.4 shows changes in S_{21} plots for different brain atrophy cases based on simulations compared to the S_{21} of a normal brain with a *mean* ± *standard deviation* of -57.3593 ± 7.4864. The plots indicate that as the brain's size decreases, a downward shift in the S_{21} plots is present, indicating that the signal is not transmitted properly to the other antenna due to the decrease in brain tissues and increase in the higher-dielectric CSF layer that absorbs most of the transmitted signals. This trend can be seen

in the case of 20% and 25% brain atrophy where the change in S_{21} is between 20 and 40 dB across the bandwidth between 0.84 GHz to 2.4 GHz, which corresponds with the antennas' operating frequency range. This proves that based on simulations, the antennas can detect brain atrophy in transmission mode.

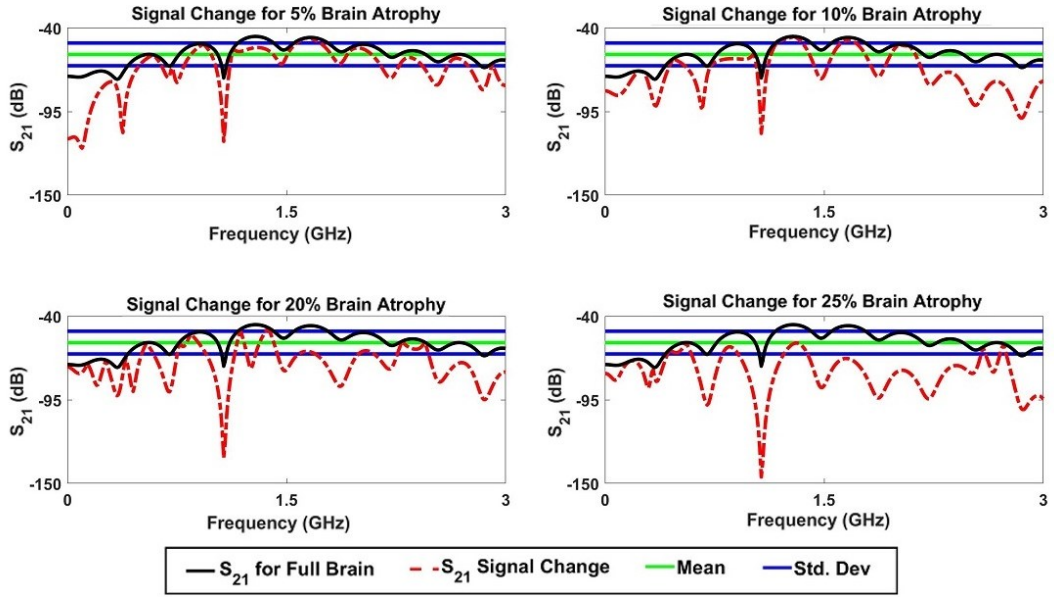

Figure 4.4: Simulation plots showing changes in transmission coefficient between a normal brain and a brain with 5%, 10%, 20%, and 25% brain atrophy.

4.2 Experimental Validation of Antennas for Brain Atrophy

4.2.1 Measurement Setup

The setup that was used for experiments is shown in Figure 4.5. The experimental setup consists of a PC, VNA, 2 fabricated felt-based SPMA, and the skull model which contains the lamb brains. The experiments were conducted using a host PC that was connected to the VNA via a GPIB. The PC allows the user to setup the VNA and send a command to the VNA to start generating signals and capture S_{11} and S_{21} data from the ports directly into the PC using a built-in software. The VNA that was used for the experiments is a HP 8753 that has a frequency range of 300 kHz to 3 GHz with a dynamic range of up to 100 dB. Felt-based SPMAs were connected to the 50-ohm ports

on the VNA using SMA cables. Calibration was performed by using the open, short, and load connections for each antenna. The antennas were first placed at two opposite sides of the skull model and S_{11} and S_{21} data was measured. Since the VNA only has two ports, this process for placing antennas and capturing measurements from the different locations of the skull, as shown in Figure 4.1, had to be repeated 2 more times to get the measurements from the 6 locations. The measured reflection and transmission coefficient data for these areas were then averaged and processed for further analysis. The average S_{11} and S_{21} measurements of the normal brain phantom would then be recorded and utilized as the benchmark for all other measurements to validate the changes in the signal related to BA.

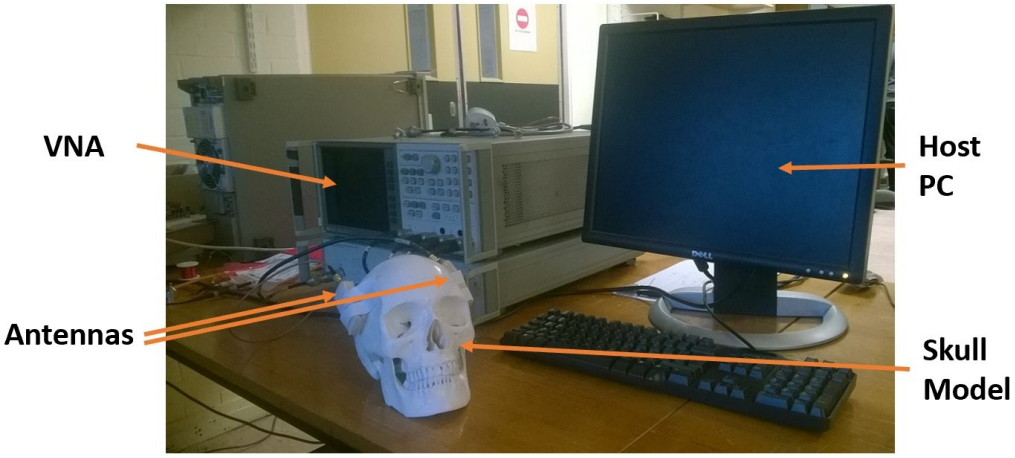

Figure 4.5: Experimental setup that is used for obtaining measurements on the skull model with the antenna.

For the experiments, a life-size skull model, as shown in Figure 4.5, was used containing similar indentations that are present in human beings. In addition, the skull model could be disassembled easily, allowing contents to be placed inside. While the skull model is similar in shape, size, and geometric indentations to an actual human skull, it is still not a suitable representation. This is because of two main reasons. First, the skull model used is made up of plastic, which is a lower dielectric constant compared to the actual bone tissue that makes up a skull. As a result, the propagation of microwaves may propagate more freely in this model as opposed to the actual skull. Second, it is also important to note that the model does not include the skin and hair layers, which are two outer layers on top of the actual skull. These layers have their

own dielectric properties which may affect the propagation of RF waves. However, because the skin and hair layers are thin, and the transmitted power of the antennas allow the waves to penetrate beyond the superficial layers of the skull, it is therefore safe to assume that this limitation will not affect the readings. Nonetheless, in future experiments, a more realistic head model will be used that is like an actual human head in order to validate the antenna sensors.

4.2.2 Phantom Fabrication of Brain Atrophy

To create a realistic representation of a human brain, real lamb brains were used and placed inside the skull model. A typical lamb brain is about $1/10^{th}$ the size of a human brain. As a result, 10 whole lamb brains were molded into the skull cavity and frozen to provide the representation of a complete normal brain structure with a volume of 1200 cm^3. To mimic the characteristics of brain atrophy in this first experiment, a measured amount of the lamb brain sample was removed uniformly around the outer layer for each atrophy case and replaced with a layer of artificial phantom that represents cerebrospinal fluid (CSF). This phantom was fabricated using salty water, agar, and a color dye to make it distinguishable in the experiments. For example, in the first experiment, 5% of the lamb brain was removed uniformly around the outer layer of the lamb brain. This empty region is replaced with an artificial phantom to mimic the characteristics of CSF. In the second experiment, another 5% of the lamb brain was removed again and replaced with a thicker layer of the artificial CSF phantom, resulting in a total decrease of 10% from the original complete model. Finally, for the third and fourth experiments, a 20% reduced-sized lamb brain model and a 25% reduced-sized lamb brain model were used, respectively. Figures 4.6 (a)-(e) show images of the actual lamb brain skull models used in the brain atrophy experiments.

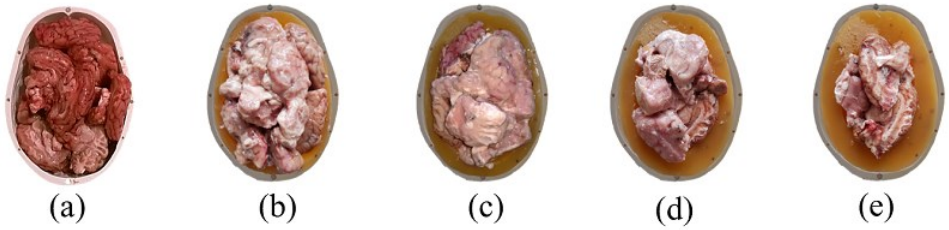

Figure 4.6: Images showing different compositions of lamb brains and outer CSF layer (light brown colour) inside the skull model representing brain atrophy for the following cases: (a) full brain volume, (b) 5%, (c) 10%, (d) 20%, and (e) 25% brain atrophy, respectively.

4.2.3 Reflection Coefficient Measurements

Results were obtained from experiments and compared with those from simulations to verify antennas' capability of detecting brain atrophy and lateral ventricle enlargement. Figure 4.7 shows changes in S_{11} for different cases of brain atrophy and a normal full brain. The S_{11} plot of a normal full brain has a *mean* ± *standard deviation* of -9.1587 ± 6.1556, while the S_{21} plot has a *mean* ± *standard deviation* of -25.1777 ± 7.0757, respectively. Figure 4.7 shows that as brain atrophy increases, the resulting S_{11} plots displays more loss in the signal and therefore an oscillating downward shift in the overall trend between 0.8 to 2.5 GHz. Oscillations may be due to noise that is emitted from the surroundings in the experimental setup or by the movements in the cables or connectors. However, the overall trend is expected based on simulation results and verifies the antennas' ability to detect brain atrophy in the reflection mode. In particular, the change in S_{11} loss increases significantly to -30 dB, -40 dB, and -55 dB for 10%, 20%, and 25% brain atrophy cases, respectively.

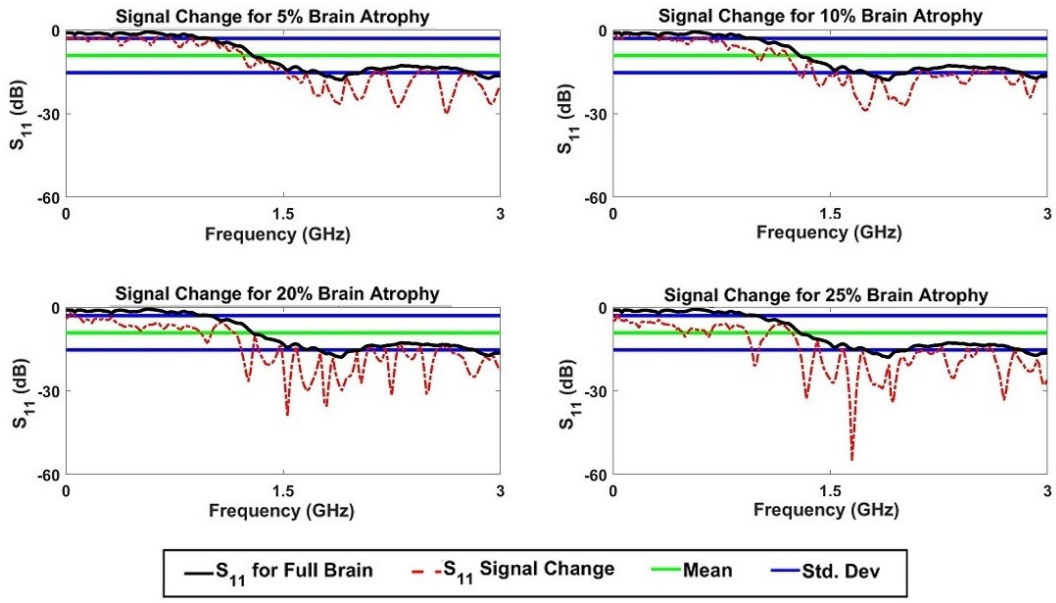

Figure 4.7: Plots showing changes in the reflection coefficient between a normal brain and brain with 5%, 10%, 20%, and 25% brain atrophy obtained from experiments.

4.3 Simulation Models of Lateral Ventricle Enlargement Cases

In order to simulate LVE in CST, the same human head model was used with the same properties. However, an additional object was placed inside the grey matter layer and was defined to have properties of CSF. This object was first defined to have a very small volume, approximately 15 mm^3 within the brain to represent a normal condition. To emualte the lateral ventricle size expanding, the size of the object corresponding to CSF would be enlarged to different sizes. S_{11} and S_{21} data would then be measured and compared for different sizes of lateral ventricles within the brain. Figure 4.9 shows the simulation cases that were used to model LVE. As in the previous simulations for BA, 6 felt-based antennas were used and placed on the sides of the head model as shown in Figure 4.1.

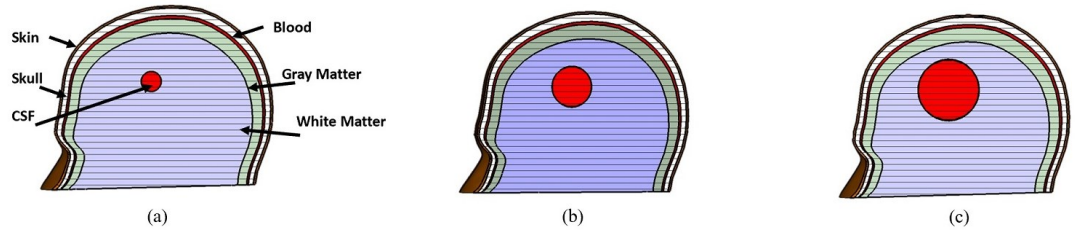

Figure 4.8: Simulation models that were used to represent the following LVE cases: (a) Normal brain with normal CSF levels (i.e., 15 mm^3), (b) 2x CSF levels (i.e., 30 mm^3), and (c) 4x CSF levels (i.e., 60 mm^3 in the lateral ventricles respectively.

4.3.1 Reflection Coefficient Measurements

Simulations for lateral ventricle enlargement were also conducted and results were analyzed. Figure 4.10 shows changes in S_{11} plots obtained from simulations between a brain with no CSF in the brain, with a *mean* ± *standard deviation* of -7.3700 ± 5.6154, and one with CSF levels increased by 2 times and 4 times in the lateral ventricles, respectively. As the amount of CSF increases in the ventricles from 2 times to 4 times the amount, the S_{11} plots shows an increasing downward shift in the reflected signal, which indicates an increased loss in the signal. This is due to the higher dielectric difference of the CSF object compared to brain tissues. The change in the S_{11} loss increases from -11 dB to -17.5 dB at 1.35 GHz when a quadruple increase in CSF object occurs in the lateral ventricle. This validates the antennas' ability to detect lateral ventricle enlargement in the reflection mode.

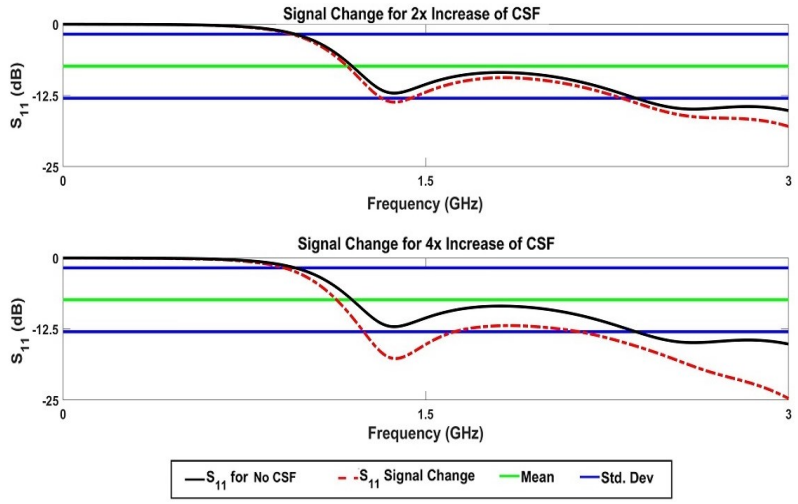

Figure 4.9: Simulation plots showing changes in S_{11} between a brain with normal CSF levels and brain with 2x and 4x CSF levels in the lateral ventricles.

4.3.2 Transmission Coefficient Measurements

Simulations were also performed to investigate the transmission characteristics due to increasing lateral ventricle sizes and shown in Figure 4.11. In Figure 4.11, the plot for a brain with no CSF in the ventricle has a *mean* ± *standard deviation* of -57.2078 ± 6.9762. As the levels of CSF increases, a downward shift is present in the S_{21} plots that is significant between 0.84 GHz and 1.5 GHz. This loss is due to the CSF in between that hinders the signal from transmitting to the other antenna. In addition, when the size of the CSF increases from 2 times to 4 times, the S_{21} plot at 1.05 GHz shows a sudden increase in the loss from -86 dB to -150 dB. This result validates that the antennas can detect lateral ventricle enlargement in the transmission mode.

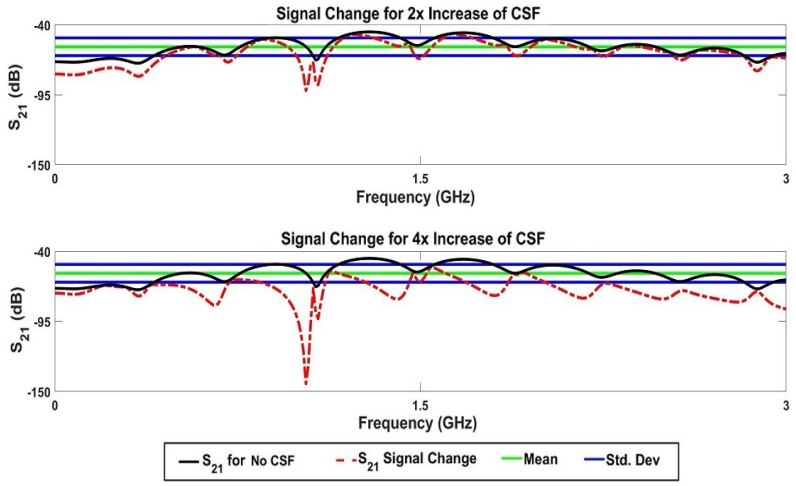

Figure 4.10: Simulation plots showing changes in S_{21} between a brain with normal CSF levels and brain with 2x and 4x CSF levels in the lateral ventricles.

4.4 Experimental Validation of Antennas for Lateral Ventricle Enlargement

4.4.1 Measurement Setup

The same experimental setup that was used for BA and shown in Figure 4.5, was used for experimental validation of MWS for detecting increasing levels of LVE in the brain. Again, the antennas were first placed at two opposite sides of the skull model with a

full human brain phantom, calibrated, and S_{11} and S_{21} data was measured. Subsequent measurements were obtained 2 more times from the other regions of the head as shown in Figure 4.1. The measured reflection and transmission coefficient data for these areas were then averaged and processed for further analysis. The average S_{11} and S_{21} measurements of the normal brain phantom would then be recorded and utilized as the benchmark for all other measurements to validate the changes in the signal related to LVE.

4.4.2 Phantom Fabrication for Lateral Ventricle Enlargement

For emulating LVE in the brain, several objects of different volumes were created to mimic the CSF inside the ventricles in the brain. The same full-brain lamb brain phantom was used and placed in the skull model; however, a 6-mm diameter cavity was created in both halves of the brain to insert the CSF object inside the brain. This 6-mm diameter cavity was created by first filling both halves of the skull model with lamb brains and then placing a plastic ball in the center of these halves. The model would then be frozen to ensure that the lamb brains remain fixed in the same location. Once frozen, the plastic ball would be removed, and the resulting cavity is created. Fig. 4.12 (a) shows the resulting cavity that was created in one half of the skull model.

To create the CSF objects, different sizes of an artificial phantom were created by mixing coconut oil, and salt to create a semisolid, high dielectric object that could be inserted into the cavity (shown in Figs. 4.12 (b)-(e)). Once inserted into the cavity, the lamb brains would be allowed to thaw out so that it can conform around the shape of the CSF object and fill up any gaps left behind. A green color dye was utilized to make the objects distinguishable in the experiments. The volumes of the CSF objects were: 1) 22.6 mm^3, 2) 56.5 mm^3, 3) 113 mm^3, and 4) 226 mm^3.

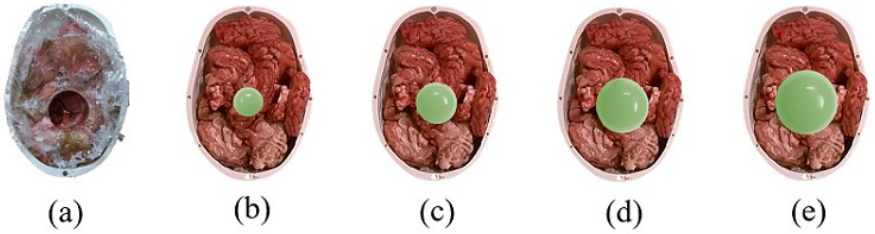

Figure 4.11: Images of (a) frozen lamb brain with 6-mm diameter cavity and (b)-(e) several CSF objects (light green colour) used in the experiments: (b) 22.6 mm^3, (c) 56.5 mm^3, (d) 113 mm^3, and (e) 226 mm^3.

4.4.3 Transmission Coefficient Measurements

Similarly, S_{21} plots in Figure 4.8 shows that as brain atrophy increases, there is more loss displayed in the transmitted signal due to the increasing presence of a thicker CSF layer that hinders the signal from transmitting to the receiving antenna. This leads to a larger difference in S_{21} data that can be seen in 10%, 20%, and 25% brain atrophy cases, respectively. In addition, both the S_{11} and S_{21} plots show this behaviour occurring in the frequency range of 0.85 GHz to 2.6 GHz which corresponds with the operating frequency of the antenna design.

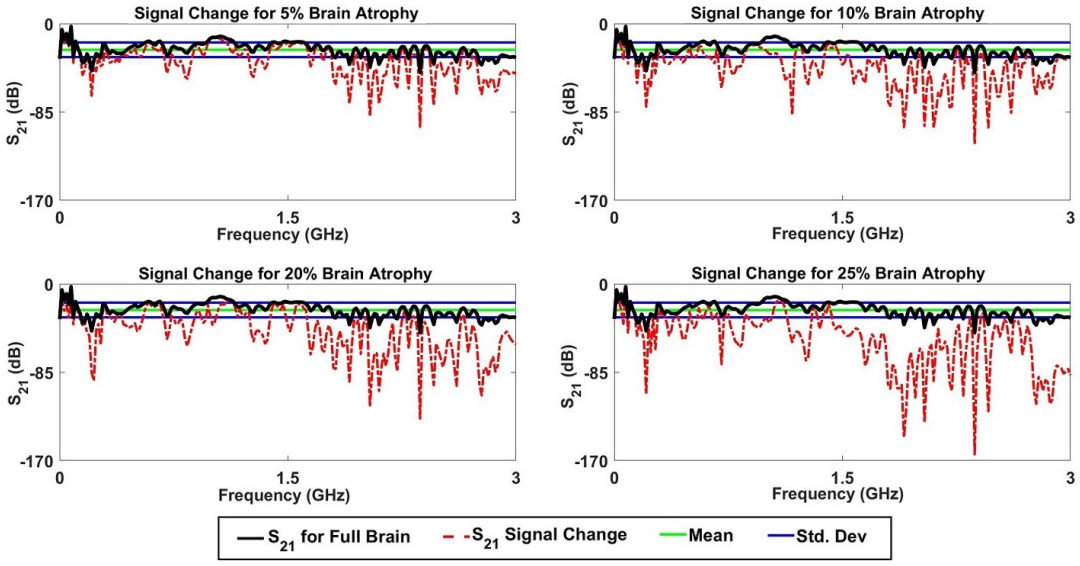

Figure 4.12: Plots showing changes in the transmission coefficient between a normal brain and brain with 5%, 10%, 20%, and 25% brain atrophy obtained from experiments.

4.4.4 Reflection Coefficient Measurements

Figure 4.13 shows the resulting S_{11} plots for the different LVE cases. The S_{11} plot for no CSF has a *mean* ± *standard deviation* of -10.0821 ± 5.9123, while the S_{21} plot has a *mean* ± *standard deviation* of -25.6884 ± 4.7394, respectively. Results in Figure 4.13 shows a similar trend found in the simulation results where the S_{11} loss increases because of increasing CSF volume, due to the change in the dielectric properties.

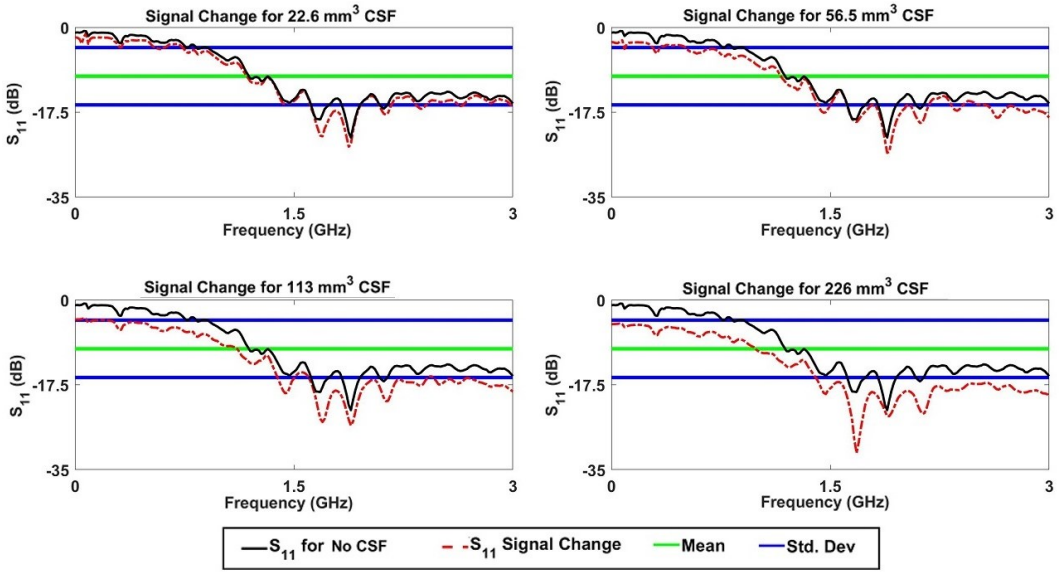

Figure 4.13: Plots showing changes in S_{11} signals obtained from experiments for increasing volumes of CSF because of lateral ventricle enlargement.

4.4.5 Transmission Coefficient Measurements

The characteristics of the resulting S_{21} plots are shown in Figure 4.14. The results are similar to those seen in the S_{11} plots discussed in Section 4.4.3 where the transmitted signal is not propagated completely to the receiving antenna due to the increasing CSF sample that hinders the signal in between. This characteristic can be seen between 0.86 to 1.7 GHz, where the change in S_{21} is increased to almost three times the original value. Therefore, the antennas can detect lateral ventricle enlargement in both reflection and transmission modes.

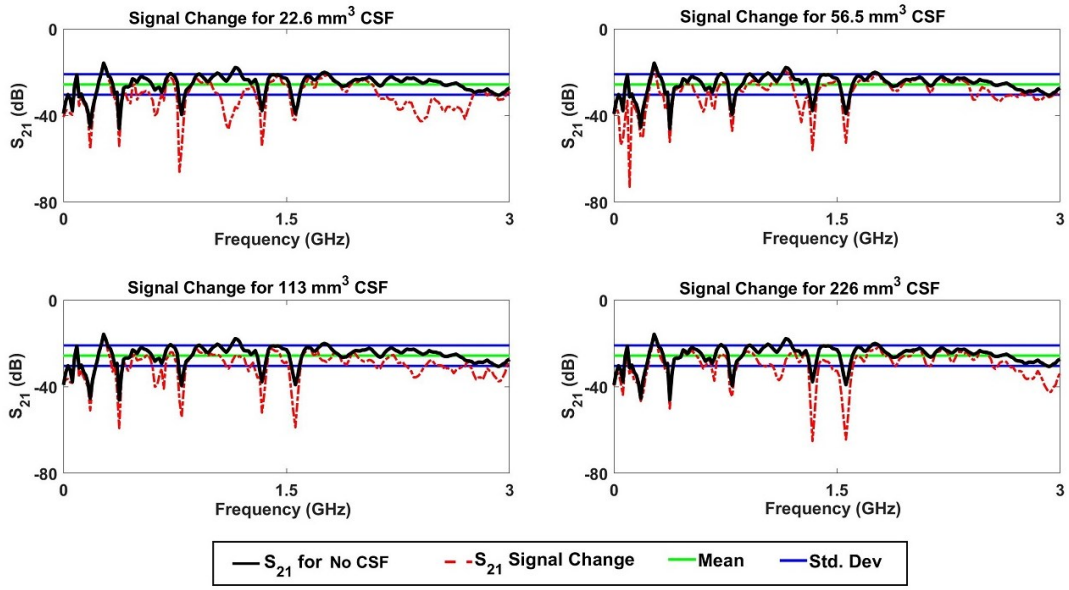

Figure 4.14: Changes in S_{21} plots obtained from experiments for increasing volumes of CSF because of lateral ventricle enlargement.

4.5 Closed Form Equations Relating S-Parameters with Physiological Changes

A closed form expression can also be proposed that provides a general relationship between the S-parameters and the amount of either brain atrophy or lateral ventricle enlargement that occurs in the brain. To obtain such expressions, curve fitting analysis was performed in MATLAB on the measured data for cases of brain atrophy and lateral ventricle enlargement, separately. With this tool, a general expression could be obtained for percentage change in S_{11} and S_{21} separately by "fitting" a polynomial line with each of the dataset and introducing a variable in the equation that represents either brain atrophy or lateral ventricle enlargement. To validate that the obtained equations fit the model, the following conditions were evaluated as part of the goodness of fit criteria for this study:

1. Sum of squares due to error (SSE) should be close to 0.
2. R-square should be greater than 0.85 and less than 1.
3. Adjusted R-square should be greater than 0.85 and less than 1.

4. Root mean squared error (RMSE) should be close to 0.

In addition to these conditions, the toolbox also allows us a window to visually inspect the plot and how it fits the data, so that overfitting and underfitting can be avoided when the fitting the expressions. Based on these conditions, the following closed form expression was obtained for percentage changes in S_{11} (4.1) and S_{21} (4.2) with respect to percentage change in brain atrophy, represented by the variable *x*:

$$\begin{aligned} \%\ change\ in\ S_{11} = {} & -1.41 + 0.068\cos(1.05x) \\ & + 2.21\sin(1.05x) + 1.29\cos(2.1x) \\ & - 0.077\sin(2.1x) - 0.028\cos(3.15x) \\ & - 0.46\sin(3.15x) \end{aligned} \tag{4.1}$$

$$\begin{aligned} \%\ change\ in\ S_{21} = {} & -55.83 - 11.19\cos(1.63x) \\ & - 0.44\sin(1.05x) - 2.32\cos(3.26x) \\ & - 0.79\sin(3.26x) + 2.03\cos(4.89x) \\ & + 2.297\sin(4.89x) \end{aligned} \tag{4.2}$$

In addition, the data for S_{11} and S_{21} that were obtained for the CSF measurements were used in the curve fitting toolbox to obtain a general expression that relates the change in ventricle enlargement with the obtained S-parameter values. These are given in the following equations for S_{11} (4.3) and S_{21} (4.4), where the variable *y* represents the volume of CSF in the lateral ventricles used in the experiments (i.e., 22.6 mm^3, 113 mm^3, etc.):

$$\begin{aligned} \%\ change\ in\ S_{11} = {} & -0.04 + 0.037\cos(1.11y) \\ & - 0.02\sin(1.11y) - 0.02\cos(2.22y) \\ & - 0.05\sin(2.22y) - 0.025\cos(3.32y) \\ & + 0.02\sin(3.32y) \end{aligned} \tag{4.3}$$

$$\begin{aligned} \%\ change\ in\ S_{21} = {} & -0.065 - 0.012\cos(5.74y) \\ & + 0.01\sin(5.74y) - 0.007\cos(11.48x) \\ & + 0.012\sin(11.48y) + 0.01\cos(17.2y) \\ & + 0.035\sin(17.2y) \end{aligned} \tag{4.4}$$

4.6 Summary

In this chapter, MWS was used to test the antennas and validate its performance in detecting different levels of BA and LVE that occur in the brain. In the first part of the chapter, simulation models were created for different BA levels in the head and using the felt-based antennas as an initial proof-of-concept. Simulations showed that the smallest level of BA that could be distinguished from the antennas was 5% decrease in the brain volume. Furthermore, this characteristic was visible in both the reflection and

transmission coefficients. Based on this result, experiments were carried to validate this in a practical scenario. The brain phantom was created using lamb brains because of its compositions that mimic the heterogeneous nature of the human brain. BA was emulated by removing outer layers of the lamb brain, and replacing the gap with an artificial phantom, made of water, sugar, and agar, that represents the CSF. Fabricated felt-based SPMAs, discussed in Chapter 3, were used for the measurement. discussed the validation of microwave antennas in detecting the progression of the BA as a symptom of AD. The S_{11} and S_{21} responses showed a detectable variation as the level of BA increases. The variation, and therefore relationship, of the S_{11} and S_{21} signals with respect to BA could be represented by close-form equations shown in Eqs. 4.1 and 4.2, respectively.

In e second part of this chapter, MWS techniques were used to test and validate its performance in detecting different levels of LVE. Simulation models were created to test the felt-based antennas on increasing levels of CSF inside the lateral ventricles of the brain. Simulations showed that variations in S_{11} and S_{21} could be detected with increasing levels of LVE. Given this finding, experiments were carried to validate this in a practical scenario. The same brain phantom from Chapter 4 was created using lamb brains because of its compositions that mimic the heterogeneous nature of the human brain. In addition to this, several objects of different volumes were fabricated using coconut oil and salt, to represent CSF that accumulate in the lateral ventricles. These objects are placed in the centre of the lamb brain phantom and subsequent reflection and transmission coefficient data were recorded. The resulting S_{11} and S_{21} responses showed a detectable variation as the level of LVE increased in the brain. This variation, and therefore relationship, of the measured S_{11} and S_{21} signals with respect to increasing volumes of the CSF objects in the brain phantom could be represented by the close-form equations shown in Eqs. 4.3 and 4.4, respectively.

Overall, the results presented in this chapter confirms the validation of MWS techniques for detecting and monitoring the progression of two physiological changes in the brain because of AD: brain atrophy and lateral ventricle enlargement. While the experiments validated MWS in detecting these physiological changes in the brain, it is worth mentioning about the potential repeatability of the measurements. There are several

factors that can change between each set of measurements, such as: placement of antenna sensors, connection of SMA cables, change in antenna structure due to movement of its flexible materials, and other similar changes. As a result of these changes, it is expected that one will not obtain the exact same S-parameter measurements between two different sets of experiments (i.e., measurements obtained from two different days of measurements). Nonetheless, it is important to mention that this thesis specifies that to detect brain atrophy and lateral ventricle enlargement, the overall changes in the S-parameters needs to be recorded. Based on the experiments and measurements obtained in this chapter, it can be concluded that the overall S-parameters change will be present no matter when the measurements are obtained and given relative tolerance levels. Given this promising validation, the focus of the thesis now moves into the final, and important, symptom of AD that needs to be investigated and validated with antennas and MWS techniques, which is the pathological change in the brain that occurs due to the accumulation of Aβ plaques and tau tangles in the brain.

Chapter 5

Validation of Microwave Sensing for Alzheimer's Disease – Pathological Changes

In this chapter, microwave sensing is validated for detecting increasing levels of brain tissues affected by Aβ plaques and tau tangles as a pathological cause of AD. This is done through simulations on CST and experiments using artificial head phantoms that mimic the electrical properties of brain tissues affected with AD and differentiating those from healthy brain tissues. The first part of this chapter focuses on measuring and recording dielectric properties of human brain tissues with severe AD pathology and comparing them to dielectric properties of healthy human brain tissues that were obtained in [30]. Tissue samples were taken from a patient with severe AD and measurements were obtained on the grey matter and white matter portions of the tissue samples using a VNA, dielectric probe, and PC.

The second part of this chapter discusses about the simulation models that were developed in CST using the measured dielectric properties of AD brain tissues to recreate different stages of AD (i.e., MCI, Mild AD, Moderate AD, and Severe AD, respectively) inside a realistic human voxel model. In addition, six felt-based SPMA antennas, as discussed in Chapter 3, were used, and placed around the head model. Subsequent S_{11} and S_{21} data were recorded, averaged, and processed for analysis.

The third part of this chapter discusses about the experiments that were performed using multi-layered artificially fabricated phantoms to represent a human brain with varying levels of brain tissues affected with plaques and tangles. S_{11} and S_{21} data was collected from the antennas, averaged, and processed for further analysis.

Finally, in the last part of this chapter, an initial attempt was made in validating a MWI algorithm with the S_{11} data to determine if areas of the brain affected with plaques and tangles could be highlighted. A MIST algorithm was developed to correlate with

the locations of the antennas on the head. S_{11} data from the experiments were then used in the developed MIST algorithm to reconstruct images of the affected tissues in the brain.

5.1 Dielectric Properties of Brain Tissues with Alzheimer's Disease Pathology in the Microwave Region

Pathological changes in the brain that occur due to AD are based on the accumulation of beta-amyloid plaques and tau tangles inside the brain [49]. Beta-amyloid proteins show up as irregular clumps in the brain that stick together to form plaques, causing the signals between synapses to get interrupted [50]. In addition, neurofibrillary tangles are also present in large numbers in the brain as AD progresses. These tangles are disorganized cytoplasmic filaments in the neuronal cytoplasm formed by tau proteins. Tau protein, which is used to stabilize microtubules in the brain and functions as a bridge between axons, are found to build up in large numbers, causing them to detach from the microtubules and accumulate in the soma. This causes the microtubules to wither and get tangled, resulting in the brain not being able to transport cell nutrients properly and eventually leads to the death of the neurons [50]. These plaques and tangles tend to form in the hippocampus region of the brain before spreading to other regions. Figure 5.1 shows a screenshot of beta-amyloid plaques and tau tangles in the brain.

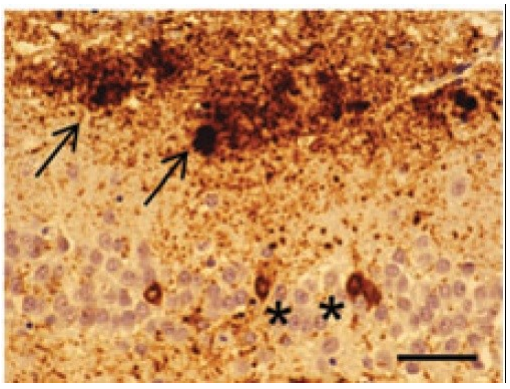

Figure 5.1: Image of brain tissue with Aβ plaques (arrows) and neurofibrillary tau tangles (asterisk) [194].

Although AD takes several years to develop, it is difficult to confirm AD until a patient dies and the brain is examined. In addition, an early confirmed diagnosis of AD is not possible with current diagnostic scans, such as computed tomography (CT) and magnetic resonance imaging (MRI) scans [195].

Recent research in AD has found that beta-amyloid plaques and tau tangles are key indicators of AD in a patient [196]. As a result, many studies have been performed to understand the properties of these cells and how they accumulate in the brain [197]-[198]. In addition, several studies have been performed to investigate methods to detect plaques and tangles as early as possible, such as the positron emission tomography (PET) scans, where patients are injected with a radioactive substance that sticks to plaques and are highlighted in the resulting scan [199]. However, the high costs and invasive approach of PET scans makes it unsuitable for some to use [200]. In addition, PET scans can sometimes not highlight deeper areas of the brain where plaques and tangles are located, thus giving a wrong indication of the progression of AD in a patient [50].

It is therefore of paramount importance that other properties of plaques and tangles should be investigated, namely its dielectric properties. The dielectric properties indicate how electromagnetic fields are transmitted, absorbed, and reflected in different biological tissues [27]. These properties, the relative permittivity and conductivity, are inherent characteristics of all tissues. Understanding these properties is therefore important for dosimetry studies, optimizing wireless telecommunication devices, and designing electromagnetic (EM) or radio frequency (RF) medical diagnostic devices [28]-[29]. Several studies have also investigated dielectric properties of brain tumors and strokes [201]-[202]; however, to the best of my knowledge, there have been no studies reported on the measurement of dielectric properties for a brain with AD pathology.

5.1.1 Dielectric Measurement Setup

Dielectric properties of the samples were determined by measuring the input reflection coefficient of the sample using the two-port VNA, HP8753C controlled by a laptop PC.

Measurements were taken between 200 MHz and 3 GHz using an Agilent high-temperature dielectric probe 85070E-0020 that was connected to the VNA and used to capture dielectric properties from the samples. A GPIB connector was used to connect the VNA with the laptop, and a software associated with the dielectric probe was utilized for capturing the dielectric properties from the probe. Figure 5.2 shows the complete experimental setup that was used for the dielectric measurements which includes the laptop, VNA, category 2 biosafety cabinet, and the dielectric probe.

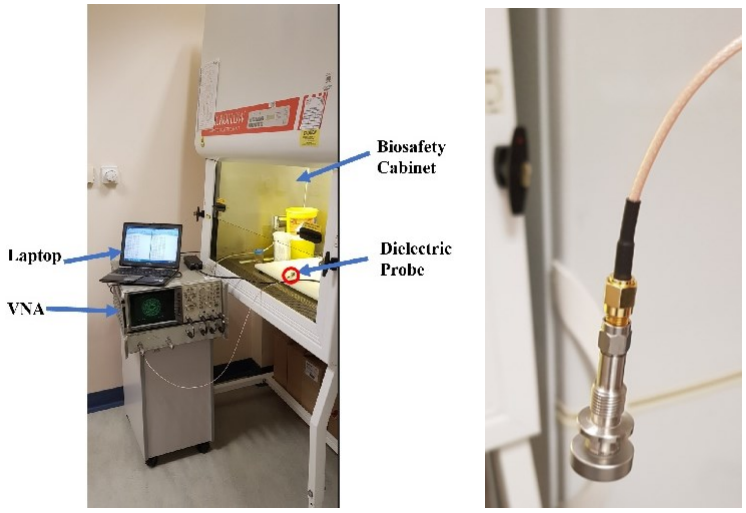

Figure 5.2: (a) Dielectric measurement setup showing the VNA, laptop, biosafety cabinet, and dielectric probe used, and (b) close-up view of the dielectric probe.

Dielectric measurements were taken continuously at 200 discrete frequencies evenly distributed in the frequency range. Specifically, dielectric measurements were taken at each unit temperature point between 5 to 25 °C. Measurements were taken on the gray matter and white matter areas respectively of the AD brain tissue samples. Measurements at each frequency were then averaged and recorded using a built-in software. The measured dielectric properties were then compared between the AD and healthy tissue samples and used for simulation models and experiments.

5.1.2 Brain Tissue Samples used in Measurements

Brain tissue samples from a single patient with severe AD were obtained from the Edinburgh Brain Bank and used in the dielectric measurements. The tissue samples

were freshly excised and obtained after around 15 hours postmortem. A total of 15 samples were utilized in the measurements, each with a dimension of 2 cm x 1 cm x 1 cm. The samples were taken from the frontal cortex region of the brain and contained substantial amounts of beta-amyloid plaques and tau tangles, which were categorized as Braak stage C for amyloid plaques and 5 or 6 for tau tangles, and Thal phase 1, which correlates to a severe progression of AD in the patient's brain. Samples were handled inside a Category 2 biosafety cabinet to safely work with the samples and maintain its temperature and humidity throughout the measurements. The biosafety cabinet was equipped with temperature and humidity controllers to control the environment inside the cabinet where the samples were placed, specifically keeping the humidity low such that no moisture is generated in the samples. Measurements were taken on both the gray and white matter regions of the tissue samples in the temperature range of 5 to 25 °C. Figure 5.3 (a) and (b) show screenshots of some of the samples used in the experiments in their frozen state and defrosted state, respectively.

Figure 5.3: Selection of brain tissue samples of AD patient used in dielectric measurements.

5.1.3 Comparison with Dielectric Properties of Healthy Brain Tissues

This section focuses on the comparison of the measured dielectric properties from AD brain tissue samples with those of healthy brain tissue samples in both the grey and white matter regions. Dielectric properties of healthy brain tissue samples were obtained from a database [203] that was built based on data from a comprehensive and

well-known study conducted by Gabriel in [30] of dielectric properties of several biological tissues. Since the dielectric properties obtained for AD brain tissue samples was at a different temperature than the ones obtained for the healthy brain tissue samples, the measured dielectric properties had to be adjusted to a reference temperature (i.e., body temperature) using a temperature conversion equation for both relative permittivity and conductivity that was presented in [204]. Next, the measured dielectric properties of AD tissue samples were represented in terms of the Four-pole Cole-Cole model using the Curve Fitting Toolbox in MATLAB that was used to estimate and optimize all the parameters of the model to each of the 2 measured datasets (i.e., Gray Matter-AD and White Matter-AD). Four-pole Cole-Cole model parameters were also generated for the dielectric properties of healthy brain tissues obtained in [203]. These parameters are shown in the Appendix section in Table A.1. Finally, comparisons are shown of the adjusted measured dielectric properties of AD brain tissue samples and those of the healthy brain tissue samples, respectively.

A. Dielectric Properties of Healthy Brain Tissue Samples

Dielectric properties of healthy brain tissue samples that were used in this thesis were obtained from a database in [203] and based off a comprehensive study of measured dielectric properties for different tissues which was reported by Gabriel in [30]. The dielectric measurements of the healthy brain tissues were conducted on both the gray and white matter regions. The measurements were conducted ex-vivo between the frequency range of 10 Hz to 20 GHz. The temperature of the tissue samples during the measurements were at body temperature (37°C). In addition, the measurements were performed on brain tissues that was obtained from an adult human between 24 to 48 hours postmortem.

B. Adjustment of Measured Dielectric Properties to Reference Body Temperature

An important point to note is that the dielectric measurements of the healthy brain tissue samples obtained in [203] were conducted on tissues at a temperature of 37 °C. This is significantly different from the temperatures of the dielectric measurements on AD brain tissue samples that were conducted as part of this thesis, which was in the range of 5 to 25 °C. Although reliable detailed information on temperature of the dielectric

properties of tissues is scarce, it is known that equivalent conductivity has a positive temperature coefficient, while permittivity has a negative temperature coefficient [205]. In order to avoid any uncertainties in comparing the two dielectric datasets (i.e., AD brain tissues vs healthy brain tissue samples), it is important to adjust the measured dielectric properties to body temperature.

The first step is to obtain the average temperature coefficient for the measured dielectric properties of both gray and white matter regions of the AD brain tissue samples. Temperature coefficients at each frequency point were obtained by plotting the measured dielectric properties between 5 to 25 °C and obtaining the slope of the plot. This was done for each of the 200 discrete frequency points between 0.2 to 3 GHz. The next step was to obtain the average temperature coefficient of the measured dielectric properties for both permittivity and conductivity of gray and white matter. This was done by performing linear interpolation on the set of temperature coefficients to yield the average temperature coefficient for permittivity and conductivity of each region. Based on the measurements conducted in this thesis, the average temperature coefficients for both permittivity and conductivity of gray and white matter are shown in Table 5.1.

Table 5.1: Average temperature coefficients (%/°C)

	Relative Permittivity	**Conductivity**
AD Gray Matter	-0.236	0.487
AD White Matter	-0.315	0.604

Finally, after obtaining the average temperature coefficients, the measured dielectric properties of the AD tissue samples were adjusted to a reference temperature of 37 °C by using the following equations [204]:

$$\sigma_{37^\circ} = (1 + (37 - T_t)TC_\sigma)\sigma_m \tag{5.1}$$

$$\varepsilon_{r,37^\circ} = (1 + (37 - T_t)TC_\varepsilon)\varepsilon_{r,m} \tag{5.2}$$

where σ_{37° and $\varepsilon_{r,37^\circ}$ are the adjusted dielectric values (i.e., conductivity and relative permittivity, respectively), and σ_m and $\varepsilon_{r,m}$ are the measured values of the dielectric properties. TC_σ and TC_ε are the derived average temperature coefficients of conductivity and relative permittivity, respectively, and T_t is the temperature of the tissue when the dielectric measurement was taken. The adjusted dielectric values were obtained for all the temperature points between 5 and 25 °C. Once this was done, the data were averaged and compared to the dielectric properties of the healthy brain tissues as reported in [203], which is discussed about extensively in Section 5.1.3.D.

C. Four-Pole Cole-Cole Model

Complex relative permittivity of biological tissues is frequency-dependent and characterized by the following equation [205]:

$$\varepsilon(\omega) = \varepsilon'(\omega) - j\varepsilon''(\omega) \tag{5.3}$$

where $\varepsilon'(\omega)$ is the real part known as relative permittivity, $\varepsilon''(\omega)$ is the imaginary part known as loss factor, and ω is the angular frequency in rad/s. The real part of (5.3) defines the ability of the tissue to store energy from electromagnetic fields, whereas the imaginary part indicates the dissipation of energy into heat by frictional motion of elements carrying charges [30]. As a result, the imaginary part is also related to conductivity by the following:

$$\varepsilon''(\omega) = \frac{\sigma}{\varepsilon_0 \omega} \tag{5.4}$$

where σ is the conductivity and ε_0 is the permittivity of free-space and equals to 8.8854 $\times 10^{-12}$ F/m. Dielectric properties of biological tissues are frequency dependent and vary across any given frequency range [205]. In the microwave frequency range, permittivity tends to decrease while conductivity tends to increase with respect to frequency. This variation in complex permittivity is called dispersion curve for the permittivity and absorption curve for the loss factor [200].

Typically, to represent the dispersion and absorption curves, the complex permittivity needs to be modeled using a dielectric model, such as the Debye or Cole-Cole model. A multi-pole or higher order model is recommended to fit the

inhomogeneous and heterogeneous tissues because the single order dielectric models may not fit the complex human tissues [30]. A fourth order model is shown to provide a good fitting for tissues [205]. The four-pole Cole-Cole model for dielectric properties ($\varepsilon_C(\omega)$) is defined as:

$$\varepsilon_C(\omega) = \varepsilon_C'(\omega) - j\varepsilon_C''(\omega) = \varepsilon_\infty + \sum_{i=1}^{4} \frac{\Delta\varepsilon_i}{1+(j\omega\tau_i)^{1-\alpha_i}} + \frac{\sigma_s}{(j\omega\varepsilon_0)} \qquad (5.5)$$

where τ_i is the relaxation time, α_i is the exponent describing the dispersion regions, and σ_s is the static conductivity. The magnitude of the dispersion is represented by $\Delta\varepsilon_i = \varepsilon_{si} - \varepsilon_\infty$, where ε_{si} is the static permittivity when $\tau_i \ll 1/\omega$, and ε_∞ is the infinite permittivity when $\tau_i \gg 1/\omega$. In this paper, the four-pole Cole-Cole model was used to fit the measured dielectric properties for gray matter and white matter regions of both AD and healthy tissue sample sets, respectively. Estimation and optimization of the four-pole Cole-Cole model parameters were carried out using the Curve Fitting ToolBox in MATLAB. Table A.1 in the Appendix shows the list of four-pole Cole-Cole model parameters that were obtained for each of the measured sample sets compared with the healthy brain tissue samples obtained in [30].

D. Measured Dielectric Properties

Dielectric properties of the samples were measured, adjusted based on the formulas in Equations 5.1 and 5.2, and compared with those of a healthy human brain sample. Figure 5.4 shows the plot of the relative permittivity (real and imaginary) of the gray matter region of AD-infected brain tissue as compared to those of gray matter from a healthy human brain. The mean and standard deviation of the measured datasets for gray matter are provided in Table 5.2.

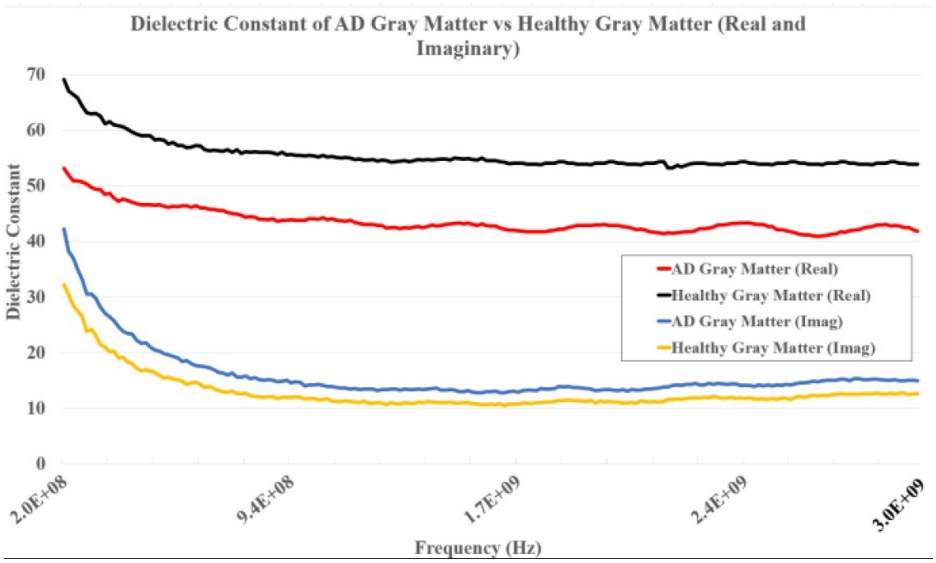

Figure 5.4: Measured dielectric constant (real and imaginary) of grey matter section of AD vs healthy human brain tissues.

Table 5.2: Comparison of dielectric constants for grey matter

Frequency (GHz)	**AD Tissue (Real)**	**AD Tissue (Imag)**	**Healthy Tissue (Real)**	**Healthy Tissue (Imag)**
0.2	52.09	49.292	65.22	32.3
0.77	45.921	16.76	53.49	12.5
1.5	44.04	12.6	50.77	10.62
1.8	44.053	12.02	50.14	10.25
2.1	43.88	12.10	49.5	10.67
2.4	43.48	12.11	49.05	11.24

Analyzing the trends of the relative permittivity plots, there is a clear distinction between the gray matter readings from a healthy brain and a brain with AD. For instance, at 770 MHz, the real part of the relative permittivity is 56.434 for gray matter in a healthy brain and 44.89 for gray matter in the AD-infected brain, which represents a 20.46% decrease in the real part of the relative permittivity.

At 2.4 GHz, the real part of the relative permittivity is 54.263 for gray matter in the healthy brain and 42.939 for gray matter in the AD-infected brain. The relative permittivity is slightly lower, but the percentage of change at this frequency is 20.87%,

which is like that found in 770 MHz. It can be concluded that AD-infected brain sample has a lower relative permittivity compared to that of a healthy brain sample. In addition, it can also be seen that the imaginary part of the relative permittivity for gray matter is higher for the brain with AD compared to the healthy brain. For instance, at 2.4 GHz, there is a 16.17% increase in the value for the imaginary part of the relative permittivity for gray matter in the brain with AD.

In addition to understanding the effects of plaques and tangles on gray matter, it is also important to investigate its effects on white matter since that layer would get affected first by plaques and tangles before spreading to the gray matter layer of the brain. Figure 5.5 shows the plot of measured relative permittivity (real and imaginary) for the white matter region of AD-infected brain samples and compared to the measurements for the white matter region of healthy brain tissue samples. The mean and standard deviation of the measured datasets for white matter are provided in Table 5.3.

Analyzing the relative permittivity plots in Figure 5.5, a visible trend shows that there is a similar difference in the relative permittivity data across the frequency spectrum for the white matter region as in gray matter. For example, at 770 MHz the relative permittivity is 40.138 for white matter in the healthy brain and 32.32 for white matter in the AD-infected brain, which corresponds to a 19.48% decrease in the relative permittivity.

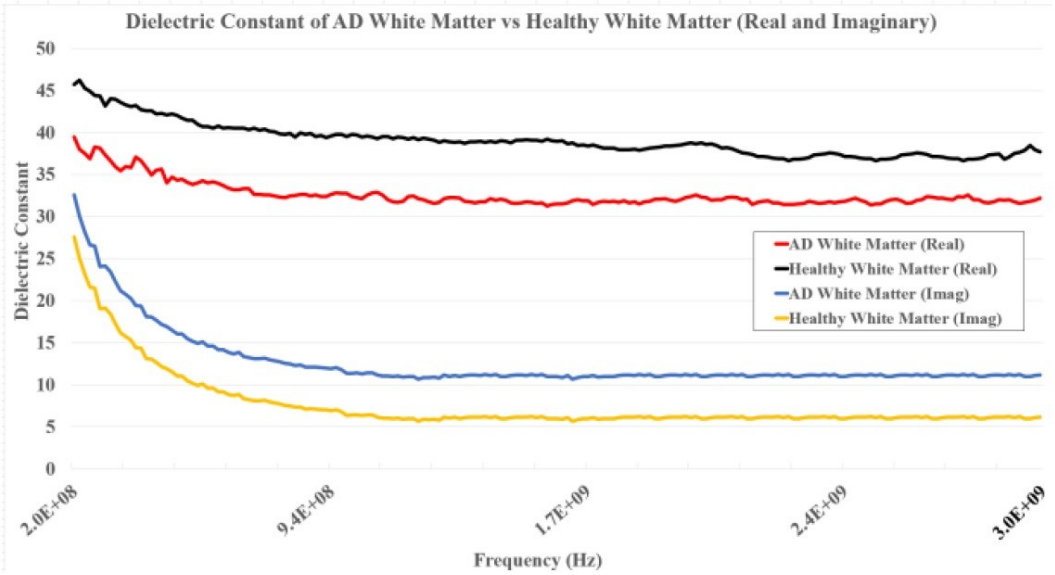

Figure 5.5: Measured dielectric constant (real and imaginary) of the white matter section of AD vs healthy human brain tissues.

Table 5.3: Comparison of dielectric constants for white matter

Frequency (GHz)	**AD Tissue (Real)**	**AD Tissue (Imag)**	**Healthy Tissue (Real)**	**Healthy Tissue (Imag)**
0.2	37.48	34.31	47.17	21.51
0.77	32.57	12.75	39.41	17.47
1.5	31.66	10.69	37.56	16.73
1.8	31.73	10.27	37.06	16.63
2.1	32.25	10.74	36.59	17.35
2.4	31.63	11.04	36.26	16.78

At 2.4 GHz, the relative permittivity is 37.517 for white matter in the healthy brain, and 31.824 for white matter in the AD-infected brain, corresponding to a 15.17% change. As in the plots for gray matter results, there is a decrease in relative permittivity between the healthy brain sample and AD-infected brain samples. In addition, a similar trend can be seen for the imaginary part of the relative permittivity for white matter, as in the gray matter measurements, where there is an increase in the imaginary part value for white matter in a brain with AD compared to white matter from the healthy brain.

For instance, at 2.4 GHz, there is a 44.88% increase in the value for the imaginary part for white matter in the brain with AD. Table 5.4 also shows the statistical analysis of the measured dielectric constants for the AD brain tissues compared to those obtained in [30] for the healthy brain tissues.

Table 5.4: Statistical analysis of measured dielectric constants

Tissue Type	**Mean (Real)**	**Std. Dev. (Real)**	**Mean (Imag)**	**Std. Dev. (Imag)**
Gray Matter - AD	43.612	±2.2700	15.9041	±4.9033
Gray Matter – Healthy	55.455	±2.7066	12.9433	±3.6475
White Matter – AD	32.610	±1.5320	12.6695	±3.841
White Matter - Healthy	39.064	±1.9958	7.6695	±3.7356

5.2 Simulation Models of Different Stages of Alzheimer's Disease

After obtaining the dielectric measurements, computational models were developed in CST Microwave Studio Suite. A realistic human head voxel model, initially reported in [206], was used and modified in CST. Figure 5.6 shows the CST head voxel model and cross-sectional view of the head model that illustrates the different regions, tissues, and geometries that were implemented in the model.

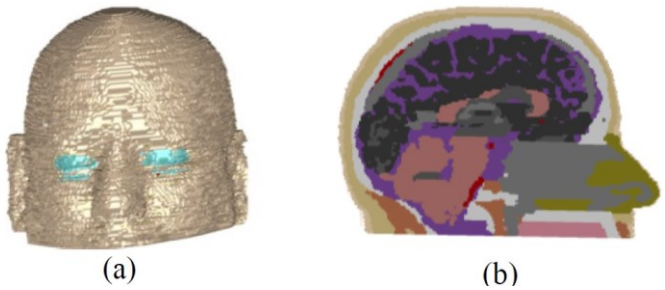

Figure 5.6: (a) Realistic human head model used for simulations in CST, and (b) cross-sectional view of the human head model showing the different layers, tissues, and geometries of the brain.

The head model contained geometries and materials that were defined to represent different regions, tissues, and ventricles that are present in the brain. In addition, the model portrayed a realistic representation of the human head with different layers, such as skin, skull (bone), CSF, gray matter, and white matter. The advantage of the model was that the properties of individual areas or tissues could be controlled and modified for different conditions. The model proved to be useful for defining certain areas of the brain that contain plaques and tangles during different stages of Alzheimer's disease.

To represent each stage of AD in the simulations, the dielectric properties of certain regions and tissues were changed to match those obtained from the dielectric measurements on the tissues. Table 5.5 lists the regions of the brain that were affected by AD in each stage and the corresponding dataset that was used to represent the plaques and tangles. Some of the cases required both the gray matter and white matter regions to be changed as both sets of tissues were found to be affected by AD in those stages based on the work by Braak in [26].

Table 5.5: Regions of the head model used for stages of Alzheimer's disease

Stage	**Brain Region Affected**	**Dataset Used**
MCI	Medial Temporal Lobe	AD White
Mild AD	Medial Temporal Lobe Temporal Lobe Parietal Lobe	AD White AD White and Gray AD White and Gray
Moderate AD	Medial Temporal Lobe Temporal Lobe Parietal Lobe Frontal Lobe	AD White AD White and Gray AD White and Gray AD White and Gray
Severe AD	Medial Temporal Lobe Temporal Lobe Parietal Lobe Frontal Lobe Occipital Lobe	AD White AD White and Gray AD White and Gray AD White and Gray AD White and Gray

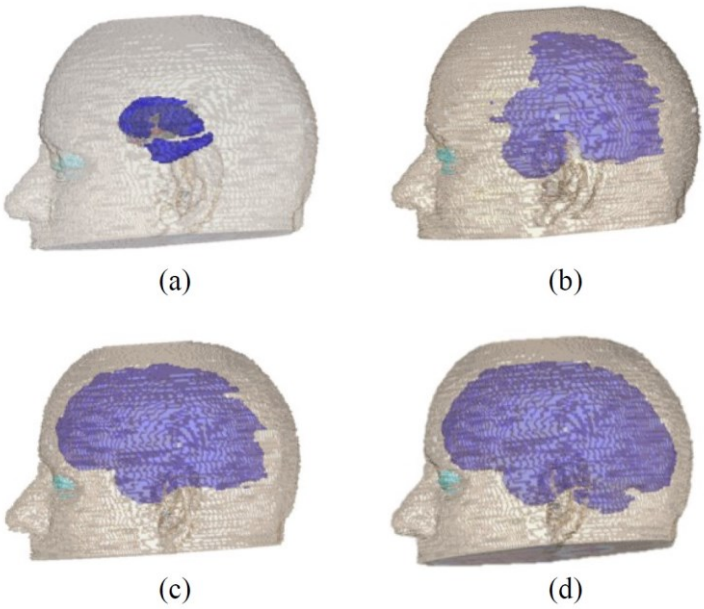

Figure 5.7: Simulation models used to represent the amount of AD-affected tissues (highlighted in blue) for the following stages of AD: (a) MCI, (b) Mild AD, (c) Moderate AD, and (d) Severe AD.

Figure 5.7 (a)-(d) shows the simulation models that were created to represent the four different stages of AD, namely mild cognitive impairment (MCI), mild AD, moderate AD, and severe AD, respectively. In addition, each of these stages, apart from MCI, are based on the progression and location of amyloid plaques and tau tangles in the brain because of AD, that was originally presented by Braak in [26]. MCI has been defined in some follow up studies [207]-[208] to be the earliest known stage where plaques and tangles start to form in the hippocampus region of the brain and are characterized as either Braak stage 0, 1, 2, before spreading to other areas as mentioned in [26].

5.2.1 Reflection Coefficient Measurements

Simulations for different stages of AD were also conducted and results were analyzed. Figure 5.8 shows changes in S_{11} plots obtained from simulations between a healthy brain model, with a *mean* ± *standard deviation* of -6.9392 ± 5.1699, and brain models having properties of MCI, Mild AD, Moderate AD, and Severe AD.

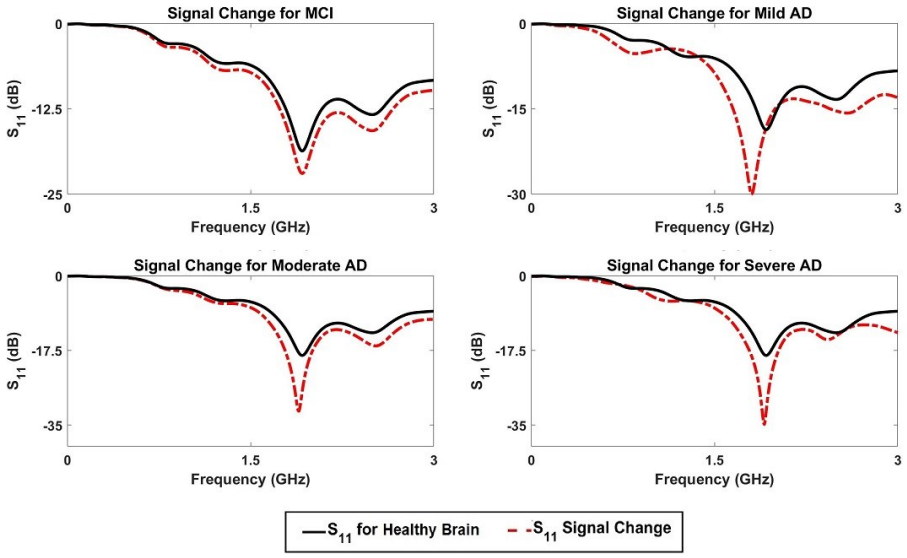

Figure 5.8: Changes in S_{11} signals obtained from simulations for different stages of AD compared to S_{11} for a healthy brain.

As the disease progresses in the brain, plaques and tangles spread to other regions of the brain and affects nutrients from reaching those areas of the brain. This results in S_{11} plots showing an increasing downward shift in the reflected signal in the operating frequency range of 1.5 to 2.1 GHz, which indicates an increased loss in the signal. This is due to the dielectric changes occurring between the healthy brain and those representing different stages of AD. In particular, the change in S_{11} loss increases from -21.97 dB in MCI to -34.54 dB in the Severe AD case at 1.901 GHz. In addition, it should be noted that in the case of Mild AD, where plaques and tangles affect the medial temporal, temporal, and parietal lobes, the plot shifts to the left by about 0.2 GHz. This is due to the averaged data collected from Antennas placed around the head model. The sensors closest to the affected regions will generate higher losses, whereas those placed on the head in the frontal lobe and occipital lobe regions, will generate less loss across the frequency range, due to those regions having healthy tissues. Due to the low relative permittivity and high conductivity of brain tissues with AD, electromagnetic waves generated by the sensors are not reflected easily as they pass through the infected areas of the brain. Instead, they tend to propagate more freely, thus causing a downward shift in the S_{11} plots. This validates the sensors' ability to differentiate different stages of AD by detecting accumulation of plaques and tangles in the reflection mode.

5.2.2 Transmission Coefficient Measurements

Figure 5.9 shows changes in the transmission coefficients that were observed for the different simulation cases.

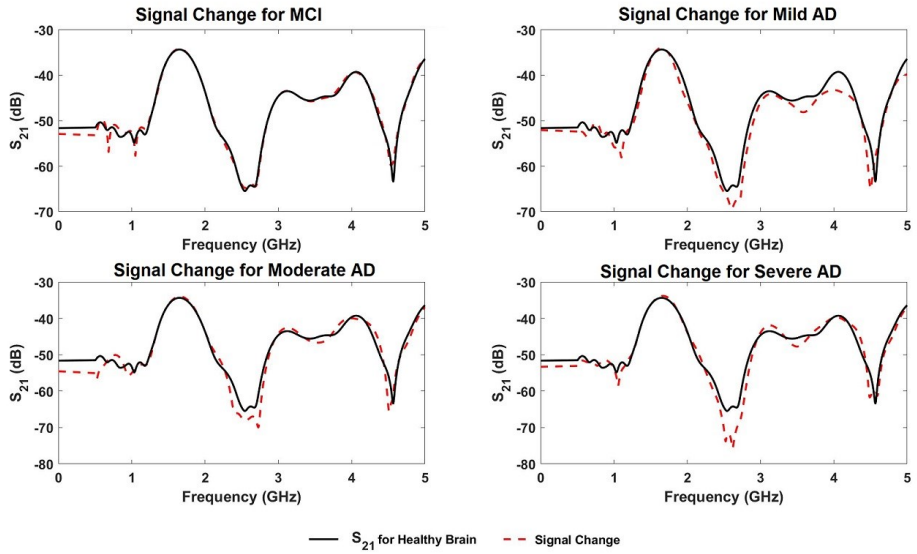

Figure 5.9: Changes in S_{21} signals obtained from simulations for different stages of AD compared to S_{21} for a healthy brain.

It can be deduced from the plots that there are no distinct characteristic traits which relates the change in S_{21} with the accumulation of affected AD tissues in the brain. However, at around 2.5 to 2.6 GHz, it can be noted that there is a considerable change in the amount of radiated RF waves that is detected by the second antenna. There is a 11 dB decrease in the loss of S_{21} signals between the MCI case and severe AD case, respectively. However, because this behavior is not seen in other frequencies, it can be difficult to detect as compared to the S_{11} results which showed distinct shifts in the reflection coefficients that were consistent across all frequencies.

5.3 Validating Antennas on Brain with Plaques and Tangles

5.3.1 Measurement Setup

The same experimental setup described in Chapter 4, and shown in Figure 4.5, was also used for validating the use of antennas and MWS for detecting increasing levels of AD-affected brain tissues. In addition, the same methodology for measuring and averaging the reflection and transmission coefficients in the brain was also used as well. Average S_{11} and S_{21} measurements of the normal brain phantom would then be recorded and utilized as the benchmark for all other measurements to validate the changes in the signal related to increasing volumes of AD-affected brain tissues.

5.3.2 Phantom Fabrication for Brain with Alzheimer's Disease Pathology

A set of artificial brain phantoms were fabricated based on a method given in [31]. Each phantom contains 3 layers: a gray matter layer, white matter layer, and a target object of varying sizes that represent AD-affected brain tissues. To recreate an artificial replica of an average adult human brain with dielectric properties of gray matter and white matter, each layer had to be fabricated separately. For the gray matter region, 1400 mL of tap water was collected. Since water has a high dielectric constant, sugar was dissolved in the water to lower the dielectric constant of the mixture. Once the ideal mixture of sugar and water was reached, the mixture was boiled with 100 g of agar powder. Once boiled, the solution was poured into the skull model and left to cool for a few hours for the mixture to solidify. Once solidified, cutting tools were used to carve out the central part of the phantom and leave 0.8 cm of the outer layer that covers the inner side of the skull.

Next, to create phantoms representing AD-affected brain tissues, coconut oil and salt were mixed. Dielectric properties of the mixture were measured until it reached the measured properties of AD white matter tissue samples. It was found that the dielectric property of the fabricated AD-affected phantoms was 1.08% lower than the measured

dielectric properties of the AD white matter tissues, making it a suitable representation of the AD-affected brain tissues for the experiments. The mixture was then cooled to solidify it. After the AD-brain tissue phantom solidified, it was carefully placed in the carved-out area of the gray matter layer. Finally, the white matter layer was created using the same method for the gray matter layer, ensuring that the water and sugar mixture has a similar dielectric property as obtained in the dielectric measurements. The mixture was then boiled with 100 g of agar and poured into the empty space inside the skull model such that it covers the AD-affected brain tissue object inside the phantom. It was then left to cool for a few hours to solidify and stick to the existing gray matter layer. Figure 5.10 (a) shows an example of the fabricated phantoms used in the experiments and (b) shows the cross-sectional view of the fabricated phantom with the gray matter layer (blue), white matter layer (red), and embedded plaques and tangles object (white).

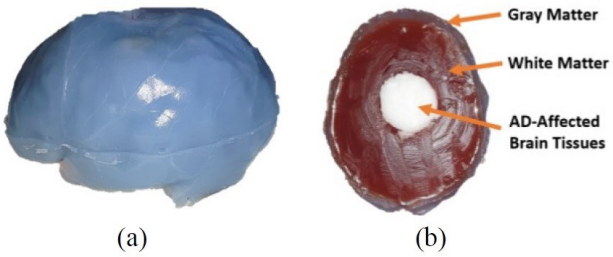

Figure 5.10: (a) Fabricated human brain phantom used in the experiments, and (b) Cross-sectional view of the phantom showing the grey matter (blue), white matter (red), and AD-affected tissue object (white) embedded in the phantom.

To ensure that the fabricated gray matter and white matter layers had the correct dielectric constant, dielectric measurements were taken for the water and sugar mixture in the liquid stage, until it was within 2% of the actual values. This is because the addition of agar had to be taken into consideration as a potential effect on the dielectric constant. Once solidified, the total volume for the phantom would equal 1400 mL, which corresponds to the total brain volume of an average adult human [209]. A final dielectric measurement was taken of the gray and white matter layers of the brain phantom after it solidified. It was found that the dielectric properties of the fabricated gray and white matter phantoms was 1.13 to 1.56% lower than measured dielectric

properties of those from the healthy brain tissues, making the phantoms a suitable representation of the actual tissues to be used in the experiments.

To emulate the spread of plaques and tangles in the brain, a total of 5 phantoms were created, each with varying volumes of AD-affected brain tissue phantom embedded in the 2-layer brain phantom. The volumes of the AD-affected brain tissue phantom in each case are the following: 1) 22.6 mm^3, 2) 56.5 mm^3, 3) 113 mm^3, and 4) 226 mm^3 and are shown in Figures 5.11 (a) to (d).

(a) (b) (c) (d)

Figure 5.11: Fabricated phantoms with the following volumes of the AD-affected brain tissues: (a) 22.6 mm^3, (b) 56.5 mm^3, (c) 113 mm^3, and 226 mm^3.

To perform the experiments, first the normal brain phantom (i.e. without the embedded AD-affected tissue objects) was inserted in the skull model. S_{11} measurements were captured for each antenna sensor and then averaged to obtain the reference dataset for a healthy brain model (i.e., brain not affected with plaques/tangles). This reference dataset would be used later when reconstructing images for the experimental cases. Next, each of the phantom with the embedded plaques/tangles object (i.e., 22.6 mm^3, 56.5 mm^3, 113 mm^3, and 226 mm^3) is placed in the skull model. Subsequent S_{11} data was collected from each antenna and averaged. This data is then processed in the imaging algorithm to reconstruct the images associated with the experimental case.

5.3.3 Reflection Coefficient Measurements

Experiments were performed to validate the antennas in detecting increasing levels of AD-affected tissues in the brain. The resulting S_{11} plot is shown in Figure 5.12. The S_{11} plot for a healthy brain has a *mean* ± *standard deviation* of -10.0821 ± 5.9123. Results in Figure 5.12 shows a similar trend found in the simulation results where the S_{11} loss

increases because of increasing volumes of AD-affected brain tissue phantom, due to changes in the dielectric properties from accumulation of plaques and tangles. At 1.8 GHz, the change in S_{11} increases to more than double, from -19.08 dB for 22.6 mm^3 of AD-affected tissues, to -40.9 dB for 226 mm^3 of AD-affected tissues in the brain phantom.

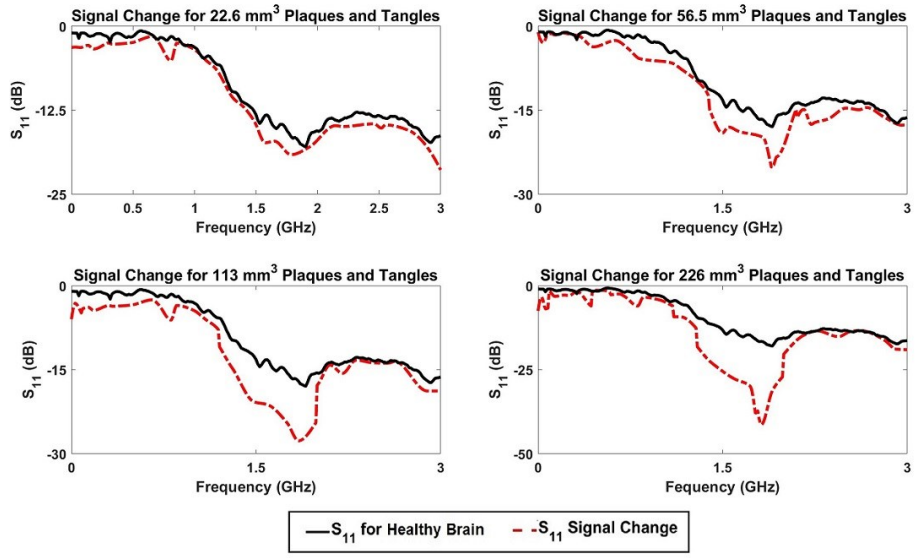

Figure 5.12: Changes in S_{11} signals obtained from experiments for increasing volumes of the AD-affected tissue object in the brain phantom compared to S_{11} for normal brain phantom.

Similar trends can be seen in the operating frequency range of the antenna between 1.5 to 2.1 GHz, which matches the results from the simulation as well. It is also worth noting that as the AD-affected tissue volume increases inside the brain phantom, there is more change in the S_{11} loss measured outside the operating frequency range. For example, at 1.30 GHz, the change in S_{11} increases from -10.46 dB for 22.6 mm^3 to -18.62 dB for 226 mm^3 of AD-affected tissues in the brain phantom. This indicates the progression of plaques and tangles in the brain as the disease "spreads" to other regions, thus providing a promising validation of the sensors' capability in detecting and monitoring the progression of AD in the brain. The last part of this paper will utilize the measured reflection coefficient signals in the modified MIST algorithm to reconstruct images of the plaques and tangles in the brain phantom.

5.3.4 Transmission Coefficient Measurements

Figure 5.13 shows the plots of changes in the transmission coefficients that were measured during the experiments for the different observed for the different simulation cases.

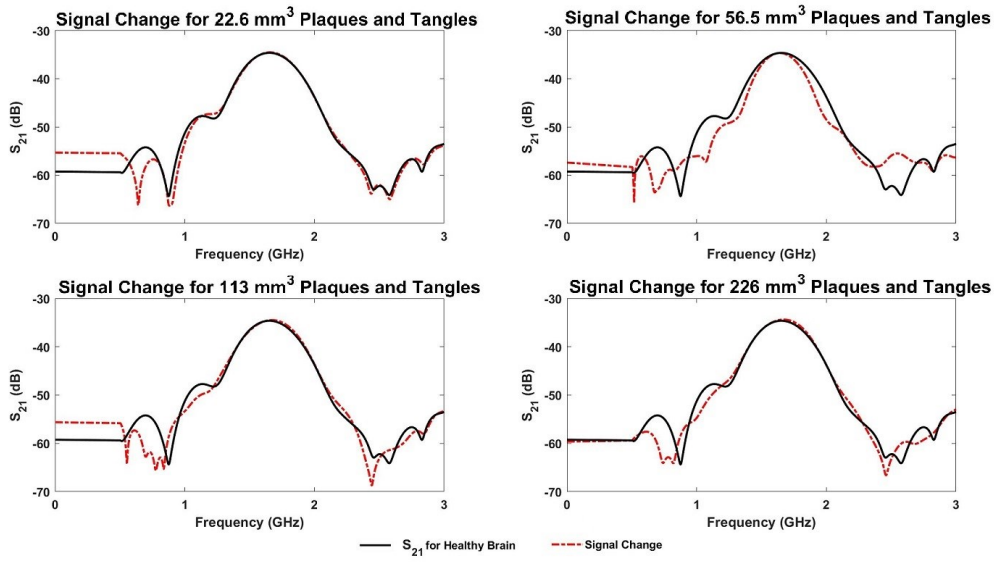

Figure 5.13: Changes in S_{21} signals obtained from experiments for increasing volumes of the AD-affected tissue object in the brain phantom compared to S_{21} for normal brain phantom.

It can be seen from the resulting measured S_{21} plots that, as in the S_{21} plots obtained in the simulation results, there are no distinct changes in the transmission coefficient as the volume of AD infected brain tissues increase. This can be attributed to the multiple layers in the phantom and its effect on hindering the propagation of the RF waves from one antenna to the other.

5.4 Microwave in Space-Time (MIST) Beamforming Imaging Algorithm

In contrast to tomography, UWB radar techniques do not attempt to reconstruct the dielectric properties profile, but instead seek to identify the presence and location of significant backward scatters in the brain. A study [125] showed the potential of detecting and imaging millimeter-sized strokes or blood clots in an anatomically

realistic head model using the simpler approach known as confocal microwave imaging. However, the previous time-shift and summing techniques do not compensate for frequency-dependent propagation effects and have limited ability to discriminate against artifacts and noise. To achieve high resolution and accurate imaging results, more complex radar-based algorithms are implemented such as microwave imaging in space-time (MIST) and multiple signal classification algorithm (MUSIC) [33],[210]. This increases the computational requirement and makes the execution time longer, which is not suitable for applications that require detecting objects in real-time. MIST beamforming offers significant improvement over the previously reported techniques of simple time-shifting and summing of backscattered signals to create a synthetically focused signal.

In this thesis, the imaging algorithm that was used is a slightly modified version of the MIST beamforming algorithm originally presented in [32]. In this algorithm, each antenna sequentially illuminates the head region with an UWB pulse signal and records the backscattered data. The space-time beamformer first time-shifts the returned signals to align them from a particular point in space. The time-aligned signals are then passed through a finite-impulse response (FIR) filter and summed to obtain the beamformer output. The result is time-gated and the energy for the point of interest is calculated. A block diagram of the MIST beamforming process is shown in Figure 5.14 and illustrated in Figure 5.15.

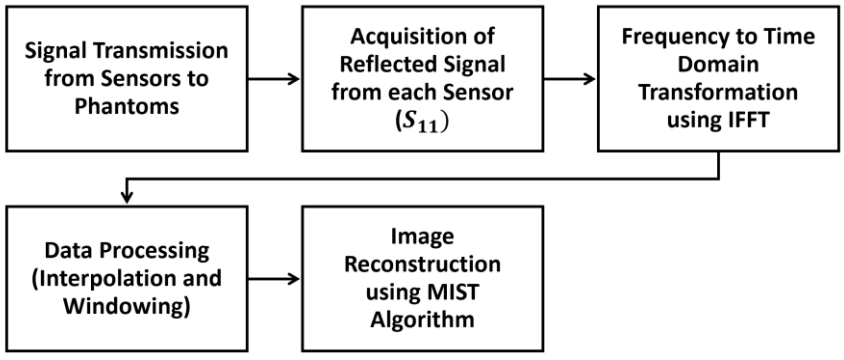

Figure 5.14: Block diagram illustrating the MIST beamforming process.

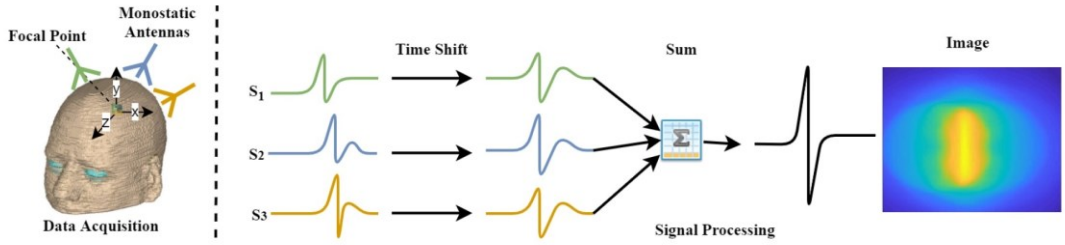

Figure 5.15: MIST beamforming process diagram.

To correctly highlight the areas of the brain containing the AD-affected brain tissues object, a reference image matrix was generated for the skull model that only contains the healthy brain phantom and no plaques/tangles objects. This image matrix is then subtracted from the image matrices generated for each experiment case to filter the data associated with the healthy brain phantom. The remaining data that is present in the image matrices therefore corresponds to the AD-affected brain tissue object that is in the skull model. An energy map is created utilizing all the beamformer outputs, further iterations are conducted to enhance the objects' image and filter out any noise in the image data. The resulting images highlight the location and general amount of AD-affected brain tissues.

The original MIST algorithm that was reported in [32] was used for breast cancer detection; therefore, it was not suitable to use, in its original form, for the purpose of head imaging due to differences in the location of the antennas used in the original algorithm, as well as the resulting time delay that was derived. However, to modify this algorithm to use in head imaging, the antennas' location had to be updated to match with those used in the experiments, where 6 antennas were placed around the circumference of the head. By updating the antennas' location, the calculated time shift for each returned signal is changed to match with the distance associated with the sensor on the head. As a result of this slight modification, the modified MIST algorithm is capable of correctly aligning the backscattered signal data from the head with the correct time shift and reconstruct images in the head.

The space-time beamformer assumes that each antenna in an array sequentially transmits a low power ultrawideband (UWB) signal into the brain and records the

backscattered signals. The UWB signal may be generated physically as a time-domain impulse or synthetically by using a swept frequency input. The beamformer spatially focuses the backscattered signals to discriminate against clutter caused by the heterogeneity of normal brain tissue and noise while compensating for frequency-dependent propagation effects.

The space-time beamformer achieves this spatial focus by first time shifting the received signals to align the returns from a hypothesized scatterer at a candidate location. The time-aligned signals are passed through a bank of finite-impulse response (FIR) filters, one in each antenna channel, and summed to produce the beamformer output. The weights in the FIR filters are designed using a least squares technique so the beamformer passes the components of the backscattered signal originating from the candidate location with unit gain while compensating for frequency-dependent propagation effects. The beamformer output is time gated to the time interval which would contain the backscattered signal from the candidate location, and then the energy is calculated. If a scattering object, such as a malignant tumor, exists at the candidate location, a relatively large energy spike occurs. The beamformer is scanned to different locations by appropriately changing the time shifts, gating, and FIR filter weights. A display of energy as a function of location provides an image of backscattered signal strength.

In contrast to direct matched filtering techniques, MIST beamforming does not assume a specific backscattered signal. As a result, the beamformer maintains robustness with respect to the uncertainty in the shape of the signal that arises from variations in the malignant tissue's properties, such as size and shape. The beamformer also provides an estimate of the backscattered signal from a specific location that may be further analyzed to gain insight into local tissue properties. Such analysis, e.g., spectral analysis of the backscattered signal, is likely to be useful characterizing unhealthy tissues. While post-beamforming analysis of backscattered signals is beyond the scope of this paper, the potential of such analysis is strong motivation for a beamforming approach.

The backscattering signals were collected at different antenna locations and recorded in the frequency domain using the VNA. An array of 6 antennas is placed at equal distance of 9 mm between each other surrounding the head. The location of each of the antennas in Cartesian coordinate can be represented as:

$$L_n = [x_n, y_n] \tag{5.6}$$

where *n* is the *nth* antenna of the antenna array. The received signal at each antenna is represented by a column vector of 201 points on a frequency range of 1 to 3 GHz. These points are converted to time domain using Inverse fast Fourier transform (IFFT). Spectral interpolation, as part of IFFT process, is applied to the time domain signals to increase the sampling rate before it is passed to the MIST algorithm for image construction. This process results in increased sampling rate, thus allowing fine time delays to be inserted in the beamforming process and produce a greater number of beams. The purpose of spectral interpolation is to increase the resolution of output images. To generate the energy map for the brain, the energy at each point needs to be calculated. To accomplish this, the distance between each antenna and different points should be calculated, to identify the signal delay in time. To get correct backscattered signals, each delay for pixel is calculated to shift the signal. The signals are then summed up to obtain the energy at that point. The distance, *d*, can be calculated as:

$$d = \frac{\sqrt{(x_n - x_0)^2 + (y_n - y_0)^2}}{a} * N \tag{5.7}$$

where x_0 and y_0 are x and y coordinates of the image, a is the diameter and *N* represents the number of input samples for each antenna. These values are then rounded, to get integer values to reduce the complexity of algorithm, without effecting the results. Finally, the delay shift results are stored in the form of a matrix that is later used for the calculations of intensity values of pixels. The intensity values are calculated using the following equation from [211]:

$$I[n] = \left[\sum_{i=1}^{N_A} A_n * d\right]^2 \tag{5.8}$$

where N_A is the total number of antennas, A_n is the signal of antenna at location *n*. In medical imaging, the brightness and contrast control are performed through windowing. There are several techniques applied to signal before image construction. Two

parameters define the range: the middle point, or sometimes called "level," and the width of the range, sometimes called "window." Before generating the final image, windowing was used to remove the clutter effect outside the portion of brain reflection. Making the window size wider or narrower, decreases or increases the display contrast. As a result, different window values were tested during the experiments and a suitable value was chosen and used for the test cases. The resulting image is then shown in the following form:

$$f(x,y) = \begin{bmatrix} f(1,1) & \cdots & f(1,N) \\ \vdots & \ddots & \vdots \\ f(M,1) & \dots & f(M,N) \end{bmatrix} \tag{5.9}$$

where *M* represents the number of rows and *N* represents the number of columns.

5.5 Image Reconstruction of AD Head Phantoms using Experimental Data

For the imaging process using the experimental data, the differential signals method is utilised for calibration purposes [16]. The data from the antennas at the 6 locations of the head have different responses among them making it impossible to use the averaging method or neighbouring antenna subtraction for the calibration step without invalidating the accuracy and detection capability of the overall system [212]. To obtain the differential signals, head scans without and with the AD-affected tissue objects are carried out. The signals for both cases are then subtracted to create the differential signals where they are input into the imaging algorithm. This method will be useful in detecting the location of AD-affected tissues where it is able to compare the S_{11} variation over time particularly for monitoring purposes. Throughout the thesis, the differential signals will be used for the imaging process. In addition, any unwanted effects due to reflections from the surroundings will be cancelled out.

In the experiments for validating MWS for AD-affected tissues (see Section 5.3), S_{11} measurements were carried out in the frequency domain using a vector network analyser rather than in time domain. As such, to adapt the MIST algorithm, the S_{11} data must be converted to the time domain [213]. The inverse Fourier transform is

implemented for the conversion from frequency domain to time domain. Then, the signals are calibrated by subtracting the signal received at the antennas with and without the AD-affected brain tissue target to create the differential signals. After the conversion of the S_{11} data from the frequency domain to time domain, the recreated pulse is then shifted to the time window that represents the location of the AD-affected tissues.

After the conversion from frequency domain and to time domain, an interpolation method is applied to estimate the delay of the synthetic pulse and generate the 2-D image of the head phantom with highlighted areas affected with AD pathology as shown in Figure 5.16. Based on the reconstructed image, it is seen that the antennas can detect and reconstruct the location of the AD-affected tissues. In general, the size of the highlighted area (yellow and orange areas) increases as the AD object increases in the phantom. However, the reconstructed image does not accurately show the actual shape of the target. In addition, there is a lot of noise that has generated into the unaffected areas that can be attributed to some of the filter, window size, and interpolation method which required further optimization. Several modifications were attempted to increase the windowing size, change the filter, and increase the number of iterations of the algorithm to refine the energy values. The resulting image after these modifications is shown in Figure 5.17. It can now be seen that there is a stronger accuracy in the reconstructed images as they are able to show the size and location of the AD-affected tissues as it increases. As more plaques and tangles are accumulated, the radius of the highlighted area increases as well and the central area of the affected tissues is denser (as can be seen in the dark red color in the reconstructed images, thus signifying the volume of the AD-affected tissues.

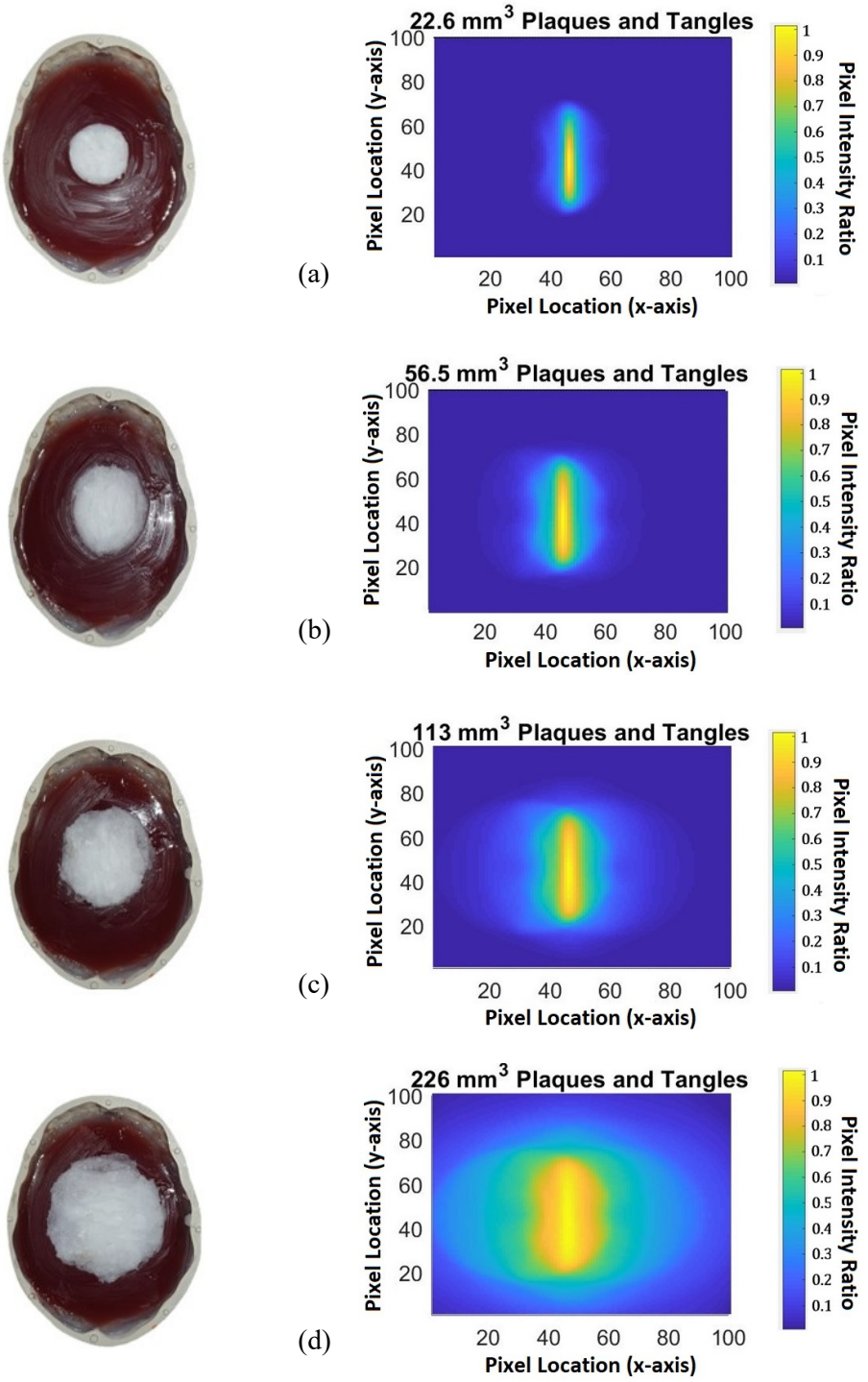

Figure 5.16: Reconstructed images of the four volumes of AD-affected brain tissues in the brain phantom using the MIST algorithm (right column) along with the actual pictures of the objects and their placements in the brain phantom (left column).

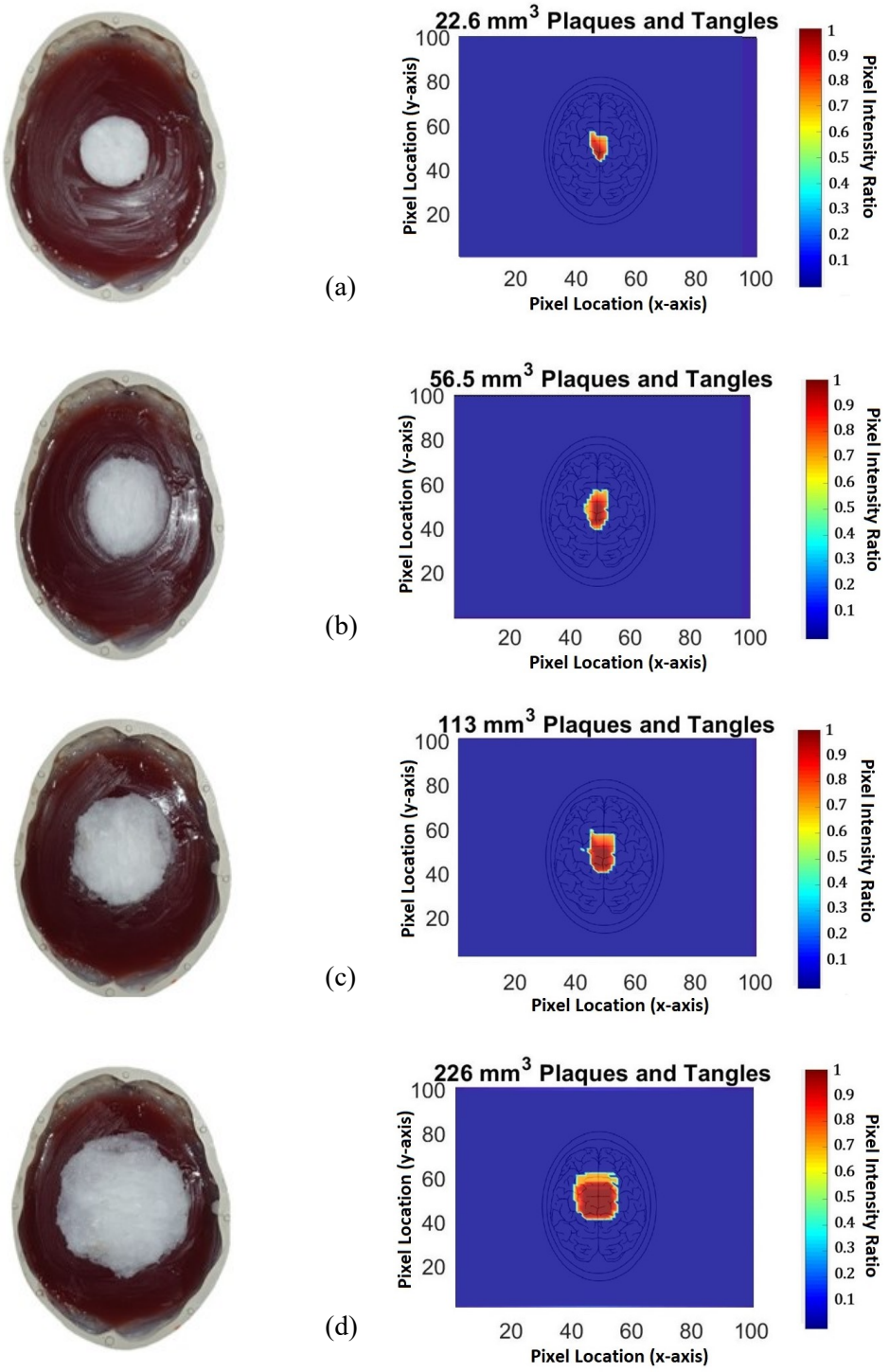

Figure 5.17: Reconstructed images after improvements in the MIST algorithm of the four volumes of AD-affected brain tissues in the brain phantom using the MIST algorithm (right column) along with the actual pictures of the objects and their placements in the brain phantom (left column).

To further validate the accuracy of the improved MIST algorithm, the Dice similarity coefficient was calculated and compared for each case between the two sets of reconstructed images as shown in Figs. 5.16 and 5.17. The Dice similarity coefficient (DSC), also known as the Sorensen-Dice index, is a statistical took which measures the similarity between two sets of data. This index has become a broadly used tool in validating image segmentation algorithms and has been applied extensively for medical diagnostic imaging [214]. The DSC can be represented in the following formula:

$$DSC = \frac{2|X \cap Y|}{|X|+|Y|} \tag{5.10}$$

where X and Y are two sets of image data, $|X|$ and $|Y|$ are the number of elements in set X and Y respectively, and $\cap$ represents the intersection of two sets and means the elements that are common to both sets [214]. Table 5.6 shows the calculated DSC for each case.

Table 5.6: Dice Similarity Coefficients for Reconstructed Images

Experiment Cases	**Original MIST (Fig. 5.16)**	**Improved MIST (Fig. 5.17)**
22.6 mm^3	0.7068	0.7038
56.5 mm^3	0.3237	0.7016
113 mm^3	0.4876	0.7040
226 mm^3	0.5287	0.7322

Table 5.6 shows that the reconstructed images from the improved MIST algorithm all yield a DSC value of at least 70% for all the cases, whereas the reconstructed images from the original MIST algorithm yielded low DSC values less than 55% for the larger objects. This could be due to the inability of the original MIST algorithm to segment the different objects in the image, and therefore shows the importance of adding extra iterations and filters to improve the overall quality and accuracy of the reconstructed images. Nonetheless, the high DSC values of the images from the improved MIST algorithm shows the promising potential of using MWI to non-invasively image areas of the brain affected by AD.

One of the limitations of the proposed interpolation technique is that it mainly depends on the difference in magnitude of the S_{11} response between a reference signal (healthy condition) and the signal of unhealthy head to estimate presence of AD-affected brain tissues. However, the S_{11} responses for AD-affected brain tissues may not be the same between two different patients. This can be due to factors such as: different head shapes and thickness of brain tissue layers. As a result, this can lead to inaccuracies in estimating the pulse delays, therefore providing a different localization of AD-affected brain tissues. Nevertheless, this technique can be improved by collecting data from several different AD patients where a database can be created and used when performing the interpolation step [215]. Furthermore, the database can also be improved to include the S_{11} responses of different stages of AD where a combination of both information can provide accurate estimations for both the distance and volume of AD-affected brain tissues.

It is seen in the MIST algorithm that the size of the AD-affected tissues in the reconstructed image depends on the width of the recreated pulse and the number of the antennas used in the array. However, a smaller pulse width requires higher bandwidth where this can be very challenging for microwave head imaging considering that frequency above 3 GHz is not effective in providing sufficient penetration depth inside the human head. Since the imaging algorithm utilises differential signals, the formations of clutter do not exist in the image. All the unwanted reflections from the surroundings were successfully removed during the calibration process and imaging algorithm. In addition, it is important to ensure that the antennas are placed at the same positions when two successive scans are made to assist with the calibration process.

5.6 Summary

In this chapter, MWS techniques were used to test and validate its performance in detecting different levels of brain tissues that are affected with plaques and tangles. In the first study, brain tissue samples from a patient with severe AD were obtained and its dielectric properties were measured on the gray and white matter regions. The dielectric properties were compared to those of healthy brain tissue samples that was

obtained from [30],[203]. It was found that the real dielectric properties for gray and white matter regions was smaller in the tissues with AD pathology, while the imaginary part had increased. Four-pole Cole-Cole model parameters were generated based on the measured dielectric properties and presented in Table A.1 (See Appendix section).

Based on this, the second part of this chapter discussed about the simulation models that were created to emulate the distribution of AD-affected brain tissues at different stages of AD. The measured dielectric properties were used in the simulations for the areas affected with AD pathology. Simulations showed that variations in S_{11} could be detected at different stages of AD and differentiated between MCI, Mild, Moderate, and Severe AD cases. However, S_{21} did not show any distinguishable variation except at a very narrow frequency band (2.5 to 2.6 GHz). Finally, the last part of the chapter discusses the experiments that were performed to validate MWS and fabricated antenna in detecting the accumulation of AD-affected tissues in the brain. For this experiment, a multi-layer phantom was created that has gray matter, white matter, and an embedded object that emulates the AD-affected brain tissues. The gray and white matter phantoms were made using sugar, agar, and water, while the AD-affected tissue phantom was created using coconut oil and sugar. this in a practical scenario.

The resulting S_{11} responses showed a detectable variation as the volume of the AD-affected tissue phantom increased. However, as in the simulation models, there were no distinguishable variations in the S_{21} responses. As a result, changes in the brain based on the accumulation of plaques and tangles can be confirmed by analysing the reflection coefficients of the antennas and comparing them to those of a healthy brain.

Finally, the MIST algorithm was adapted and modified to reconstruct images of the brain that are affected with AD pathology (i.e., plaques and tangles). Reflection coefficient data was obtained from the experiments for the different AD phantom objects. The MIST algorithm was modified to have the antenna locations match with those around the head model. Finally, changes were made to the hamming window size, interpolation methods, image noise filter, and number of iterations. These modifications allowed the algorithm to process the S_{11} data effectively and generate an accurate image of the location and size of the AD affected tissues. The resulting reconstructed images

were good and almost matched with the actual cases, with few notable differences in the shape and locations of the affected areas. However, the generated results are promising and provides a novel and transformative method of non-invasively detecting and imaging AD-affected tissues in the brain that can challenge those from PET scans which rely on the use of invasive biomarkers to highlight areas of the brain affected by AD. Based on these results, the focus now shifts to the development of wearable prototypes for MIND that incorporates antennas and a flexible switching circuit, which will be discussed about in the next chapter.

Chapter 6

Wearable Neurodegeneration Monitoring Devices

In this chapter, prototypes of wearable devices made from arrays of flexible antenna elements designed in the previous chapters are developed. For wearable applications, array configuration is the best solution where it can eliminate the need for mechanical instruments, such as a rotating platform to support the sensing device hence making it compact and lightweight [6], [16], [28]. However, there are several limitations and challenges that must be considered when designing an antenna array for microwave head imaging applications. One challenge is to determine the number of antennas that can be used in the array. This number is limited by the amount of available space available depending on the antenna size and the human head, while at the same time making sure sufficient antennas are utilised to probe the head for detecting the different symptoms of AD. Moreover, mutual coupling between adjacent antennas could pose a risk in detecting weakly reflected signals that may come from the brain tissues. Therefore, a trade-off needs to be made to ensure that all areas of the brain are probed by sensing antennas while reducing the effect of coupling between adjacent antennas by keeping enough distance between them.

The initial prototype uses an elliptical-shaped wearable base structure fabricated from a flexible conductive sheet and lossy dielectric absorber to hold the antennas in place. This prototype is used to attach the textile-based antennas using Velcro. A second prototype, based on a commercially available deerstalker hat, is developed with the silicone rubber-based antennas and has the advantage of showcasing how antennas can be implemented into commercial caps in everyday use. Finally, a flexible switching network was developed using off-the-shelf components that could be placed on the wearable devices. Each switching circuit connects 3 antennas to a single port on a VNA. These prototypes serve as proof-of-concept wearable devices for MIND applications to further improve the current available technologies for static microwave head imaging, which can facilitate real-time monitoring of AD patients' brain health, as well as

determine the progression of their condition, and being comfortable and portable to the user.

6.1 Development of Wearable Prototype with Felt-Based SPMA

An elliptical array configuration was chosen in this research where sensing antennas are arranged around the human head. The antenna array needs to be mounted on the head and be held firmly in place when measurements are taken. Therefore, a hat-like structure is devised and developed as a mounting base for the array where the antennas can be accommodated.

In [216], it was reported that the antennas' performance for microwave biomedical imaging could be improved by utilising directional antennas. The radiation beams of such antennas can be focused on the area of the target region of the body, while suppressing radiations coming from other directions. Although the radiation pattern of the proposed felt-based SPMA has nearly directional radiation (see Figures 3.17 and 3.18), having an absorber will help to block outside radiations from distorting the antenna's generated or received radiations. In [217], a metal backed dielectric absorber was used to improve the directionality of a spiral antenna. It was reported in [218] that by using a metal reflector at more than 1 cm from a monopole antenna, the propagated EM waves inside the tissue could be increased without any deterioration in the S_{11}. In addition, a UWB monopole antenna with a reflector was presented in [219] for breast microwave imaging. Since the reflector was kept at a distance of 6.58 mm, a slight deterioration of the impedance matching of the antenna was observed. Nonetheless, the directionality of the antenna was improved compared to when it operated without the reflector.

Theoretically, a reflector should be placed at a distance of $\frac{\lambda}{4}$ from the antenna where λ is the wavelength of the lowest frequency edge of the antenna in free space to increase its directivity where the reflected wave will combine coherently with the forward travelling wave. At 1.5 GHz, the calculated quarter wavelength of the EM wave in free space is about 50 mm. However, based on the simulation conducted as illustrated

in Figure 6.1, when the antenna was near the human head, strong coupling could be observed between the antenna and the head tissues. It was found that by changing the distance of the reflector from the antenna with the presence of human head, a distance that is shorter than quarter wavelength could be achieved to improve the directivity of the antenna without sacrificing the impedance matching performance of the felt-based SPMA. A simulation of the probing antenna with a reflector as shown in Figure 6.2 was carried out and Figure 6.3 demonstrates the reflection coefficients at various distances of the reflector from the antenna.

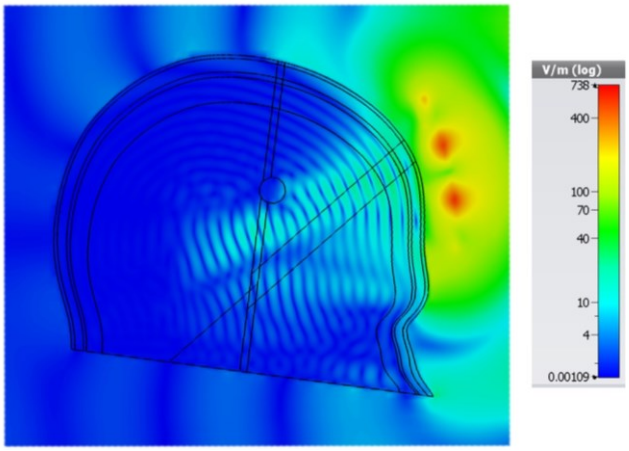

Figure 6.1: Simulated E-field distribution of the textile-based SPMA inside the head model at 1.5 GHz.

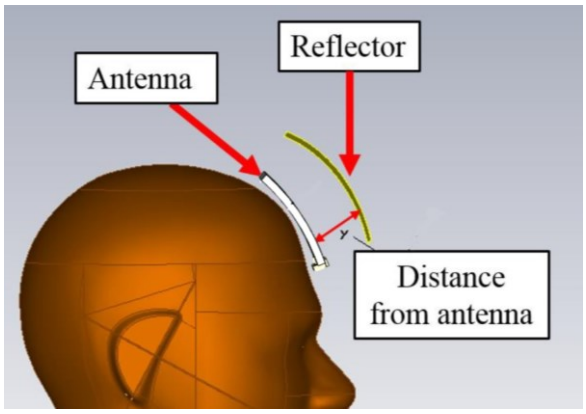

Figure 6.2: Position of the reflector that is used to block backward and outside radiations for improved antenna directivity.

Based on the S_{11} plots in Figure 6.3, it was found that a minimum separation of 25mm between the reflector and the probing antenna provided the optimal result in maintaining the impedance bandwidth of the antenna. The penetration of the EM waves inside the head phantom with the addition of the reflector is shown in Figure 6.4. It can be observed in Figure 6.4 that the RF signal penetration inside the head is much improved with the addition of a reflector, and that sufficient EM waves reach the areas of the brain where LVE and initial accumulation of plaques and tangles take place.

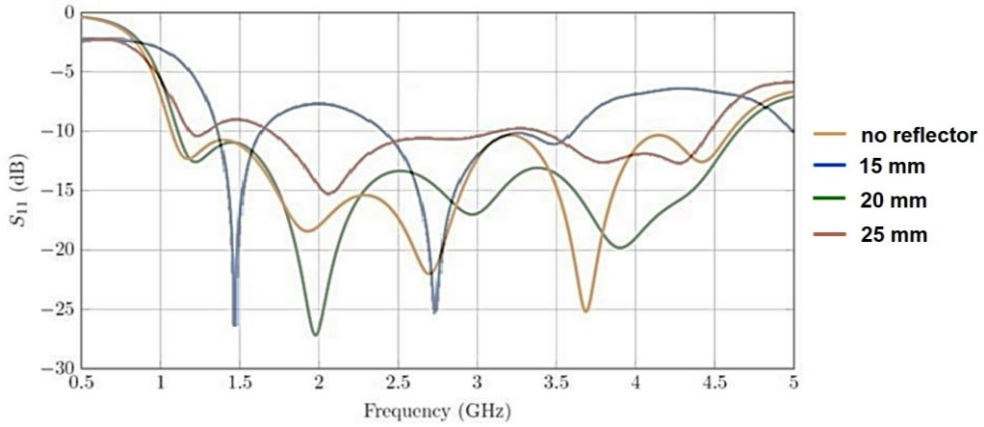

Figure 6.3: Reflection coefficients of the textile-based SPMA for various distance separations between the antenna and reflector.

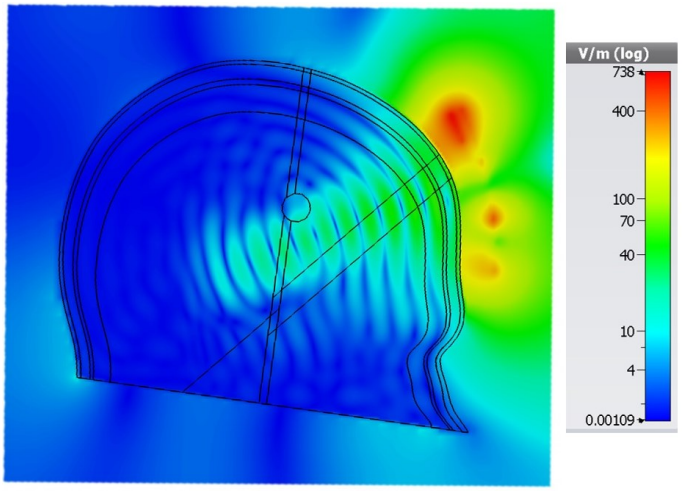

Figure 6.4: Simulated E-field distribution of the textile-based SPMA inside the head with the use of reflector.

Based on simulation results, the placement of a reflector must be closer to the probing antenna due to the strong coupling between the head and the antenna.

Therefore, a flexible conductive sheet was considered as a reflector to suppress any unwanted radiations from the surroundings. To facilitate the placement of the reflector sheet away from the antenna and provide the specified gap of 25 mm, a base structure is required. The proposed base structure is aimed to act as a wearable item that is similar to hats and caps, with the additional function of accommodating the sensing antennas and other extra circuitry, such as the switching circuit.

In [220], it was shown that a short metallic shield could be placed around the antenna to increase the directionality of a parabolic antenna. However, reflections coming from the shield affected the performance of the antenna. To mitigate this issue, an absorbing material was suggested to eliminate any reflections from the utilisation of the metallic shield where the absorbing material was fit on the inside of the shield. Therefore, a flexible dielectric absorber, AN70 from Emerson & Cuming covered with the flexible conductive sheet was explored and utilised in this prototype to suppress the back lobe radiation of the felt-based SPMAs used in this prototype [221].

The thickness of the absorber is 19 mm. With the use of felt to cover the antenna, it provides additional separation between the antenna and the flexible conductive sheet. The final separation between the antenna and the conductive sheet is 25 mm. This corresponds to one-eighth of the free-space wavelength at 1.5 GHz. It is noted that due to the strong coupling of the EM wave between the antenna and the head, a minimum separation of only 25 mm is permitted with no degradation on the impedance matching of the antenna as explained earlier. The absorber was cut and shaped to conform to a commercially available skull phantom. The general shape of the final structure of the absorber base is elliptical as shown in Figure 6.5 a). A hook and strap was used to attach the antennas to the base as shown in Figure 6.5 b).

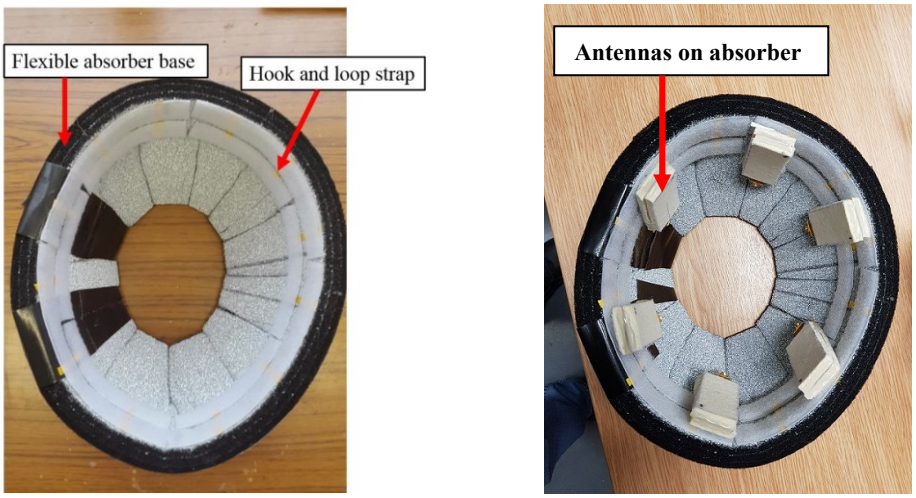

(a) (b)

Figure 6.5: (a) Wearable MIND prototype that has the absorber base shaped for placing on the head, and (b) placement of antenna elements on the absorber base MIND device.

In order to evaluate the effectiveness of the flexible EM absorber on the antenna array, time-domain characterisation and simulations was conducted in the EM solver where the E-field strengths at various locations around the antenna was calculated. By observing the received E-field strengths in Figure 6.6, the effect of using a flexible absorber backed with a reflector to suppress the back lobe radiation of the antenna can be seen by the significant reduction of the amplitude of the pulse at 180º angle as compared to the one without the reflector backed absorber that is shown in Figure 3.19. By using the received time-domain electrical signal's amplitudes, the calculated front-to-back (FTB) ratio of the signal is found to be around 11.5:1. This shows an improvement on the antenna's directivity.

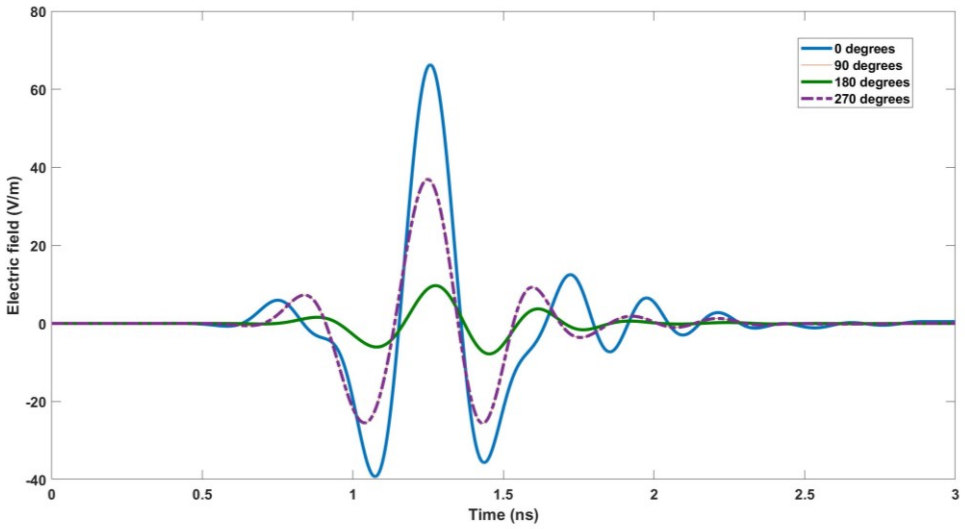

Figure 6.6: E-field strength of the transmitted Gaussian pulse of the felt-based SPMA antenna with use of flexible absorber.

6 felt-based SPMA antenna elements were fabricated. Simulations were conducted to investigate the spatial penetration of the propagated EM waves into a head phantom from the wearable antennas by observing the radiation power density inside the head model from all the antenna elements. In addition, the attenuation of the transmitted EM wave was calculated to estimate the power required for a pulse to make a round trip from the mono-static antennas to an AD-affected brain tissue target. Moreover, the areas of the brain covered by the 6 antennas in the array were selected to ensure that each lobe (i.e., frontal, temporal, parietal, and occipital) was covered to detect the changes of AD in each region separately.

Although the minimum number of the antennas used for monostatic approach in wideband microwave head imaging reported in the literature was 16 [43], the use of 6 antennas for this thesis is sufficient to determine the presence of BA, LVE, or accumulation of AD-affected tissues as AD progresses. This has been verified through simulations and experiments that were reported in Chapters 4and 5, respectively. Figure 6.7 shows the radiation power density at the cross section 40 mm below the head crown when probed by the proposed array at 1.5 GHz. There is enough penetration from the transmitted signal at the operating frequency of the proposed antenna array configuration such that all the symptoms related to AD can be detected. Thus, this

makes this a viable array configuration for MIND devices and systems. Given the antenna size, sufficient gaps between adjacent antennas, and the circumference of average human head, further antenna elements can be added into the existing array configuration, which will be conducted as future work.

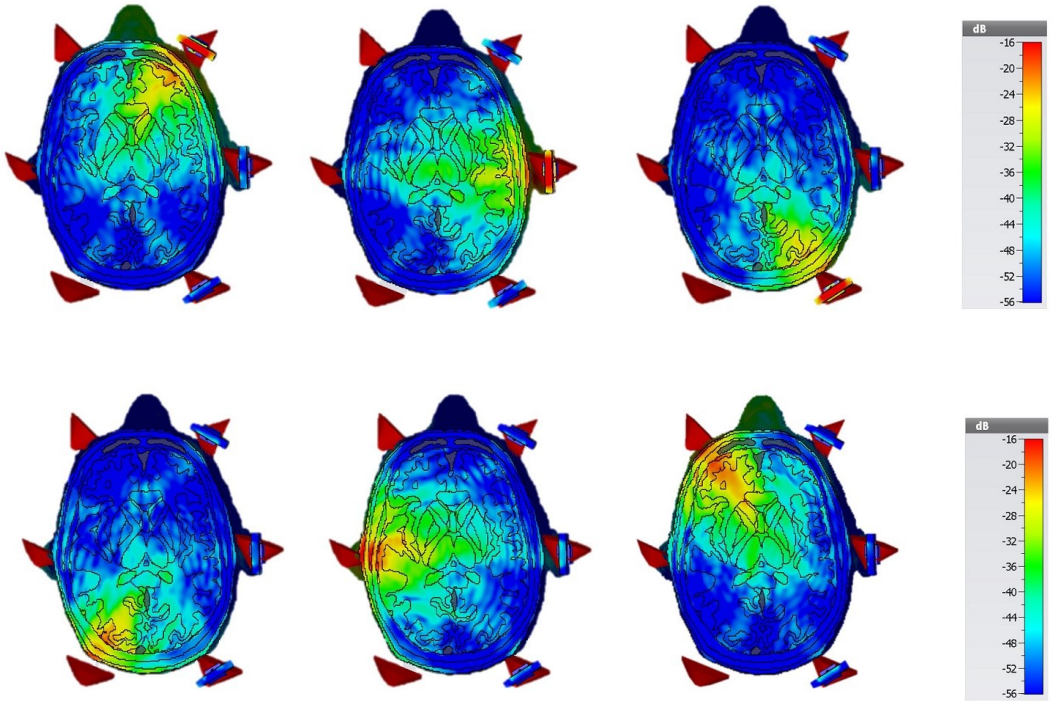

Figure 6.7: Simulated power density inside the head model for each antenna element in the array: (a) Antenna 1, (b) Antenna 2, (c) Antenna 3, (d) Antenna 4, (e) Antenna 5, and (f) Antenna 6.

The next step is to experiemntally verify the wearable MIND prototype with the felt-based SPMA. The wearable MIND prototype is assembled and placed on a human skull model. Reflection coefficient and transmission coefficient data is obtained and used to validate the performance the antennas when placed in the given absorber-based structure and configuration. The setup of the system is shown in Figure 6.8 where each antenna of the the MIND device is connected to a VNA and data is recorded using the host PC.

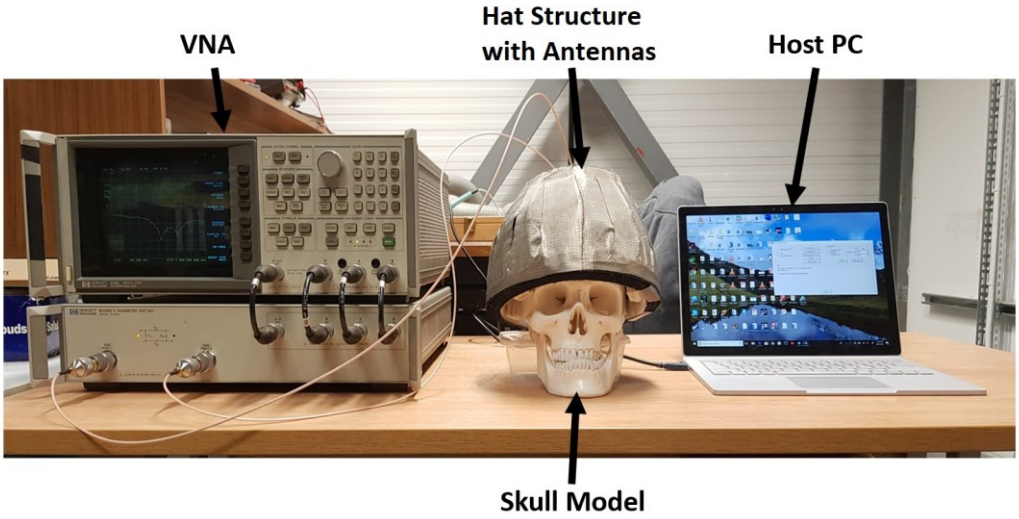

Figure 6.8: Experimental setup of the absorber-based wearable MIND prototype.

6.1.1 Reflection Coefficients

Figure 6.9 shows the S_{11} signals for all the 6 antenna elements in the array for the SPMA on felt substrate. It is seen that the highest measured lower frequency edge of the antennas is 1.605 GHz for Ant4. It should be noted that the upper frequency edge of the antennas is more than 3 GHz. Since the VNA is limited to only record measurements up to only 3 GHz, the maximum and average bandwidth of the felt-based SPMA could not be determined. In addition, it was also found that higher frequency content does not provide sufficient penetration inside the human head [121]. Therefore, it is not the intention of the wearable imaging system to be used at frequencies above 3 GHz. Variation of the S_{11} signals among the antennas in the array, as shown in Figure 6.9, can be due to inconsistencies in the fabrication process and the soldering effects of the SMA connectors.

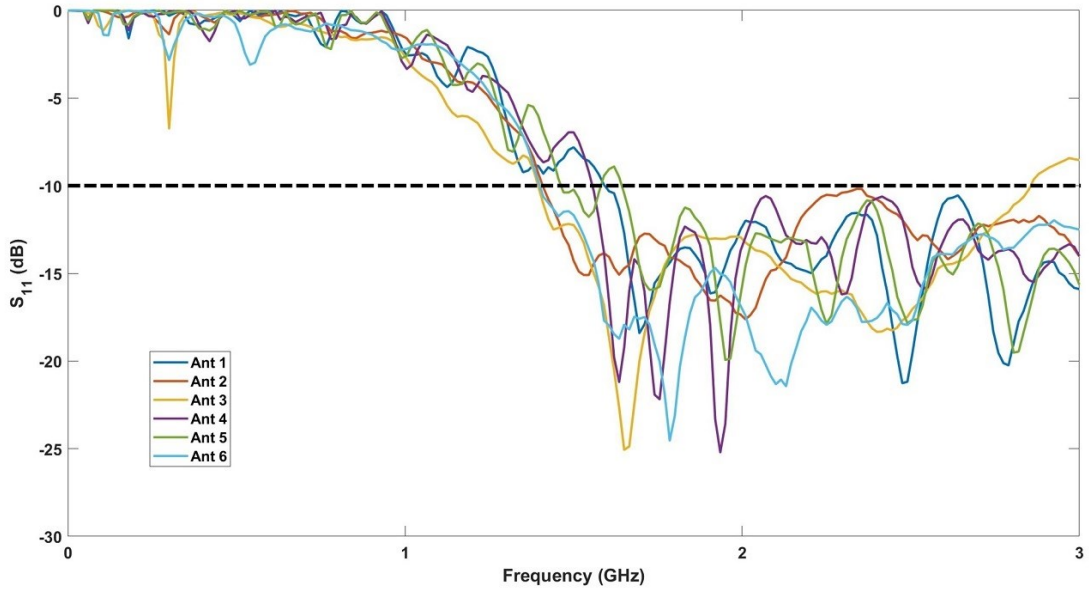

Figure 6.9: Measured S_{11} data for Antennas 1 to 6 for the absorber-based wearable MIND device.

6.1.2 Mutual Coupling between Adjacent Antennas

Mutual coupling between adjacent antennas for the textile antenna design is evaluated and analysed next. This is done by measuring the transmission coefficient between two adjacent antennas in the array, namely Ant 1 and Ant 2 and shown in Figure 6.10. It is seen that the highest S_{21} value for the antenna array is -15.529 dB between Ant1 and Ant2 which indicates that reasonably low mutual coupling value was achieved. Based on this result, it is concluded that the distance between the antenna elements in the proposed array is sufficient to assure that the nearby antennas does not significantly interfere with the operating antenna. It is to be noted that during the scanning of the head phantom, only one antenna in the array is activated at a time while the remaining antennas are switched off.

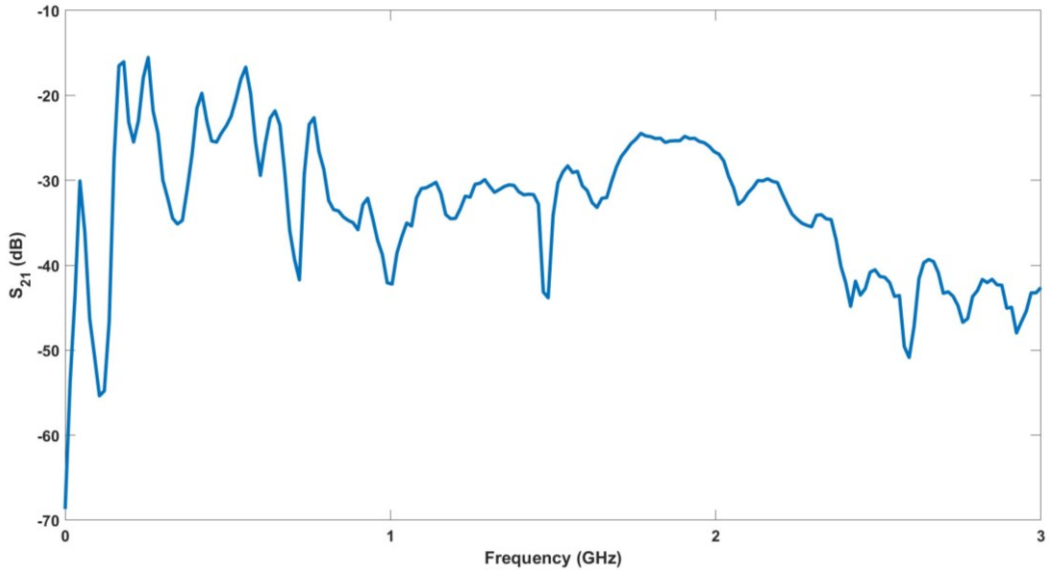

Figure 6.10: Mutual coupling between Antenna 1 and Antenna 2 for the textile-based SPMA in the absorber-based device.

6.2 Development of Wearable Prototype with Silicone Rubber-Based RPMA

Although the use of flexible absorber is beneficial to suppress the back lobe radiation and to act as the mounting base for the prototype to hold the antennas, the prototype has some setbacks. One is that it can only fit on one specific head size. In addition, the prototype is also a bit bulky and heavy, which can cause some discomfort to patients with AD. As a result, we wanted to utilise a hat that is lightweight and can easily accommodate antennas. However, to do this, a trade-off was made by sacrificing the back lobe radiation suppression to facilitate the use of a lightweight cap to hold the antennas. In this work, a deerstalker was used as it had the advantages of being lightweight and having ample space inside the inner linings to place the antennas inside. In addition, the deerstalker hat contains two brims which are stable enough to support additional electronics or circuits as needed. This prototype serves as a proof-of-concept where the wearable device can be fitted on different head sizes without requiring additional modifications on the device. In addition, because the absorber material and radiation suppression were not used, it was decided to utilise this structure to house the RPMA embedded in silicone rubber, because those antennas were found to be

directional (see Figure 3.24). The new prototype, shown in Figure 6.11, shows the deerstalker hat that contains the flexible switching circuit (discussed in Chapter 6.3), along with the silicone-rubber based RPMAs that were placed in the inner lining of the hat (Figure 6.11 c)). Compared to the previous prototype, the sensing antennas can now be firmly mounted on the head regardless of the head size. In addition, the whole structure of the new device is now more compact and lighter than the previous prototype,

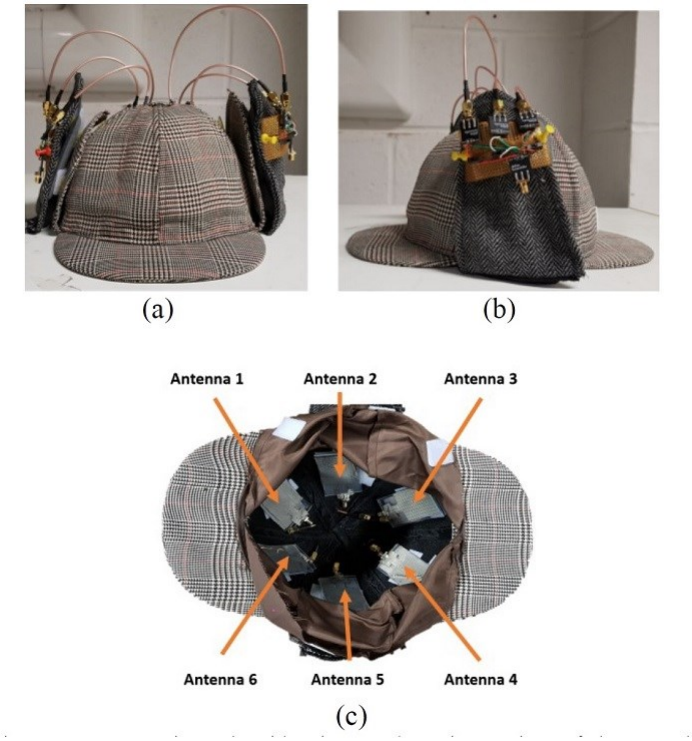

Figure 6.11: (a) Front view, (b) side view, and (c) inner view of the deerstalker-based wearable MIND device with silicone rubber-based RPMA antennas and flexible switching circuit.

The next step is to experimentally validate this new MIND prototype. Reflection coefficient and transmission coefficient data is obtained and used to validate the performance of the silicone rubber-based RPMAs when placed in the given absorber-based structure and configuration. The setup of the system is shown in Figure 6.12 where each antenna of the the MIND device is connected to a VNA and data is recorded using the host PC.

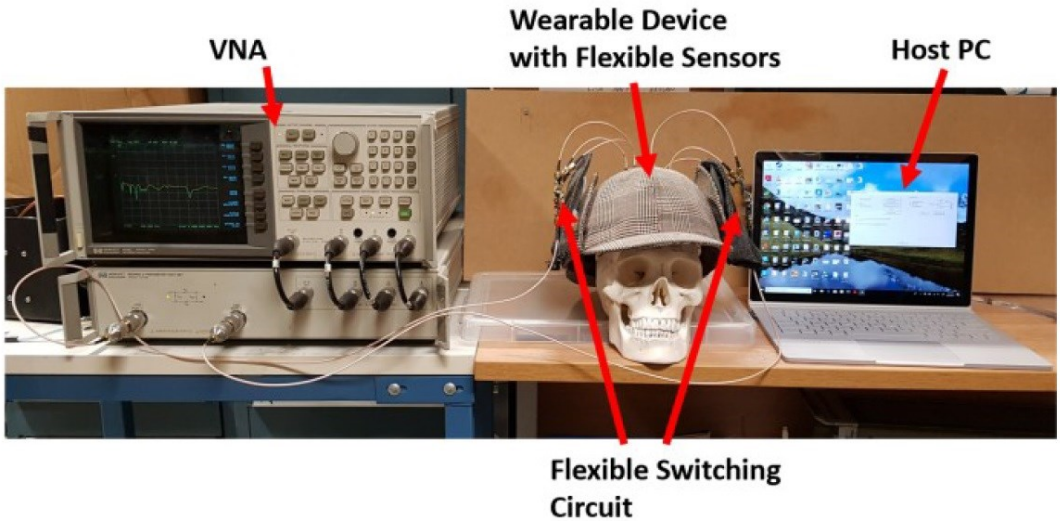

Figure 6.12: Experimental setup of the deerstalker-based wearable MIND prototype containing silicone-rubber based antennas.

6.2.1 Reflection Coefficients

Figure 6.13 shows the S_{11} signals for all the 6 antenna elements in the array for the RPMAs embedded in silicone rubber substrate. It is noted that the highest measured lower frequency edge of the proposed antennas is 1.33 GHz for Ant 5 while the lowest value recorded is 1.275 GHz for Ant 1. In terms of impedance matching, the average measured bandwidth of the array is 1.24 GHz. The wide impedance bandwidth obtained from the antennas is required for the proposed head imaging system. As for the variation of the S_{11} data among the antenna elements in the array, this due to the fabrication inconsistency and the soldering effect. It is noted that based on experience fabricating the antennas, identical S_{11} response between two antennas of the same design is almost impossible to achieve.

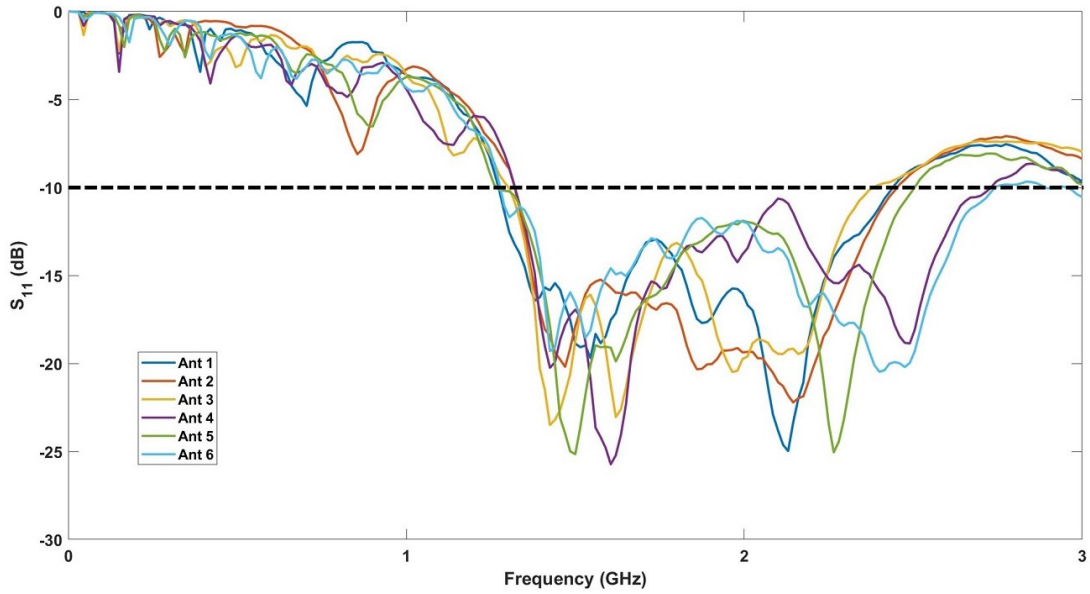

Figure 6.13: Measured S_{11} data for Antennas 1 to 6 for the deerstalker-based wearable MIND device.

6.2.2 Mutual Coupling between Adjacent Antennas

To evaluate and analyse the effect of mutual coupling between two adjacent antennas, S_{21} is again measured between two adjacent antennas in the array configuration of the new prototype and presented in Figure 6.14. It is seen that the highest S_{21} value for the antenna array is -16.946 dB between Ant1 and Ant2 which indicates that reasonably low mutual coupling value. Based on this result, it is concluded that the distance between the antenna elements in the proposed array is sufficient to assure that the nearby antennas does not significantly interfere with the operating antenna. It is to be noted that during the scanning of the head phantom, only one antenna in the array is activated at a time while the remaining antennas are switched off.

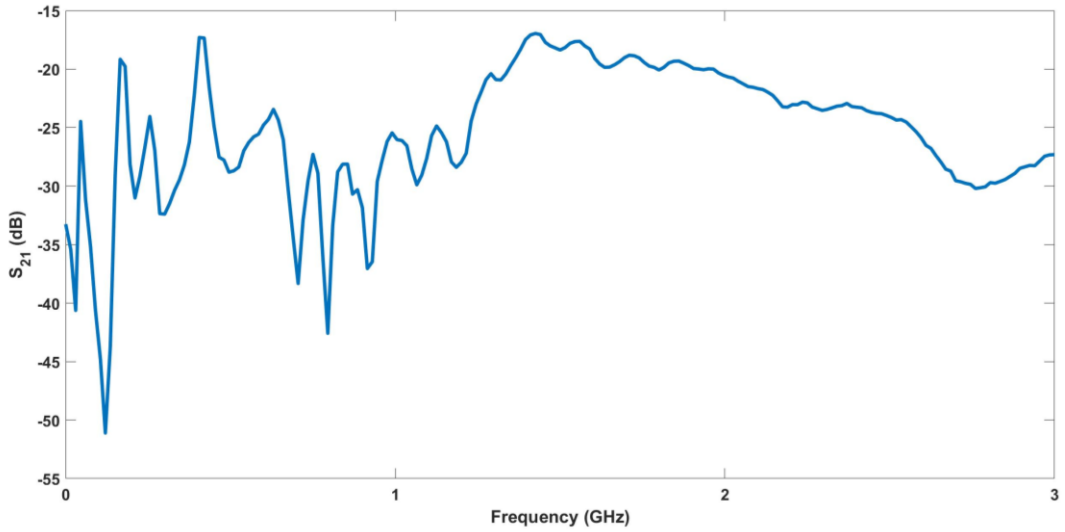

Figure 6.14: Mutual coupling between Antenna 1 and Antenna 2 for the silicone rubber-based RPMA in the deerstalker-based device.

6.3 Reconfigurable Switching Circuit

In order to easily switch between each RPMA, a reconfigurable switching circuit was developed using a flexible permaboard.

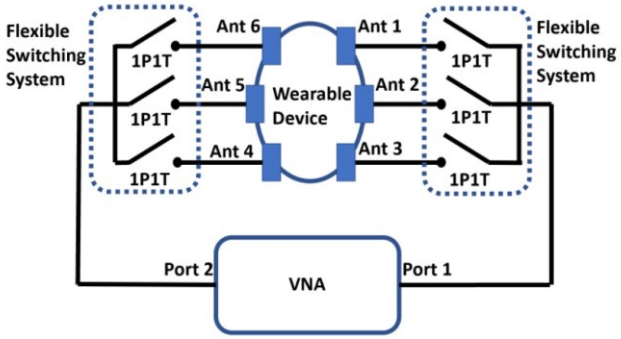

Figure 6.15: Block diagram of the overall wearable deerstalker-based MIND device with reconfigurable switching circuit connected to VNA.

The switching circuit consists of four SMA connectors and three 1P1T switches. Three SMA connectors are connected to the antennas on one side of the wearable device. The fourth SMA connector is connected to a port of the VNA. The 1P1T switches controls which antenna is active. This is manually controlled and only one switch should be turned on at a time to avoid shorting the circuit. Figure 6.15 shows a block diagram of

the overall microwave wearable device and the integration of the antennas (called Ant 1, Ant 2, …, Ant 6) and switching circuit.

6.3.1 Fabrication of Reconfigurable Switching Circuit

The reconfigurable switching circuit was developed on a flexible perma-protoboard from Adafruit. The protoboard is made from a thin polyamide film and has dimensions of 78.88 mm x 43.26 mm. The protoboard weighs 0.65 g and has a bend radius of 1 cm. By using this protoboard, the switching circuit can conform to the contours of the wearable device used in the experiments. 4 SMA breakout boards from Atlas Scientific were placed on each perma-protoboard so that it can connect 3 antennas with the VNA. All the connections switches and SMA connectors of the perma-protoboard were soldered in place. Figures 6.16 (a)-(c) shows the front, back, and side view of the developed switching circuit respectively, while Figure 6.16 (d) shows switching circuit being bent.

6.3.2 Measured Insertion Loss and Return Loss

In the final set of experiments, the reconfigurable switching circuit was tested to verify the performance of the 6 1P1T switches that are used for each antenna. Measurements were taken using the VNA to capture the insertion loss and return loss for each switch. Insertion loss is the total power lost through the insertion of a device (in this case, a switch) in a transmission line. The insertion loss for the switches is captured in its “on” state and is considered a critical parameter in designing switching circuits, as it provides an indication of how much noise is added into the system. Return loss is the loss of power in the signal reflected by a device (i.e., a switch) in a transmission line. This parameter is also important in designing switching circuits as it gives an indication of how well devices or lines are matched.

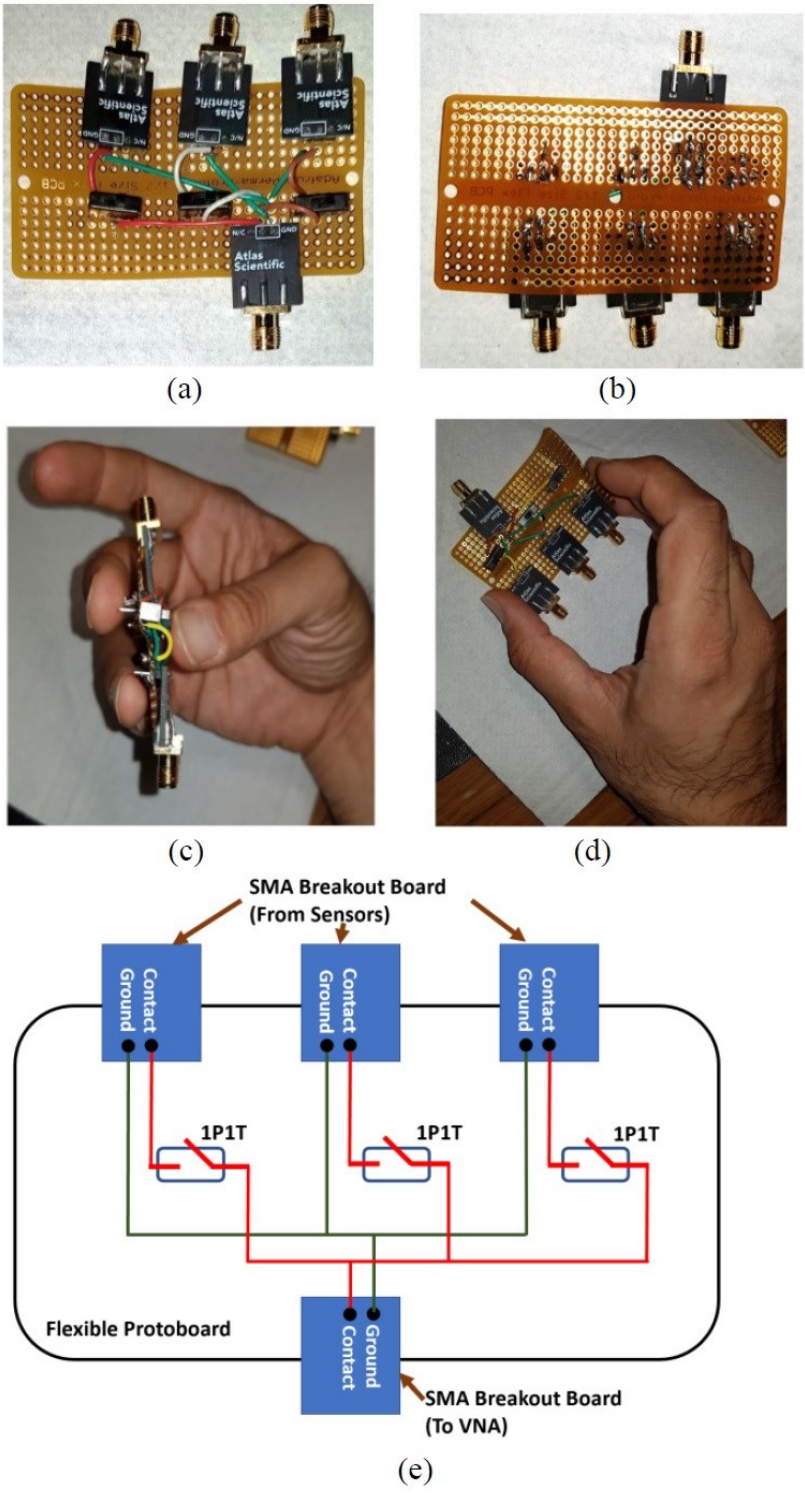

Figure 6.16: (a) Top view, (b) rear view, (c) side of the assembled reconfigurable switching circuit, (d) switching circuit being bent, and (e) schematic diagram of the reconfigurable switching circuit.

To calculate the insertion and return loss for the switching circuits, first the S-parameters were measured for the 1P1T switches using the VNA. Then, S_{11} and S_{21} were used in the following equations to calculate insertion and return loss respectively:

$$Insertion\ Loss\ (dB) = -20\ log_{10}|S_{21}| \tag{6.1}$$

$$Return\ Loss\ (dB) = -20\ log_{10}|S_{11}| \tag{6.2}$$

where S_{11} and S_{21} are the reflection and transmission coefficients, respectively. The plots of the insertion and return losses for the 6 1P1T switches are shown in Figures 6.17 and 6.18.

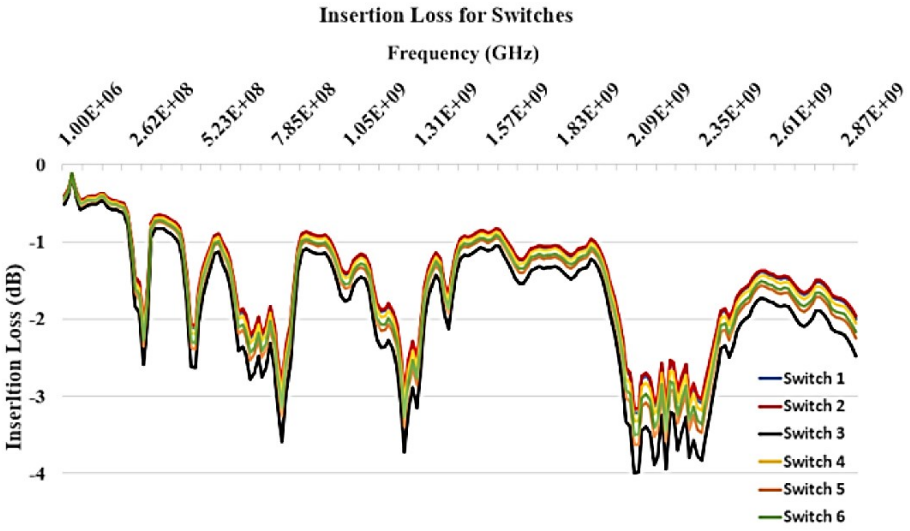

Figure 6.17: Measured insertion loss in dB for the 6 1P1T switches.

Figure 6.18: Measured return loss in dB for the 6 1P1T switches.

The plot in Figure 6.17 indicates that for all the switches, the insertion loss does not exceed more than -3.9 dB across the frequency range. In addition, in the frequency range 0.8 MHz to 1.2 GHz and 1.57 GHz to 1.85 GHz, the insertion loss is not less than -2 dB. These results indicate that the designed switching circuit is good, and that not too much unwanted noise or reflections will be generated by the switches in the region of the dual resonant frequencies of the antennas. In addition, the plots for return loss in Figure 6.18 shows that all the switches match relatively well due to the high return loss values across the frequency spectrum. Future work will be undertaken to enhance the design and fabrication of the switching circuit to ensure that connections are secured and do not vibrate or cause noise when being worn by the user.

6.4 Summary

This chapter discussed the development of two MIND devices consisting of an array of antenna elements developed in Chapter 3. Main considerations that were made while developing the wearable array are: the number of antennas in the array, minimum

separation of adjacent antennas to reduce mutual coupling effect, flexibility, and comfortability of the wearable prototype, and most importantly, coverage of the different regions of the brain to monitor the progression of AD. The first prototype is designed by attaching the flexible felt-based SPMA elements on a flexible absorber covered with a conductive sheet that was shaped according to an artificial realistic human skull. The main objective of using the reflector backed absorber is to block outside radiation and suppress any back lobe radiations of the monopole antennas that may compromise the performance of the proposed MIND device. The absorber also serves as a wearable unit that can be worn by a patient.

In the second prototype, a commercially available deerstalker hat was used as a wearable prototype that houses the silicone rubber embedded RPMA elements and reconfigurable switching circuit. The sensing antennas are placed inside the inner lining of the deerstalker hat to enable it to fit on to different head shape. This allowed the sensors to fit onto different head shapes and had the advantage of being lightweight compared to the first prototype where its structure is relatively rigid and bulky. The S_{11} signals of the antenna arrays were measured for both prototypes. Based on the measurement results, the impedance bandwidth of the antennas when arranged in an array show similar performance as a single element due to ample separation between them. In addition, mutual coupling effect between two adjacent antennas was evaluated by means of transmission coefficient and was found to have low coupling effect.

Chapter 7

Conclusion and Future Work

The core aim of this thesis is to validate MWI and MWS as viable techniques to non-invasively detect and monitor neurodegenerative diseases, such as AD, in the brain. This was presented through the development, investigation, and validation of flexible antennas on conditions such as BA, LVE, and accumulation of plaques and tangles in the brain that result from AD. This ultimately led to the development of an imaging algorithm that could image the regions of the brain affected by plaques and tangles, like a PET scan. Finally, the thesis concludes on an initial attempt at developing wearable and portable devices that can be used to monitor changes in the brain. This chapter summarises the research studies presented in this thesis. The main objectives of each chapter are reviewed and the achievements from the studies conducted are highlighted. Future directions based on the research presented in this thesis are suggested.

7.1 Chapter Summary and Conclusion

7.1.1 Chapter 2 Summary and Conclusion

Chapter 2 presents a comprehensive literature review for two areas. The first area focuses on current imaging systems and methods used to detect and monitor AD and other neurodegenerative diseases. Systems such as MRI and PET scans are currently used in hospitals to determine whether a person has AD. In addition, PET scans have the added advantage of determining the levels of plaques and tangles in the brain by using a tracer that binds to the protein, thus making them highlighted in the scans. Although these systems are regularly used by doctors and patients, they are hindered by several disadvantages which limit its use for patients. In addition, their bulky size and static fixture makes it extremely inconvenient for patients with later stages of AD to use. The second area of literature review addresses the current research that has been done for microwave head imaging. The fundamental principle behind radar-based

microwave imaging is that malignant tissues or blood in the body would scatter more energy when illuminated with electromagnetic waves. Due to the reflected signals, the sensing antennas can detect the presence of infected tissues (e.g., tumours or blood clots) by measuring the reflected signals. By applying suitable imaging or sensing algorithms, the location of infected tissues can be determined with sensible accuracy. For head imaging applications, several research studies were carried out to verify the effectiveness of the microwave technology in detecting or classifying different head diseases such as stroke, traumatic brain injuries and intracranial hematoma. In addition, a classifier system has been proposed to detect the type of stroke suffered by a patient to deliver the right treatment. Afterwards, several developed wearable prototypes were described that used flexible antenna array as sensing elements. Wearable microwave imaging devices offer many advantages such as being conformable, light weight and low cost. These advantages, along with promising research that has proven its effectiveness in detecting stroke and brain cancer, provided the incentive of pursuing this technology in this thesis to determine if it could be translated to detecting symptoms related to AD.

7.1.2 Chapter 3 Summary and Conclusion

The most vital component in any microwave imaging system is the sensing antenna. There are several main requirements in the implementation of a flexible antenna for microwave head imaging applications. In addition to typical requirements of a rigid sensing antenna, flexibility and light weight are some of the key features to ensure successful integration of the antennas into wearable devices. In Chapter 3, the design aspects of the flexible antenna are described and verified through simulations and experiments. Flexible materials, such as felt textile and silicone rubber, were used to fabricate the antennas where their performances are validated in terms of impedance matching, radiation pattern, and fidelity of the transmitted pulse. In this thesis, a stepped monopole antenna, fabricated on textiles, and a rectangular planar monopole antenna inside silicone rubber substrate were investigated. Planar monopole design is adopted in this research due to its inherent low profile and wideband characteristics. In addition, the use of the ground plane in the antenna design allowed for the generated EM waves to be directional and reach targeted regions of the brain. Parametric optimisations were

carried out mainly on the feeding lines of the antennas to optimise their impedance bandwidths. The antennas are prototyped and measured. The measured frequency of the felt-based SPMA antenna is from 1.34 GHz up to 3 GHz whereas the silicone rubber-based RPMA antenna operates at 1.3 GHz to 2.76 GHz. Based on the simulations conducted, both antennas show high fidelity factor that ensures low signal distortion. Moreover, the performances of the antennas were also found to be maintained when operating near the artificial head phantom.

7.1.3 Chapter 4 Summary and Conclusion

The core part of the research is conducted in the next couple of chapters (Chapters 4 and 5) on validating MWS for each of the key symptom of AD. In Chapter 4, the focus was on validating whether MWS could detect brain atrophy and lateral ventricle enlargement. Initial simulations were performed by reducing the size of brain (gray and white matter), while increasing the size of the outer CSF layer. The results from the simulations showed that a minimum of 5% reduction in overall brain volume could be detected by the antennas. Furthermore, this was verified in both the reflection and transmission coefficients. Based on the simulation results, the felt-based antennas were used on a skull model that contained lamb brains to emulate the BA condition. For each level of BA, a controlled amount of lamb brains was removed, and the outer space was replaced with a phantom that mimicked the property of CSF. This phantom was created using water, sugar, and agar powder. Measurements were carried out using a VNA. It was found that the results obtained from the experiments showed a similar trend in that BA could be detected in both reflection and transmission coefficients.

The investigation of MWS on detecting lateral ventricle enlargement was then carried out in the second part of Chapter 4. Simulations were initially performed by using a normal head model and placing a target object in the middle which is the approximate location of the lateral ventricles. It is found that CSF builds up in the lateral ventricles as they enlarge. Therefore, by setting the properties of the target object as that of CSF, and varying its size, the condition of LVE could be emulated. The results from simulations showed that increasing levels of LVE could be detected and was represented in both the reflection and transmission coefficients. Again, experiments

were conducted using the felt-based antennas were used on a skull model that contained lamb brains and several target objects of varying sizes that are made of coconut oil and salt. To emulate LVE, each object was placed in a cavity in the centre of the lamb brain model and subsequent measurements were taken. Measurements obtained from the experiments showed a similar trend that was seen in the simulation models. It could be seen that with increasing levels of LVE, there is a higher loss that is shown in both the reflection and transmission coefficients.

7.1.4 Chapter 5 Summary and Conclusion

Chapter 5 deals with the most important and vital validation of MWS in detecting AD, namely whether MWS could detect brain tissues affected with plaques and tangles. This chapter highlighted several novel studies that have not been conducted before. The first phase of this chapter investigated the dielectric properties of brain tissues with AD pathology (i.e., plaques and tangles) from a patient with severe AD. The goal was to understand how AD pathology can alter dielectric properties of brain tissues in both the gray and white matter regions. Measured properties indicated a distinct shift in both the real and imaginary dielectric properties of healthy brain tissues compared to the tissues with AD. Since the fundamental process of MWS and MWI relies on changes in dielectric properties, this finding provided a promising incentive to validate the technology further.

Simulation models were created using a complex head voxel model to realistically emulate different stages of AD, by changing properties of certain brain regions to those obtained in the measurements. Results showed that there were distinct shifts in the reflection coefficients as the amount of AD-affected brain regions increased. However, this trend was not shown in the transmission coefficient, which may be due to presence of several layers that distort the signal. Based on these results, experiments were conducted by creating a two-layer phantom with gray and white matter. In the middle of the two-layer brain phantom is an embedded target object that was fabricated to match the dielectric properties of the AD-affected brain tissues. Several phantoms were created to show an increase and progression of AD-affected tissues in the brain. Measurements obtained from the experiments showed a similar trend in that reflection

coefficients changed as the levels of AD-affected tissues increases, whereas there was no change in the transmission coefficient.

In order to highlight the non-invasive imaging ability of MWI, the last part of Chapter 5 touches on an initial attempt of using a modified MIST algorithm to reconstruct regions of the brain affected by AD pathology. Reflection coefficient data obtained from the experiments for different levels of AD-affected tissues was used in the imaging algorithm to generate images. The space-time beamformer assumes that each antenna in an array sequentially transmits a low-power UWB signal into the brain and records the backscattered signals. The beamformer spatially focuses the backscattered signals to discriminate against clutter caused by the heterogeneity of normal brain tissue and noise while compensating for frequency-dependent propagation effects. The algorithm first shifts the received S_{11} signals to align the returns from a hypothesized scatterer at a candidate location to obtain spatial focus. The time-aligned signals are passed through a bank of FIR filters and summed to produce the beamformer output. The beamformer output is time gated to the time interval which would contain the backscattered signal from the candidate location, and then the energy is calculated. If a scattering object, such as a malignant tissue, exists at the candidate location, a relatively large energy spike occurs at that location. A display of energy as a function of location provides an image of backscattered signal strength. Since MIST beamforming does not assume a specific backscattered signal, it maintains robustness with respect to the uncertainty in the shape of the signal that arises from variations in the affected tissue's properties, such as size and shape. Using the data from the experiments in the modified MIST algorithm, images were reconstructed that almost matched with the actual case. In addition, it was found that by modifying the algorithm further, increasing iterations, and altering filter, interpolation and windowing parameters, the resulting images were clearer and better. The resulting images also provides an important validation on MWI for non-invasive imaging AD-affected tissues, which can serve as a transformational and safer alternative to PET scans.

7.1.5 Chapter 6 Summary and Conclusion

Finally, Chapter 6 describes the development of wearable prototypes by using an array of antennas that were designed in Chapter 3. In this thesis, the number of antenna elements used is 6 as a proof-of-concept work. The number allowed for sufficient separation based on the dimensions of the antenna and ensured a reduction in mutual coupling between adjacent antennas. Extensive simulations were carried out to investigate the spatial power distribution inside a head model and validate the effectiveness of the antenna array configuration for head imaging. It was observed that all areas of the head at the cross-section 40 mm below the head crown, are covered by the antennas. The first wearable prototype is developed by using a flexible absorbing material backed with a flexible conductive sheet that suppresses the back lobe radiation of the monopole antennas. The felt-based SPMA antennas were attached to the absorber structure using Velcro. Additionally, the absorber frame serves as a support structure to mount the antennas. Owing to the strong coupling between the sensing antenna and the head, it was found that a minimum distance of only 25 mm is required between a reflector and the antenna compared to 50 mm needed in free space condition at 1.5 GHz. Low measured mutual coupling is observed between adjacent antennas in the array. However, a limitation of this prototype is its fixed size, rigid structure, and slightly bulky shape.

Therefore, a second prototype was developed that utilised a commercially available deerstalker hat as the base to mount the antenna. The inner lining of the hat was opened, and the 6 silicone-rubber based RPMAs were placed inside. To keep the structure lightweight, the absorber was not used. However, since the silicone-rubber based RPMAs are directional, and generate almost no back lobe radiation, the absorber was not needed. The design of the prototype was found to be lightweight and fit on almost all head shapes. A limitation of using the antenna array is that VNA can only connect to 2 antennas at a given time. This causes an issue when capturing measurements for each antenna and ensuring that the measurement integrity is not affected when switching between antenna manually. To mitigate this issue, a reconfigurable switching circuit was developed and integrated onto the wearable prototype to allow for 3 antennas to be connected to a single VNA port. The active antennas would then be

controlled by an onboard 1P1T switch where one antenna would be active while the others were at rest. The switching circuit was fabricated using off-the-shelf components on a flexible protoboard. Measured insertion and return loss showed that the inclusion of the switching circuit did not affect the overall performance of the antennas. In addition, the use of flexible materials allowed the switching circuit to be easily placed onto the wearable structure and be conformal to the contours of the head.

7.1.6 Overall Summary

Overall, it is concluded that MWS and MWI can be a suitable technique in detecting and monitoring the progression of AD and other neurodegenerative diseases in the brain. The ability to develop flexible sensing antennas and wearable MWI devices gives rise to a technology that is transformative for future clinical diagnosis. However, one limitation is that the technology is still in its infancy and requires more investigations and repeated tests for it to be translated into clinical trials. Another limitation is that patients will have different head shapes and different levels of AD progression, it is therefore difficult to compare antenna readings from normal cases of patients with the same head sizes. In addition, it is also not possible for antennas to obtain the same readings twice as it can differ due to noise in the environment, soldering connections, and movements of the body that can alter the EM waves that are recorded. Nonetheless, the ease of fabrication, low cost, fast diagnosis, and non-invasive approach makes MWI and MWS a technology that is worth investigating further to develop future MIND devices that can be used in places like clinics and care homes for rapid monitoring of patients' conditions.

7.2 Suggestions for Future Work

The research undertaken and discussed in this study successfully addresses the first attempt of applying MWS and MWI to detecting AD. Although the results represented are promising there are still other aspects of the research that requires further optimisations and improvements that will help to further advance this technology in terms of accuracy, efficiency, and the practicality of developed prototypes system. Some of the suggested work are summarized as follow:

7.2.1 Antenna Design

One of the key limitations of the fabricated antennas in this thesis is its size. Future work can be undertaken on the antenna design to investigate structures that are more compact in size, such as patch antennas. This would provide the advantage of occupying less space on the head and allow for more elements to be utilised in measurements, thus improving resolution of the device. The challenge would be to create a compact-size antenna that is able to achieve similar penetration depth at the frequency range specified for microwave head imaging devices. Another part of antenna design that can be investigated is the use of different materials to create a highly flexible and conformable antenna, but resilient enough to tear, bending, and other effects that are present in the textile material (i.e., fraying). Given the work presented in the thesis on embedding conductive textile with silicone rubber, another design that would be of interest is the use of liquid metal that is embedded with silicone rubber or PDMS. Liquid metal, such as Galinstan, provides the advantage of being highly conductive and having the properties of liquid, namely the ability to move freely among gaps and channels made in the substrate. Of course, this presents several challenges that would need to be investigated, such as the dynamic nature of the liquid metal and how it affects the overall antenna's performance.

7.2.2 Antenna Array and Reconfigurable Switching Circuit

In order to improve the sensitivity, resolution, and imaging of the MIND devices to accurately reflect all the changes in the brain, the number of antenna elements utilised in the array needs to be increased. A challenge that needs to be considered is the available space on the structure and the maximum number of antennas it would allow. In addition, the antennas need to be properly spaced to avoid mutual coupling affects. Finally, future integration of the antenna elements needs to be investigated to minimize the profile of the antennas on the wearable structures that may cause patients to feel uncomfortable when wearing the MIND devices.

Another aspect of the MIND device that was developed in this thesis was the reconfigurable switching circuit. Future work on improving the design of the switching circuit should be undertaken to ensure that connections between the components are

not hindered by the bending of the protoboard. In addition, additional elements should be placed in the circuit that will help minimize insertion and return loss and have the EM waves be transmitted and received efficiently. Finally, another area of future investigation is the implementation of Bluetooth or wireless control modules that will allow users to switch between active antennas without the need of manually switching between the antennas using the on-board switches.

7.2.3 Imaging Algorithm

A limitation of the imaging algorithm used in this thesis is that it cannot differentiate between the plaques and tangles. Furthermore, more work needs to be undertaken with the imaging algorithm in testing how the reconstructed images for AD-affected tissues compare with those of other head diseases such as stroke and brain tumour. This would provide an indication of whether the imaging algorithm can differentiate between different diseases and is crucial for doctors to provide the right treatment. In addition, because the algorithm provides a 2-D overhead view of the brain, it does not provide an accurate representation of the exact location of the brain tissues affected by AD. Therefore, more advanced microwave imaging algorithms need to be investigated and developed that will provide 3-D representations of the brain.

Another limitation of the imaging algorithm is that the reconstructed images are based off obtaining a reading of the same person, or one with the same head shape, who is healthy. Such image data can be achieved through methods and techniques such as Big Data, Machine Learning, and AI that can be used to accumulate data from a wide variety of cases, people, and head shapes. This can in turn be used to compare images reconstructed from the antennas to determine the proposed progression of AD in the brain. A recent paper was published that utilised data from the BA and LVE experiments discussed in this thesis on a parallel microwave image reconstruction algorithm based on Apache Spark on high-performance computing and Google Cloud Platform that was described, which had an average speed increase of 28.56 times, resulting in fast reconstruction of images from radio frequency sensor's data [222]. Such studies and future work can improve the processing, accuracy, and speed of the imaging algorithm.

7.2.4 Alzheimer's Disease Phantom Development

Another aspect of the research that requires further improvements is the development of more realistic brain phantoms that emulate the progression of AD. In particular, the thesis showed dielectric properties that were measured for brain tissues from a patient with severe AD. These tissues contained a high level of plaques and tangles. These properties need to be validated from patients with other stages of AD. This will ensure that the recorded dielectric properties of AD-affected tissues can be generalized for all the other stages of AD.

In addition, the phantoms that were used in the experiments need to be further improved to show the different stages of AD. In order to be as realistic as possible, phantoms need to contain multiple layers that represent gray matter, white matter, CSF, and blood. In addition, channels and pumps can be utilised to dynamically change and control dielectric properties of certain regions of the brain phantom. This will allow for experiments to be conducted more conveniently without the need of creating several phantoms for each stage of AD.

7.2.5 Development of Phantoms Emulating Other Neurodegenerative Diseases

While this thesis focused on the investigation, application, and validation of MWI and MWS with AD, it is also important to validate the technology with other neurodegenerative diseases such as PD, LBD, and ALS. This can be achieved by creating the advanced phantom alluded to in the previous section. By dynamically controlling the dielectric properties for different brain regions, we can emulate the presence of other neurodegenerative diseases. However, prior to doing this, it is also important to measure and record dielectric properties of brain tissues from patients with other ND. This is because some of the other ND do not have plaques and tangles but are affected by other proteins in the brain.

7.3 Final Comments

MWI and MWS offer several advantages compared to the conventional systems for AD diagnosis (e.g., MRI, PET, and CT scan), such as low-cost, non-invasive and non-ionisation. Although the main aim of microwave imaging is not to replace current imaging systems for AD detection, it is expected that this technology will be able to complement the existing imaging systems to provide more access for people that require an imaging tool for quick and convenient medical check-ups or understanding the current stage of AD so that the right treatment can be provided as early as possible. Recently, radar-based head imaging system has gained a lot of attention from the research community due to its effectiveness in detecting brain diseases such as stroke, traumatic brain injuries and intracranial hematoma. However, very few research works have been conducted to implement the system for wearable applications. One of the main advantages of a flexible sensing device is that it can provide more comfort to the wearer which makes the patient more relaxed while undergoing a test. Moreover, with the rapid progress in electronics, wearable health monitoring systems are much needed in the community. The realisation of wearable and wireless head monitoring systems will allow the monitoring of patients or personnel of intermediate risks at home or at work.

References

[1] Alzheimer's Association, "2019 Alzheimer's disease facts and figures," *Alzheimer's Dementia Journal*, vol. 5, pp. 321-387, 2019.

[2] Alzheimer's Society, "What is Alzheimer's Disease: Factsheet 401LP July 2017," *Factsheet 401LP*, pp. 1-10, 2017.

[3] K. A. Johnson, N. C. Fox, R. A. Sperling, and W. E. Klunk, "Brain imaging in Alzheimer disease," *Cold Spring Harb Perspect Med.*, vol. 4, pp. 1-23, 2012.

[4] C. Susskind, "Possible Use of Microwaves in the Management of Lung Disease," in *Proceedings of the IEEE*, 1967, pp. 673–674.

[5] P. C. Pedersen, C. C. Johnson, C. H. Durney, and D. G. Bragg, "Microwave Reflection and Transmission Measurements for Pulmonary Diagnosis and Monitoring," *IEEE Trans. Biomed. Eng.*, vol. BME-25, no. 1, pp. 40–48, 1978.

[6] A. W. Preece, I. Craddock, M. Shere, L. Jones, and H. L. Winton, "MARIA M4: clinical evaluation of a prototype ultrawideband radar scanner for breast cancer detection," *J. Med. Imaging*, vol. 3, no. 3, p. 33502, 2016.

[7] S. Y. Semenov and D. R. Corfield, "Microwave Tomography for Brain Imaging: Feasibility Assessment for Stroke Detection," *Int. J. Antennas Propag.*, pp. 1–8, 2008.

[8] E. C. Fear, X. Li, S. C. Hagness, and M. A. Stuchly, "Confocal microwave imaging for breast cancer detection: Localization of tumors in three dimensions," *IEEE Trans. Biomed. Eng.*, vol. 49, no. 8, pp. 812–822, 2002.

[9] J. M. Sill and E. C. Fear, "Tissue sensing adaptive radar for breast cancer detection-experimental investigation of simple tumor models," *IEEE Trans. Microw. Theory Tech.*, vol. 53, no. 11, pp. 3312–3319, 2005.

[10] A. T. Mobashsher, A. M. Abbosh, and Y. Wang, "Microwave System to Detect Traumatic Brain Injuries Using Compact Unidirectional Antenna and Wideband Transceiver with Verification on Realistic Head Phantom," *IEEE Trans. Microw. Theory Tech.*, vol. 62, no. 9, pp. 1826–1836, 2014.

[11] S. Candefjord, J. Winges, A. A. Malik, Y. Yu, T. Rylander, T. McKelvey, A. Fhager, M. Elam, and M. Persson, "Microwave Technology for Detecting Traumatic Intracranial Bleedings: Tests on Phantom of Subdural Hematoma and Numerical Simulations," *Med. Biol. Eng. Comput.*, pp. 1–12, 2016.

[12] J. C. Ljungqvist, S. Candefjord, M. Persson, L. Jönsson, T. S. Skoglund, and M. Elam, "Clinical Evaluation of a Microwave-Based Device for Detection of Traumatic Intracranial Hemorrhage," *J. Neurotrauma*, vol. 7, p. neu.2016.4869, 2017.

[13] S. A. Rezaeieh, A. Zamani, K. S. Bialkowski, and A. M. Abbosh, "Foam Embedded Wideband Antenna Array for Early Congestive Heart Failure Detection with Tests Using Artificial Phantom with Animal Organs," *IEEE Trans. Antennas Propag.*, vol. 63, no. 11, pp. 5138–5143, 2015.

[14] S. A. Rezaeieh, A. Zamani, and A. M. Abbosh, "Three-Dimensional Wideband Antenna for Head Imaging System with Performance Verification in Brain Tumor Detection," *IEEE Antennas Wirel. Propag. Lett.*, vol. 14, pp. 910–914, 2015.

[15] S. A. Rezaeieh, A. Zamani, K. S. Bialkowski, and A. M. Abbosh, "Novel Microwave Torso Scanner for Thoracic Fluid Accumulation Diagnosis and Monitoring," *Sci. Rep.*, vol. 7, no. 1, p. 304, 2017.

[16] H. Bahramiabarghouei, E. Porter, B. Gosselin, M. Popovi, and L. A. Rusch, “Flexible 16 antenna array for microwave breast cancer detection,” *IEEE Trans. Biomed. Eng.*, vol. 62, no. 10, pp. 2516–2525, 2015.

[17] R. Yahya, M. R. Kamarudin, and N. Seman, “New Wideband Textile Antenna for SAR Investigation in Head Microwave Imaging,” in *RF and Wireless Technologies for Biomedical and Healthcare Applications (IMWS-Bio)*, 2014, pp. 1–3.

[18] A. T. Mobashsher, B. J. Mohammed, S. Mustafa, and A. Abbosh, “Ultra-Wideband Antenna for Portable Brain Stroke Diagnostic System,” in *IEEE MTT-S International Microwave Workshop Series on RF and Wireless Technologies for Biomedical and Healthcare Applications, IMWS-BIO 2013 -Proceedings*, 2013, pp. 2–4.

[19] B. J. Mohammed, A. M. Abbosh, S. Mustafa, and D. Ireland, “Microwave system for head imaging,” *IEEE Trans. Instrum. Meas.*, vol. 63, no. 1, pp. 117–123, 2014.

[20] A. T. Mobashsher and A. M. Abbosh, “On-site Rapid Diagnosis of Intracranial Hematoma using Portable Multi-slice Microwave Imaging System,” *Sci. Rep.*, vol. 6, no. 1, p. 37620, 2016.

[21] R. Paradiso, G. Loriga, and N. Taccini, “A Wearable Health Care System Based on Knitted Integrated Sensors,” *IEEE Trans. Inf. Technol. Biomed.*, vol. 9, no. 3, pp. 337–344, 2005.

[22] S. Salman, Z. Wang, E. Colebeck, A. Kiourti, E. Topsakal, and J. L. Volakis, “Pulmonary edema monitoring sensor with integrated body-area network for remote medical sensing,” *IEEE Trans. Antennas Propag.*, vol. 62, no. 5, pp. 2787–2794, 2014.

[23] D. L. Weimer and M. A. Sager, “Early identification and treatment of Alzheimer's disease: Social and fiscal outcomes,” *Alzheimer's & Dementia*, vol. 5, no. 3, pp. 215-226, 2009.

[24] H. Förstl, R. Zerfaß, C. Geiger-Kabisch, H. Sattel, C. Besthorn, & F. Hentschel, “Brain Atrophy in Normal Ageing and Alzheimer's Disease: Volumetric Discrimination and Clinical Correlations,” *British Journal of Psychiatry*, 167(6), 739-746, 1995, doi:10.1192/bjp.167.6.739

[25] L. G. Apostolova, A. Green, S. Babakchanian, K. Hwang, Y. Chou, A. W. Toga, & P. M. Thompson, “Hippocampal atrophy and ventricular enlargement in normal aging, mild cognitive impairment (MCI), and Alzheimer disease,” *Alzheimer Disease & Associated Disorders*, 26(1), 17 – 27, 2012, https://doi.org/10.1097/WAD.0b013e3182163b62.

[26] H. Braak and E. Braak, “Neuropathological stageing of Alzheimer-related changes.” *Acta Neuropathologica, vol. 82*, no. 4, 2015, pp. 239-259.

[27] C. Gabriel, S. Gabriel, and E. Corthout, “The dielectric properties of biological tissues: I. Literature survey,” Phys. Med. Biol., Vol. 41, pp. 2231-2249, 1996.

[28] E. Porter, H. Barami, A. Santorelli, B. Gosselin, L. Rusch, and M. Popovic, “A Wearable Microwave Antenna Array for Time-Domain Breast Tumor Screening,” IEEE Trans. Med. Imag., Vol. 35, No. 6, pp. 1501-1509, 2016.

[29] P. T. Nguyen, A. Abbosh, and S. Crozier, “Microwave Hyperthermia for Breast Cancer Treatment Using Electromagnetic and Thermal Focusing Tested on Realistic Breast Models and Antenna Arrays,” IEEE Trans. Antennas Propag., Vol. 63, No. 10, pp. 4426-4434, 2015.

[30] C. Gabriel, S. Gabriel, and E. Corthout, “The dielectric properties of biological tissues: II. Measurements in the frequency range 10 Hz to 20 GHz,” *Phys. Med. Biol.*, Vol. 41, pp. 2231-2249, 1996.

[31] A. T. Mobashsher and A. M. Abbosh, "Artificial Human Phantoms: Human Proxy in Testing Microwave Apparatuses That Have Electromagnetic Interaction with the Human Body," in *IEEE Microwave Magazine*, vol. 16, no. 6, pp. 42-62, July 2015.

[32] E. Bond, X. Li, S. Hagness and B. Van Veen, "Microwave imaging via space-time beamforming for early detection of breast cancer," in *Proceedings of International Conference on Acoustics, Speech and Signal Processing (CASSP'02)*, Orlando, FL, 2002 pp. III-2909-III-2912.

[33] E. J. Bond, X. Li, S. C. Hagness, and B. D. Van Veen, 2003, "Microwave imaging via space-time beamforming for early detection of breast cancer," *IEEE Transactions on Antennas and Propagation*, vol. 51, no. 8, pp. 1690-1705, 2003.

[34] M. Persson, A. Fhager, H. Dobsicek Trefna, Y. Yu, T. Mckelvey, G. Pegenius, J.-E. Karlsson, and M. Elam, "Microwave-based stroke diagnosis making global prehospital thrombolytic treatment possible," *IEEE Trans. Biomed. Eng.*, vol. 61, no. 11, pp. 2806–2817, 2014.

[35] M. S. R. Bashri and T. Arslan, "Low-cost and compact RF switching system for wearable microwave head imaging with performance verification on artificial head phantom," *IET Microwaves, Antennas & Propagation*, vol. 12, no. 5, pp. 706-711, 18 4 2018.

[36] M. Klemm, J. A. Leendertz, D. Gibbins, I. J. Craddock, A. Preece, and R. Benjamin, "Microwave Radar-Based Differential Breast Cancer Imaging: Imaging in Homogeneous Breast phantoms and Low Contrast Scenarios," *IEEE Trans. Antennas Propag.*, vol. 58, no. 7, pp. 2337–2344, 2010.

[37] A. Alemaryeen, S. Noghanian and R. Fazel-Rezai, "Antenna Effects on Respiratory Rate Measurement Using a UWB Radar System," in IEEE Journal of Electromagnetics, RF and Microwaves in Medicine and Biology, vol. 2, no. 2, pp. 87-93, June 2018.

[38] B. Schleicher, I. Nasr, A. Trasser and H. Schumacher, "IR-UWB Radar Demonstrator for Ultra-Fine Movement Detection and Vital-Sign Monitoring," in IEEE Transactions on Microwave Theory and Techniques, vol. 61, no. 5, pp. 2076-2085, May 2013.

[39] L. M. Thompson, "Neurodegeneration: a question of balance". *Nature*, vol. 452, no. 7188, pp. 707–708, April 2008.

[40] L. C. Walker, H. LeVine, "The cerebral proteopathies," *Neurobiol Aging*, vol. 21, no. 4, pp. 559–561, 2000.

[41] H. W. Querfurth, F. M. LaFerla, "Alzheimer's disease," *The New England Journal of Medicine*, vol. 362, no. 4, pp. 329–344, 2010.

[42] C. A. Raji et al, "Age, Alzheimer Disease, and Brain Structure," *Neurology*, vol. 73.22, pp. 1899–1905, 2009

[43] Marino, S., Bonanno, L., Lo Buono, V., Ciurleo, R., Corallo, F., Morabito, R., et. al., "Longitudinal analysis of brain atrophy in Alzheimer's disease and frontotemporal dementia," *Journal of International Medical Research*, pp. 5019–5027, 2019.

[44] N. C. Fox, P.A. Freeborough, "Brain atrophy progression measured from registered serial MRI: Validation and application to alzheimer's disease," *J. Magn. Reson. Imaging*, 7: 1069-1075, 1997.

[45] R. Peters, "Ageing and the Brain," *Postgraduate Medical Journal*, vol. 82.964, pp. 84–88, 2006.

[46] P. Coupé, J. V. Manjón, E. Lanuza, et al., "Lifespan Changes of the Human Brain In Alzheimer's Disease," *Sci Rep*, vol. 9, no. 3998, 2019. https://doi.org/10.1038/s41598-019-39809-8

[47] G. D. Pearlson, L. E. Tune, "Cerebral ventricular size and cerebrospinal fluid acetylcholinesterase levels in senile dementia of the Alzheimer type," *Psychiatry Research*, vol. 17, no. 1, Pages 23-29, 1986.

[48] S. M. Nestor et al. “Ventricular Enlargement as a Possible Measure of Alzheimer’s Disease Progression Validated Using the Alzheimer’s Disease Neuroimaging Initiative Database.” *Brain*, vol. 131.9, pp. 2443–2454, 2008.

[49] C. Reitz, R. Mayeux, “Alzheimer disease: Epidemiology, Diagnostic Criteria, Risk Factors and Biomarkers,” *Biochemical Pharmacology*, vol. 88, no. 4, pp. 640–651, 2014.

[50] C. R. Harrington, “The molecular pathology of Alzheimer’s disease,” *Imaging in Alzheimer’s Disease and Other Demantias: Neuroimaging Clinics of North America*, pp. 11-22, 2012.

[51] Niklas Mattsson, Philip S. Insel, Michael Donohue, Jonas Jögi, Rik Ossenkoppele, Tomas Olsson, Michael Schöll, Ruben Smith, Oskar Hansson, “Predicting diagnosis and cognition with 18F-AV-1451 tau PET and structural MRI in Alzheimer's disease,” *Alzheimer's & Dementia*, vol. 15, no. 4, pp. 570-580, 2019.

[52] D. Chan, N. C. Fox, R. I. Scahill, W. R. Crum, J. L. Whitwell, G. Leschziner, A. M. Rossor, J. M. Stevens, L. Cipolotti, M. N. Rossor, “Patterns of temporal lobe atrophy in semantic dementia and Alzheimer’s disease,” *Ann Neurol* 49: 433–442, 2001.

[53] B. C. Dickerson, I. Goncharova, M. P. Sullivan, C. Forchetti, R. S. Wilson, D. A. Bennett, L. A. Beckett, L. deToledo-Morrell, “MRI-derived entorhinal and hippocampal atrophy in incipient and very mild Alzheimer’s disease,” *Neurobiol Aging,* 22: 747–754, 2001.

[54] S. Lehericy, M. Baulac, J. Chiras, L. Pierot, N. Martin, B. Pillon, B. Deweer, B. Dubois, C. Marsault, “Amygdalohippocampal MR volume measurements in the early stages of Alzheimer disease,” *Am. J. Neuroradiol.,* 15: 929–937, 1994.

[55] H. Braak, E. Braak, “Neuropathological staging of Alzheimer-related changes,” *Acta. Neuropathol. (Berl.)*, 82:239–259, 1991.

[56] D. Chan, J. C. Janssen, J. L. Whitwell, H. C. Watt, R. Jenkins, C. Frost, M. N. Rossor, N. C. Fox, “Change in rates of cerebral atrophy over time in early-onset Alzheimer’s disease: Longitudinal MRI study,” *Lancet*, 362: 1121–1122, 2003.

[57] C. R. Jack Jr., S. D. Weigand, M. M. Shiung, S. A. Przybelski, P. C. O’Brien, J. L. Gunter, D. S. Knopman, B. F. Boeve, G. E. Smith, R. C. Petersen, “Atrophy rates accelerate in amnestic mild cognitive impairment,” *Neurology*, 70: 1740–1752, 2008.

[58] B. H. Ridha, J. Barnes, J. W. Bartlett, A. Godbolt, T. Pepple, M. N. Rossor, N. C. Fox, “Tracking atrophy progression in familial Alzheimer’s disease: A serial MRI study,” *Lancet Neurol.* 5: 828–834, 2006.

[59] B. Dubois, H. H. Feldman, C. Jacova, S. T. Dekosky, P. Barberger-Gateau, J. Cummings, A. Delacourte, D. Galasko, S. Gauthier, G. Jicha, et al., “Research criteria for the diagnosis of Alzheimer’s disease: Revising the NINCDS-ADRDA criteria,” *Lancet Neurol.*, 6: 734–746, 2006.

[60] G. Lombardi, G. Crescioli, E. Cavedo, E. Lucenteforte, G. Casazza, et. al., “Structural magnetic resonance imaging for the early diagnosis of dementia due to Alzheimer's disease in people with mild cognitive impairment,” *Cochrane Database of Systematic Reviews*, no. 3, 2020.

[61] I. G. McKeith, D. W. Dickson, J. Lowe, M. Emre, J. T. O’Brien, H. Feldman, J. Cummings, J. E. Duda, C. Lippa, E. K. Perry, et al., “Diagnosis and management of dementiawith Lewy bodies: Third report of the DLB Consortium,” *Neurology*, 65: 1863–1872, 2005.

[62] G. Waldemar, B. Dubois, M. Emre, P. Scheltens, P. Tariska, M. Rossor, “Diagnosis and management of Alzheimer’s disease and other disorders associated with dementia. The role of neurologists in Europe. European Federation of Neurological Societies.” *Eur J Neurol*, 7: 133–144, 2000.

[63] F. de Vos, M. Koini, T. M. Schouten, S. Seiler, J. van der Grond, A. Lechner, R. Schmidt, M. de Rooij, S. A. R. B. Rombouts, "A comprehensive analysis of resting state fMRI measures to classify individual patients with Alzheimer's disease," *NeuroImage*, vol. 167, Pages 62-72, 2018, https://doi.org/10.1016/j.neuroimage.2017.11.025.

[64] S. Ogawa, T. M. Lee, A. S. Nayak, P. Glynn, "Oxygenationsensitive contrast in magnetic resonance image of rodent brain at high magnetic fields," *Magn Reson Med*, 14: 68–78, 1990.

[65] N. K. Logothetis, J. Pauls, M. Augath, T. Trinath, A. Oeltermann, "Neurophysiological investigation of the basis of the fMRI signal," *Nature*, 412: 150–157, 2001.

[66] S. A. Small, G. M. Perera, R. DeLaPaz, R. Mayeux, Y. Stern, "Differential regional dysfunction of the hippocampal formation among elderly with memory decline and Alzheimer's disease," *Ann Neurol*, 45: 466–472, 1999.

[67] T. Kato, D. Knopman, H. Liu, "Dissociation of regional activation in mild AD during visual encoding: A functional MRI study," *Neurology*, 57: 812–816, 2001.

[68] M. M. Machulda, H. A. Ward, B. Borowski, J. L. Gunter, R. H. Cha, P. C. O'Brien, R. C. Petersen, B. F. Boeve, D. Knopman, D. F. Tang-Wai, et al., "Comparison of memory fMRI response among normal, MCI, and Alzheimer's patients," *Neurology*, 61: 500–506, 2003.

[69] F. Remy, F. Mirrashed, B. Campbell, W. Richter, "Mental calculation impairment in Alzheimer's disease: A functional magnetic resonance imaging study," *Neurosci Lett*, 358: 25–28, 2004.

[70] A. Hamalainen, M. Pihlajamaki, H. Tanila, T. Hanninen, E. Niskanen, S. Tervo, P. A. Karjalainen, R. L. Vanninen, H. Soininen, "Increased fMRI responses during encoding in mild cognitive impairment," *Neurobiol Aging*, 28: 1889–1903, 2007.

[71] H. S. Hani, E. Ata, B. F. Abbas, "Identification of the Early Stage of Alzheimer's Disease Using Structural MRI and Resting-State fMRI," *Frontiers in Neurology*, vol. 10, 2019.

[72] C. Sole-Padulles, D. Bartres-Faz, C. Junque, P. Vendrell, L. Rami, I. C. Clemente, B. Bosch, A. Villar, N. Bargallo, M. A. Jurado, et al., "Brain structure and function related to cognitive reserve variables in normal aging, mild cognitive impairment and Alzheimer's disease," *Neurobiol Aging*, 30: 1114–1124, 2009.

[73] I. M. McDonough, S. B. Festini, M. M. Wood, "Risk for Alzheimer's disease: A review of long-term episodic memory encoding and retrieval fMRI studies," *Ageing Research Reviews*, vol. 62, 2020.

[74] R. A. Sperling, P. S. Laviolette, K. O'Keefe, J. O'Brien, D. M. Rentz, M. Pihlajamaki, G. Marshall, B. T. Hyman, D. J. Selkoe, T. Hedden, et al., "Amyloid deposition is associated with impaired default network function in older persons without dementia," *Neuron*, 63: 178–188, 2009.

[75] B. C. Dickerson, F. Agosta, M. Filippi, "fMRI in Neurodegenerative Diseases: From Scientific Insights to Clinical Applications. In: Filippi M. (eds) fMRI Techniques and Protocols," *Neuromethods*, vol 119. Humana Press, New York, NY, 2016.

[76] F. Clement, S. Belleville, "Test-retest reliability of fMRI verbal episodic memory paradigms in healthy older adults and in persons with mild cognitive impairment," *Hum Brain Mapp*, 30: 4033–4047, 2009.

[77] D. Putcha, et al., "Hippocampal hyperactivation associated with cortical thinning in Alzheimer's disease signature regions in non-demented elderly adults," *J Neurosci* 31(48):17680–17688, 2011.

[78] E. M. Reiman, R. J. Caselli, L. S. Yun, K. Chen, D. Bandy, S. Minoshima, S. N. Thibodeau, D. Osborne, "Preclinical evidence of Alzheimer's disease in persons homozygous for the 14 allele for apolipoprotein E," *New Engl J Med* 334: 752–758, 1996.

[79] N. L. Foster, T. N. Chase, P. Fedio, N. J. Patronas, R. A. Brooks, G. Di Chiro, "Alzheimer's disease: Focal cortical changes shown by positron emission tomography," *Neurology* 33: 961–965, 1983.

[80] S. Minoshima, B. Giordani, S. Berent, K. A. Frey, N. L. Foster, D. E. Kuhl, "Metabolic reduction in the posterior cingulate cortex in very early Alzheimer's disease," *Ann Neurol* 42: 85–94, 1997.

[81] S. De Santi, M. J. de Leon, H. Rusinek, A. Convit, C. Y. Tarshish, A. Roche, W. H. Tsui, E. Kandil, M. Boppana, K. Daisley, et al., "Hippocampal formation glucose metabolism and volume losses in MCI and AD," *Neurobiol Aging*, 22: 529–539, 2001.

[82] M. E. Raichle, A. M. MacLeod, A. Z. Snyder, W. J. Powers, D. A. Gusnard, G.L. Shulman, "A default mode of brain function," *Proc Natl Acad Sci* 98: 676–682, 2001.

[83] W. E. Klunk, Y. Wang, G. F. Huang, M. L. Debnath, D. P. Holt, L. Shao, R. L. Hamilton, M. D. Ikonomovic, S. T. DeKosky, C. A. Mathis, "The binding of 2-(40-methylaminophenyl)-benzothiazole to postmortem brain homogenates is dominated by the amyloid component," *J Neurosci* 23:2086–2092, 2003.

[84] R. L. Buckner, A. Z. Snyder, B. J. Shannon, G. LaRossa, R. Sachs, A. F. Fotenos, Y. I. Sheline, W. E. Klunk, C. A. Mathis, J. C. Morris, et al., "Molecular, structural, and functional characterization of Alzheimer's disease: Evidence for a relationship between default activity, amyloid, and memory," *J Neurosci*, 25: 7709–7717, 2005.

[85] N. L. Foster, J. L. Heidebrink, C. M. Clark, W. J. Jagust, S. E. Arnold, N. R. Barbas, C. S. DeCarli, R. S. Turner, R. A. Koeppe, R. Higdon, et al., "FDG-PET improves accuracy in distinguishing frontotemporal dementia and Alzheimer's disease," *Brain*, 130: 2616–2635, 2007.

[86] M. Ortner, R. Drost, D. Heddderich, et al., "Amyloid PET, FDG-PET or MRI? - the power of different imaging biomarkers to detect progression of early Alzheimer's disease," *BMC Neurol*, vol. 19, no. 264. 2019. https://doi.org/10.1186/s12883-019-1498-9

[87] Y. Ou, W. Xu, J. Li, et al., "FDG-PET as an independent biomarker for Alzheimer's biological diagnosis: a longitudinal study," *Alz Res Therapy*, vol. 11, no. 57, 2019, https://doi.org/10.1186/s13195-019-0512-1.

[88] K. Chen, J. B. Langbaum, A. S. Fleisher, N. Ayutyanont, C. Reschke, W. Lee, X. Liu, D. Bandy, G. E. Alexander, P. M. Thompson, et al., "Twelve-month metabolic declines in probable Alzheimer's disease and amnestic mild cognitive impairment assessed using an empirically pre-defined statistical region-of-interest: Findings fromthe Alzheimer's Disease Neuroimaging Initiative," *Neuroimage* 51: 654–664, 2010.

[89] V. L. Villemagne, C. A. McLean, K. Reardon, A. Boyd, V. Lewis, G. Klug, G. Jones, D. Baxendale, C. L. Masters, C. C. Rowe, et al., "11C-PiB PET studies in typical sporadic Creutzfeldt–Jakob disease," *J Neurol Neurosurg Psychiatry* 80: 998–1001, 2009.

[90] N. M. Kemppainen, S. Aalto, I. A. Wilson, K. Nagren, S. Helin, A. Bruck, V. Oikonen, M. Kailajarvi, M. Scheinin, M. Viitanen, et al., "Voxel-based analysis of PETamyloid ligand [11C]PIB uptake in Alzheimer disease," *Neurology*, 67:1575–1580, 2006.

[91] P. Edison, H. A. Archer, A. Gerhard, R. Hinz, N. Pavese, F. E. Turkheimer, A. Hammers, Y. F. Tai, N. Fox, A. Kennedy A, et al., "Microglia, amyloid, and cognition in Alzheimer's disease: An [11C](R)PK11195-PET and [11C]PIB-PET study," *Neurobiol Dis*, 32: 412–419, 2008.

[92] V. J. Lowe, B. J. Kemp, C. R. Jack Jr, M. Senjem, S. Weigand, M. Shiung, G. Smith, D. Knopman, B. Boeve, B. Mullan, et al., "Comparison of 18F-FDG and PiB PET in cognitive impairment," *J Nucl Med*, 50: 878–886, 2009.

[93] N. Tolboom, W. M. van der Flier, J. Boverhoff, M. Yaqub, M. P. Wattjes, P. G. Raijmakers, F. Barkhof, P. Scheltens, K. Herholz, A. A. Lammertsma, et al., "Molecular imaging in the diagnosis of Alzheimer's disease: Visual assessment of [11C]PIB and [18F]FDDNP PET images," *J Neurol Neurosurg Psychiatry*, 81: 882–884, 2010.

[94] W. E. Klunk, H. Engler, A. Nordberg, Y. Wang, G. Blomqvist, D. P. Holt, M. Bergstro¨m, I. Savitcheva, G. F. Huang, S. Estrada, et al., "Imaging brain amyloid in Alzheimer's disease with Pittsburgh Compound-B," *Ann Neurol*, 55:306–319, 2004.

[95] C. M. Clark, J. A. Schneider, B. J. Bedell, T. G. Beach, W. B. Bilker, M. A. Mintun, M. J. Pontecorvo, F. Hefti, A. P. Carpenter, M. L. Flitter, et al., "AV45-A07 Study Group. Use of florbetapir-PET for imaging b-amyloid pathology," *J Am Med Assoc*, 305: 275–283, 2011.

[96] A. Kadir, O. Almkvist, A. Forsberg, A. Wall, H. Engler, B. Långström, A. Nordberg, "Dynamic changes in PET amyloid and FDG imaging at different stages of Alzheimer's disease," *Neurobiology of Aging*, vol. 33, no. 1, 2012, pp. 198.e1-198.e14

[97] C. R. Jack Jr, D. S. Knopman, W. J. Jagust, L. M. Shaw, P. S. Aisen, M. W. Weiner, R. C. Petersen, J. Q. Trojanowski, "Hypothetical model of dynamic biomarkers of the Alzheimer's pathological cascade," *Lancet Neurol*, 9: 119–128, 2010.

[98] N. J. Cairns, M. D. Ikonomovic, T. Benzinger, M. Storandt, A. M. Fagan, A. Shah, R. E. Schmidt, A. Perry, L. T. Reinwald, D. Carter, et al., "Absence of Pittsburgh Compound B detection of cerebral amyloid b in a patient with clinical, cognitive, and cerebrospinal fluid markers of Alzheimer disease," *Arch Neurol* 66: 1557–1562, 2009.

[99] K. A. Johnson, A. Schultz, R. A. Betensky, J. A. Becker, J. Sepulcre, D. Rentz, et al., "Tau positron emission tomographic imaging in aging and early Alzheimer disease," *Annals of Neurology*, 79(1):110–119, 2016.

[100] R. Ossenkoppele, D. R. Schonhaut, M. Schöll, S. N. Lockhart, N. Ayakta, S. L. Baker, et al., "Tau PET patterns mirror clinical and neuroanatomical variability in Alzheimer's disease," *Brain*, 139(5):1551–1567, 2016.

[101] E. Giacobini, G. Gold, "Alzheimer disease therapy: moving from amyloid-β to tau," *Nature Reviews Neurology*, 9(12):677–686, 2013. [PubMed: 24217510]

[102] H. Wood, "Alzheimer disease: [11C]PBB3—a new PET ligand that identifies tau pathology in the brains of patients with AD," *Nature Reviews Neurology*, 9(11):599–599, 2013.

[103] N. Okamura, S. Furumoto, R. Harada, T. Tago, T. Yoshikawa, M. Fodero-Tavoletti, et al., "Novel 18F-Labeled Arylquinoline Derivatives for Non-invasive Imaging of Tau Pathology in Alzheimer Disease," *Journal of Nuclear Medicine*, 54(8):1420–1427, 2013.

[104] V. Villemagne, C. Rowe, G. Tamagnan, M. Fodero-Tavoletti, N. Okamura, S. Furumoto, et al., "In vivo Tau Imaging with 18F-THK5105 and 18F-THK5117," *Alzheimer's & Dementia*,10(4):P241, 2014.

[105] R. Harada, N. Okamura, S. Furumoto, T. Tago, K. Yanai, H. Arai, et al., "Characteristics of Tau and Its Ligands in PET Imaging," *Biomolecules*, 6(1):7, 2016.

[106] C. Lois, I. Gonzalez, K. A. Johnson, et al., "PET imaging of tau protein targets: a methodology perspective," *Brain Imaging and Behavior*, 13, 333–344, 2019.

[107] M. Marquie, M. D. Normandin, C. R. Vanderburg, I. M. Costantino, E. A. Bien, L. G. Rycyna, et al., "Validating novel tau positron emission tomography tracer [F-18]-AV-1451 (T807) on postmortem brain tissue," *Annals of Neurology*, 78(5):787–800, 2015.

[108] M. Dani, D. Brooks, P. Edison, "Tau imaging in neurodegenerative diseases," *Eur J Nucl Med Mol Imaging*, 43:1139–50, 2016.

[109] C. R. Jack, D. A. Bennett, K. Blennow, M. C. Carrillo, et. al., "NIA-AA Research Framework: Toward a biological definition of Alzheimer's disease," *Alzheimer's & Dementia*, vol. 14, 2018, pp. 535-562.

[110] D. A. Bennett, J. A. Schneider, R. S. Wilson, J. L. Bientas, and S. E. Arnold, "Neurofibrillary tangles mediate the association of amyloid load with clinical Alzheimer disease and level of cognitive function," *Arch. Neurol.*, vol. 61, 2004, pp. 378-384.

[111] C. Xiong, M. S. Jasielee, H. Weng, A. M. Fagan, T. L. Benzinger, et. al., "Longitudinal relationships among biomarkers for Alzheimer disease in the Adult Children Study," *Neurology*, vol. 86, 2016, pp. 1499-1506.

[112] B. T. Hyman, C. H. Phelps, T. G. Beach, E. H. Bigio, et. al., "National Institute on Aging Alzheimer's Association guidelines for the neuropathologic assessment of Alzheimer's disease: a practical approach," *Acta Neuropathol.*, vol. 123, 2012, pp. 1-11.

[113] P. M. Rossini, R. Di Iorio, M. Bentivoglio, G. Bertini, F. Ferreri, et. al., "Conversion from mild cognitive impairment to Alzheimer's disease is predicted by sources and coherence of brain electroencephalography rhythms," *Neuroscience*, vol. 143, 2006, pp. 793-803.

[114] Y. Han, T. Lauteslager, T. S. Lande and T. G. Constandinou, "UWB Radar for Non-contact Heart Rate Variability Monitoring and Mental State Classification," 2019 41st Annual International Conference of the IEEE Engineering in Medicine and Biology Society (EMBC), Berlin, Germany, 2019, pp. 6578-6582.

[115] B. Hsieh, E. C. Harding, W. Wisden, N. P. Franks, and T. G. Constandinou, "A Miniature Neural Recording Device to Investigate Sleep and Temperature Regulation in Mice," 2019 IEEE Biomedical Circuits and Systems Conference (BioCAS), Nara, Japan, 2019, pp. 1-4, doi: 10.1109/BIOCAS.2019.8918722.

[116] P. M. Rossini, R. Di Iorio, F. Vecchio, M. Anfossi, C. Babiloni, et. al., "Early diagnosis of Alzheimer's disease: the role of biomarkers including advanced EEG signal analysis. Report from IFCN-sponsored panel of experts," *Clinical Neurophysiology*, vol. 131, 2020, pp. 1287-1310.

[117] C. Huang, L. Wahlund, T. Dierks, P. Julin, B. Winblad, and V. Jelic, "Discrimination of Alzheimer's disease and mild cognitive impairment by equivalent EEG sources: a cross-sectional and longitudinal study," *Clin. Neurophysiol.*, vol. 111, 2000, pp. 1961-1967.

[118] G. Adler, S. Brassen, and A. Jajcevic, "EEF coherence in Alzheimer's dementia," *J. Neural Trasnm.*, vol. 110, 2003, pp. 1051-1058.

[119] W. de Haan, K. Mott, E. C. Straaten, P. Scheltens, and J. C. Stam, "Activity dependent degeneration explains hub vulnerability in Alzheimer's disease," *PLOS Comput. Biol.*, vol 8, 2012a e1002582.

[120] X. Hadoux, F. Hui, J. K. Lim, et al., "Non-invasive in vivo hyperspectral imaging of the retina for potential biomarker use in Alzheimer's disease," *Nat Commun*, vol. 10, no. 4227, 2019, https://doi.org/10.1038/s41467-019-12242-1.

[121] D. Ireland and M. Bialkowski, "Feasibility Study on Microwave Stroke Detection using a Realistic Phantom and the FDTD Method," in *Microwave Conference Proceedings (APMC), 2010 Asia-Pacific*, 2010, pp. 1360–1363.

[122] B. Smith and M. H. Carpentier, The Microwave Engineering Handbook. Chapman & Hall, 1993.

[123] J. C. Maxwell, "On Physical Lines of Force," *Philosophical Magazine*, vol. 90, pp. 11-23, 1861.

[124] M. Golio and J. Golio, *RF and Microwave Applications and Systems*, CRC Press, 2008.

[125] S. Semenov, B. Seiser, E. Stoegmann, E. Auff, and E. Gmbh, “Electromagnetic Tomography for Brain Imaging : from virtual to human brain,” in IEEE Conference on Antenna Measurements & Applications (CAMA), 2014, pp. 1–4.
[126] S. Semenov, R. Planas, M. Hopfer, A. Hamidipour, A. Vasilenko, E. Stoegmann, and E. Auff, “Electromagnetic tomography for brain imaging: Initial assessment for stroke detection,” *2015 IEEE Biomed. Circuits Syst. Conf.*, pp. 1–4, 2015.
[127] A. Fhager and M. Persson, “A Microwave Measurement System for Stroke Detection,” *Loughbrgh. Antennas Propag. Conf.*, no. November, pp. 14–15, 2011.
[128] J. C. Ljungqvist, “Diagnostic Methods in Traumatic Brain Injury,” University of Gothenburgh, 2017.
[129] A. G. Lalkhen and A. McCluskey, “Clinical tests: Sensitivity and specificity,” *Contin. Educ. Anaesthesia, Crit. Care Pain*, vol. 8, no. 6, pp. 221–223, 2008.
[130] M. Jalilvand, T. Zwick, W. Wiesbeck, and E. Pancera, “UWB synthetic aperture-based radar system for hemorrhagic head-stroke detection,” *2011IEEE RadarCon*, pp. 956–959, 2011.
[131] H. Zhang, B. Flynn, A. T. Erdogan, and T. Arslan, “Microwave Imaging for Brain Tumour Detection using an UWB Vivaldi Antenna Array,” in *Loughborough Antennas & Propagation Conference*, 2012, pp. 1–4.
[132] M. S. R. Bashri, “Wearable Devices for Microwave Head Diagnostic Systems,” University of Edinburgh, 2018.
[133] B. J. Mohammed, A. M. Abbosh, and D. Ireland, “Stroke Detection Based on Variations in Reflection Coefficients of Wideband Antennas,” in *IEEE Antennas and Propagation Society International Symposium (APSURSI)*, 2012, pp. 1–2.
[134] A. T. Mobashsher and A. M. Abbosh, “Compact 3-D Slot-Loaded Folded Dipole Antenna with Unidirectional Radiation and Low Impulse Distortion for Head Imaging Applications,” *IEEE Trans. Antennas Propag.*, vol. 64, no. 7, pp. 3245–3250, 2016.
[135] A. Abbosh and A. T. Mobashsher, “Development of Compact Directional Antenna utilising Plane of Symmetry for Wideband Brain Stroke Detection Systems,” *Electron. Lett.*, vol. 50, no. 12, pp. 850–851, 2014.
[136] A. E. Stancombe, K. S. Bialkowski and A. M. Abbosh, "Portable Microwave Head Imaging System Using Software-Defined Radio and Switching Network," in *IEEE Journal of Electromagnetics, RF and Microwaves in Medicine and Biology*, vol. 3, no. 4, pp. 284-291, Dec. 2019, doi: 10.1109/JERM.2019.2901360.
[137] A. S. M. Alqadami, K. S. Bialkowski, A. T. Mobashsher and A. M. Abbosh, "Wearable Electromagnetic Head Imaging System Using Flexible Wideband Antenna Array Based on Polymer Technology for Brain Stroke Diagnosis," in *IEEE Transactions on Biomedical Circuits and Systems*, vol. 13, no. 1, pp. 124-134, Feb. 2019, doi: 10.1109/TBCAS.2018.2878057..
[138] M. S. R. Bashri, T. Arslan, W. Zhou and N. Haridas, "Wearable device for microwave head imaging," 2016 46th European Microwave Conference (EuMC), London, 2016, pp. 671-674.
[139] M. S. R. Bashri and T. Arslan, "Low-cost and compact RF switching system for wearable microwave head imaging with performance verification on artificial head phantom," in IET Microwaves, Antennas & Propagation, vol. 12, no. 5, pp. 706-711, 18 4 2018.
[140] M. Manoufali, A. T. Mobashsher, B. Mohammed, K. S. Bialkowski, P. Mills and A. M. Abbosh, "Implantable Sensor for Detecting Changes in the Loss Tangent of Cerebrospinal Fluid," in IEEE Transactions on Biomedical Circuits and Systems, 2020.

[141] S. Yan, P. J. Soh and G. A. E. Vandenbosch, "Wearable Dual-Band Magneto-Electric Dipole Antenna for WBAN/WLAN Applications," in IEEE Transactions on Antennas and Propagation, vol. 63, no. 9, pp. 4165-4169, Sept. 2015.

[142] H. Lee, J. Tak and J. Choi, "Wearable Antenna Integrated into Military Berets for Indoor/Outdoor Positioning System," in IEEE Antennas and Wireless Propagation Letters, vol. 16, pp. 1919-1922, 2017.

[143] Z. H. Jiang, D. E. Brocker, P. E. Sieber and D. H. Werner, "A Compact, Low-Profile Metasurface-Enabled Antenna for Wearable Medical Body-Area Network Devices," in IEEE Transactions on Antennas and Propagation, vol. 62, no. 8, pp. 4021-4030, Aug. 2014.

[144] A. Smida, A. Iqbal, A. J. Alazemi, M. I. Waly, R. Ghayoula and S. Kim, "Wideband Wearable Antenna for Biomedical Telemetry Applications," in IEEE Access, vol. 8, pp. 15687-15694, 2020.

[145] A. S. M. Sayem, R. B. V. B. Simorangkir, K. P. Esselle and R. M. Hashmi, "Development of Robust Transparent Conformal Antennas Based on Conductive Mesh-Polymer Composite for Unobtrusive Wearable Applications," in IEEE Transactions on Antennas and Propagation, vol. 67, no. 12, pp. 7216-7224, Dec. 2019.

[146] W. T. Li, Y. Q. Hei, P. M. Grubb, X. Shi, and R. T. Chen, "Inkjet Printing of Wideband Stacked Microstrip Patch Array Antenna on Ultrathin Flexible Substrates," in IEEE Transactions on Components, Packaging and Manufacturing Technology, vol. 8, no. 9, pp. 1695-1701, Sept. 2018.

[147] L. Zhang, Z. Wang, and J. L. Volakis, "Textile Antennas and Sensors for Body-Worn Applications," in IEEE Antennas and Wireless Propagation Letters, vol. 11, pp. 1690-1693, 2012.

[148] C. Lin, C. Chang, Y. T. Cheng, and C. F. Jou, "Development of a Flexible SU-8/PDMS-Based Antenna," in IEEE Antennas and Wireless Propagation Letters, vol. 10, pp. 1108-1111, 2011.

[149] G. A. Casula, G. Montisci, and G. Mazzarella, “A Wideband PET Inkjet-Printed Antenna for UHF RFID,” *IEEE Antennas Wirel. Propag. Lett.*, vol. 12, pp.1400–1403, 2013.

[150] S. Ahmed, F. A. Tahir, A. Shamim, and H. M. Cheema, “A Compact Kapton-Based Inkjet-Printed Multiband Antenna for Flexible Wireless Devices,” *IEEEAntennas Wirel. Propag. Lett.*, vol. 14, pp. 1802–1805, 2015.

[151] Jilani, S.F.; Abbasi, Q.H.; Alomainy, A. Inkjet-Printed Millimetre-Wave PET-Based Flexible Antenna for 5G Wireless Applications. In Proceedings of the 2018 IEEE MTT-S International Microwave Workshop Series on 5G Hardware and System Technologies (IMWS-5G), Dublin, Ireland, 30–31 August 2018.

[152] K. Wang and J. Li, "Jeans Textile Antenna for Smart Wearable Antenna," 2018 12th International Symposium on Antennas, Propagation and EM Theory (ISAPE), Hangzhou, China, 2018, pp. 1-3.

[153] S. J. Chen, D. C. Ranasinghe and C. Fumeaux, "A Robust Snap-On Button Solution for Reconfigurable Wearable Textile Antennas," in IEEE Transactions on Antennas and Propagation, vol. 66, no. 9, pp. 4541-4551, Sept. 2018.

[154] T. F. Kennedy, P. W. Fink, A. W. Chu, N. J. Champagne, G. Y. Lin, and M. A. Khayat, "Body-Worn E-Textile Antennas: The Good, the Low-Mass, and the Conformal," in IEEE Transactions on Antennas and Propagation, vol. 57, no. 4, pp. 910-918, April 2009.

[155] A. Yadav, V. K. Singh, M. Chaudhary et al., “A review on wearable textile antenna,” *Journal of Telecommunication Switching System and Networks*, 2(3): pp. 37–41, 2015.

[156] V. K. Singh and B. Naresh, "Multi Resonant Microstrip Antenna with Partial Ground for Radar Application, *J. Telecommun. Switch Syst. Netw.*, 2014, vol. 2, no. 2.

[157] J. G. Santasa, A. Alomainy, and Y. Hao, "Textile Antennas for On-Body Communications: Techniques and Properties," *Antennas and Propagation (EuCAP)*, Edinburgh, 2007, pp. 1-4.

[158] J. Lilja, P. Salonen, T. Kaija, P. De Maagt, "Design and Manufacturing of Robust Textile Antennas for Harsh Environments," *IEEE Trans. Antennas Propag.*, 60, 4130–4140, 2012.

[159] B. Mohamadzade, R. M. Hashmi, R. B. V. B. Simorangkir, R. Gharaei, S. Ur Rehman, Q. Abbasi, "Recent Advances in Fabrication Methods for Flexible Antennas in Wearable Devices: State of the Art," *Sensors*, 19, 2312, 2019.

[160] J. Trajkovikj, J. F. Zürcher, A. K. Skrivervik, "PDMS, a robust casing for flexibleW-BAN antennas" *IEEE Antennas Propag. Mag.*, 55, 287–297, 2013.

[161] Q. H. Abbasi, M. U. Rehman, X. Yang, A. Alomainy, K. Qaraqe, E. Serpedin, "Ultrawideband Band-Notched Flexible Antenna for Wearable Applications," *IEEE Antennas Wirel. Propag. Lett.*, 12, 1606–1609, 2013.

[162] Y. Zhou, Y. Bayram, F. Du, L. Dai, J. L. Volakis, "Polymer-Carbon Nanotube Sheets for Conformal Load Bearing Antennas," *IEEE Trans. Antennas Propag.*, 2010, 58, 2169–2175.

[163] L. Song, A. C. Myers, J. J. Adams, Y. Zhu, "Stretchable and Reversibly Deformable Radio Frequency Antennas Based on Silver Nanowires," *ACS Appl. Mater. Interfaces*, 2014, 6, 4248–4253.

[164] G. W. Huang, H. M. Xiao, S. Y. Fu, "Wearable electronics of silvernanowire/poly (dimethylsiloxane) nanocomposite for smart clothing," *Sci. Rep.*, 2015, 5, 13971.

[165] A. Kiourti, J. L. Volakis, "Stretchable and Flexible E-FiberWire Antennas Embedded in Polymer," *IEEE Antennas Wirel. Propag. Lett.*, 2014, 13, 1381–1384.

[166] R. B. V. B. Simorangkir, Y. Yang, K. P. Esselle, B. A. Zeb, "A Method to Realize Robust Flexible Electronically Tunable Antennas Using Polymer-Embedded Conductive Fabric," *IEEE Trans. Antennas Propag.*, 2018, 66, 50–58.

[167] R. B. V. B. Simorangkir, Y. Yang, R. M. Hashmi, T. Bjorninen, K. P. Esselle, L. Ukkonen, "Polydimethylsiloxane-Embedded Conductive Fabric: Characterization and Application for Realization of Robust Passive and Active Flexible Wearable Antennas," *IEEE Access*, 2018, 6, 48102–48112.

[168] M. Koohestani, M. N. Moghadasi, and B. S. Virdee, "Miniature Microstrip-Fed Ultra-Wideband Printed Monopole Antenna with a Partial Ground Plane Structure," *IET Microwaves, Antennas Propag.*, vol. 5, no. 14, p. 1683, 2011.

[169] A. Rahman and Y. Hao, "A Novel Tapered Slot CPW-fed Antenna for Ultra-Wideband Applications and its On/Off-Body Performance," in *IEEE International Workshop on Antenna Technology: Small and Smart Antennas Metamaterials and Applications, iWAT 2007*, 2007, pp. 503–506.

[170] S. W. Su, K. L. Wong, and C. L. Tang, "Ultra-Wideband Square Planar Monopole Antenna for IEEE 802.16a Operation in the 2-11-GHz Band," *Microw. Opt. Technol. Lett.*, vol. 42, no. 6, pp. 463–466, 2004.

[171] A.-C. Tarot, F. Las-Heras, M. Mantash, and M. E. de Cos, "Dual-Band Coplanar Waveguide-Fed Smiling Monopole Antenna for WiFi and 4G Long-Term Evolution Applications," *IET Microwaves, Antennas Propag.*, vol. 7, no. 9, pp. 777–782, 2013.

[172] M. Tømmer and K. G. Kjelg, "Body Coupled Wideband Monopole Antenna," in *Loughborough Antennas & Propagation Conference (LAPC)*, 2016, pp. 1–5.

[173] A. Rahman, M. T. Islam, M. J. Singh, S. Kibria, and M. Akhtaruzzaman, “Electromagnetic Performances Analysis of an Ultra-wideband and Flexible Material Antenna in Microwave Breast Imaging: To Implement A Wearable Medical Bra,” *Sci. Rep.*, vol. 6, no. 1, p. 38906, 2016.
[174] K. P. Ray, “Design Aspects of Printed Monopole Antennas for Ultra-Wide Band Applications,” Int. J. Antennas Propag., pp. 1–8, 2008.
[175] B. Allen, M. Dohler, E. Okon, and W. Malik, Ultra-wideband Antennas and Propagation for Communications, Radar, and Imaging. John Wiley & Sons, Inc., 2006.
[176] N. P. Agrawall, G. Kumar, and K. P. Ray, “Wide-band planar monopole antennas,” IEEE Transactions on Antennas and Propagation, vol. 46, no. 2, pp. 294–295, 1998.
[177] T. Stroeber, The University of Edinburgh, M.Sc. Thesis, 2017.
[178] W. Sun, Y. Li, Z. Zhang, and Z. Feng, "Broadband and Low-Profile Microstrip Antenna Using Strip-Slot Hybrid Structure," in IEEE Antennas and Wireless Propagation Letters, vol. 16, pp. 3118-3121, 2017.
[179] B. Gao, G. Wu, J. Y. huo, and X. J. Tian, “Planar Antenna Aids UWB Communications,” *Micrwoave & RF*, Oct. 2013 [Online]. Available: https://www.mwrf.com/technologies/components/article/21845337/planar-antenna-aids-uwb-communications
[180] W. S. T. Rowe and R. B. Waterhouse, "Edge-fed patch antennas with reduced spurious radiation," in IEEE Transactions on Antennas and Propagation, vol. 53, no. 5, pp. 1785-1790, May 2005.
[181] O. Barrou, A. El Amri, A. Reha, “Comparison of Feeding Modes for a Rectangular Microstrip Patch Antenna for 2.45 GHz Applications,” In: El-Azouzi R., Menasche D., Sabir E., De Pellegrini F., Benjillali M. (eds) Advances in Ubiquitous Networking 2. UNet 2016. Lecture Notes in Electrical Engineering, vol 397. Springer, Singapore, 2017.
[182] N. I. Zaidi et al., "Analysis of Different Feeding Techniques on Textile Antenna," 2019 International Symposium on Antennas and Propagation (ISAP), Xi'an, China, 2019, pp. 1-3.
[183] S. S. Chakravarthy, N. Sarveshwaran, S. Sriharini and M. Shanmugapriya, "Comparative study on different feeding techniques of rectangular patch antenna," *2016 Thirteenth International Conference on Wireless and Optical Communications Networks (WOCN)*, Hyderabad, 2016, pp. 1-6, doi: 10.1109/WOCN.2016.7759032.
[184] C. Ahumada, H. Kaschel, R. Osorio-Comparan and G. Lefranc, "Design of Microstrip Patch Antenna with quarter wave transformer for ISM Band," *2019 IEEE CHILEAN Conference on Electrical, Electronics Engineering, Information and Communication Technologies (CHILECON)*, Valparaiso, Chile, 2019, pp. 1-6, doi: 10.1109/CHILECON47746.2019.8986857.
[185] J. C. Lin, “A New IEEE Standard For Safety Levels with respect to Human Exposure to Radio-Frequency Radiation,” *IEEE Antennas Propag. Mag.*, vol. 48, no. 1, pp. 157–159, 2006.
[186] B. Rajagopal and L. Rajasekaran, “SAR Assessment on Three Layered Spherical Human Head Model Irradiated by Mobile Phone Antenna,” pp. 1–11, 2014.
[187] P. Bernardi, M. Cavagnaro, and S. Pisa, “Evaluation of the SAR distribution in the human head for cellular phones used in a partially closed environment,” *IEEE Trans. Electromagn. Compat.*, vol. 38, no. 3, pp. 357–366, 1996.
[188] S. Khalatbari, D. Sardari, A. A. Mirzaee, and H. A. Sadafi, “Calculating SAR in two Models of the Human Head Exposed to Mobile Phones Radiations at 900 and 1800 MHz,” *PIERS Online*, vol. 2, no. 1, pp. 104–109, 2006.

[189] Y.-H. Hao, L. Zhao, and R.-Y. Peng, “Effects of microwave radiation on brain energy metabolism and related mechanisms,” *Mil. Med. Res.*, vol. 2, no. 1, p. 4, 2015.
[190] R. Varghese, A. Majumdar, G. Kumar, and A. Shukla, “Rats exposed to 2.45 GHz of non-ionizing radiation exhibit behavioral changes with increased brain expression of apoptotic caspase 3,” *Pathophysiology*, vol. 25, no. 1, pp. 19–30, 2018.
[191] S. Hussein, A. A. El-Saba, and M. K. Galal, “Biochemical and histological studies on adverse effects of mobile phone radiation on rat’s brain,” *J. Chem. Neuroanat.*, vol. 78, pp. 10–19, 2016.
[192] P. a Valberg, “Ratio Frequency Radiation (RFR):the Nature of Exposure and Carcinogenic Potential,” *Cancer Causes Control*, vol. 8, pp. 323–332, 1997.
[193] S. Alves, R. Fol, and N. Cartier, “Gene Therapy Strategies for Alzheimer’s Disease: An Overview,” *Human Gene Therapy*, vol. 27, no. 2, Feb. 2016.
[194] C. Ballatore, V. Lee, and J. Trojanowski, “Tau mediated neurodegeneration in Alzheimer’s disease and related disorders,” Nat. Rev. Neurosci., vol. 8, pp. 663-672, 2007.
[195] M. Jucker and L. C. Walker, “Self-Propagation of Neurodegenerative Diseases,” *Nature*, vol. 501, pp. 45-51, 2013.
[196] H. Takahashi, T. Nagao, and G. K. Gouras, “Plaque formation and the intraneuronal accumulation of Beta-Amyloid in Alzheimer’s disease,” Pathology International, vol. 67, pp. 185-193, 2017.
[197] R. Michael, A. Lenferink, G. Vrensen, E. Gelpi, R. Barraquer, and C. Otto, “Hyperspectral Raman imaging of neuritic plaques and neurofibrillary tangles in brain tissue from Alzheimer’s disease patients,” *Scientific Reports*, vol. 7, no. 15603, pp. 1-11, 2017.
[198] O. Sabri, M. Sabbagh, J. Seibyl, H. Barthel, H. Akatsu, et. al., “Florbetaben PET imaging to detect amyloid beta plaques in Alzheimer’s disease: Phase 3 study,” *Alzheimer’s & Dementia*, vol. 11, no. 8, pp. 965-974, 2015.
[199] M. White, N. Foster, A. Fleisher, et. al., “Clinical use of amyloid-positron emission tomography neuroimaging: Practical and bioethical considerations,” *Alzheimer’s & Dementia: Diagnosis, Assessment & Disease Monitoring*, vol. 1, no. 3, pp. 358-367, 2015.
[200] M. Manoufali, S. A. R. Naqvi and A. M. Abbosh, "Accurate Fourth-Order Debye Model for the Head Tissues Across the 0.1–1 GHz Band Using Metaheuristic Genetic Algorithm," in *IEEE Journal of Electromagnetics, RF and Microwaves in Medicine and Biology*, vol. 2, no. 2, pp. 79-86, June 2018.
[201] M. Lazebnik, M. Okoniewski, J. H. Booske and S. C. Hagness, "Highly Accurate Debye Models for Normal and Malignant Breast Tissue Dielectric Properties at Microwave Frequencies," in *IEEE Microwave and Wireless Components Letters*, vol. 17, no. 12, pp. 822-824, Dec. 2007, doi: 10.1109/LMWC.2007.910465.
[202] S. Semenov, T. Huynh, T. Williams, B. Nicholson, A. Vasilenko, “Dielectric properties of brain tissue at 1 GHz in acute ischemic stroke: Experimental study on swine,” *Bioelectromagnetics*, vol. 38, no.2, pp.158-163, 2017, doi: 10.1002/bem.22024.
[203] P.A. Hasgall, F. Di Gennaro, C. Baumgartner, et. al., “IT’IS Database for thermal and electromagnetic parameters of biological tissues,” Version 4.0, May 15, 2018 [Online], DOI: 10.13099/VIP21000-04-0. https://itis.swiss/database
[204] G. Schmid, G. Neubauer, U. M. Illievich, F. Alesch, “Dielectric properties of porcine brain tissue in the transition from life to death at frequencies from 800 to 1900 MHz,” *Bioelectromagnetics*, vol. 24, no. 6, pp. 413-422, 2003, doi:10.1002/bem.10122.
[205] G. Schmid, G. Neubauer, and P. R. Mazal, “Dielectric properties of human brain tissue measured less than 10 h postmortem at frequencies from 800 to 2450 MHz,” *Bioelectromagnetics*, vol. 24, no. 6, pp. 423-430, 2003.

[206] A. Arayeshnia, A. Keshtkar and S. Amiri, "Realistic human head voxel model for brain microwave imaging," *2017 Iranian Conference on Electrical Engineering (ICEE)*, Tehran, 2017, pp. 1660-1663. doi: 10.1109/IranianCEE.2017.7985315

[207] D. Bennett, J.Scheider, J. Bienias, D. Evans, and R. Wilson, "Mild cognitive impairment is related to Alzheimer disease pathology and cerebral infarctions," *Neurology*, vol. 64, no. 5, 2005, pp. 834-841.

[208] W. Markesbery, "Neuropathologic Alterations in Mild Cognitive Impairment: A Review," *Journal of Alzheimer's Disease*, vol. 19, no. 1, 2010, pp. 221-228.

[209] S. S. Rengachary and R. G. Ellenbogen, *Principles of Neurosurgery*, Edinburgh: Elsevier Mosby, 2005.

[210] R. Solimene, A. Dell'Aversano, and G. Leone, "Interferometric time reversal music for small scatterer localization," Progress In Electromagnetics Research, vol. 131, pp. 243–258, 2012.

[211] M. A. Elahi, D. O'Loughlin, et al., "Evaluation of Image Reconstruction Algorithms for Confocal Microwave Imaging: Application to Patient Data," Sensors, vol. 18, no. 6, pp. 1-21, 2018.

[212] S. Mustafa, B. Mohammed, and A. Abbosh, "Novel Preprocessing Techniques for Accurate Microwave Imaging of Human Brain," *IEEE Antennas Wirel. Propag. Lett.*, vol. 12, pp. 460–463, 2013.

[213] L. Guo, "Processing and Imaging Techniques for Microwave-Based Head Imaging," The University of Queensland, 2016.

[214] A. D. Yao, D. L. Cheng, I. Pan, and F. Kitamura, "Deep Learning in Neuroradiaology: A Systematic Review of Current Algorithms and Approaches for the New Wave of Imaging Technology," *Radiology: Artificial Intelligence*, 2020.

[215] B. J. Mohammed, K. S. Bialkowski, and A. M. Abbosh, "Radar-based time domain head imaging using database of effective dielectric constant," *Electron. Lett.*, vol. 51, no. 20, pp. 1574–1576, 2015.

[216] A. T. Mobashsher, "Wideband Microwave Imaging System for Brain Injury Diagnosis," The University of Queensland, Queensland, Australia, 2016.

[217] N. Rahman, A. Sharma, M. Afsar, S. Palreddy, and R. Cheung, "Design and Analysis of An Optimized Cavity-Backed Zigzag Archimedean Spiral Antenna," in *4th European Conference on Antennas and Propagation (EuCAP)*, 2010, pp. 1–4.

[218] H. Bahrami, S. A. Mirbozorgi, R. Ameli, L. A. Rusch, and B. Gosselin, "Flexible, Polarization-Diverse UWB Antennas for Implantable Neural Recording Systems," *IEEE Trans. Biomed. Circuits Syst.*, vol. 10, no. 1, pp. 38–48, 2016.

[219] A. Danideh and R. A. Sadeghzadeh, "A Planar Ultrawideband Elliptical Monopole Antenna with Reflector for Breast Microwave Imaging," *Microw. Opt. Technol. Lett.*, vol. 6, no. 1, pp. 3872–3875, 2013.

[220] "Increasing Directivity in Parabolic Antennas." [Online]. Available: http://www.eccosorb.eu/sites/default/files/files/increasing_directivity_in_parabolic_antennas.pdf. [Accessed: 02-May-2020].

[221] Eccosorb, "ECCOSORB® AN - Emerson & Cuming Microwave Products." [Online]. Available: http://www.eccosorb.com/products-eccosorban.htm.

[222] R. Ullah and T. Arslan, "PySpark-Based Optimization of Microwave Image Reconstruction Algorithm for Head Imaging Big Data on High-Performance Computing and Google Cloud Platform," *Appl. Sci.*, vol. 10, no. 3382, 2020.

Appendices

Table A.1: Four-Pole Cole-Cole Model Parameters across 0.2 to 3 GHz

Tissue Type	ε_∞	$\Delta\varepsilon_1$	τ_1	α_1	$\Delta\varepsilon_2$	τ_2	α_2	$\Delta\varepsilon_3$	τ_3	α_3	$\Delta\varepsilon_4$	τ_4	α_4	σ_s
Gray Matter -AD	40.12	30.09	1.73e-8	0.9903	20.06	7.98e-9	0.9942	30.63	1.73e-8	0.9903	20.06	7.98e-9	0.9942	1.23e-17
Gray Matter -Healthy	34.56	34.53	1.28e-2	0.7747	34.53	1.28e-2	0.7747	34.53	1.28e-2	0.7747	34.53	1.28e-2	0.7747	1.64e-17
White Matter -AD	12.77	6.383	4.35e-14	0.9221	6.383	4.36e-14	0.9221	6.383	4.38e-14	0.9221	6.383	4.40e-14	0.9221	2.91e-18
White Matter -Healthy	22.35	12.35	3.95e-14	0.6606	12.35	3.87e-14	0.6608	0.661	3.71e-14	0.6611	12.35	3.79e-14	0.6611	4.858e-18